Interstellar Boundary Explorer Calibration and Measurement Algorithms Document [*IBEX CMAD*]

Digitally signed by Scott E. Weidner
Date: 2022.12.05 15:55:00 -05'00'

Scott Weidner, IBEX Project Manager — Date

Not Applicable

Project Scientist — Date

HERBERT FUNSTEN (Affiliate) Digitally signed by HERBERT FUNSTEN (Affiliate) Date: 2022.12.20 11:20:07 -07'00'

Herb Funsten, Principal Investigator for IBEX-Hi — Date

Stephen Fuselier Digitally signed by Stephen Fuselier Date: 2022.12.08 17:29:40 -06'00'

Stephen, Fuselier, Principal Investigator for IBEX-Lo — Date

Not Applicable

Instrument Scientist — Date

By signing this document, signatories are certifying that the content herein is acceptable direction for managing the project's data and that they will ensure its implementation by those over whom they have authority.

Copy to: HQ Program Scientist
Archive Project Scientist

1. Change History Log

Revision	Effective Date	Description of Changes
Baseline	10/12/2022	Original

2. Calibration and Measurement Algorithms Document Content

Interstellar Boundary Explorer CALIBRATION AND MEASUREMENT ALGORITHMS DOCUMENT

[IBEX CMAD]

1. Scope

This document summarizes the calibration of the IBEX-Hi and IBEX-Lo instruments as well as the algorithms needed to generate science products from the data produced by these instruments. The scientific objectives of the IBEX mission are described and an overview of the instruments and their measurement concept is provided. The methods used to calibrate IBEX-Hi and IBEX-Lo both prior to launch and in-flight are provided as well as the ongoing effort to evaluate instrument performance. The data algorithms used to process the instrument data into science products are described, including how they have evolved over the course of the mission thus far.

2. Related Documentations

2.1 Applicable Documents

Title	Document Number	Publication Date
ISOC Software and Operations Guide		23 June 2017

3. Overview and Background Information

The Interstellar Boundary Explorer (IBEX) is a small explorer mission that launched on 19 October 2008 with the sole, focused science objective to discover the global interaction between the solar wind and the interstellar medium. IBEX is designed to achieve this objective by answering four fundamental science questions: (1) What is the global strength and structure of the termination shock, (2) How are energetic protons accelerated at the termination shock, (3) What are the global properties of the solar wind flow beyond the termination shock and in the heliotail, and (4) How does the interstellar flow interact with the heliosphere beyond the heliopause? The answers to these questions rely on energy-resolved images of energetic neutral atoms (ENAs), which originate beyond the termination shock, in the inner heliosheath. To make these exploratory ENA observations IBEX carries two ultra-high sensitivity ENA cameras on a simple spinning spacecraft. IBEX's very high apogee Earth orbit was achieved using a

new and significantly enhanced method for launching small satellites; this orbit allows viewing of the outer heliosphere from beyond the Earth's relatively bright magnetospheric ENA emissions. The combination of full-sky imaging and energy spectral measurements of ENAs over the range from ~10 eV to 6 keV provides the critical information to allow us to achieve our science objective and understand this global interaction for the first time. The IBEX mission was developed to provide the first global views of the Sun's interstellar boundaries, unveiling the physics of the heliosphere's interstellar interaction, providing a deeper understanding of the heliosphere and thereby astrospheres throughout the galaxy, and creating the opportunity to make even greater unanticipated discoveries.

3.1 Science Objectives

The IBEX mission was designed to discover the global interaction between the solar wind and the interstellar medium by answering four primary science questions:

1) What is the global strength and structure of the termination shock?
2) How are energetic protons accelerated at the termination shock?
3) What are the global properties of the solar wind flow beyond the termination shock and in the heliotail?
4) How does the interstellar flow interact with the heliosphere beyond the heliopause?

In order to answer these questions, IBEX was designed to collect energy-resolved images of energetic neutral atoms (ENAs), particles that originate beyond the termination shock (TS), in the inner heliosheath.

The plan for science return of the IBEX mission was planned in terms of three levels of study: Discovery, Exploration, and Deep Understanding. At the Discovery level, fundamental properties of the interstellar interaction can be directly gleaned from the IBEX images, energy spectra, and interstellar neutral fluxes. At the Exploration level, observations are combined with simple physics-based calculations, theory and limited 2D and 3D modeling to explore the more detailed properties of the outer heliosphere. Finally, at the Deep Understanding level, detailed global properties of the interstellar interaction are extracted through iterative analyses using IBEX data observations in concert with detailed 3D models of the heliosphere.

The next four subsections briefly summarize the four primary science questions listed above and how IBEX was designed to answer them.

3.1.1 Question 1: What is the global strength and structure of the termination shock?

IBEX was designed to produce global images and energy-spectral information from which it is possible to derive the proton-energy distributions in the inner heliosheath and determine the shock strength as a function of position. Such global observations are the only way to answer the fundamental questions of the existence and strength of the TS in all directions of the sky.

As an example of the types of observations IBEX was designed to make, Figure 1 shows simulated all-sky maps of ENA fluxes over the energy range examined by IBEX. The model (Heerikhuisen et al. 2008) includes neutrals, the suspected external magnetic field orientation in the LISM, and a realistic κ-function ion distribution (they used $\kappa = 1.63$, based on the Voyager 1 data at higher energies Decker et al. 2005). Several features stand out in these simulations, including the highest emissions from down the tail and the bright, diffuse, and apparently banded emissions from across the nose (see Heerikhuisen et al. 2008 for details). While the real heliospheric interaction is undoubtedly much more complex than this simulation, IBEX's energy-resolved maps will clearly provide the detailed all-sky observations needed to understand the global configuration.

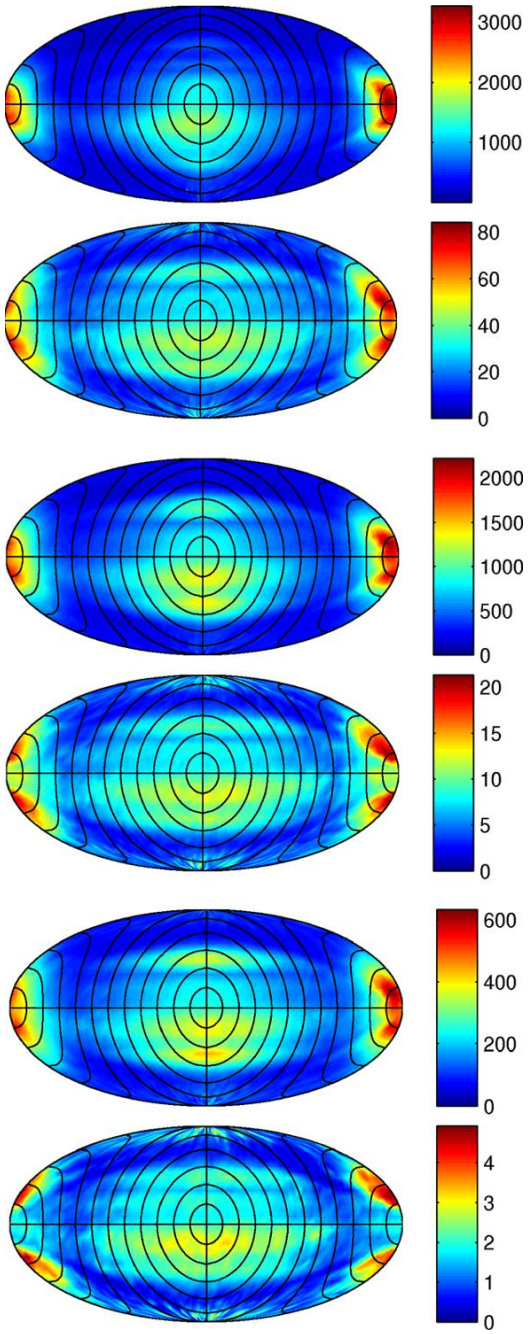

Figure 1: Simulated all-sky maps of ENAs at various energies taken from Heerikhuisen et al. (2008). The maps plot color-coded ENA fluxes in units of cm2 s sr keV−1 for energy bands of 8–12 eV, 40–60 eV, 180–220 eV, 900–1100 eV, 2200–2600 eV and 5600–6400 eV, respectively from top to bottom. In each panel, the nose of the heliosphere is in the center with the poles at the top and bottom and tail on the far left and right sides

3.1.2 Question 2: How are energetic protons accelerated at the termination shock?

The TS is a nearly perpendicular shock (shock normal perpendicular to the local magnetic field) owing to the winding up of the IMF in the outer heliosphere. This geometry leads to an “injection problem” (Lee 2000; Rice et al. 2000; Giacalone 2001) where the particles can only be efficiently accelerated at the shock if they already have very high speeds along the magnetic field. Furthermore, the TS is highly moderated by the large numbers of PUIs, suggesting that the shock acceleration is a highly non-linear process where the TS accelerates protons, and the energetic rotons in turn modify the shock, thereby changing the very nature of the acceleration.

IBEX enables us to infer the properties of accelerated protons near the TS by measuring their energy distributions via the H ENAs produced from these accelerated protons up to 6 keV. While these protons are much lower energy than ACRs or even the injected particles, they feed these higher energy protons. By measuring the intensity and energy dependence at lower energies, IBEX enables us to infer the injection and acceleration of protons at higher energies. In addition, IBEX’s energy spectral measurements from all directions in the sky are designed to enable the exploration of the variability of the TS, further informing the complicated, iterative mechanisms of shock physics. IBEX will directly observe the intensity of ENAs from accelerated protons relative to the solar wind and pickup protons below 1 keV. These observations, in concert with modeling to deconvolve the line-of-sight (LOS) integration and to extrapolate the measurements over an energy range needed to estimate the energetic proton pressure, should make it possible to determine how the TS is moderated at various locations. Finally, more advanced models of shock acceleration may be used to tally with all of the detailed IBEX spectral observations.

3.1.3 Question 3: What are the global properties of the solar wind flow beyond the termination shock and in the heliotail?

After crossing the TS, the solar wind and PUIs become swept back in the inner heliosheath by the interaction with the LISM. Ultimately, nearly all this material must flow back and down the heliotail. Various models predict the flow patterns in the heliosheath and heliotail (e.g., Baranov and Malama 1993, 1996; Zank et al. 1996; Linde 1998; Linde et al. 1998; Müller et al. 2000) with differences that depend critically on the model approach and assumptions about both the solar wind and LISM.

Global ENA observations from IBEX should provide extremely sensitive measures of the asymmetries in the properties of the ions in the inner heliosheath as well as the thickness of this region. By making all-sky observations over the full energy range of the bulk populations, IBEX will measure the thermalization and energy partition of the solar wind and PUIs and the global flow patterns of the solar wind beyond the TS.

As a simple example, Figure 2 compares model energy spectra for a strong gas-dynamic shock (black) with no contribution from PUIs and a shock weakened by PUIs (green). Differences in the source ion energy distributions generate significant differences in the ENA emissions even in this one energy band. The combination multiple images across the broad range covered by IBEX will very strongly constrain the properties and flow patterns in the inner heliosheath.

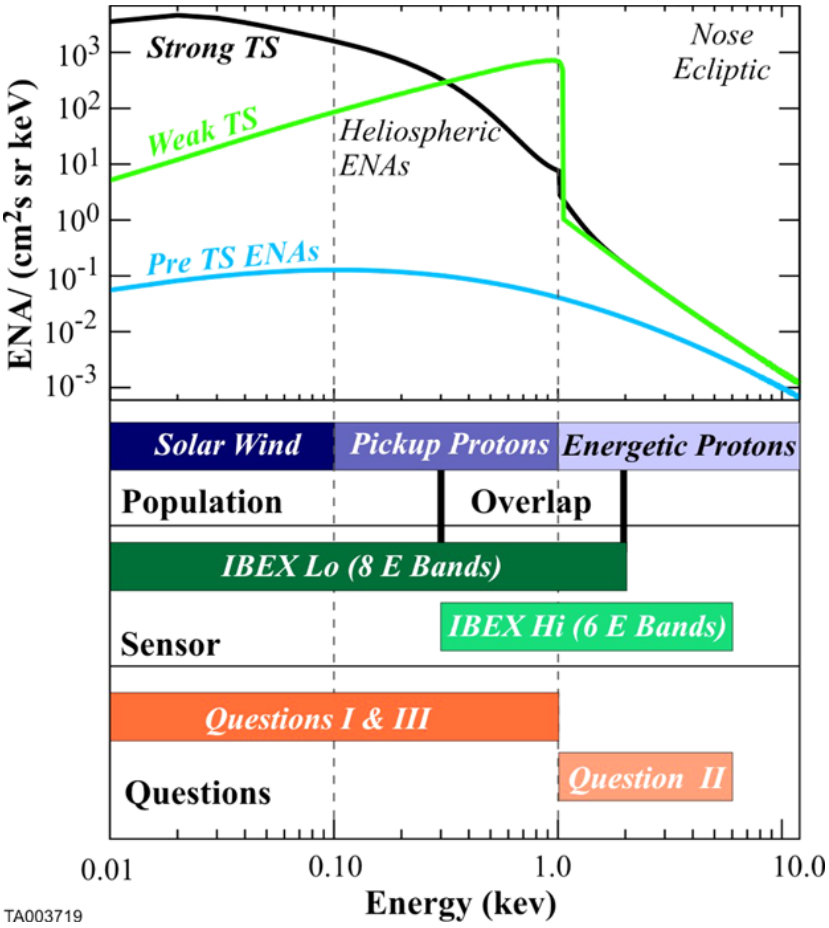

Figure 2: The IBEX H ENA energy range is designed to provide the critical distributions needed to reveal the global properties of the proton populations of the inner heliosheath. Shown here are predicted ENA energy distributions near the nose of the heliosphere for a strong (black curve) and weak (green curve) TS (Gruntman et al. 2001). These curves are for a nominal, slow (1 keV) solar wind. The blue curve shows the predicted ENA flux due to energetic protons inside the TS. Energetic ENA distributions >1 keV (black and green curves) are predicted from observed energetic proton tails (Gloeckler et al. 1994, 2000; Schwadron et al. 1996) assuming that the intensity of the tails scale with the intensity of interstellar pickup protons (Vasyliunas and Siscoe 1976)

3.1.4 Question 4: How does the interstellar flow interact with the heliosphere beyond the heliopause?

Because hydrogen and oxygen ions and atoms readily charge-exchange with each other, the filtration process that modifies the inflowing interstellar neutral H similarly modifies the interstellar neutral O. Thus, interstellar O measured by IBEX comprises two populations: an unmodified or “primary” population that reflects the undisturbed properties of the LISM and a “secondary” population, which generally reflects the ion population in the outer heliosheath. IBEX is designed to provide the first direct measurement of filtered interstellar neutrals (see Fig. 6). This is possible because the Sun’s gravity focuses the inflowing interstellar O atoms in the direction opposite to the interstellar flow. Careful measurements of the detailed distribution of the incoming neutrals’ directions by IBEX will allow differentiation between and separate quantification of the primary and secondary populations. Measurements of the primary population should provide additional direct information about the LISM, while measurements of the secondary population should allow us to measure the heating, deceleration and depletion associated with the interstellar interaction near the heliopause at the hydrogen wall. Detailed discussion of this topic is provided by Möbius et al. (2009).

3.1.5 Scientific Closure

The process we followed to define the IBEX capabilities and requirements flowed naturally from deciding what was needed to answer the above four science questions. As summarized in Table 1, for each question, we identified answers that could be provided at each of the three levels of examination: Discovery, Exploration, and Deep Understanding. Then we specifically identified what measurement requirements would allow us to fully answer these questions with sufficient margin to span unanticipated discovery science because of the extremely limited knowledge at the start of the IBEX mission of the structure and dynamics of the interaction region. As examples, the required angular and energy resolutions and ranges are shown at the bottom of Table 2. These and many other requirements went into our baseline mission requirements, which drove the entire design and development of the IBEX mission. In addition to baseline requirements, we also developed minimum mission requirements that would still provide acceptable science return for the mission if we were unable to fully meet the baseline requirements in some area. We are delighted to report that the IBEX mission as built and flown meets, and in most areas exceeds, our full baseline requirements.

Table 1: *IBEX science questions, levels of study, and derived top-level measurement requirements*

The IBEX approach and measurement requirements				
The sole IBEX objective to discover the global interaction between the solar wind and the interstellar medium is achieved by answering four fundamental science questions				
Levels \ **Fundamental Science Questions**	**I:** *TS Strength/ Structure*	**II:** *Energetic Protons Near TS*	**III:** *Solar Wind Flow Patterns of Inner Helioshealth*	**IV:** *Interstellar Flow and Interaction*
Discover (Straightforward interpretation of IBEX data products)	All-sky survey: strong vs. weak TS	Intensity and spectra of energetic protons near TS	Nose/tail asymmetries	First direct measurement of filtered interstellar neutral, O
Explore (Interpretation based on simple physics-based calculations and limited modeling)	All-sky map of shock strength	Modification of TS dynamics due to energetic particle pressure	Solar wind flow direction beyond TS vs. angle from the nose	Bulk speed, direction, and temperature of interstellar O inside TS
Understand (use data products to iteratively define, revise, and refine 3D models of the heliosphere)	-3D TS configuration incl. distance scale and strength -Energy partition of solar wind, pickup protons, and energetic protons	Bound injection processes at TS	-3D solar wind flow patterns beyond TS -LISM B	-Filtration -Ionized fraction of O in the LISM -Interstellar flow patterns beyond heliopause -Bow shock existence
Measurements Requirements				
Global heliospheric ENA imaging	7^{O}x7^{O} pixels	21^{O}x21^{O} pixels	7^{O}x7^{O} pixels	Determine O Direction to 2.0^{O} FWHM
H energy spectra: Solar wind through energetic particle ENAs	0.01-1 keV in 7 energy bands	1-6 keV in 4 energy bands	0.01-1 keV in 7 energy bands	
O fluxes and velocity direction vs. time of year				0.01-0.5 keV in 6 energy bands

Raw Images

Detailed Models

TA003718_b

3.2 IBEX Description

The IBEX payload was designed to meet or exceed all baseline requirements and answer all four science questions described in the previous section. Because technical resources in general and mass, in particular, were very limited, we needed to develop the most efficient science payload possible, making full use of all of the heritage experience and expertise from across the IBEX team. This process led to an optimized payload consisting of two very large aperture single pixel ENA cameras: IBEX-Lo (Fuselier et al. 2009a), which measures ENAs with energies from ~10 eV up to 2 keV, and IBEX-Hi (Funsten et al. 2009a), which measures ENAs with energies from ~300 eV up to 6 keV. Both sensors are served by a single combined electronics unit (CEU). Critical parameters for IBEX-Hi, Lo and the CEU are summarized in *Table 2*.

Table 2: *Key IBEX payload parameters and resources*

	IBEX-Hi	IBEX-Lo	CEU
Energy Range	300 eV–6.0 keV	10 eV–2 keV	N/A
Energy resolution ($\Delta E_{\mathrm{FWHM}}/E$)	0.47–0.66	0.8	N/A
Number of Energy Steps	6	8	N/A
FOV (FWHM)	$6.5° \times 6.5°$	$6.5° \times 6.5°$ $3.2° \times 3.2°$	N/A
Geometric Factor for H near 1 keV (double coincidence)	3×10^{-3} cm^2 sr eV/eV at 1.1 keV	8.1×10^{-4} cm^2 sr eV/eV at 0.78 keV	N/A
Geometric Factor for H near 1 keV (triple coincidence)	7.3×10^{-4} cm^2 sr eV/eV at 1.1 keV	2.9×10^{-4} cm^2 sr eV/eV at 0.78 keV	N/A
Mass	7.70 kg	12.09 kg	5.42 kg
Volume	43.94 cm Dia × 23.75 cm	40 cm Dia × 31.45 cm	43.82 cm × 27.9 cm × 9.5 cm
Power	0.7 W	3.5 W	11.2 W
Telemetry	102.6 bps	122.8 bps	11.8 bps

Both the IBEX-Hi and Lo sensor designs are based on the same physical principles, but each is tailored to optimize ENA measurements for their respective energy ranges. Figure *3Figure 1* shows schematic diagrams of the two sensors. Each is comprised of the same four subsystems: an entrance system, a charge-conversion system, an electrostatic analyzer (ESA), and a detection system.

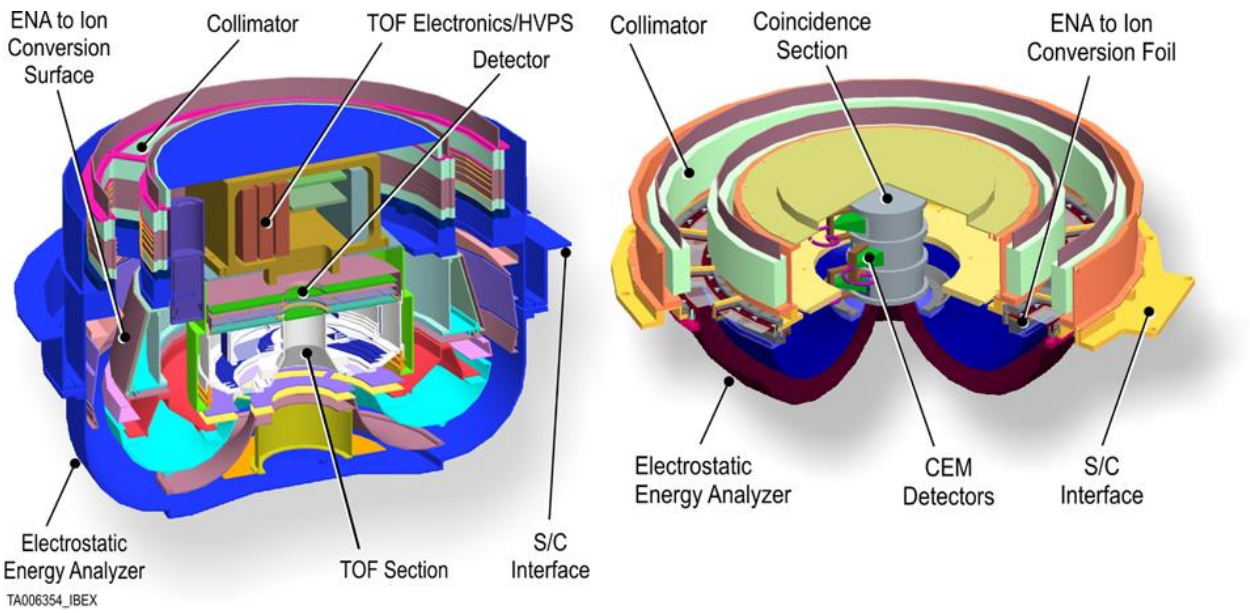

Figure 3: Schematic diagrams of the IBEX-Lo (left) and IBEX-Hi (right) sensors. Both are based on large "bundt pan" type ESAs, which focus huge aperture areas onto their central detector sections.While optimized differently for the higher and lower energy ranges, both are comprised of the same four basic subsystems

ENAs enter the IBEX sensors through entrance systems, which are comprised of a sun shield, electron rejection ring, pre-collimator, and collimator. A slanted sunshade shields the rest of the entrance system components from any direct solar illumination during normal operations. The electron rejection ring imposes a negative potential across the aperture without any grids or other structures that could generate neutral particles. This potential excludes all except the highest-energy electrons (>600 eV) from reaching the aperture.

The pre-collimators and collimator set the intrinsic angular resolution of our measurements to ~6.5◦ FWHM in both sensors. In addition, IBEX-Lo has a higher angular resolution quadrant (~3.2◦ FWHM) that is used for direct detection of the low-energy interstellar oxygen (science question 4 above). The entire collimator is biased to +10 kV, which rejects positive ions from the surrounding space environment with energies <10 keV/q. UV light, which can be a significant source of background for these measurements, passes unaffected through the collimators as do the ENAs.

The next step in detecting the ENAs is to convert them back into charged particles. ENAs are detected in the IBEX sensors using the same process that produced them in the outer heliosphere—charge exchange. In the case of IBEX-Hi some fraction of the neutrals are converted to positive ions as they pass through a set of ultra-thin carbon foils, which are only ~0.5 μgcm−2, or ~50–100 atoms thick (see McComas et al. 2004 and references therein). At even lower energies, the ENAs can't make it through even

these very thin foils. Instead, in IBEX-Lo, conversion produces negative ions, as they reflect off of special CVD diamond surfaces (Gruntman 1997 and references therein). The efficiency for both of these processes is low: ~one percent to a few tens of percent, so one of the biggest drivers for the sensor design was to find a way to maximize the aperture area.

The aperture areas of both IBEX-Lo and Hi were maximized by using “Bundt pan” shaped ESAs (Moestue 1973). With this design, truly immense open areas can be arrayed around the perimeters of the sensors, and ions produced by the incident ENAs are bent around into reasonable sized, central detector sections. Thus, in addition to removing the UV that enters the sensors and setting a voltage-dependant energy pass band as all ESAs do, the IBEX ESAs also concentrate the particles from a very large aperture onto a small, central detector in a way that greatly increases both sensors’ signals and signal-to-noise ratios.

The final stage of measuring the heliospheric ENAs is the detection process. In both detector subsystems, the converted incident ions pass through a pair of ultra-thin carbon foils, which then emit secondary electrons. In IBEX-Lo, both the primary particle and the secondary electrons are detected on a microchannel plate (MCP) detector, and the time-offlight (TOF) of the primary is measured, allowing determination of its species (e.g., H, He, or O). In the case of IBEX-Hi, the ionized ENA transits three stacked detection chambers separated by the two foils, and secondary electrons generated in each chamber are detected by the channel electron multiplier (CEM) in that chamber. Both sensors have both double and triple coincidence data products, with the triple coincidence ones having exceptionally low background (false positive) rates. Both of these designs are optimized to suppress the intrinsic detector section backgrounds. The backgrounds of both sensors and the overall mission noise and background have been carefully studied and painstakingly minimized (Wurz et al. 2009).

Finally, both IBEX sensors have small additional components that support their science observations. For IBEX-Lo, a small star sensor has been added that allows extremely precise knowledge of this sensor’s pointing. These measurements greatly increase the precision with which the interstellar neutrals can be measured and the primary and secondary populations can be separated (Möebius et al. 2009). In IBEX-Hi, we added a small background monitor to provide independent measurements of the local energetic ion environment (Allegrini et al. 2009). These observations enhance our ability to identify and remove times when the local plasma environment could be contaminating the ENA observations.

Both sensors are served by the CEU. This box provides the single spacecraft interface, data processing, low-voltage power supplies, and high-voltage power supplies for both sensors. As part of the spacecraft interface, the CEU accepts, parses and routes commands and stores and plays back spacecraft and science telemetry. The command and data handling is based on a 8051 core processor. As the CEU steps the various

sensor high voltages, it gathers, bins, and processes the raw science data. A two-gigabit solid state recorder makes it possible to store multiple orbits' worth of science data and spacecraft telemetry.

The CEU's low-voltage power supplies create and distribute separate custom low voltages for the two sensors and provide monitoring as well as solid-state relay switching for all of these outputs. The high-voltage system comprises four independent high-voltage supplies, which have a resonant (at ~100 kHz) fly-back-type topology and contain collimator supplies and combined bulk supplies separately for each sensor. Other than one additional high-voltage supply located inside IBEX-Lo, the CEU supplies all 16 sensor high-voltage outputs on coaxial high-voltage cables.

3.2.1 IBEX Measurement Concept

IBEX was designed to make the first all-sky observations of the heliosphere's interaction with the LISM by imaging energetic neutral atoms (ENAs) produced largely beyond the TS, in the inner heliosheath, where the solar wind and imbedded PUIs have been slowed and heated. In the heliosheath, these populations of predominantly hydrogen ions produce a significant flux of detectable inward moving ENAs via charge-exchange with local interstellar neutrals. Only one potential observation of ENAs produced from PUI populations in the heliosphere has been reported to date. Wurz et al. (2008, and references therein), reported ENAs with limited spatial and temporal coverage in the energy range from 200 eV to 80 keV. In contrast, IBEX was optimized to provide all-sky imaging of the ENA fluxes, which are spatially resolved in both latitude and longitude, and does so over the critical energy range that covers both the solar wind and much of the PUI population in the inner heliosheath.

IBEX carries two very large geometric factor ENA cameras: IBEX-Lo, which measures ENAs from ~10 eV to 2 keV and IBEX-Hi, which measures them from ~300 eV to 6 keV. Both sensors have angular resolutions of ~6.5◦ ×6.5◦, enabling well-resolved images with ~1800 pixels covering the whole sky. Furthermore, IBEX-Lo has eight energy-resolved channels covering its energy range and IBEX-Hi six, thus producing images at many different energies, and even more importantly, energy spectral information for each direction in the sky. The two IBEX sensors' energy ranges also overlap from ~300 eV to 2 keV to provide independent observations across the critical energy range. Thus, IBEX is optimized to globally image ENAs from the outer heliosphere for the first time. Over a single IBEX orbit of about 8 days, a single 6.5°×360° swath of the sky is viewed, and re-pointing of the spin axis toward the Sun near perigee of each IBEX orbit moves the ecliptic longitude by about 8° every orbit such that a full sky map is acquired every six months. At the end of 6 months of operation, full sky maps of heliospheric neutral hydrogen from are accumulated. Figure 4 provides a summary of the charge-exchange process and how IBEX rotation and motion naturally generate all-sky maps of the ENAs propagating in from the inner heliosheath each six months.

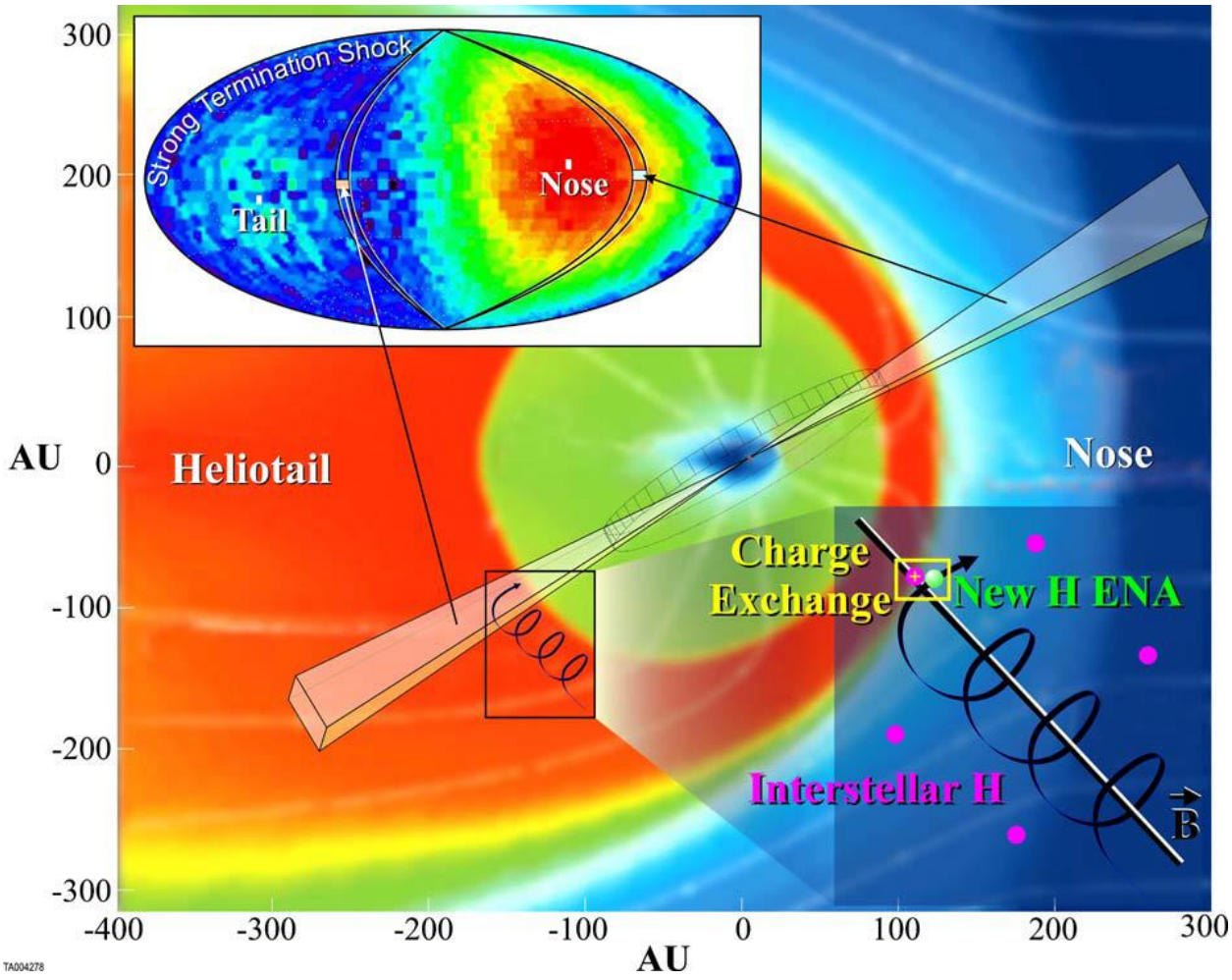

Figure 4: Charge exchange between hot ions and cold interstellar neutrals (lower right inset) produce ENAs, some of which happen to be directed inward and propagate all the way into the inner heliosphere where they can be detected by the IBEX spacecraft in a very high-altitude Earth orbit. The two instantaneous ~6.5° × 6.5° fields-of-view of the IBEX-Hi and Lo sensors are depicted in the main image; these map to the two indicated pixels in the all-sky map (top left). As the sun-pointed IBEX spacecraft spins, the pixels viewed move repeatedly around the two indicated crescents in the sky map. Then, as IBEX repoints at the end of each orbit, the viewed crescents move across the sky producing all-sky maps each six months

3.2.1.1 IBEX-Hi Measurement Concept

IBEX-Hi is a high sensitivity, single pixel sensor. A critical priority of the IBEX-Hi sensor design and development was maximizing the sensitivity to ENAs while minimizing noise and backgrounds. This drove the detailed designs of each subsystem: the collimator is biased at +10 kV to reject ions up to 10 keV/q and is fabricated using nonlinearly stacked thin plates having collinear aperture holes to minimize ion scattering; the charge conversion subsystem ionizes ENAs so they can be electrostatically removed from the UV and electron background; the energy analysis subsystem projects the

enormous entrance aperture area of the sensor onto a small detector area and is serrated to prevent UV and ions >10 keV/q from reflecting into the detector subsystem; and the detector subsystem uses channel electron multiplier (CEM) detectors to minimize noise from penetrating radiation and to measure coincidence between these detectors to discriminate between noise and a true ENA that is detected in multiple CEMs as it transits the subsystem.

Prior to launch, the ENA flux originating from beyond the termination shock and measured at 1 AU by IBEX was anticipated to lie within the range of 1 to 500 cm^{-2} s^{-1} sr^{-1} keV^{-1} at ~1 keV (Gruntman et al. 2001; Wurz et al. 2008b). Because of this low ENA flux, the designs of the IBEX sensors have been driven toward maximizing the sensitivity and minimizing the noise and the backgrounds that would otherwise masquerade as ENAs. The numerous sources of background and noise (see Wurz et al. 2009) include ENAs of magnetospheric origin, ionization and acceleration of ambient gas molecules within the sensor, detection of ambient ions that are beyond the maximum rejection energy of the entrance subsystem, and coincidence events generated by penetrating radiation.

A second unique aspect of measuring these ENAs is their energy-dependent transit time from their formation beyond the termination shock to their detection by IBEX at 1 AU. This is illustrated in Fig. 1, which shows the time for a hydrogen ENA to travel 100 AU as a function of its energy. The transit times for ENAs within the energy range of IBEX-Hi to travel 100 AU range from 196 days at the central energy (4.09 keV) of the highest energy passband to 591 days at the central energy (0.45 keV) of the lowest energy passband. Furthermore, the range of travel times of ENAs emitted from a point source at 100 AU from the Earth that are detected within the full width at half maximum (FWHM) of a single energy passband ranges from 62 days at the highest energy passband to 143 days at the second lowest energy passband. This time uncertainty for an individual energy passband corresponds to ~1/3 and ~2/3, respectively, of the 6-month period over which IBEX generates a complete sky map. These time resolutions represent a lower limit because the ENA source region may be quite thick and extend significantly beyond the termination shock and because ENAs from source regions at the flanks and tail of the interaction region travel distances that can be substantially farther than 100 AU.

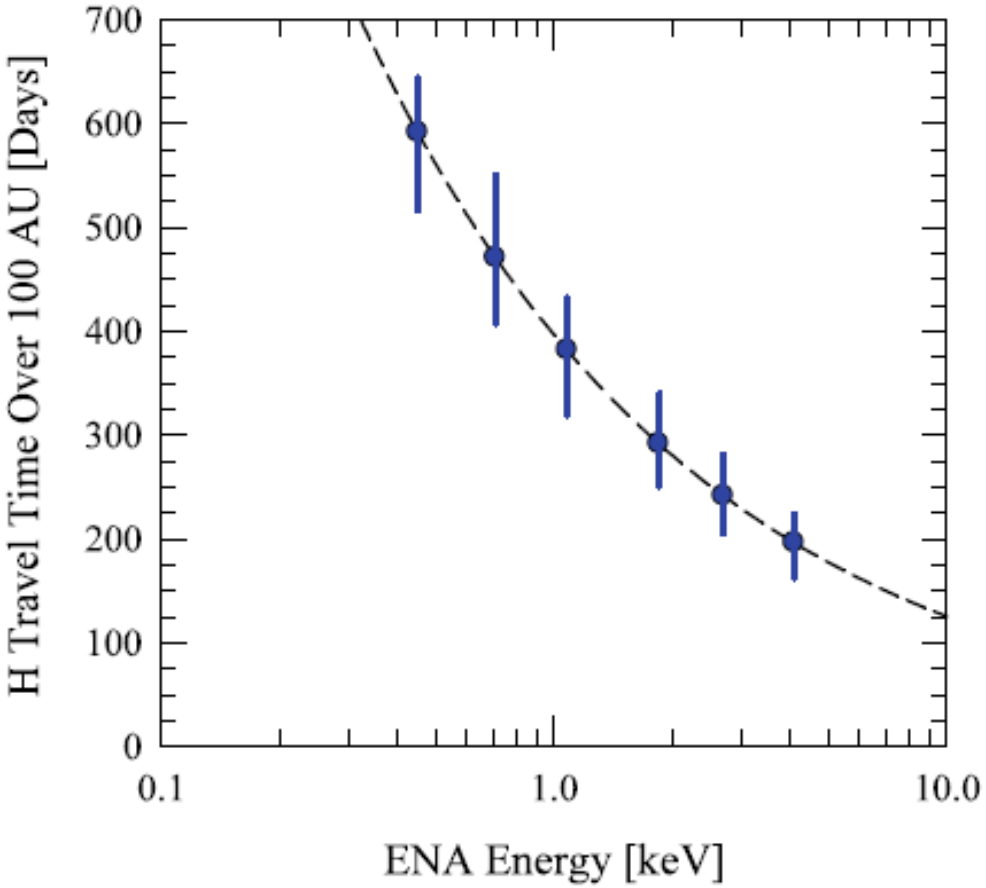

Figure 5: The points show the travel time for a hydrogen ENA to transit 100 AU at the central energy of each of the six IBEX-Hi energy passbands. The error bars at these points represent the travel time uncertainty due to the energy FWHM of each of the energy passbands for events detected through triple coincidence

3.2.1.2 IBEX-Hi Operations

IBEX-Hi operates in science mode over the portion of the IBEX orbit when the spacecraft is above 15 RE, which is about 93% of the ~8-day orbital period. In this mode, all high voltages are at nominal operating levels, and the ESA voltages are stepped once every two spacecraft spins. A complete energy sweep over all six passbands is therefore completed every 12 spins, which corresponds to 3 min based on a nominal spin rate of 4 rpm.

In science mode, IBEX-Hi reports two data products: (1) histograms of accumulated counts as a function of angle, energy step, and coincidence type, and (2) direct event data consisting of individual coincidence events selected using a prioritization scheme and reported at high time (and therefore angular) resolution. The telemetry rate is 42 bps for histogram data, 57 bps for direct event data, and 12 bps for housekeeping that is shared with IBEX-Lo.

Histograms are constructed from accumulated counts from coincident and non-coincident (single) events and sorted by event type. Each histogram is a 6 × 60 array of counts for the six energy passbands and 60 angular bins around the spin axis, each 6° wide. The angular bins of eight primary event type histograms are summed over four ESA cycles (12 minutes); another three secondary histograms are summed over eight ESA cycles. The counts in each angular bin are compressed from 16 bits to 8 bits and stored in the solid-state recorder (SSR) for downloading during the next IBEX perigee pass.

The primary histograms include non-coincident (singles) counts in each detector (Long A, Long B, Long C), four double coincident types (Long AB, Qual AB, Qual AC, and Qual BC), and one triple coincident type (Qual ABC). The secondary histograms include Long AC, Long BC, and Long ABC. The qualification scheme, either Not_C or Not_Equal, can be independently selected for each of the qualified coincidence event types. The histogram data also includes accumulated counts from the IBaM as a function of spin angle.

Direct event data consists of individual coincidence events whose coincidence type is reported along with the spin angle and energy passband at the time that the event was detected. Direct events are recorded at higher time resolution (4.2 ms, or ~0.1° of spin angle) than used for acquisition of the histograms. Because of telemetry constraints, IBEX-Hi is limited to recording ~800 direct events per 12-spin cycle, which corresponds to an average of ~67 events per spin. Therefore, a culling process is used by the CEU to telemeter only the highest priority direct events. The prioritization scheme, which lies in a changeable look up table in the CEU, currently has Qual(Not_C) ABC as the highest priority because these triple coincidences represent the measurement with the lowest noise. These high priority events are stored up to the limit of ~800 events per 12 spins. If space remains, the second priority events, which currently include Long AB, Long BC, and Qual(Not_C) AC, are included in the direct event data. No other event types are stored as direct event data. Because direct events are recorded at greater time resolution and greater coincidence type specificity than the histograms (for example, the qualified-triples histogram includes three different types of direct events), they represent key data for deeper analysis of the global ENA maps.

IBEX-Hi has three other operational modes: high voltage standby mode, gain test mode, and functional test mode. High voltage standby mode is entered every orbit when the spacecraft passes below 15 R_E as it approaches the radiation belts. At these low altitudes, the magnetospheric ENA signal can be significantly greater than that of heliospheric ENAs, and detector background from penetrating radiation may also be substantial. Upon entering this mode, the collimator voltages are turned off, the voltage applied to the detector chambers is reduced from −6 kV to −4 kV, and the voltage across each CEM is decreased by 0.6 kV, which is below the threshold for electron avalanche in the CEM.

Gain tests are run periodically to ensure that the CEMs are operating on the plateaus of their respective gain curves. During a gain test, each CEM voltage is alternately stepped between its current operating voltage and offsets of −200 V, −100 V, +100 V and +200 V from operating voltage. Because the heliospheric ENA signal rate is quite low, gain tests are performed at ~12 RE to utilize the stronger magnetospheric ENA signal in some of the magnetospheric-viewing azimuthal pixels, resulting in anticipated ENA count rates of ~10 s^{-1} in these pixels. Based on these count rates, the planned integration time per energy passband setting is ~12 minutes. The scheme of returning to the current operating voltage before proceeding to the next voltage offset minimizes the impact of natural fluctuations in the ENA rate on the test results. If a gain test shows that a CEM detector gain has decreased, the gain will be increased by an appropriate increase of the CEM operating voltage.

The electronics functional test is periodically executed to assess the health of the IBEX-Hi amplification and signal processing electronics. This is a shortened and automated version of the electronics checkout performed throughout calibration and during commissioning. Specific diagnostics include determination of the electronic noise floor discriminator setting and the lower level discriminator below which crosstalk between separate detectors is observed.

3.2.1.3 IBEX-Lo Measurement Concept and Requirements

The IBEX-Lo sensor measures the low-energy part of the heliospheric neutral spectrum. The energy range for this sensor is from 10 eV to 2000 eV. The lower bound of the energy range is set by sensor sensitivity and practical interpretation of the observations. A 10 eV neutral from the heliospheric termination shock requires almost 11 years to complete a trip from the shock to the inner heliosphere. Neutrals with energies less than 10 eV would take more than a solar cycle to complete the trip. In addition, the sensitivity decreases relatively rapidly below 10 eV because the neutral-to-ion conversion efficiency decreases at energies below 10–20 eV (see 3.2.2.2.2 and also see Wurz et al. 2006).

The upper bound of the energy range is set by electric fields in the sensor, voltages on the electrodes, and, ultimately, on sensor mass resources. In total, the IBEX-Lo energy range covers very low energy neutrals expected to survive the journey into the inner heliosphere, through nominal solar wind energy neutrals (and the expected energy peak in heliospheric neutral flux for some heliospheric interaction models) and into the energy range for suprathermal neutrals accelerated in the solar wind and at the heliospheric termination shock. Since the IBEX-Hi sensor measures down to ~ 300 eV and has very good sensitivity at ~ 1000 eV, there is significant energy overlap between the two sensors for important heliospheric measurements near the nominal solar wind energy of 1000 eV.

IBEX-Lo also provides measurements that are used to answer the fourth IBEX mission science question: How does the interstellar flow interact with the heliosphere beyond the heliopause? Because interstellar oxygen and helium neutrals have energies up to several hundred electron volts, contributions to this science question come primarily from the IBEX-Lo sensor. *Figure 6* shows locations in the Earth's orbit plane where interstellar oxygen and helium will be measured and also shows predicted energies of the neutrals. The Earth is in the upwind direction in June. Each year in the "northern hemisphere fall" (135° from the upwind direction, with prime viewing from 17 Sept to 21 October), the Earth is moving in the same direction as interstellar neutrals from the upwind direction. Because interstellar neutrals are accelerated by the Sun's gravitational force, they have higher energies than when they first enter the solar system, but they have to "catch up" to the Earth. IBEX-Lo will observe oxygen at a center energy of only 32 eV and helium will be at 8 eV energy with respect to the Earth's motion. Thus, helium will be just below the sensor's 10 eV low energy cutoff. Each year in the "northern hemisphere winter/early spring" (hereafter referred to as "spring") (225° from the upwind direction, with prime viewing from about 10 January to 23 February), the Earth's velocity vector and the interstellar neutral velocity vector are directed nearly opposite one another, so neutrals have considerably higher energies. IBEX-Lo will observe oxygen at 522 eV and helium at 130 eV.

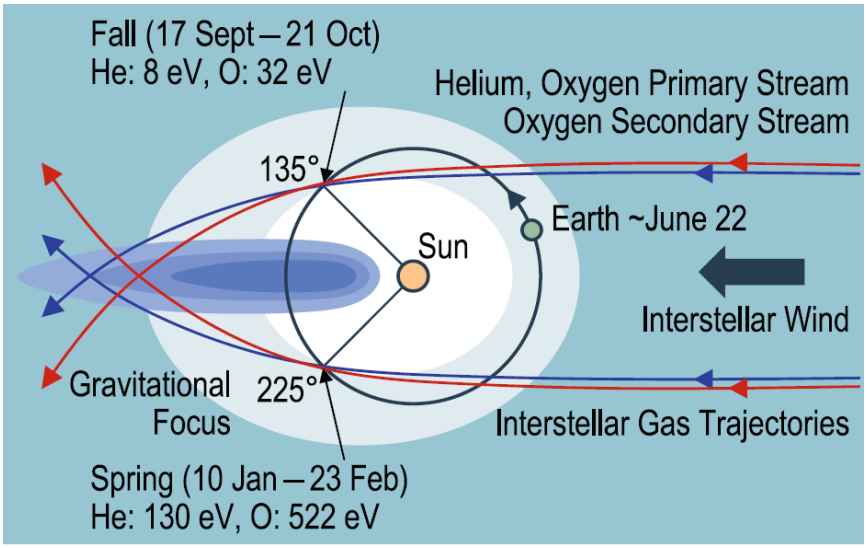

Figure 6: Interstellar oxygen and helium observations occur in the fall and spring, where the streams intersect the Earth's orbit and the IBEX-Lo sensor FOV. In the fall, the interstellar neutral flux vector is in the same direction as the Earth's orbit velocity, so energies are low. In the spring, the two vectors are nearly oppositely directed, so energies are high

A key observable parameter for science question 4 (from Section 3.1: "How does the interstellar flow interact with the heliosphere beyond the heliopause?") is the arrival direction of the primary and secondary "filtered" neutral oxygen streams relative to the

helium arrival direction. Measuring this arrival direction drives the IBEX-Lo sensor design in several ways discussed in Section 3.2.2.2.

Heliospheric and interstellar neutral fluxes are low and potential background contributions are very high. For comparison, 1000–2000 eV neutral fluxes from the Earth's magnetosphere (ring current) are ~ 4 × 104 ENAs/(cm^2 s sr) and ~ 50 eV neutral fluxes from high latitude ionospheric outflow range from 6 × 10^4 to 1 × 10^6 ENAs/(cm^2 s sr). These neutral fluxes can vary significantly on timescales of tens of minutes. Magnetospheric and ionospheric neutrals are readily imaged with moderately large neutral atom imagers like the ones that were on the IMAGE spacecraft (Pollock et al. 2000; Moore et al. 2000; McComas et al. 2002; Fuselier et al. 2006). These imagers have time resolution of minutes, commensurate with the variability timescales of the source neutrals.

In contrast, ~ 1000 eV neutral fluxes from the outer heliosphere are predicted to range from 10^1 to 10^3 ENAs/(cm^2 s sr) and ~ 50 eV fluxes are predicted to range from 3 × 10^1 to 3 × 10^3 ENAs/(cm^2 s sr), depending on several factors including the termination shock strength (Gruntman et al. 2001). Recent measurements of energetic neutral atoms from the heliosheath suggest that these estimates may be somewhat low (Galli et al. 2006; Wurz et al. 2008b). However, heliospheric neutral fluxes are still considerably lower than magnetospheric ENA fluxes.

Variability timescales for ENAs from the outer heliosphere are not known. However, propagation times for neutrals from the vicinity of the termination shock to the inner solar system range from months (for ~ 1 keV ENAs) to years (for ~ 50 eV ENAs). ENAs from the termination shock propagating into the inner heliosphere have a 10–20% probability of charge exchange with solar wind protons, (i.e., only 80–90% of the original ENA signal can be detected at Earth orbit). This charge exchange is localized within the last 10 AU. However, if the ENA path goes through the plasma of a coronal mass ejection (CME), where there can be significantly higher proton densities, complete extinction of the ENA signal is possible. Given the typical CME frequencies with respect to propagation times of the ENAs, signal fluctuations at timescales of the order of days are possible.

Thus, compared to magnetospheric neutral fluxes, heliospheric neutral fluxes are from 10 to more than 1000 times lower, but the required time resolution for the observations is much longer. The very low fluxes and long timescales drive the IBEX sensor design away from imaging systems (like those used on the IMAGE mission) and to a large geometric factor, single pixel camera. Full energy and angle images with appropriate time resolution are accumulated by reorienting the (spinning) IBEX spacecraft over the course of 6 months, as described in the mission overview (McComas et al. 2009b).

Potentially high contributions from background ions and UV also drive sensor design. For magnetospheric imagers, one can use a large geometric factor, pinhole camera (e.g., Pollock et al. 2000) for imaging because the signal to noise ratio is relatively large. This technique of direct detection of neutrals is not possible for the IBEX mission because creation of ions within the sensor from, for example, UV background could overwhelm the heliospheric signal. Furthermore, for IBEX-Lo, heliospheric neutrals have too low an energy to be directly detected with any reasonable efficiency (Wurz 2000). These background considerations and detection efficiencies drive the overall sensor design away from a direct detection, pinhole camera concept. Instead, heliospheric neutrals are ionized in the sensor and resulting ions are accelerated (to improve detection efficiency) and deflected away from their incident trajectory (to separate signal ions from potential backgrounds such as UV). Finally, coincidence measurements are used because this technique combines high detection efficiency with very high background rejection.

High throughput of the relatively weak heliospheric signal and very good background rejection are key elements in each of the IBEX-Lo sensor subsystems. In the next section, the sensor and these subsystems are described, with emphasis on contributions each subsystem makes to the overall signal detection and background rejection.

3.2.1.4 IBEX-Lo Operation

IBEX-Lo sensor operations on orbit are relatively simple. After initial on-orbit checkout and high voltage turn-on, the sensor operates in a single science mode during most spacecraft orbits. At low altitudes (< 10 Earth radii, R_E), the sensor is switched from science mode to a standby mode. In this mode, high voltages are turned down or off to eliminate high countrates in the Earth's radiation belts. Since science operations are performed above this altitude, there is no loss of science in these standard operations.

In science mode, the sensor is set at a fixed energy step for 2 spins, so that the entire energy range is sampled in 16 spins. These measurements are repeated without interruption over the entire science operations part of the spacecraft orbit.

Twice per year, the sensor is switched into a special interstellar neutral oxygen and helium mode in the science operations part of the spacecraft orbit. These times are shown in Figure 6 and this mode is described in more detail in Möbius et al. (2009). During the fall interstellar neutral observing period, only oxygen is observed (helium is below the energy range of the sensor). In the part of the spacecraft spin when the IBEX-Lo sensor is viewing ±30° around the ecliptic, the standard 2-spin energy step sequence is interrupted and the sensor is set at a fixed energy corresponding to the expected energy of interstellar neutral oxygen.

In the spring interstellar neutral observing period, there is a similar interruption of the standard 2-spin energy stepping sequence. This time, low resolution sectors are electrostatically switched off in the region ±30° around the ecliptic and the sensor is set at a fixed energy corresponding to the expected energy of the interstellar neutral oxygen. This sequence is repeated for 7 spins. Every 8th spin, the sensor is set at a fixed energy corresponding to the expected energy of interstellar neutral helium.

3.2.2 Instrument Subsystem Descriptions

IBEX is designed with an optimized payload consisting of two very large aperture single pixel ENA cameras: IBEX-Lo (Fuselier et al. 2009a), which measures ENAs with energies from ~10 eV up to 2 keV, and IBEX-Hi (Funsten et al. 2009a), which measures ENAs with energies from ~300 eV up to 6 keV. Both sensors are served by a single combined electronics unit (CEU). Both the IBEX-Hi and Lo sensor designs are based on the same physical principles, but each is tailored to optimize ENA measurements for their respective energy ranges. Each is comprised of the same four subsystems: an entrance system, a charge-conversion system, an electrostatic analyzer (ESA), and a detection system.

The ENA flux originating from beyond the termination shock and measured at 1 AU by IBEX is anticipated to lie within the range of 1 to 500 $cm^{-2}\ s^{-1}\ sr^{-1}\ keV^{-1}$ at ~1 keV (Gruntman et al. 2001; Wurz et al. 2008b). Because of this low ENA flux, the designs of the IBEX sensors have been driven toward maximizing the sensitivity and minimizing the noise and the backgrounds that would otherwise masquerade as ENAs. The numerous sources of background and noise (see Wurz et al. 2009) include ENAs of magnetospheric origin, ionization and acceleration of ambient gas molecules within the sensor, detection of ambient ions that are beyond the maximum rejection energy of the entrance subsystem, and coincidence events generated by penetrating radiation.

A second unique aspect of measuring these ENAs is their energy-dependent transit time from their formation beyond the termination shock to their detection by IBEX at 1 AU. This is illustrated in Figure 7, which shows the time for a hydrogen ENA to travel 100 AU as a function of its energy. The transit times for ENAs within the energy range of IBEX-Hi to travel 100 AU range from 196 days at the central energy (4.09 keV) of the highest energy passband to 591 days at the central energy (0.45 keV) of the lowest energy passband. Furthermore, the range of travel times of ENAs emitted from a point source at 100 AU from the Earth that are detected within the full width at half maximum (FWHM) of a single energy passband ranges from 62 days at the highest energy passband to 143 days at the second lowest energy passband. This time uncertainty for an individual energy passband corresponds to ~1/3 and ~2/3, respectively, of the 6-month period over which IBEX generates a complete sky map. These time resolutions represent a lower limit because the ENA source region may be quite thick and extend significantly beyond the termination shock and because ENAs from source regions at the flanks and tail of the interaction region travel distances that can be substantially farther than 100 AU.

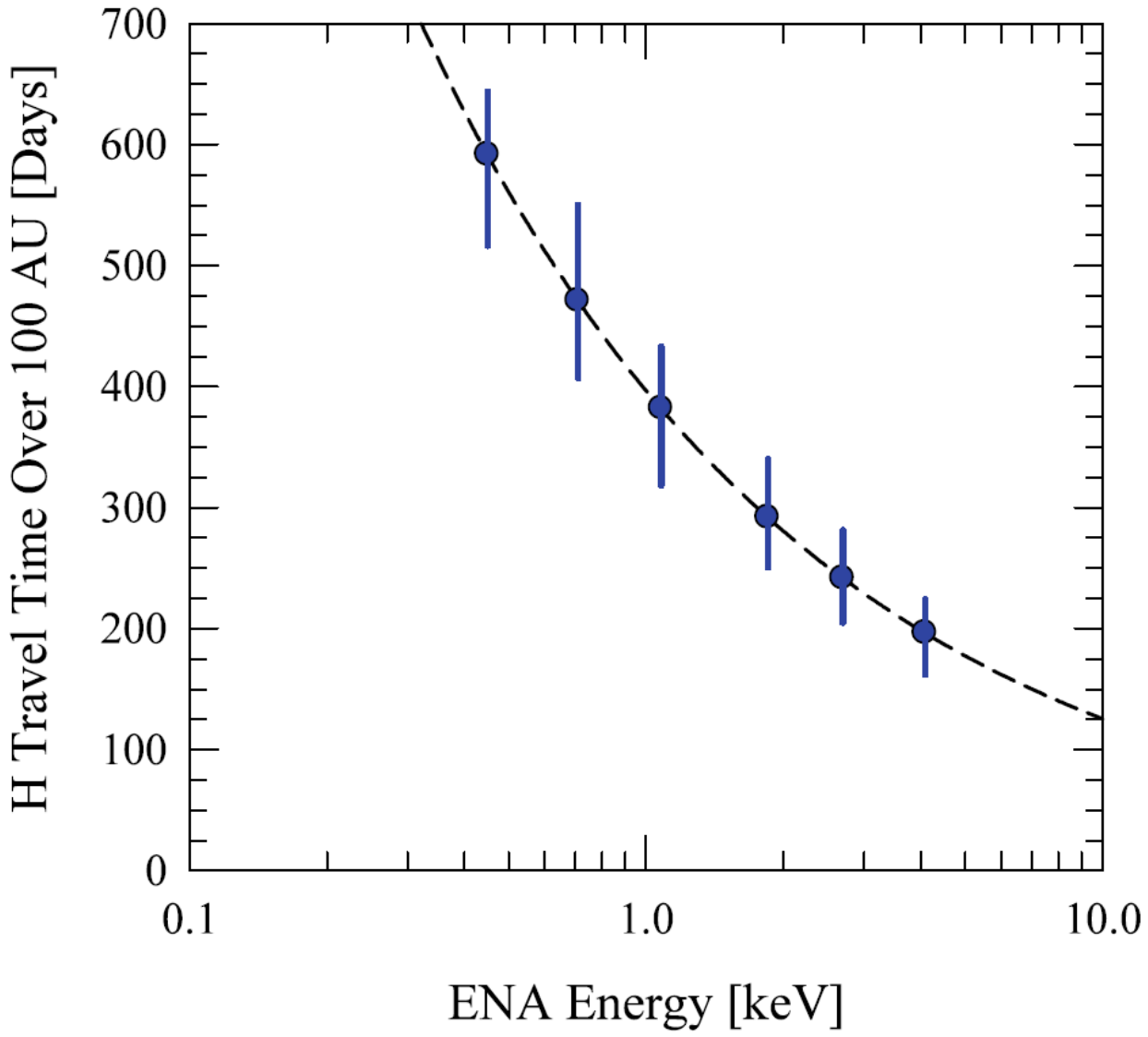

Figure 7: The points show the travel time for a hydrogen ENA to transit 100 AU at the central energy of each of the six IBEX-Hi energy passbands. The error bars at these points represent the travel time uncertainty due to the energy FWHM of each of the energy passbands for events detected through triple coincidence

IBEX-Hi is designed to measure energetic neutral atoms originating from the interaction region between the heliosphere and the local interstellar medium. These ENAs are plasma ions that have been heated in the interaction region and neutralized by charge exchange with the cold neutral atoms of the LISM that freely flow through the interaction region. IBEX-Hi is a single pixel ENA imager that covers the ENA spectral range from 0.38 to 6 keV and shares significant energy overlap and overall design philosophy with the IBEX-Lo sensor. Because of the anticipated low flux of these ENAs at 1 AU, the sensor has a large geometric factor and incorporates numerous techniques to minimize

noise and backgrounds. The IBEX-Hi sensor has a field-of-view (FOV) of 6.5° × 6.5° FWHM, and a 6.5° × 360° swath of the sky is imaged over each spacecraft spin. IBEX-Hi utilizes an ultrathin carbon foil to ionize ENAs in order to measure their energy by subsequent electrostatic analysis. A multiple coincidence detection scheme using channel electron multiplier (CEM) detectors enables reliable detection of ENAs in the presence of substantial noise. During normal operation, the sensor steps through six energy steps every 12 spacecraft spins.

The IBEX-Lo sensor covers the low-energy heliospheric neutral atom spectrum from 0.01 to 2 keV. It shares significant energy overlap and an overall design philosophy with the IBEX-Hi sensor. Both sensors are large geometric factor, single pixel cameras that maximize the relatively weak heliospheric neutral signal while effectively eliminating ion, electron, and UV background sources. The IBEX-Lo sensor is divided into four major subsystems. The entrance subsystem includes an annular collimator that collimates neutrals to approximately 7° × 7° in three 90° sectors and approximately 3.5° × 3.5° in the fourth 90° sector (called the high angular resolution sector). A fraction of the interstellar neutrals and heliospheric neutrals that pass through the collimator are converted to negative ions in the ENA to ion conversion subsystem. The neutrals are converted on a high yield, inert, diamond-like carbon conversion surface. Negative ions from the conversion surface are accelerated into an electrostatic analyzer (ESA), which sets the energy passband for the sensor. Finally, negative ions exit the ESA, are post-accelerated to 16 kV, and then are analyzed in a time-of-flight (TOF) mass spectrometer. This triple-coincidence, TOF subsystem effectively rejects random background while maintaining high detection efficiency for negative ions. Mass analysis distinguishes heliospheric hydrogen from interstellar helium and oxygen. In normal sensor operations, eight energy steps are sampled on a 2-spin per energy step cadence so that the full energy range is covered in 16 spacecraft spins. Each year in the spring and fall, the sensor is operated in a special interstellar oxygen and helium mode during part of the spacecraft spin. In the spring, this mode includes electrostatic shutoff of the low resolution (7° × 7°) quadrants of the collimator so that the interstellar neutrals are detected with 3.5° × 3.5° angular resolution. These high angular resolution data are combined with star positions determined from a dedicated star sensor to measure the relative flow difference between filtered and unfiltered interstellar oxygen.

3.2.2.1 IBEX-Hi

IBEX-Hi is a high sensitivity, single pixel sensor. A critical priority of the IBEX-Hi sensor design and development was maximizing the sensitivity to ENAs while minimizing noise and backgrounds. This drove the detailed designs of each subsystem: the collimator is biased at +10 kV to reject ions up to 10 keV/q and is fabricated using nonlinearly stacked thin plates having collinear aperture holes to minimize ion scattering; the charge conversion subsystem ionizes ENAs so they can be electrostatically removed from the UV and electron background; the energy analysis subsystem projects the enormous entrance aperture area of the sensor onto a small detector area and is serrated to prevent UV and ions >10 keV/q from reflecting into the detector subsystem;

and the detector subsystem uses channel electron multiplier (CEM) detectors to minimize noise from penetrating radiation and to measure coincidence between these detectors to discriminate between noise and a true ENA that is detected in multiple CEMs as it transits the subsystem. The summary of IBEX-Hi performance and resources is listed in Table 3.

Table 3: IBEX-Hi sensor parameters and resources

Energy range	0.38–6.0 keV
Energy resolution ($\Delta E_{\mathrm{FWHM}}/E$)	0.47–0.70
Number of energy steps	6
Field-of-view	6.5° FWHM
	(0.0147 sr)
Mass	7.37 kg
Power (W)	0.65 W
Telemetry	99 bps

Figure 8 shows a cross-sectional illustration of the IBEX-Hi sensor. The sensor is divided into four subsystems that are sequentially encountered by an ENA. The entrance subsystem serves multiple purposes, including limiting the angular field-of-view (FOV) to 6.5◦ FWHM and electrostatic rejection of ambient electrons with energies up to 0.6 keV and ions with energies up to 10 keV/q. The ENA then encounters the charge conversion subsystem that utilizes ultrathin carbon foils to positively ionize a fraction of ENAs that transit a foil. The ionized ENAs then enter the electrostatic energy analysis subsystem, which consists of nested toroidal analyzer plates that project the large entrance aperture onto a small detector subsystem. The bias of the inner ESA plate sets the energy passband for ionized ENAs to enter the detector subsystem. ENAs entering the detector subsystem are accelerated by a bias of −6 kV for increased detection efficiency. The detector subsystem consists of three stacked cylindrical chambers (designated A, B, and C as shown in Figure 8) with each chamber separated by an ultrathin carbon foil. Each chamber has a CEM detector that detects secondary electrons generated by the interaction of the ENA with a foil or an interior wall of a chamber. An ionized ENA can transit all three chambers and register a pulse in multiple detectors, generating a double (AB, BC, AC) or triple (ABC) coincidence event. The following sections describe in detail these subsystems.

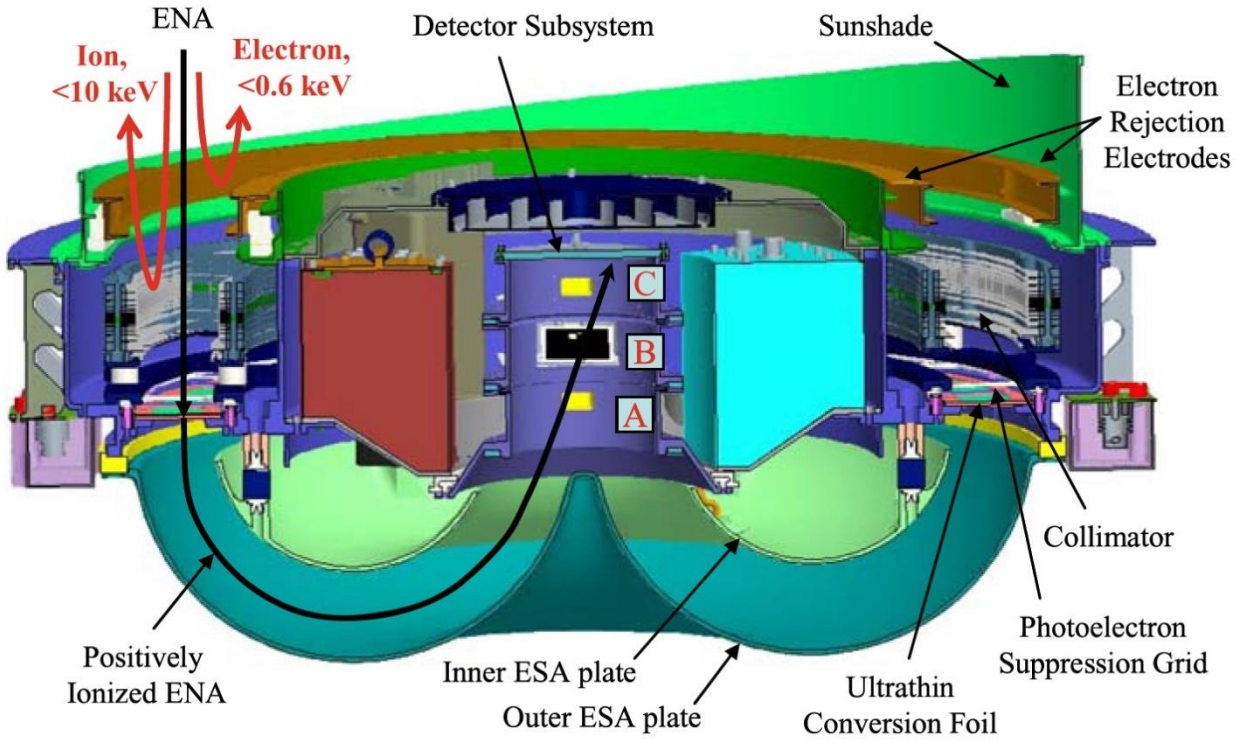

Figure 8: This cross-sectional view of the IBEX-Hi sensor illustrates the subsystems and the trajectory of an ENA through the sensor

3.2.2.1.1 Entrance Subsystem

The IBEX-Hi collimator subsystem, which is nearly identical to that of IBEX-Lo, serves multiple purposes. First, it defines the instantaneous FOV of 6.5° FWHM. Second, appropriately biased electrodes successively prevent electrons and ions from entering the sensor aperture. Third, it limits the access of light into the sensor. The collimator has been optimized to provide maximum ENA transmission for the size and geometry of the sensor. The collimators for IBEX-Hi and -Lo are identical in their design except for small differences in inner and outer radii and a high angular resolution quadrant in IBEX-Lo that is not present in IBEX-Hi.

The collimator consists of stacked plates, each with arrays of collinear hexagonal, photoetched apertures. The use of plates minimizes the exposed surface area from which particles can scatter into the charge conversion subsystem. IBEX-Hi has the same FOV over its entire aperture.

Figure 9 shows a 2-dimensional cut through the collimator. An intrinsic complication using multiple plates with collinear apertures that form channels is leakage, in which particles with trajectories beyond the desired FOV enter one channel and can pass through to a neighboring channel. To prevent such leakage, a series of six plates with the same small separation ($h_1 = d \tan \theta_{Max}$, where θ_{Max} is the largest possible angle of

incidence of particles that must be rejected) is placed at the center of the collimator. From this set of plates in the center, additional plates are alternately stacked toward the entrance and exit ends of the collimator with the plate spacing increasing in a geometrical sequence according to $h_{i+1} = h_i(w + d)/w$ and the largest spacing at the exit plate. In the final collimator design, plate separations are slightly less than the theoretical geometric progression to account for potential leakage from manufacturing tolerances and deviations from plate planarity. The angle θMax is limited to ≤50° at the collimator entrance by a precision-milled pre-collimator with trapezoid-shaped hexagon ribs, whose width is not larger than d − 50 μm.

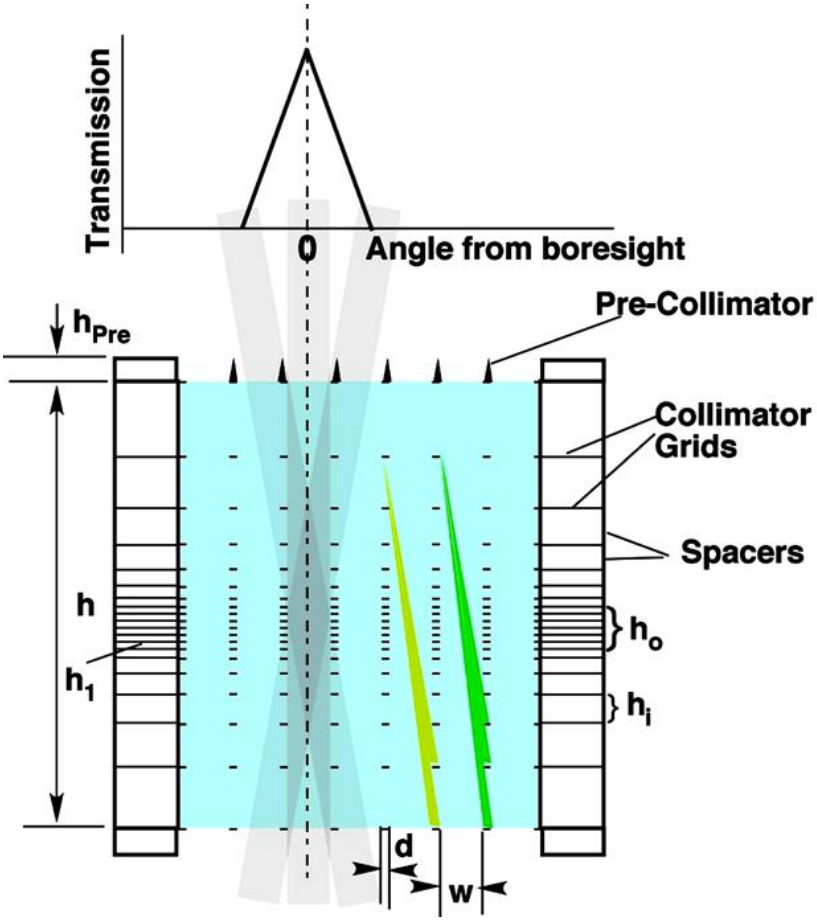

Figure 9: The cross-sectional cut through the collimator illustrates the sequence of identical collimator plates that successively clip trajectories of particles (e.g., ENAs, ions >10 keV, electrons >0.6 keV, and UV light) incident at higher angles. For example, the yellow and green trajectories represent rejection of particles that are outside of the collimator FOV. The pre-collimator prevents particles from entering at very high angles

Assuming no leakage, the angular response of the collimator is solely determined by the width w of the hexagonal openings and the total distance h between the entry and exit plates, and the FWHM is approximately $\theta_{FWHM} = \tan^{-1}(w/h)$. For a geometry with close-packed hexagonal openings in each plate, the transparency T of the collimator at normal incidence is $T = 1/(1+ d/w)^2$, where d is the width of the plate between adjacent apertures.

3.2.2.1.2 Collimator Field-of-View (FOV)

Figure 10 shows the hexagonal point spread function P(θ,φ) of IBEX-Hi as derived using a Monte-Carlo simulation of a single hexagonal channel. The maximum transmission of 0.67 lies at P(0, 0), and the integrated FOV is 0.0147 sr. Modeling of the collimator based on worst-case manufacturing and plate alignment tolerances of 100 μm indicates a cumulative transmission of $<10^{-6}$ for particle trajectories over all angles beyond the nominal FOV. Testing of the IBEX-Lo and IBEX-Hi collimators with an Ar^{+} beam showed that the combined effects of leakage through neighboring channels and scattering from edges of the collimator plates resulted in a transmission of $<10^{-5}$.

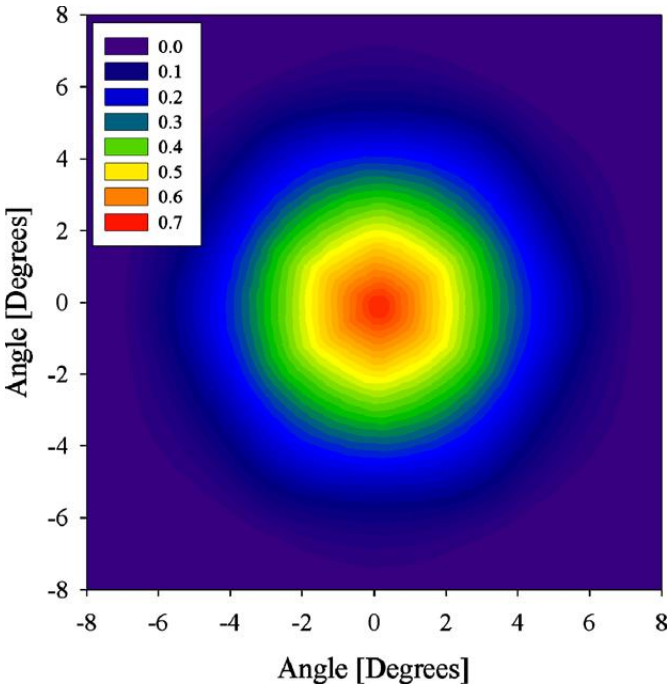

Figure 10: The IBEX-Hi collimator transmission as a function of incident ENA angle is derived using Monte-Carlo simulations of the geometric response of a single hexagonal channel with an aspect ratio of length h to major hexagonal cell width w of 26.83 : 1. This collimator point spread function P(θ,φ) has a maximum transmission of 0.67 and an integrated FOV of 0.0147 sr

The FOV and the overall transparency of the collimator were determined using an optical comparator, which measured the total line width of the collimator stack. The FOV was measured to be 6.44 ± 0.15° FWHM across the hexagon base and 6.5 ± 0.15° FWHM across the hexagon corners. The transparency of the IBEX-Hi collimator was found to be 66.85 ± 0.75%. Angular and linear scans with a narrow 20 keV Ar+ beam across the base and the corners of the hexagon have verified these optical measurements as shown in Figure 11.

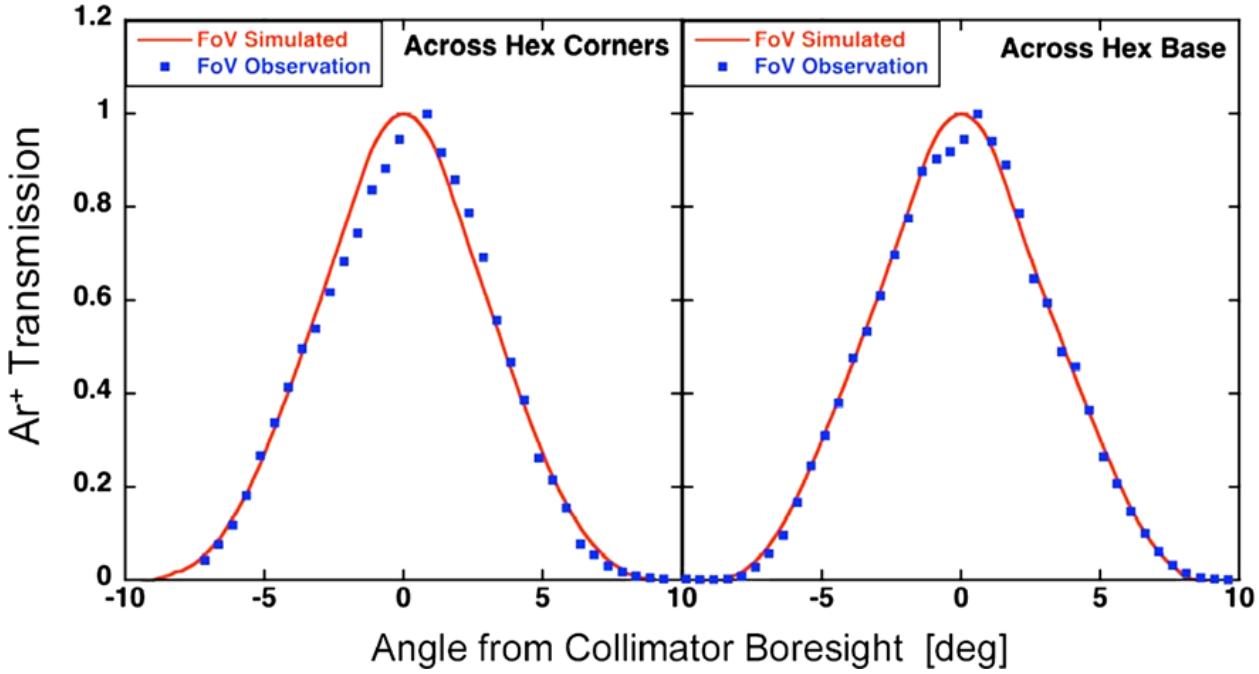

Figure 11: Measured 20 keV Ar^+ transmission through the collimator as a function of incident beam angle θ, where θ = 0° corresponds to the boresight direction, for angular scans across the hexagon corners (left) and across the hexagon base (right). The collimator was grounded during the tests. The simulated angular response is shown in red and agrees well with the data except near 0°, which is an artifact of non-uniform illumination of the ion beam over a small region of the collimator

3.2.2.1.3 Suppression of Ambient Charged Particles

In order to minimize background, the IBEX sensors must reject ambient (positive) ions up to 10 keV/q and electrons, including ubiquitous photoelectrons, up to 0.6 keV. If ions were allowed to enter IBEX-Hi, they would be indistinguishable from ENAs of similar energy. Rejection of ions up to 10 keV/q was chosen because ion fluxes at energies >10 keV decrease rapidly with increasing energy for most plasma environments encountered over the IBEX orbit. This ion rejection is achieved by biasing the entire collimator structure to +10 kV. Furthermore, the pre-collimator imposes electrostatic troughs at the entrance of each hexagonal channel that act as defocusing lenses, so most incident ions between 10 and 16 keV are deflected to angles significantly outside the collimator acceptance range and thus are substantially prevented from reaching the conversion foil.

Figure 12 shows the observed ion transmission through the IBEX-Hi collimator as a function of incident angle for 7.5 keV Ar+ in a test configuration in which the collimator was biased to +8 kV and used to validate the collimator electro-optic model. Maximum transmission values of ~2×10−4 were obtained. This represents an upper bound to the actual ion transmission due to neutralization of a small fraction of the ion beam by

charge exchange with the residual gas in the vacuum chamber; these neutrals can pass through the collimator and be detected.

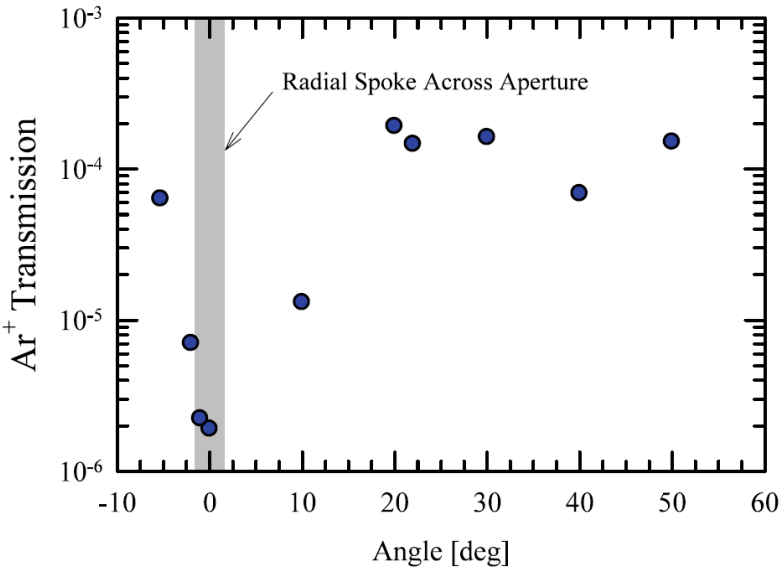

Figure 12: Transmission of 7.5 keV Ar^+ as a function of the azimuthal angle around the annular collimator entrance. The collimator is biased to +8 kV and the electron repeller electrode is biased to −2.5 kV. A radial spoke spanning the aperture at 0° completely blocks the incident beam. Except for measurements at the spoke, these measured transmission values represent an upper limit because of the small fraction of Ar^0 in the incident beam that passes through the collimator and is detected

If left exposed to the space environment, the collimator biased to +10 kV would attract and collect ambient electrons, including copious photoelectrons from the sunlit side of the spacecraft, resulting in a total electron current approaching 100 μA. Furthermore, many of these electrons would transit the collimator and ionize the residual gas in the space between the collimator and charge conversion subsystem; these ionized atoms and molecules would then be accelerated to the conversion foil and could masquerade as legitimate ENAs. To avoid both effects, negatively biased electron repeller ring electrodes are placed in front of the inner and outer radii of the collimator but completely outside of the collimator FOV. Figure 13 shows a cut through the entrance subsystem with simulated equipotential lines. To achieve a closed potential surface of −0.6 kV in front of the +10 kV collimator, the electron repeller electrodes are biased to −3.125 kV. Tests with an electron beam and the collimator biased to +10 kV demonstrated that rejection of electrons up to 0.6 keV is achieved with this configuration. We note also that photoelectrons and secondary electrons emitted from the electron repeller electrodes are accelerated to the collimator but only at high incident angles significantly outside of the collimator FOV, thus preventing these electrons from reaching the critical volume between the back of the collimator and the charge conversion subsystem.

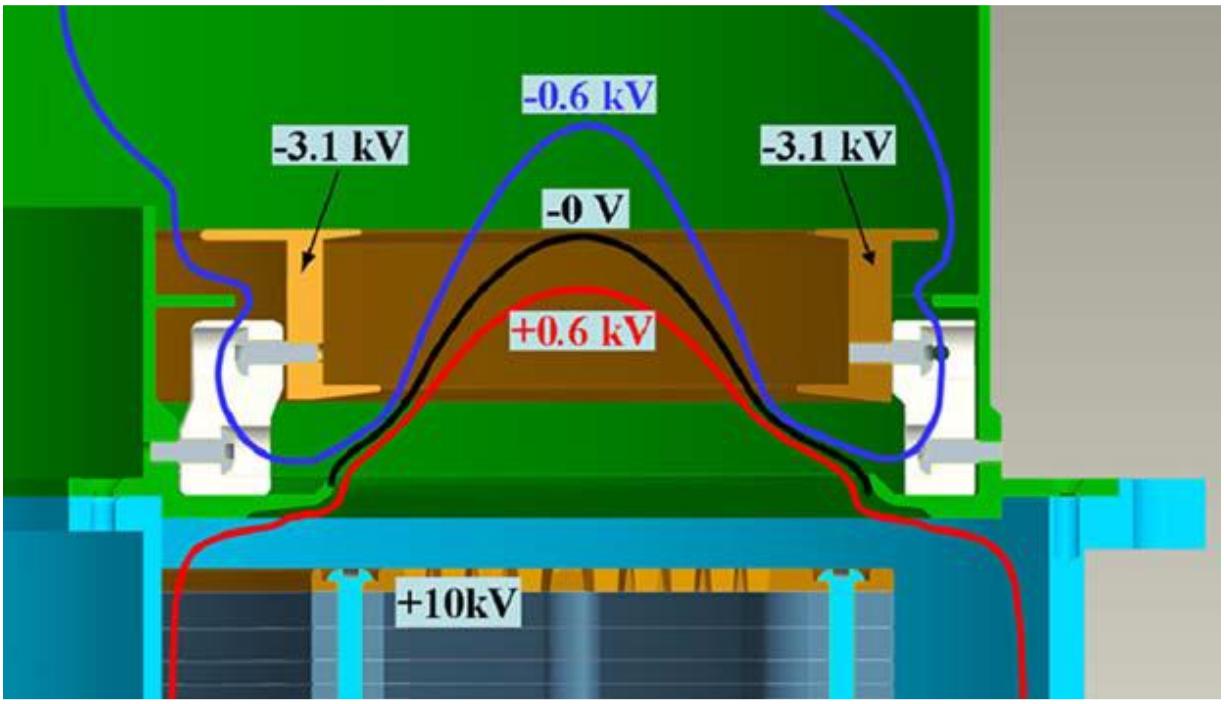

Figure 13: The radial cut through the IBEX entrance subsystem illustrates equipotential field lines based on the subsystem's SIMION electro-optic model. When the collimator and electron repeller electrodes are biased to +10 kV and −3.1 kV, respectively, a closed −0.6 kV equipotential surface spans the entrance region, thereby rejecting all electrons with energies ≤0.6 keV

3.2.2.1.4 Charge Conversion Subsystem: ENA Ionization

ENAs that transit the collimator enter the charge conversion subsystem whose purpose is to convert the ENAs to positive ions by transmission through an ultrathin foil. A total of 15 foils are distributed in a circular array as shown in Figure 14 with inner and outer radii of 14.41 cm and 16.56 cm, respectively. These foils are nominal 0.6 μg cm^{-2} carbon from ACF Metals and are mounted on 333 line-per-inch (lpi) Ni grids that have a typical transmission of 73.4% as measured using a 50 keV H^+ beam. Each foil is mounted on a two-window foil frame that was determined by analysis and testing to be the optimal geometry for acoustic survival during launch. The foil frames each have an open area of 10.44 cm^2 for a total conversion foil area of 156.6 cm^2. The conversion foil grid transmission was measured to be 73.4%, and the transmission of the photoelectron suppression grid located immediately in front of the conversion foils was 95%.

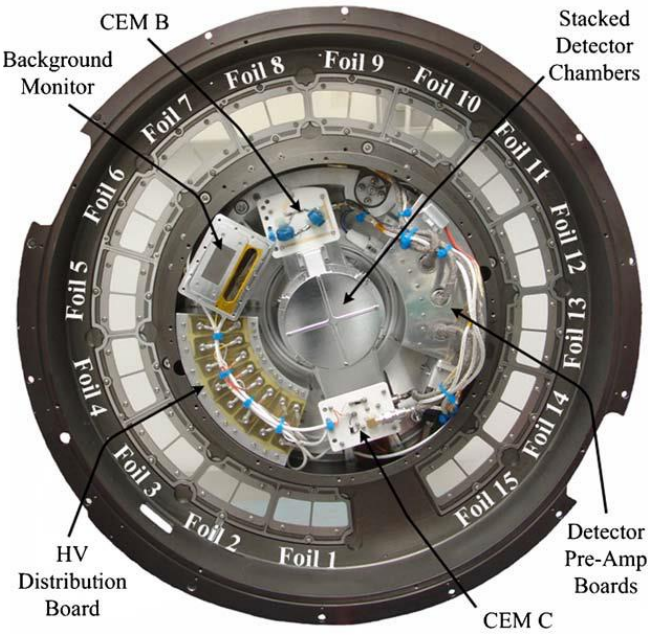

Figure 14: The charge conversion foil locations are noted in this front view of the IBEX-Hi sensor that has its entrance subsystem, ESA subsystem, and detector cover removed

The probability of H0 exiting the foil as H^+ is shown in Figure 15 (Funsten et al. 2001). The ionization probability ranges from 0.013 at 0.33 keV to 0.13 at 6 keV, and the laboratory data infer two different ionization regimes by their different energy dependence. ENAs also lose energy in the foil as measured by Allegrini et al. (2006).

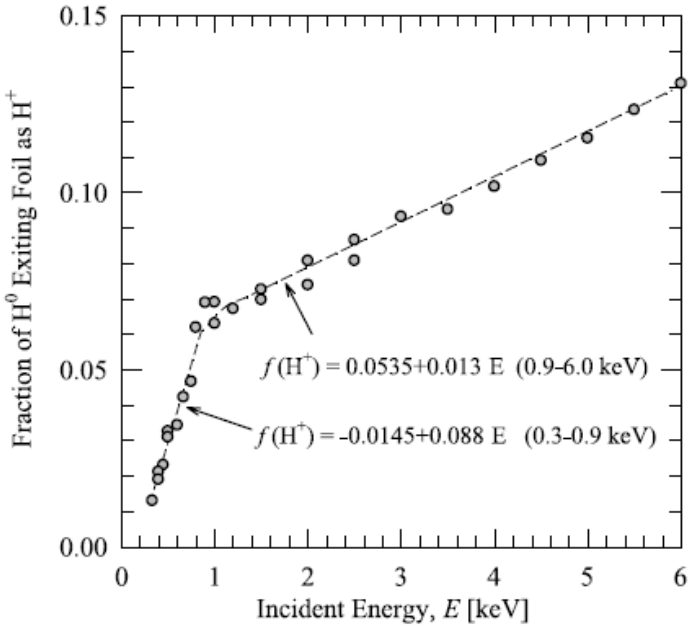

Figure 15: The measured ionization probability of H^0 transmitted through an ultrathin carbon is shown as a function of incident energy

The foil constant $kF = E_0\psi_{1/2}$, in which E_0 is the energy of an incident H^+ ion beam and $\psi_{1/2}$ is the angular halfwidth of the scattered beam after transit through the foil, was measured for each foil as a proxy for foil thickness (Funsten et al. 1993) and to quantify its energy-dependent angular scattering, which is an important part of the end-to-end sensor model. The angular halfwidth $\psi_{1/2}$ was determined by integrating the 2-D scatter distribution in one (x,y) dimension and dividing by 1.19 to correct for integration of a Lorentzian distribution. The measured foil constant, frame serial number, and location in IBEX-Hi of each foil are listed in Table 4. The average foil constant for all foils is 18.5 keV deg. The foils were additionally analyzed for pinholes using Ar^+ beam analysis (Funsten et al. 1992), and the pinhole fraction was less than 1% for all foils.

Table 4: IBEX-Hi foil placement and measured foil constant k_F. The requirement for IBEX-Hi is $kF \leq 25$ keV deg

Foil location	Foil number	Foil constant, k_F [keV deg]
1	27	16.8
2	30	19.3
3	19	19.3
4	31	16.8
5	42	20.2
6	43	17.6
7	17	18.5
8	38	18.5
9	41	18.5
10	48	18.5
11	33	19.3
12	49	16.8
13	40	20.2
14	36	19.3
15	50	16.8
Average		18.4

One possible source of significant background is electron impact ionization of outgassing atoms and molecules in the region between the conversion foils, which lie at ground potential, and the collimator, which lies at +10 kV. Ionization is caused by photoelectrons or secondary electrons that are emitted from the entrance surface of a foil or a foil frame surface and then accelerated toward the collimator. Ionized atoms and molecules are accelerated in the opposite direction of electron acceleration, directly toward the conversion foils. These ions could exit the foil within the energy range of IBEX-Hi, therefore masquerading as heliospheric ENAs. We have minimized this “ion gun effect” background in two ways. First, the charge conversion foils act as a seal to block gas in the energy analysis and detector subsystems from entering the collimator region, which minimizes the pressure of the ambient gas in the “ion gun” region. Second, the charge conversion subsystem incorporates a 25 lpi nickel grid with 95% transmission located 0.48 cm in front of the charge conversion foils and biased to −300 V to suppress the photoelectrons and secondary electrons. Simulations show complete suppression of photoelectrons and secondary electrons emitted from the conversion foils and foil frames with energies up to at least 30 eV; this value is significantly lower than might be expected from a −300 V grid bias because of the large field leakage due to the high geometrical grid transmission (Read et al. 1998). The suppression grid reduces the “ion gun” background by a factor of ∼20.

3.2.2.1.5 Energy Analysis Subsystem

Positively ionized ENAs exiting the charge conversion foil enter the electrostatic energy analyzer (ESA), whose inner and outer analyzer plates are shaped like a “Bundt” baking pan (Moestue 1973). This geometry was successfully used on the Russian Interball mission (Vaisberg et al. 1995) and on the ISTP/POLAR mission (Shelley et al. 1995). The radius of the electro-optic surface of the inner (outer) ESA plate is 5.32 cm (8.34 cm), with the center of this radius located 8.76 cm (8.83 cm) from the central symmetry axis of the ESA plates and 0.82 cm (1.15 cm) below the plane of the conversion foils.

The inner ESA plate can be biased up to −7 kV and is the primary control for the central energy of each of the six energy passbands of IBEX-Hi, where we define the central energy as the energy of the maximum of the sensor response function for the passband. The ESA plates had serrations of hemispherical troughs of radius 0.76 mm machined such that the troughs are concentric relative to the symmetry axis of the sensor and, therefore, are aligned perpendicular to the direction of electrostatic deflection of ionized ENAs in the ESA. The serrations minimize scattering of many background particles into the detector subsystem, including UV light, ENAs exiting the foil as neutrals, ionized ENAs outside of the set energy passband, and ions >10 keV that can successfully transit the entrance and charge conversion subsystems.

The outer ESA plate is biased to −90 V, −80 V, and −20 V for the lowest three energy passbands (passbands 1, 2, and 3, respectively) for two purposes, both of which increase the energy analysis subsystem throughput. First, ENAs scatter in the foil, especially at lower energies, to an angle at which they cannot transit the ESA even though their energy resides within the energy passband. For the lowest energy

passband, the −90 V on the outer ESA plate coupled with the −780 V on the inner ESA plate accelerate and proximity focus ionized ENAs so they have a higher probability of transiting the ESA. Second, ENAs lose proportionately more energy in the foil at lower energies, so fewer ENAs that would otherwise transit the ESA actually do. Because all ionized ENAs are accelerated by the same energy into the ESA, they are subsequently analyzed at a higher central energy and, importantly, at a broader energy passband. This shift of ionized ENAs to higher energies in the ESA and the wider energy passband at these higher energies therefore enable a higher throughput to compensate for the larger energy loss in the foil at lower incident ENA energies.

The intrinsic geometry of the toroidal ESA plates provides azimuthal focusing throughout the first 90◦ of deflection and azimuthal defocusing beyond 90◦. The detector subsystem is biased to −6 kV to accelerate ionized ENAs into the detector subsystem to counteract this defocusing and also to increase the detection efficiency of the ionized ENAs. Electro-optic simulations of the coupled ESA and detector subsystems optimized the design so that the focal points of ENA trajectories at the central energy of each passband are located near the center of the detector subsystem and along its central axis.

3.2.2.1.6 Detector Subsystem

The detector subsystem consists of three nearly identical, stacked cylindrical chambers, each 5.6 cm in diameter and 2.6 cm tall and each having a CEM detector as shown in Figure 16. The chambers, designated A, B, and C as sequentially encountered by an ionized ENA, are separated by two thin (nominal 2 μg/cm2) carbon foils (McComas et al. 2004). The ionized ENAs transit the foils and generate secondary electrons (e.g., Ritzau and Baragiola 1998; Allegrini et al. 2003) at their entrance and exit surfaces. Similarly, the ionized ENAs generate secondary electrons when they impact the aluminum interior walls of the chambers or the back wall of Chamber C. As shown in Figure 16 secondary electrons generated within one chamber are electrostatically attracted towards the CEM detector of the same chamber by the potential difference between the CEM funnel (−1.7 kV) and the chamber (−6.0 kV). The secondary electrons subsequently generate a pulse in the CEM, and detection of pulses in more than one CEM detector within a prescribed time window is registered as a coincident event.

Penetrating radiation (e.g., >5 MeV electrons or >100 keV photons) can generate a coincidence signal that can be mistaken for a detected heliospheric ENA. To minimize this effect, the CEMs are positioned so that no straight penetrating particle trajectory can go through all three CEMs. Thus, a triple coincidence is limited to penetrating particles actually crossing the two carbon foils.

The Sjuts CEMs have a rectangular funnel with a sensitive area of 1.20 × 2.47 cm. The carbon foils, procured from ACF Metals, are mounted on electro-formed 200 lpi nickel grids with a transmission of ∼78%. The entrance grid of Chamber A is covered by a 70 lpi electroformed nickel grid, with a transmission of ∼90% but no foil.

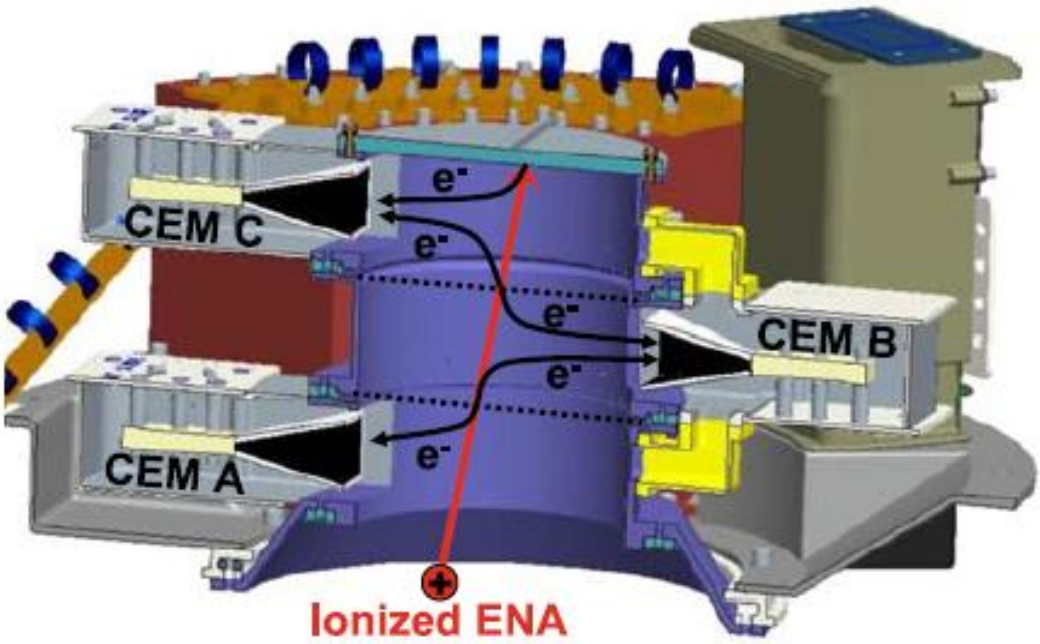

Figure 16: Ionized ENAs enter the IBEX-Hi detector subsystem and generate secondary electrons (e^-) at interior chamber surfaces including the foils between Chambers A and B and between Chambers B and C. These secondary electrons are detected in each chamber, enabling double (two chamber) or triple (three chamber) coincidence detection of a single ENA

When a secondary electron is detected by any of the three CEM detectors, short (3 ns) and long (96 ns) electronic coincidence windows are opened. During these intervals the electronics are triggered to accept and record events detected in the other CEMs. At the end of the long coincidence window, 18 unique combinations of events are possible. We note that an ionized ENA may not be detected for at least three reasons: the secondary electron yield from carbon foils is statistical (Poisson) with the non-zero probability that no secondary electron is produced (Gruntman et al. 1990); the electro-optic model shows that not all secondary electrons impact the sensitive area of the CEM detector; and the CEM detection efficiency for electrons at ~4 keV is ~70–80% (Paschmann et al. 1970).

The shortest travel time for a 6 keV ENA to traverse the two foils of the detector subsystem is about 17 ns, which is much longer than the short coincidence window duration of 3 ns. Because an ionized ENA enters Chamber A first and reaches Chamber C last, a coincident event with CEM C registering a pulse in the short time window when an event in CEM A is also detected is unlikely to be a real ENA. Therefore, we developed two qualification schemes, discussed in the next section, to prioritize coincidence combinations that are most likely associated with ENAs rather than penetrating radiation or accidental coincidences.

3.2.2.1.7 Electronics

The IBEX-Hi electronics are designed to capture coincident events between any of the three CEM detectors and to record counts from the CEM detector in the IBEX Ion Background Monitor (IBaM) (Allegrini et al. 2009). The electronics are distributed between the Combined Electronics Unit (CEU) and the IBEX-Hi sensor.Within the IBEX-Hi sensor, high voltage filters eliminate noise and charge amplifier electronics convert CEM charge outputs into digital signals for processing on the Digital Board in the CEU.

The CEU also contains the high voltage power supplies (HVPS) for both sensors that generate and control voltages for the CEM detectors, collimator electrodes, and electro-optic elements. While the HVPS for both IBEX-Lo and IBEX-Hi reside on the same CEU board, their physical layouts are completely separated so that a fault on the HVPS of one sensor will not affect the HVPS performance of the other. The IBEX-Hi HVPS, their maximum and nominal operating voltages, and maximum output currents are listed in Table 5. Except for the Collimator (+) voltage, the high voltages for IBEX-Hi are generated by linearly regulating the output voltage from bulk high voltage supplies, which increases the overall efficiency. The step settling time of the inner ESA plate supply is 0.2 s for a step from −7.0 kVto −0.5 kV and 0.05 s for a step from −0.5 kVto −7.0 kV, both of which are much shorter than the measurement time at a single energy step of two consecutive spacecraft spins.

Table 5: IBEX-Hi high voltage power supplies (HVPS)

High voltage power supply	Max. voltage (kV)	Nominal operating voltage (kV)	Max. current (μA)
Collimator (+)	11.0	10.0	4
Collimator (−)	−4.6	−3.1	4
CEM_A	−4.6	−1.7	23
CEM_B	−4.6	−1.7	23
CEM_C	−4.6	−1.7	23
CEM_D	−4.6	−1.7	23
Detector Chambers	−6.0	−6.0	1
Inner ESA	−7.0	Energy dependent	1
Outer ESA	−0.30	Energy dependent	1
Suppression Grid	−0.30	−0.30	1

The high voltages applied to the CEM detectors and the chamber stack are filtered to prevent the introduction of noise in the signal electronics. Each CEM detector has a onepole low-pass filter with a cut-off frequency of 72 Hz. The coaxial return line for each CEM HVPS has a “zap-trap” of back-to-back diodes and a capacitor to provide a chassis return path to dissipate the large filter capacitor in the event of a high voltage discharge, thus protecting the electronics within the sensor. The high voltage to the chamber stack uses a two-pole filter with a cut-off frequency of 127 Hz.

Amptek A121 fast hybrid charge amplifiers convert the electronic pulse outputs from the CEMs into digital pulses. The Amptek A121 was selected because of its relatively low power, voltage-adjustable threshold, and small package. The amplifier electronics were housed in separate, grounded enclosures for each CEM to maximize isolation and therefore minimize crosstalk between the CEMs’ electronics chains. The anode output of each CEM is connected to the input of the charge amplifier by an RG-178 coaxial cable that is ~15 cm long. The charge amplifier is protected from high voltage discharge by a 100 Ω carbon composition resistor that is mounted away from other board components and followed by back-to-back input protection diodes.

The threshold for the A121 is voltage controllable within the range 5×10^4–5×10^6 electrons and commanded through software at a nominal operating value of 3×10^5 electrons. This is well above the analog noise floor, ensuring that no electronic noise can trigger a false coincidence in the measurement, and well below the centroid of the CEM pulse height distribution, ensuring no loss of valid counts. A filtered, differential-receive circuit processes the analog threshold that is generated in the CEU, reducing noise and re-referencing the threshold to the charge amplifier’s ground. The output pulse width is set to 75 ns. The dead-time is 525 ns, implying a maximum theoretical periodic throughput for each channel of 1.9 MHz.

The TTL-level output of the charge amplifier is converted to Low Voltage Differential Signal (LVDS) levels before being transmitted to the CEU. This current-steering output produces small voltage swings that are equal and opposite, which minimizes noise on the power and ground lines. This is an important feature which greatly reduces the possibility of cross-talk between channels as well as feedback into the front-end of the amplifiers.

Besides the three CEM detectors (A, B, and C) in the IBEX-Hi detector subsystem, a fourth CEM detector (D) is used in the IBaM. CEM D plays no role in the coincidence measurement and simply accumulates counts to measure the ion background. The detector type and analog electronics (including input filtering, zap-trap protection, and charge amplifier board) for CEM D are identical to the other CEM detectors.

Test pulsers enable testing and exercising of the charge amplifier channels and the downstream coincidence circuitry. Each test pulse is equivalent to a CEM pulse magnitude of 6.8×10^6 electrons. The test pulsers are controlled by registers within the CEU field programmable gate array (FPGA). Various pulse patterns and coarse time delays can be generated to simulate all possible coincidence event types, providing tremendous flexibility to test the electronics chain.

The CEU receives the digital signals from CEM detectors A, B, and C and uses a novel polling scheme at the ends of two time windows to classify coincident events rather than more traditional and much more complex time-of-flight (TOF) measurement. As shown in Figure 17, the digital signals from each CEM are split. The first lines are each input into a 4 ns fixed pre-delay and subsequently into a gated D-latch. When a pulse is detected in any CEM, its individual state is latched “hi” for the duration of the coincidence measurement.

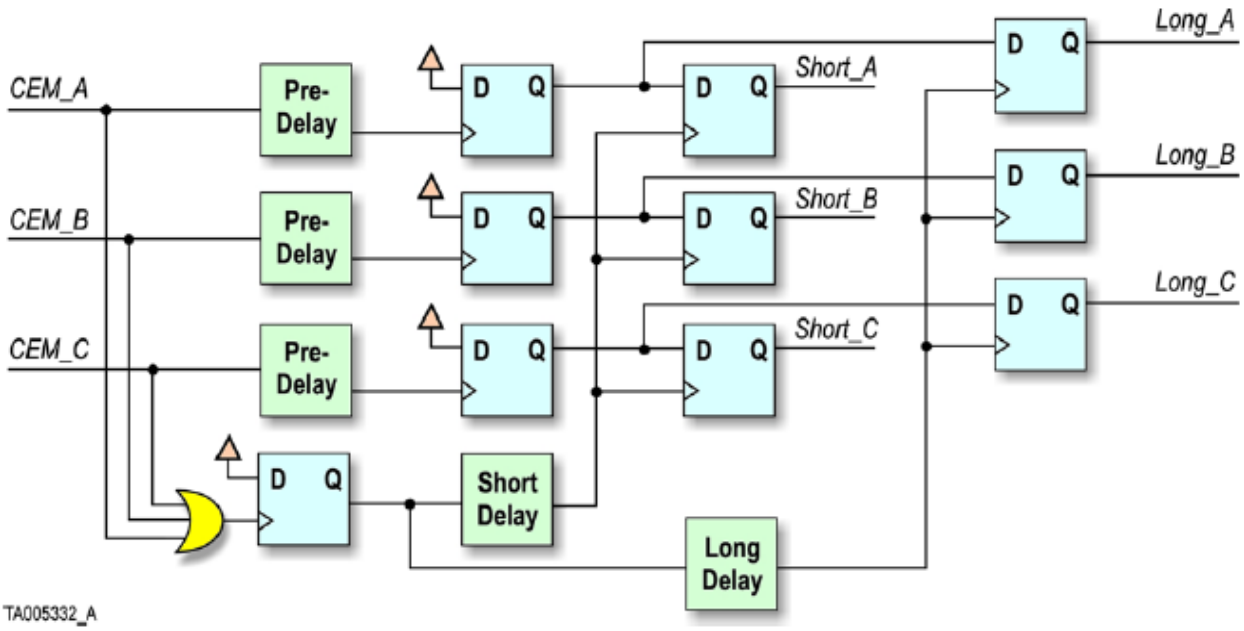

Figure 17: The coincidence circuit within the CEU FPGA provides a novel polling scheme for capturing whether an event was detected in any of the three CEM detectors at the end of short and long time windows

The second lines split from the CEMs are used to poll the state of each CEM at two prescribed times (designated as “short” and “long”) using the following method. The CEM outputs are input into an OR gate to register if any CEM detected an event, and the output of the OR gate is latched for the duration of the coincidence measurement. The latch output is then split and input into a “short” time delay (controllable within a range of 1–8 ns in steps of 1 ns) and a “long” time delay (controllable within a range of 30–100 ns in 10 ns steps). The outputs of the time delays are used as the clock inputs, or triggers, for the final gated Dlatches to record snapshots of which detectors register

an event at the ends of the short and long time windows. The contribution of the pre-delay of 4 ns combined with the nominal (but adjustable) settings for the short and long time delays of 7 ns and 100 ns, respectively, correspond to nominal short and long coincidence windows of 3 ns and 96 ns, respectively.

When an event is detected, the latched outputs of Short_A, Short_B, and Short_C are registered at the end of the short time window, and the latched outputs of Long_A, Long_B, and Long_C are registered at the end of the long time window. If a latched state is “hi”, which corresponds to a detected event, then this state is recorded for the appropriate time window and detector. A “hi” event state captured at the end of the short window is designated as lowercase “a”, “b”, or “c” and at the end of the long window is designated as uppercase “A”, “B”, or “C” according to the CEM detector in which the event occurred. Note that an event registered in the short window will also be registered in the long window.

We define a “Long” event as any non-coincident or coincident event that has registered at least one “hi” state at the end of the long time window, irrespective of whether it was registered as a “hi” in the short time window. The set of Long events therefore includes all single events and coincidence combinations. For example, a “Long AB” corresponds to all possible coincident AB events: aAB, bAB, and abAB.

Because an ionized ENA sequentially traverses Chambers A, B, and C, we find that some coincidence combinations more likely result from detection of ENAs, such as an A event first observed in the short time window and a C event only observed in the long time window. Conversely, other combinations more likely result from penetrating radiation, such as both A and C events detected in the short time window. Therefore, IBEX-Hi has two qualification schemes, either of which can be invoked by the CEU for any coincidence combination, to prioritize individual coincident events for the histogram data and the direct event data stream

The first qualification scheme, denoted as Qual(Not_C), retains all coincident events of a coincidence combination in which the short time window never includes an event in Detector C. For example, “Qual(Not_C) ABC” retains only the triple coincidence events aABC, abABC, and bABC.

The second qualification scheme, denoted as Qual(Not_Equal), retains all events in which the events in the short and long windows are different. For triple coincidences, “Qual(Not_Equal) ABC” includes all triple coincidence events except for abcABC; in another example, “Qual(Not_Equal) AB” includes aAB and bAB but excludes abAB.

We note two additional features of this implementation. First, the pre-delay of 4 ns mentioned above combined with the adjustable short time delay provides a trim range to set a short coincidence window that includes 0 ns and record a snap-shot of the

combination of CEM signals that caused the event to start. Second, the coincidence measurement can statistically identify and quantify the abundance of heavy ions in the measurement (Allegrini et al. 2008).

3.2.2.2 IBEX-Lo

The IBEX-Lo sensor is a large geometric factor, single pixel camera. It uses a large annular entrance to collimate the neutral flux. This entrance has positive and negative electrodes that reject incoming ions and electrons. The neutrals pass through the collimator and strike a conversion surface at a shallow angle (nominally 15°) where a fraction of them are converted to negative ions. These negative ions are accelerated in an electrostatic analyzer (ESA) that also selects the sensor energy range and resolution. Upon exiting the ESA, negative ions are further accelerated into a multiple carbon foil time-of-flight (TOF) mass spectrometer that measures ion mass.

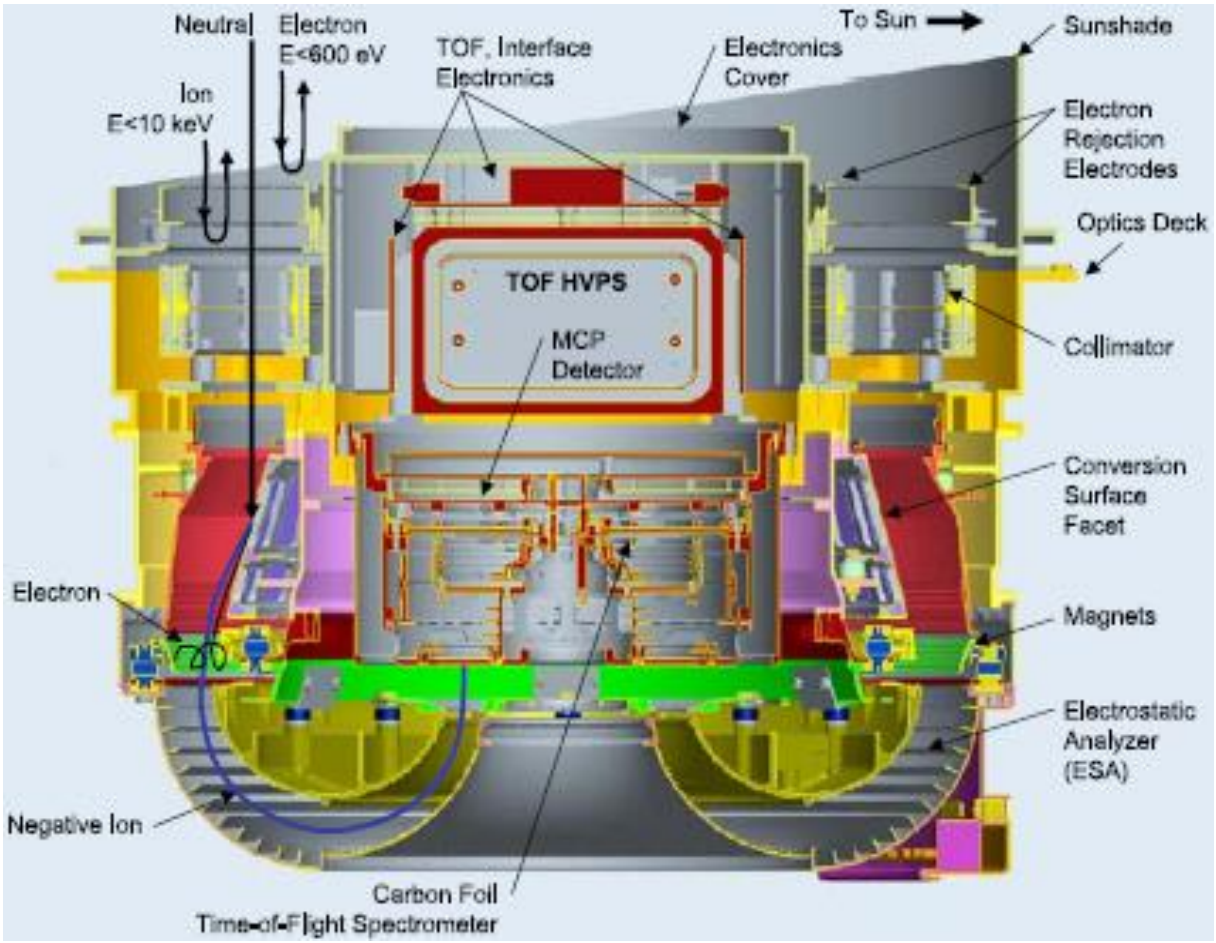

Figure 18: Cross-section of the IBEX-Lo sensor showing the primary components. The sensor is rotationally symmetric about the centerline axis of the figure. Electrons, neutrals, and ions all enter the sensor through the collimator. Charged particles are rejected by the collimator and electron rejection electrodes. Neutrals pass through the

collimator and strike a conversion surface. A fraction of these incident neutrals leave the conversion surface as negative ions and pass through the electrostatic analyzer. Electrons from the conversion surface are deflected by two concentric rings of permanent magnets. Negative ions exit the ESA, are accelerated and enter a triple coincidence time-of-flight (TOF) mass spectrometer. In this subsystem, the ion mass is determined

Figure 18 shows a cross-section of the sensor (rotationally symmetric about the centerline of the figure with a maximum radius of about 15 cm). Major components are labeled on the right hand side, and representative trajectories of neutrals, ions, and electrons, are shown on the left hand side. A picture of the front entrance of the sensor (in the calibration vacuum chamber) with some of the components labeled is shown in *Figure 19*. Table 6 shows a summary of the sensor parameters and resources.

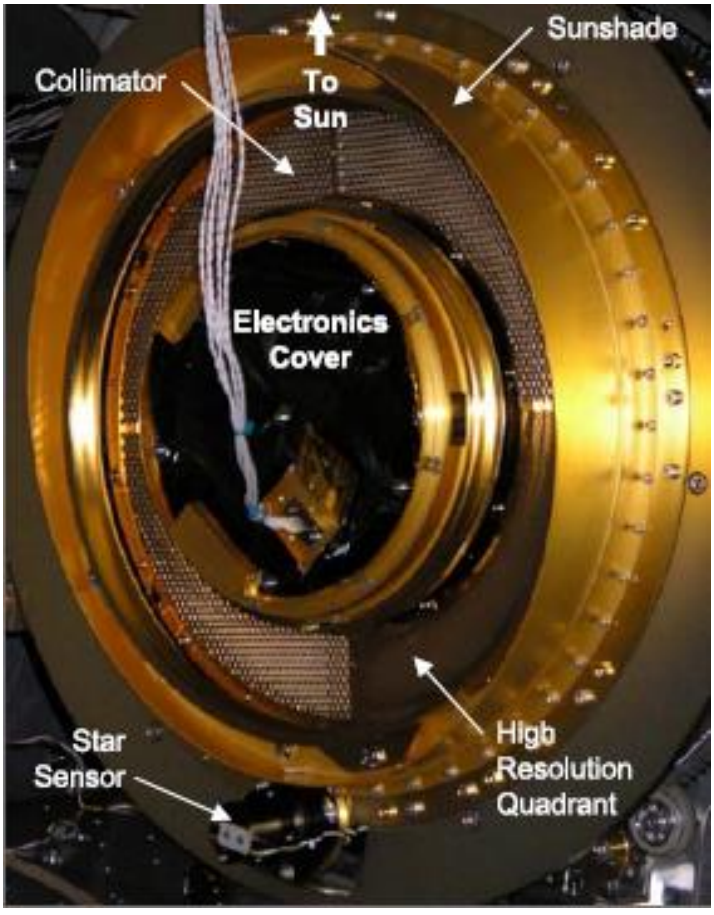

Figure 19: Photograph of the IBEX-Lo sensor entrance system in the calibration vacuum chamber. The star sensor is at the bottom and, in this orientation, the Sun direction is up. The collimator is divided into 4 quadrants by thin spokes located at 0°, 90°, 180°, and 270° relative to the Sun direction. In the lower left hand quadrant, the hexagon pattern that defined the FOV is smaller than the one in the other three quadrants. This high resolution sector is used to determine the flow direction of the interstellar neutral oxygen during the spring observing period

Table 6: IBEX-Lo sensor parameters and resources

Energy Range (eV)	10–2000
Energy resolution ($\Delta E/E$)	0.8
Mass Range	1–32 amu
Mass Resolution $M/\Delta M$	> 4
Field of View—Low Resolution	$6.54° \times 6.54°$
Field of View—High Resolution	$3.19° \times 3.19°$
Geometric Factor* (cm^2 sr)	0.91
Mass (kg)	11.5
Power (W)	3.46
Telemetry (bps)	122

* *This geometric factor refers only to the collimator opening and is the sum of the high and low resolution sectors, not including grid transmission factors, neutral-to-ion conversion efficiencies, ESA or TOF efficiencies*

The sensor consists of four major subsystems: the entrance, ENA to ion conversion, energy analysis, and mass (TOF) analysis subsystems. These four subsystems are attached to the "optics deck", which provides the stable mechanical platform for the ion optics and also a stable connection to the IBEX spacecraft. The four subsystems operate together, maximizing sensitivity and minimizing background to produce the highest possible signal to noise measurements over the IBEX-Lo energy range.

3.2.2.2.1 IBEX-Lo Entrance Subsystem

The entrance subsystem consists of the sunshade, electron rejection electrodes, and collimator. The sunshade is cut at an angle so that sunlight cannot reflect off any part of the sensor onto the collimator. Eliminating scattered sunlight from the collimator entrance is critical for background reduction. The sensor views 90° away from the spacecraft spin axis and the spin axis is reoriented towards the Sun every orbit (8 days). By setting the spin vector a few degrees off the Sun and letting it precess through the Sun direction, the spin vector will move a maximum of about ±4° off the Sun direction over the course of an orbit. Thus, with margin, the sunshade was designed to block sunlight for a spin axis that is up to 8° off of the Sun direction. Elimination of sunlight reduces UV flux into the sensor to interstellar levels (~ 800 Rayleighs maximum flux at Lyman Alpha wavelength) during prime science observations. The UV flux will be considerably greater (~ 20 kRayleighs at Lyman Alpha wavelength) when the sensor views the Earth (twice per year), but, at those times, the sensor will be viewing through the Earth's magnetosphere and not making prime heliospheric science measurements.

Since the sensor views 90° from the Sun direction, the cold (temperatures of ~ 10's of eV maximum), flowing (~ 400 km/s away from the Sun) solar wind ion distribution does not have direct access to the sensor through the collimator. However, the solar wind (halo) electron distribution has sufficient temperature that a significant electron flux in the energy range from 10's to 100's of eV could enter the sensor. These electrons could

ionize residual gas inside the sensor through electron impact ionization. The newly created ions would be accelerated into the conversion surface, and resulting negative ions would be indistinguishable from those created by source heliospheric neutrals. To eliminate low-energy electrons, a pair of electron rejection electrodes encircles the entrance to the collimator. The electrodes are charged to −3.1 kV, creating a field that rejects up to 600 eV electrons from the collimator.

The collimator defines the instantaneous fields-of-view (FOVs) of the sensor and is held at a positive high voltage of 10 kV to keep energetic, positive ions (up to 10 keV) out of the sensor. The collimator designs for IBEX-Hi and -Lo are identical except that the annular diameter of the IBEX-Lo collimator is smaller and the IBEX-Lo collimator has two separate FOVs. The two FOVs are a high (angular) resolution FOV (one 90° azimuthal quadrant) and a low resolution FOV (three 90° azimuthal quadrants). The high resolution FOV has approximately one fourth the intrinsic angular FOV of the low resolution quadrant and is used to measure interstellar neutral oxygen in the springtime (see Fig. 1). The full sensor (combined high and low resolution FOVs) is used for heliospheric neutral hydrogen measurements throughout the year and for measurements of interstellar neutral oxygen in the fall.

To provide a well-defined angular FOV with the largest possible collection area for neutral atoms, the collimator has a hexagon shape multi-hole aperture that uses a stack of identical photo-etched plates. A linear version of this type of collimator was used on the ACE/SEPICA instrument (Möbius et al. 1998a).

Figure 19 shows the front of the collimator hexagon pattern. The collimator is divided into four 90° quadrants by 4 spokes at approximately 0°, 90°, 180°, and 270° from the vertical (Sun) direction. The high-resolution quadrant is between the 90° and 180° spokes measured clockwise from vertical in Figure 19. Optical tests of the IBEX-Lo collimator show that the full-width half-max (FWHM) FOV of the low-resolution quadrants is 6.54° ±0.23° and the FWHM FOV of the high-resolution quadrant is 3.19° ± 0.2°, or very close to the designed low- and high-resolution FOVs of 7° ×7° and 3.5° ×3.5°, respectively.

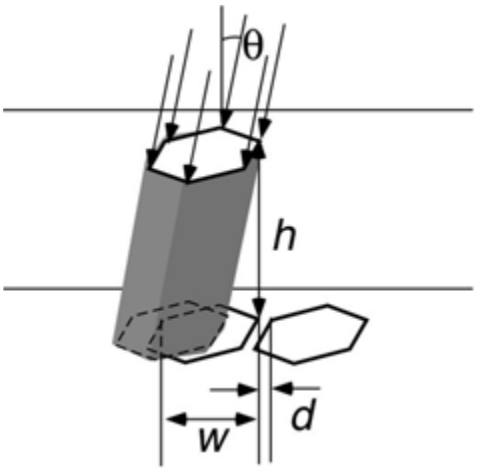

Figure 20: Pair of entry and exit aperture holes of the IBEX-Lo collimator. As indicated by the shaded hexagon shape, only the fraction of particles pass the collimator that fall into the intersection of the two hexagon areas at the exit plate. The fraction depends on the distance h between the plates, the opening width w, and the separation d between hexagons

The FOV is determined solely by the width w (~ 4 mm for the low-resolution sectors) of the hexagon openings and the total height h (~ 25.9 mm) of the collimator stack, i.e., between the entry and exit plate, as shown in *Figure 20*. The angular width of the FOV in each direction is calculated from progressive clipping of trajectories through the aperture pair as the angle θ relative to the normal direction of the collimator plates increases. The maximum throughput is at normal incidence and is determined by the transparency T of the collimator. The transparency is dependent solely on the ratio of the line width d and the width of the hexagons w, and is written as:

$$T = \frac{1}{1} + d/w)2. \quad (1)$$

The collimator has a transmission of 68.8 ± 0.3% for the low-resolution quadrants and 61.7±0.5% for the high resolution quadrant.

In *Figure 20*, particles can pass through neighboring channels in a multi-hole collimator as long as their angle θ exceeds $\theta \geq d/h$. To prevent such “leakage” of particle trajectories, identical collimator plates are stacked in a roughly geometric sequence, with the largest plate separation $h_n \leq d \cdot h/w$ and the smallest separation so that $h_1 \leq d \cdot \tan\theta_{Max}$, where θ_{Max} is the largest possible incidence angle for particles. The angle θ_{Max} is limited to ≤ 50° by a precision-milled pre-collimator with trapezoid-shaped hexagon ribs, whose width is ≥ 50 μm less than d. The geometric sequence of plate separations starts with the largest one at the exit plate and alternates to smaller and smaller separations from both the top and bottom toward the center so that a series of 6

plates with the smallest identical separations is placed at the center of the collimator. With this pattern, the fraction of particles scattered at the edges of the holes into the FOV (an unavoidable effect) is minimized. Very thin (0.5 mm thick) etched plates with sharp edges are also used to reduce the scattered particle fraction. Finally, plate separations are reduced compared to a strictly geometric progression to account for manufacturing tolerances and deviations from planarity in the collimator plates.

Accounting for collimator transmission, correcting for losses due to spokes, incomplete hexagons at the edges, and shadowing at the edges, and combining the FOVs of 3 low resolution quadrants and one high resolution quadrant, the total geometric factor of the collimator is 0.91±0.04 cm^2 sr.

The collimator floats at +10 kV relative to the spacecraft (and sensor) ground potential and is attached to the optics deck by 16 high voltage insulators. This positive potential keeps up to 10 kV ions out of the sensor. While nominal solar wind ion fluxes directed into the sensor with energies above a few 10's of eV are very low, energetic ion fluxes (up to several keV) in the magnetosheath and in the Earth's foreshock upstream from the bow shock can be high enough to create measurable background in the sensor. The positively biased collimator rejects these ions.

Without the +10 kV collimator voltage, the IBEX-Lo design provides some mitigation against ion background. First, the negative electrodes in front of the collimator act as a defocusing lens for low energy ions. Simulations show that ions below about 200 eV are defocused enough that they hit the collimator plates before entering the sensor. Second, there is a conical-shaped grid between the collimator and the ENA to ion conversion subsystem (described in Section 3.2.2.2.2 below) that deflects ions away from the conversion surface. Finally, IBEX-Lo is inherently a negative ion sensor. Any positive ion that enters the sensor must be converted to a negative ion on the conversion surface in order to be detected as background.

3.2.2.2.2 IBEX-Lo Conversion Subsystem

By rejecting the majority of high energy ions and nearly all electrons, only UV, a very low flux of solar wind energetic ions with energies > 10 keV, and neutrals exit the back of the collimator. These constituents enter the subsystem where a fraction of the neutrals are converted to negative ions. The key to this subsystem is a diamond-like carbon (DLC), or more accurately described as a tetrahedral amorphous carbon (ta-C), conversion surface (e.g., Wieser et al. 2005).

As stated in the introduction, 10 eV to several hundred eV neutrals do not have sufficient energy to be detected directly with any efficiency using standard detector technology. Furthermore, heliospheric neutrals are accompanied by interstellar UV fluxes that would overwhelm a detector placed directly behind the IBEX-Lo collimator. Thus, neutrals must be converted to ions so that they can be accelerated (thereby

raising their detection efficiency) and deflected away from the direct path taken by UV background (Wurz 2000; Wurz et al. 2006).

Ionization by scattering from charge-state conversion surface offers the highest ionization efficiencies in the energy range below 1 keV. This technique was first proposed for space applications by Gruntman (1993) and Wurz et al. (1993). Early low energy neutral atom imager designs were proposed using low work function surfaces for converting neutrals to ions during surface impact and reflection (e.g., Ghielmetti et al. 1994). However, these surfaces must be re-conditioned and regenerated often, placing difficult requirements on sensor resources and operations. Furthermore, changing surface conditions result in variable conversion efficiencies and ultimately result in uncertainties in overall sensitivity of the sensor. This uncertainty creates the need for a separate, accurate monitor of conversion efficiency.

Since these early designs, there has been a concerted search for a stable, inert, high-yield, low-scatter conversion surface. The Low Energy Neutral Atom (LENA) imager on the IMAGE mission was the first to use this type of surface conversion. A highly polished polycrystalline tungsten surface was used for neutral to ion conversion, with ionization facilitated by natural contaminants, most likely adsorbed water (Moore et al. 2000). Surface conversion efficiencies were much less than 1% for hydrogen.

Since this pioneering mission, several surfaces have been identified that have better negative ion yield. Among these, natural diamond crystals demonstrated reasonably high negative ion production for hydrogen and oxygen (Wurz et al. 1997). The large conversion surface area required for most neutral atom imagers makes the use of natural diamond surfaces impractical from a cost standpoint. Instead, diamond-like carbon surfaces make an excellent substitute (Scheer et al., 2005, 2006; Wieser et al. 2005; Wurz et al. 2006). These diamond-like carbon surfaces are readily grown on large, very smooth silicon substrates, retaining the surface smoothness of the underlying substrate.

For IBEX-Lo, 3 inch silicon wafers were cut into trapezoidal facets 62 mm long and $\sim$ 30 mm wide at the center. The edges of the trapezoids were beveled so that they fit together to form an annular cone that is inclined at 15° from the incident direction of the neutrals that pass straight through the collimator. A 100 nm thick tetrahedral amorphous carbon (ta-C) layer was grown on each trapezoid facet. At the start of this process, the silicon surface smoothness was < 0.1 nm RMS and, at the end, the DLC layer had surface smoothness $\sim$ 0.1 nm RMS. These surfaces were then treated with a hydrogen beam in a vacuum. This process, called hydrogen termination, is used to chemically terminate exposed, non-diamond-like carbon bonds on the surface. It removes oxygen from the surface, making it more inert, and it also lowers the work function of the surface and does not add to surface roughness.

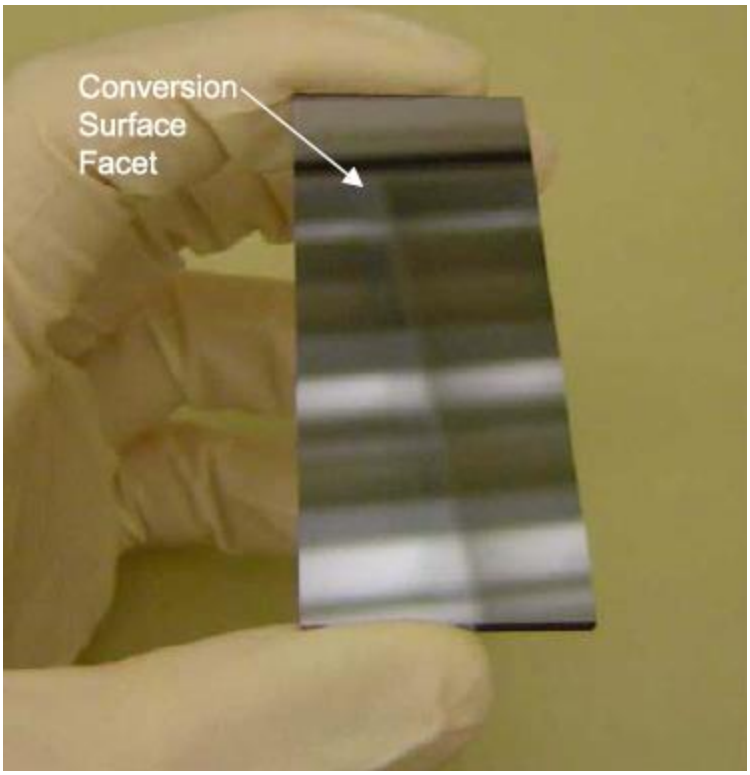

Figure 21: Photograph of a conversion surface facet. The substrate is a highly polished silicon wafer cut into a trapezoid. A ~100 nm diamond surface is grown on this surface. The resulting conversion surface is smooth to within ~0.1 nm. Twenty-eight of these facets are used in a conical configuration in the sensor

The end result was 28 facets that are inert, slightly conductive, extremely smooth, and have reasonably high negative ion yield for neutral impact at grazing (15°) incidence. A picture of one of the facets is shown in *Figure 21*. The negative ion yield properties for hydrogen are shown in *Figure 22*. Ionization efficiencies increase with increasing energy, reaching ~ 5% for hydrogen. Measurements of 4 of the facets are shown at 4 different energies. The empirical curve is based on measurements over the entire energy range using a variety of conversion surfaces and detectors (Wieser 2005; Wurz et al. 1998, 2006; Wieser et al. 2007). Tests of these surfaces over periods of more than several years indicate that the conversion efficiency is stable for many years (Scheer et al. 2005, 2006).

While *Figure 22* shows relatively high ionization efficiencies for the conversion surfaces, the conversion efficiency is the product of the ionization efficiency and the reflection efficiency. That is, the total negative ion yield is the ratio of the number of negative ions off the surface divided by the number of neutral atoms incident on the surface. The reflection efficiency plays an important role in determining the overall conversion efficiency for these diamond-like surfaces. The reflection efficiency is also energy and mass dependent (Scheer et al. 2008). The reflection efficiency is the number of scattered particles (atoms and negative ions) in the specular direction within the ion-

optical acceptance angle of the ion optical system. The roughness of the surface determines the fraction of negative ions that scatter in the specular direction. The IBEX-Lo conversion surfaces are smooth on an atomic level, maximizing this fraction of scattered negative ions. However, even these surfaces are corrugated at an atomic level. Therefore, there is always angular scatter away from the specular direction. The number of particles that scatter away from the specular direction increases with particle energy and with angle of incidence because the incoming particles probe deeper into the surface potential well of the conversion surface. Thus, the reflection efficiency decreases with particle energy, since the angular scatter increases (Wahlström et al. 2008), and a lower fraction of the angular scatter width is within the angular acceptance of the ion optical system. In addition to this effect, there is the possibility that incoming particles get stuck in the surface.

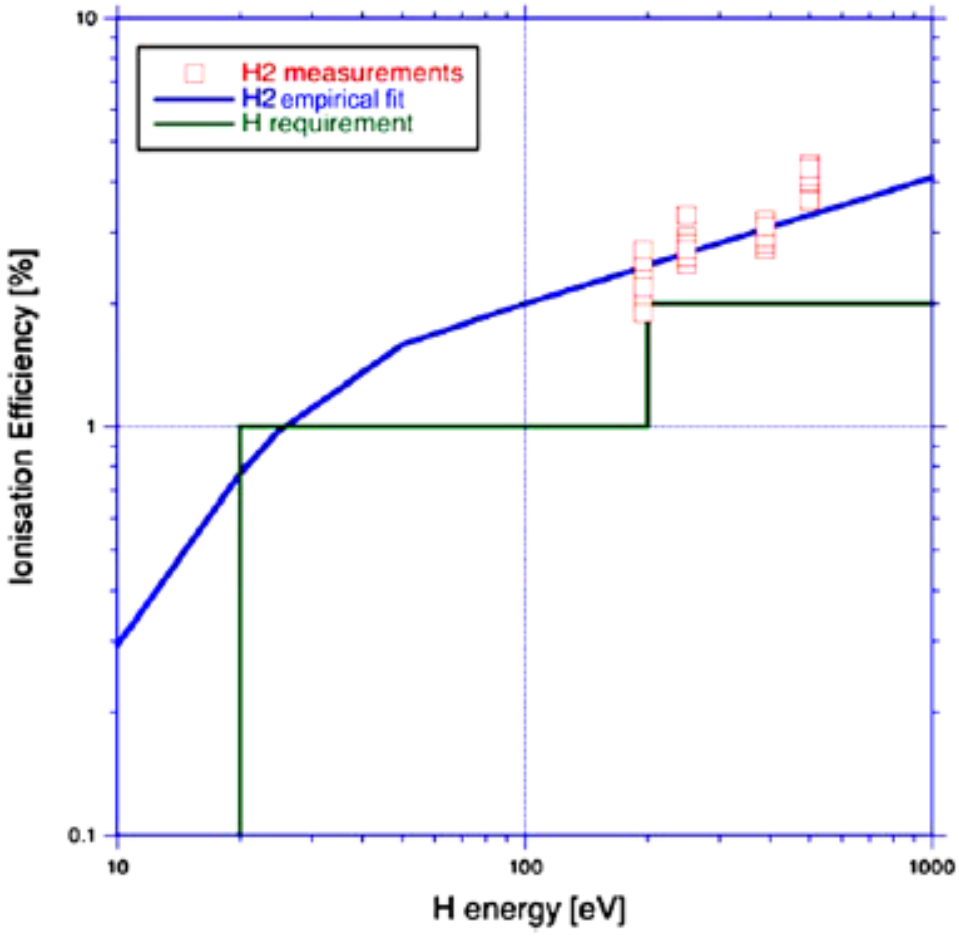

Figure 22: Measured neutral to negative ion ionization efficiencies of IBEX-Lo conversion surfaces for hydrogen. The green line indicates the sensor requirement and the blue line is an empirical fit to measurements from different synthetic diamond coatings on silicon (Wieser 2005). The conversion efficiency is the product of these ionization efficiencies times the (energy dependent) reflection efficiencies

Tests using the University of Bern's conversion surface test facility (Wurz et al. 1997; Jans et al. 2000) show that the reflection efficiency for the IBEX-Lo DLC surfaces is of the order of 10% for 200 eV hydrogen and of the order of 4% for 700 eV hydrogen (Scheer et al. 2008). Combined with the ionization efficiency (Figure 22), these tests result in an overall conversion efficiency for hydrogen neutrals that is < 1% over the IBEX-Lo energy range. However, the IBEX-Lo sensor has ion optics that are designed to maximize capture of reflected negative ions, even some ions that scatter away from the specular direction, so the DLC surfaces in the sensor have measured conversion efficiencies that approach 1% at the upper energy limit. While this efficiency seems low, it is still one of the highest for inert conversion surfaces like the DLC surface.

Finally, ionization and reflection efficiencies also depend on incidence particle type. Ionization efficiencies are a strong function of the electron affinity of the incident neutral. Oxygen has a higher electron affinity than hydrogen and a much higher negative ion yield (~30% compared to ~ 5% for hydrogen). Reflection efficiency is also dependent on mass. Tests conducted at the University of Bern's conversion surface test facility indicate that oxygen has, on average, a lower reflection efficiency than hydrogen. Also, the energy loss upon reflection is greater for oxygen than for hydrogen. Differences in the reflection efficiency and energy loss between oxygen and hydrogen are probably associated with the fact that hydrogen is much lighter than carbon (the conversion surface material) while oxygen and carbon have similar masses. The details of this interaction are still the subject of investigation (Wahlström et al. 2008).

3.2.2.2.3 IBEX-Lo Energy Analysis Subsystem

Negative ions from the conversion surface facets are accelerated away because the facets are held at a negative potential. Another electrode that faces the annular ring of conversion surface facets is also at a negative potential. In combination, these fields deflect and focus negative ions in the radial direction into the entrance of the Electrostatic Analyzer (ESA) (see the negative ion trajectory in Figure 18). Large angle scattering off the conversion surface facets in this direction is at least partially compensated for by this focusing effect.

The energy analysis subsystem consists of a toroidal electrostatic analyzer (ESA), two electrodes at the entrance to the ESA that help deflect and focus the negative ions into the ESA, and a third electrode at the ESA exit that helps focus the negative ion beam into the mass analysis subsystem.

The toroidal ESA defines the sensor energy pass band. The analyzer has the shape of a "bundt" baking pan (Moestue 1973), and this geometry was used in the Toroidal Imaging Mass Angle Spectrograph (TIMAS) on the Polar spacecraft (Shelley et al. 1995). Parameters were adjusted so that the annular ring at the ESA exit was the same size as a standard size microchannel plate in the TOF spectrometer. Also, the plate separation between the inner and outer ESA is quite large (see Figure 18), commensurate with the large passband of the sensor (the ESA ΔE/E is estimated to be

0.67). With such a large plate separation, there could be considerable UV background. To reduce the background, the ESA outer shell has very large “fins” that are very effective light traps (see Figure 18). In addition, the inner ESA shell is serrated and both the inner and outer shells were blackened with a porous black coating that further reduces UV reflection. These measures counteract the effect of the large plate gap and maintain an overall approximately 3-bounce system for UV to reach the entrance to the TOF system. Before the design of the IBEX-Lo sensor, a prototype sensor was built and all ion-optical properties were verified (Wieser 2005; Wieser et al. 2007) (see also Section 4.2.2.1).

In addition to setting the energy passband of the sensor, the ESA folds the ion optics so a smaller, standard size detector can be used. This reduction does not come without a price. Two fundamental ion optics properties of the ESA are that it focuses in the radial direction, but it disperses in the azimuthal direction. A narrow-angle beam entering the collimator at one point will disperse into an arc that is greater than ∼180° in azimuthal extent at the detector. Since it is not necessary to image in the azimuthal direction, this dispersive property is not an issue for IBEX-Lo. However, ions that disperse to large azimuthal angles will exit the ESA at a very large angle with respect to the normal angle of the TOF entrance. The sensor properties at the ESA exit are designed to help deflect the azimuthal trajectories of negative ions so the ions arrive at the TOF entrance with a small angle relative to the normal. This deflection is done in two ways: by shaping the ESA exit so that it focuses ions and by applying a large acceleration voltage between the ESA exit and the TOF entrance. However, ions with very large azimuthal trajectories exit the ESA with too large an angle from the radial direction. These ions do not pass completely through the TOF system and are lost.

This fundamental property of the ESA feeds back to conversion surface smoothness. If negative ions leave the conversion surface with more than 10° azimuthal angle relative to their incident direction, then their trajectories in the ESA become large spirals and they exit the ESA at very oblique angles with respect to the normal to the TOF entrance and are lost. These ions are lost in the TOF system. Tests of the IBEX-Lo conversion surface facets indicates that they are smooth to ∼ 0.1–0.2 nm RMS. Nonetheless, a significant fraction of the ions are lost in this manner and that fraction is energy dependent.

In addition to negative ions, incident neutrals produce electrons from the conversion surface. In fact, many more electrons are produced than negative ions because UV photons also reach the conversion surface. Since the ESA and energy analysis system are designed to accelerate negative ions, electrons could become a serious background in the TOF subsystem. Specifically, if a sufficient number of electrons are accelerated through the ESA and hit the first carbon foil in the TOF system, then they could overwhelm the TOF electronics.

To counter this background, the sensor takes advantage of the azimuthal defocusing property of the ESA. The energy analysis subsystem uses permanent magnets to deflect the electron trajectories so they have a large azimuthal component to their velocities. This electron suppression scheme was used effectively on the IMAGE/LENA imager (Moore et al. 2000) and tested in the IBEX-Lo prototype (Wieser et al. 2007) (see Section 4.2.2.1). For IMAGE/LENA, the electrons were suppressed after they were accelerated to several keV in the ion optics, and relatively large permanent magnets were needed (Moore et al. 2000). For IBEX-Lo, it was possible to design a magnetic suppression system for the electrons before they were accelerated significantly (electrons leaving the conversion surface have only a few eV energy) (Wieser et al. 2007). Furthermore, instead of deflecting the electrons so that they cannot enter the ESA, all that was required was to add a large azimuthal component to their velocities. Two nearly concentric circles of permanent magnets were used on the inner and outer electrodes that define the entrance to the ESA (see Figure 18). These magnets (~ 1.5 mm in diameter) face each other across the ESA entrance gap and create a 3 millitesla field directed radially across the gap. Electrons up to a few 10's of eV are effectively deflected in this field and, if they enter the ESA, their trajectories have significant azimuthal components, and therefore they do not reach the TOF entrance. The magnetic field is low enough that trajectories of even the lowest energy negative ions are unaffected.

Finally, the energy analysis subsystem has one more requirement. As discussed in Section 3.2.2.2.1 (the entrance subsystem), one of the four quadrants of the collimator has a high resolution, 3.2° × 3.2° FOV. For interstellar neutral oxygen measurements in the springtime, this quadrant must be used, and the other three quadrants must be "shut off". Shutoff is achieved electrostatically by applying a large, negative voltage (−2.5 kV) to the inner electrode at the entrance to the ESA for the three quadrants behind the low-resolution collimator quadrants. This potential pushes negative ions in the three low resolution quadrants to the outer wall, where they scatter and do not enter the ESA. Tests of the IBEX-Lo sensor demonstrate that this shutoff works very well. The edges of the high-resolution sector were of particular concern since fringe fields could affect ion trajectories in the low-resolution sector and possibly allow "leakage" of these ions from low resolution sectors to the detector. Field termination electrodes are used to minimize fringe fields and therefore minimize leakage. Tests indicate that leakage is < 1.5% and, at this level, leakage does not affect high angular resolution measurements.

3.2.2.2.4 IBEX-Lo Mass (TOF) Analysis Subsystem

The mass (time-of-flight, TOF) analysis subsystem is a triple coincidence carbon foil-based time-of-flight ion mass spectrometer. It is designed to distinguish hydrogen and oxygen negative ions and suppress background random events through triple coincidence measurements. While distinguishing hydrogen and oxygen is the minimum mass resolution that is required, the TOF is designed with the goal to distinguish hydrogen and helium negative ions so that interstellar neutral helium fluxes can be measured separate from the interstellar neutral oxygen. This type of double and triple coincidence TOF system is a novel design that is based on the TOF systems used on

FAST, Cluster, Equator-S, and STEREO/PLASTIC (e.g., Möbius et al. 1998b). The triple TOF system has several major advantages over previous designs. Advantages such as the superior background suppression and higher efficiency when single TOF channels are used are important for the IBEX-Lo sensor (Möbius et al. 2007).

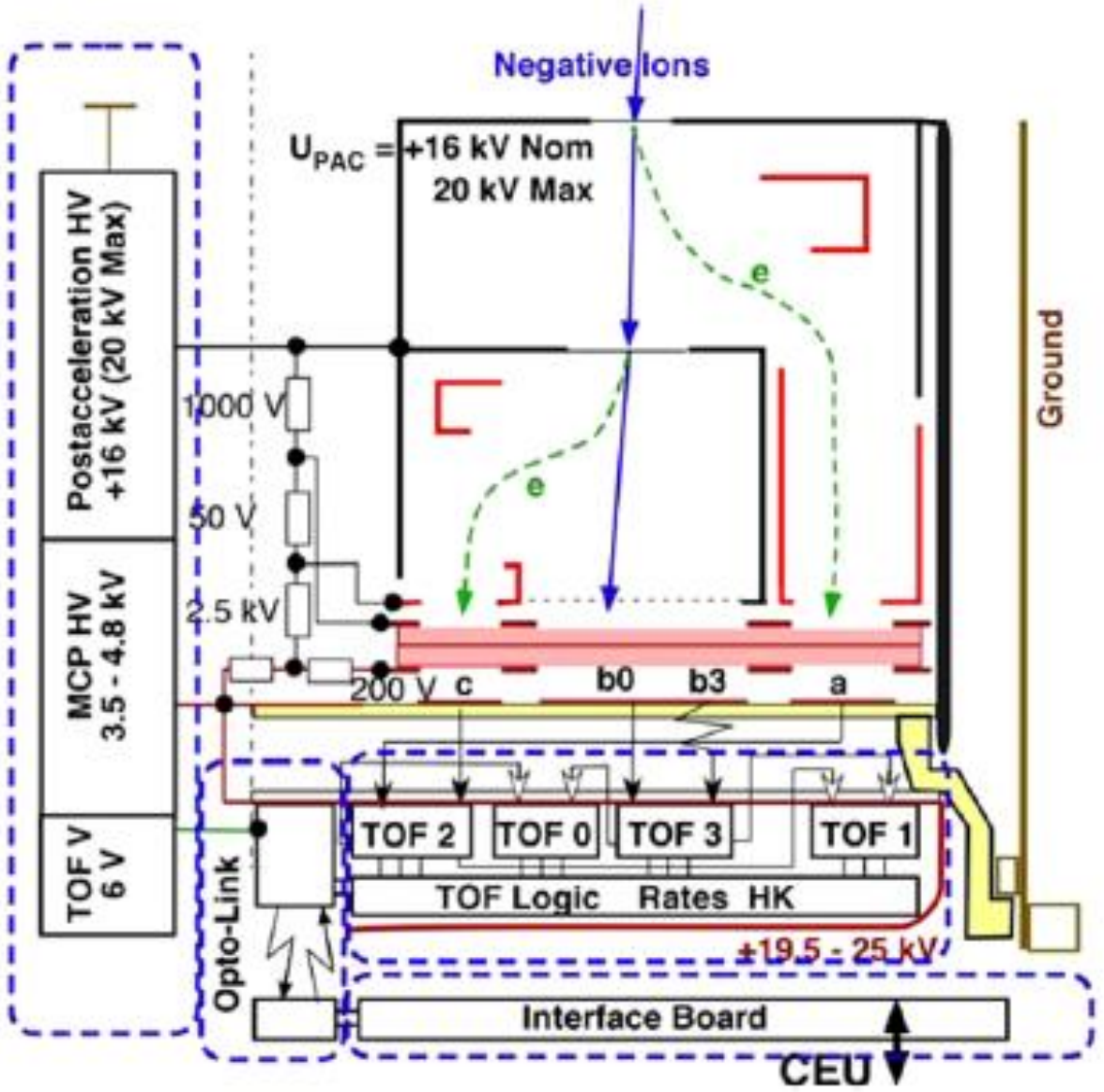

Figure 23: Schematic of the TOF mass spectrometer. The TOF is rotationally symmetric about the right hand side of the figure. Negative ions from the ESA strike the first foil at the top. These ions pass through the foil (some become neutral) and knock off electrons that are accelerated and steered to the outer edge of the annular microchannel plate stack. The signal from these ions (a, on the anode below the pink MCP stack) is the start 1 signal. Ions and neutrals pass through a second, interior foil. Electrons from this foil are accelerated to the inner edge of the MCP stack and create the start 2 signal. Finally, ions and neutrals strike the MCP stack at position b0/b3 and create the stop signal. By combining the starts and stops, the mass of the incident negative ion is determined

The basic TOF operation is shown in *Figure 23*. This figure shows a radial cross-sectional cut of the TOF subsystem. It is rotationally symmetric about the left hand side of the figure, so that the microchannel plate (MCP) detector stack (pink in the *Figure 23*) is an annular ring. The section of the TOF in *Figure 23* is shown in the inverse orientation compared to Figure 18. A picture of the entrance end of the flight model of the TOF is shown in *Figure 24*. The eight carbon foils that make up the first set are supported on grids that are seen through the ultra-thin foils. Vent holes surround the foils to protect them from perforation by acoustic shock.

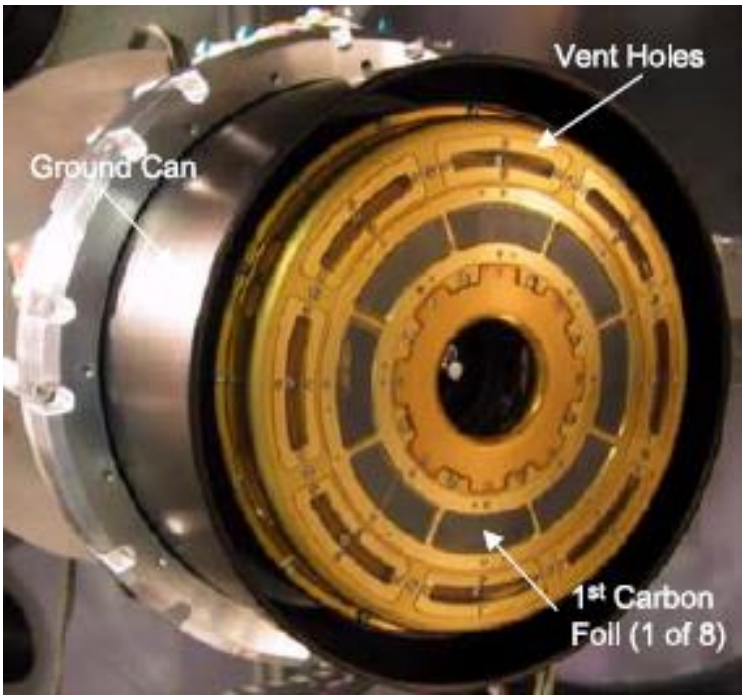

Figure 24: Photograph of the front entrance of the TOF mass spectrometer in the test vacuum chamber. The 8 ultra-thin carbon foils are transparent and are mounted on high transmission grids. Vent holes around the grids and a general open design minimize possible acoustic damage to the foils. The entire TOF floats at 16 kV and is surrounded by the blackened aluminum ground can

Negative ions are accelerated into the first set of foils at the top of Figure 23 because the entire TOF ion optics section floats at a nominal +16 kV post-acceleration (PAC) high voltage. (The blackened ground cylinder that surrounds the optics is shown in Fig. 8). As discussed in Sect. 3.4, this high post acceleration voltage helps straighten out negative ion trajectories between the ESA exit and TOF entrance foils. More importantly, high post acceleration allows a TOF measurement with high enough resolution after energy loss in the entrance foil.

Upon striking the first set of carbon foils, negative ions knock off secondary electrons. These secondary electrons are focused on the outmost radius of the MCP and constitute the first start pulse (start 1 or “a” in *Figure 23*). As the negative ions pass through the first foil, a fraction of them become neutral again. The ions and neutrals strike a second foil and knock off secondary electrons. These electrons are focused on the innermost radius of the MCP and constitute the second start pulse (start 2, or “c” in *Figure 23*). Finally, the ions and neutrals pass through the second foil and strike the MCP in the center radius. The signal from these ions and neutrals constitutes the stop pulse (stop, or “b0” in Figure 23). The stop anode is segmented into 4 quadrants, labeled b0, b1, b2, and b3 in *Figure 25*. Delay lines are placed between anodes b0 and b1, b1 and b2, and b2 and b3. Using the delay between the signals from anodes b0 and b3, the arrival quadrant of the signal is determined. Although it is relatively crude angular information, this sectoring of the signal provides important additional background rejection when the high-resolution mode is used. Since three of the four collimator quadrants are shut off in this mode, there should be minimum signal from quadrant b1, the quadrant opposite the high-resolution quadrant. Tests conducted during the sensor calibration show that the ratio of the quadrant that has maximum counts to the opposite (background) quadrant is ~ 2000. This high ratio indicates that the ion optics is behaving as designed and that the delay line detection of the ion arrival location is an effective additional background suppression technique for the interstellar neutral oxygen measurements.

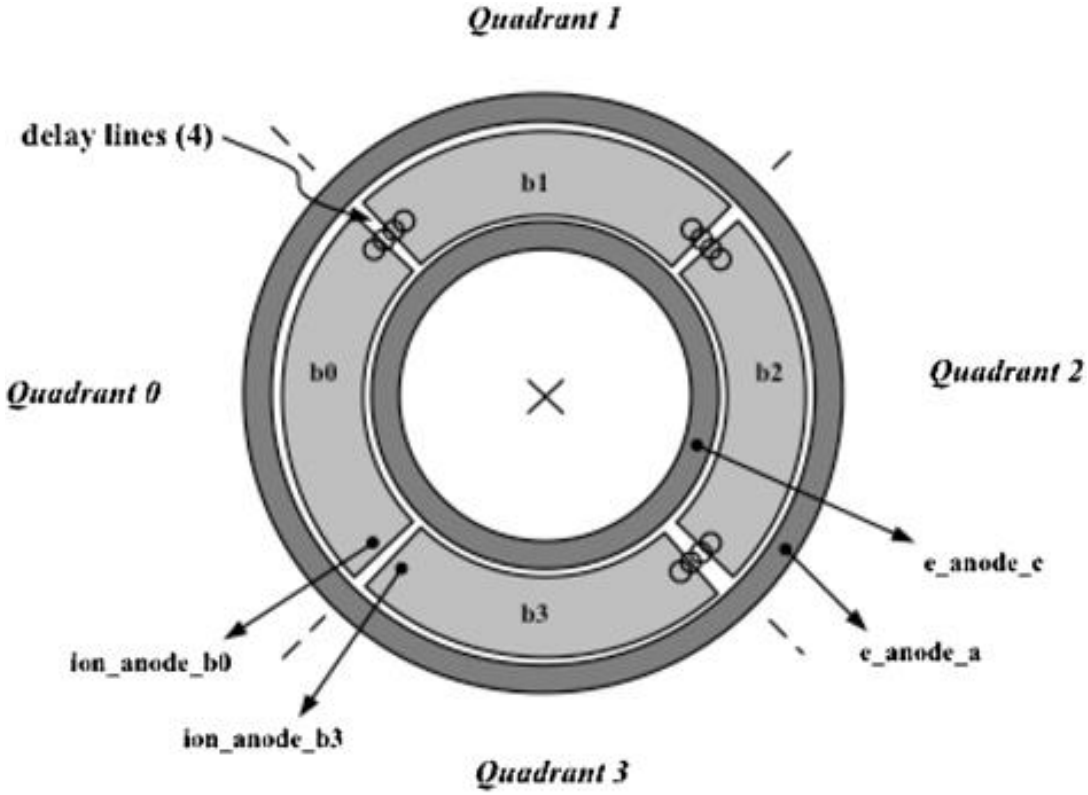

Figure 25: The TOF anode is divided into four sectors with delay lines between three sectors. By analyzing the signal delay between anode b0 and b3, the quadrant for the stop signal is determined

3.2.2.2.5 IBEX-Lo TOF and Other Electronics

Electron avalanches from the back of the MCP are collected on the start 1 (a), start 2 (c), and stop (b0, b1, b2, and b3) anodes. These anodes are biased 200 V positive relative to the MCP back to accelerate the electrons from the MCP back (see *Figure 23*). Four TOF ASIC chips (Paschalidis et al. 2002, 2003) combine the signals to give the ion TOF over the entire path from the first foil to the stop MCP, the half path from the second foil to the stop MCP, and between the stop anodes b0 through b3. A valid double coincidence event requires a start (two possibilities) and stop. A valid triple coincidence event requires both starts and a stop. Furthermore, a valid triple event meets the criterion that the TOF over the full 60 mm distance from the first foil to the stop MCP is equal to the sum of the TOF over the 30 mm distance from the first to the second foil and the TOF over the 30 mm distance from the second foil to the MCP. Checking that this criterion is met greatly reduces background due to random double coincidences. In particular, it eliminates events where one TOF is very near zero.

The TOF board located directly behind the MCP anode (Figure 23) performs these logic timing determinations, monitors overall rates, and performs other housekeeping duties. Signals from this board (at the MCP high voltage) are transferred to the interface board (at sensor ground) through a pair of optical links (one for signals into the board and the other for signals out). The interface board controls TOF and PAC high voltages and is connected to the IBEX Combined Electronics Unit (CEU) through a serial port. The CEU provides conditioned, low-voltage power (±12 V, +5 V) to the interface board, and this board distributes power that is used to create the PAC, MCP, and TOF digital voltages in the TOF HV supply (see Figure 18).

Voltages for other parts of the IBEX-Lo sensor come from the CEU. These include the entrance subsystem voltages (high voltages for the electron repeller (CO−=−4.1 kV) and the collimator (CO+ = +11 kV)), optics voltages (U+, 4.8 kV and U−, −2.1 kV) and the voltage used to shut off low-resolution quadrants when in the high-resolution mode (Uso=−2.5 kV). All of these voltages are commandable to several levels, even voltages that are “fixed” at a specific voltage (e.g., Uso) in nominal science operations. Ion optics voltages on various electrodes are determined by the set point of the U+ and U− voltages and two high precision, high resistance resistor strings, one for each voltage. The CEU sets the five high voltages, controls their changes, and commands the TOF interface board for a particular science or engineering mode. The CEU is described in the IBEX flight segment description (Scherrer et al. 2009).

Set points for the optics voltages are shown in *Table **7***. For the eight energy channels in the normal (heliospheric hydrogen) science mode, the voltages fix center energies of the ESA passband that are 15% lower than the center energies of the incident neutral hydrogen. These settings assume that negative ions leave the conversion surface with 15% less energy than the incident neutrals. In the calibration, it was discovered that this energy loss is energy and mass dependent. Therefore, the highest two energy channels are not evenly logarithmically spaced from the first six channels. Also, for the special oxygen and helium modes in the spring and fall, the energy loss for oxygen off the

conversion surface is much larger than that for hydrogen, so the voltages are set for correspondingly lower negative ions off the conversion surface.

Table 7: Optics voltage settings for the IBEX-Lo sensor for the normal and special oxygen science modes

Heliospheric hydrogen science mode			
Energy Step	U+ Voltage (volts)	U− Voltage (volts)	Center energy of incident H neutrals (eV)
1	42.1	−16.8	14
2	81.2	−32.3	27
3	156	−62.2	52
4	307	−122	102
5	592	−236	197
6	1212	−482	451
7	2346	−934	908
8	4511	−1795	1903
Interstellar oxygen mode			Center energy of incident O neutrals (eV)
Jan–Feb	1035	−414	534
Oct–Nov	81	−32	33
Interstellar helium mode			Center energy of incident He neutrals (eV)
Jan–Feb	381	−152	134
Oct–Nov	41	−16	8.3

3.2.2.2.6 IBEX-Lo Star Sensor

Accurate, absolute directional determination of interstellar neutral oxygen is critical for IBEX science closure. Therefore, a star sensor is co-aligned with the IBEX-Lo sensor to determine the absolute neutral oxygen arrival direction with respect to several stars. The star sensor provides data for determining positions of as many stars as possible to an accuracy of ±0.1° relative to the IBEX-Lo collimator bore sight (after ground processing).

The star sensor basic design is shown in *Figure 26*, and a picture of the star sensor attached to the optics deck (with a protective cover over the aperture) is shown in Figure 19. The star sensor operates similarly to a Sun sensor on a spinning spacecraft. It consists of an entrance aperture and collimation tube, exit pinhole, and photomultiplier tube (PMT). The entrance aperture has two slits in the shape of a “V”. As the spacecraft spins, the light curve from a star in the FOV generates two 3° wide triangular shaped peaks with full-width half-maximum separation equal to the angular aperture width. The time difference between peaks determines the elevation angle of the star with respect to

the star sensor bore sight. The IBEX spin period is planned to be 4 ± 0.5 rpm. Calculations show that an integration period of 11 ms is equivalent to 1° in the spin direction. Given a FWHM of 3° for the triangular shaped peak for a star, this resolution is adequate for determining star directions within the accuracy requirements. The star sensor is sensitive to between 50 and 100 stars brighter than magnitude 2.5 in the visible part of the spectrum.

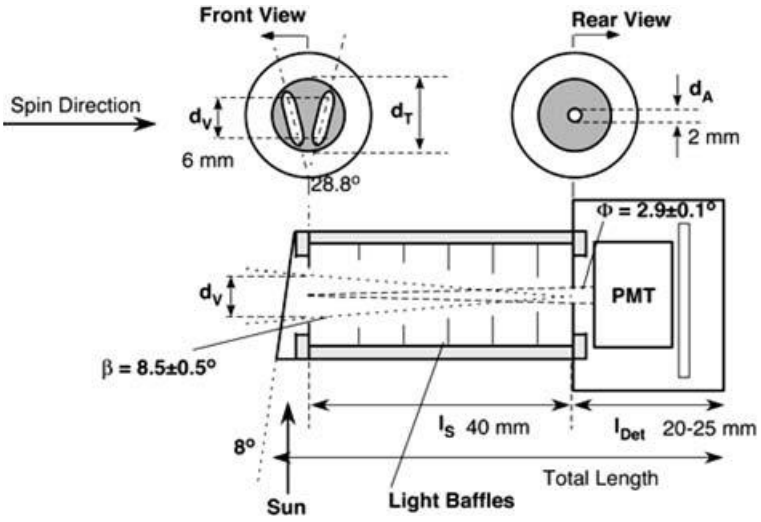

Figure 26: Schematic of the IBEX-Lo star sensor. The front aperture is shaped into a "v" so that as a star passes in front of the spinning aperture, a double pulse is produced in the photomultiplier tube (PMT). The time between the two pulses is used to determine the elevation angle (up/down in the figure) of a star. The azimuthal (within the spin plane) direction is determined from the center time of the two pulses and spacecraft attitude information

Star sensor signals are accumulated in CEU memory over multiple spins (typically ~ 64) in 720, 0.5° bins to form a 360° histogram. The absolute reference of this histogram is the spacecraft spin pulse, which is provided by the spacecraft to the CEU. These data are processed on the ground to determine the absolute direction of the star from the azimuth location of the two peaks in the spin plane and the time separation of the two peaks.

3.2.3 IBEX Heritage

IBEX is a groundbreaking mission, being the first mission to image the heliosphere using measurements of neutral atom, and as such it was not directly based on a heritage mission/instrument. However, perhaps the closest previous mission in terms of its measurement concept is the Imager for Magnetopause-to-Aurora Global Exploration (IMAGE) mission, the first mission in NASA's MIDEX (Mid-size Explorer) program, which was the first mission dedicated to imaging the Earth's magnetosphere. In addition to instruments that measured ions, electrons and extreme ultraviolet (EUV), IMAGE had three instruments dedicated to imaging the Earth's magnetosphere by measuring low-

energy (LENA), medium-energy (MENA), and high-energy (HENA) neutral atoms. This section provides a brief overview of the LENA and MENA instruments, which are most similar to IBEX-Hi and IBEX-Lo and discusses their similarities and differences to the IBEX instruments.

3.2.3.1 The Medium-Energy Neutral Atom (MENA) Imager for the IMAGE Mission

The MENA imager was designed to provide ENA flux images of hydrogen and oxygen with 8-deg angular resolution, 80% energy resolution, and 2-min time resolution over the energy range from 1 keV to 30 keV for the 2-year duration of the prime mission. The MENA instrument therefore measures a similar energy range to IBEX-Hi, although extending to higher energies, and in addition to the neutral hydrogen measured by IBEX-Hi, it also measures oxygen.

Figure 27 shows a schematic of the MENA sensor, showing its concept of measurement. ENAs, charged particles, and photons incident from within a sensor's field of view enter through the collimator, where charged particles with energies up to 13 times the adjustable applied voltage are removed by electrostatic deflection. The remaining particles and photons must pass through a free-standing UV blocking grating, where the UV photons are removed around a very wide stop band by the optical properties of the grating. The grating structure was designed to eliminate the 121.6 nm (solar hydrogen Ly-) light reflected from the geocorona. Within the aperture, the ENAs pass through a thin carbon foil where they produce secondary electrons and undergo angular scattering that depends upon the species and energy. Secondary electrons are accelerated to the MCP detector Start segment, while the primary ENA continues along its trajectory to impact the MCP detector Stop segment. ENAs incident on the stop detector segment and their correlated secondary electrons incident on the Start detector segment provide position measurements from which the ENA polar angle is calculated. This information is combined with TOF timing signals to yield a determination of speed. Detector pulse heights are used to provide information on species and detector health. UV photons not absorbed by the UV blocking gratings are not counted due to the TOF coincidence requirement. While the use of a TOF system to measure particle speed is similar to IBEX-Hi, MENA is different in that it does not have an ESA that enables it to select different energy ranges of the particles it measures. MENA is also similar to IBEX-Hi in that it is a singe pixel imager that relies on the spin of the spacecraft to produce 2D images, however while IBEX-Hi has a single sensor that is pointed at 90° to the spin axis, MENA has three sensors pointed at 70°, 90° and 110° to the spin axis to eliminate the blind spots and produce a constant instrument response when the three sensors are combined.

Figure 28 shows an example of magnetospheric images taken by the MENA instrument early in the IMAGE mission. The images are in some ways similar to those captured by IBEX-Hi in that they are projections of the intensities of measured ENAs onto a 2D map, however the images are also quite different, with MENA observations looking back at the Earth and its

magnetosphere “from the outside” whereas IBEX-Hi is able to create maps of the global heliosphere by imaging “from the inside out”. The MENA images also are taken over much shorter timespans of four minutes each during the course of a day, whereas it takes six months for IBEX-Hi to create a full-sky map due to its unique measurement concept.

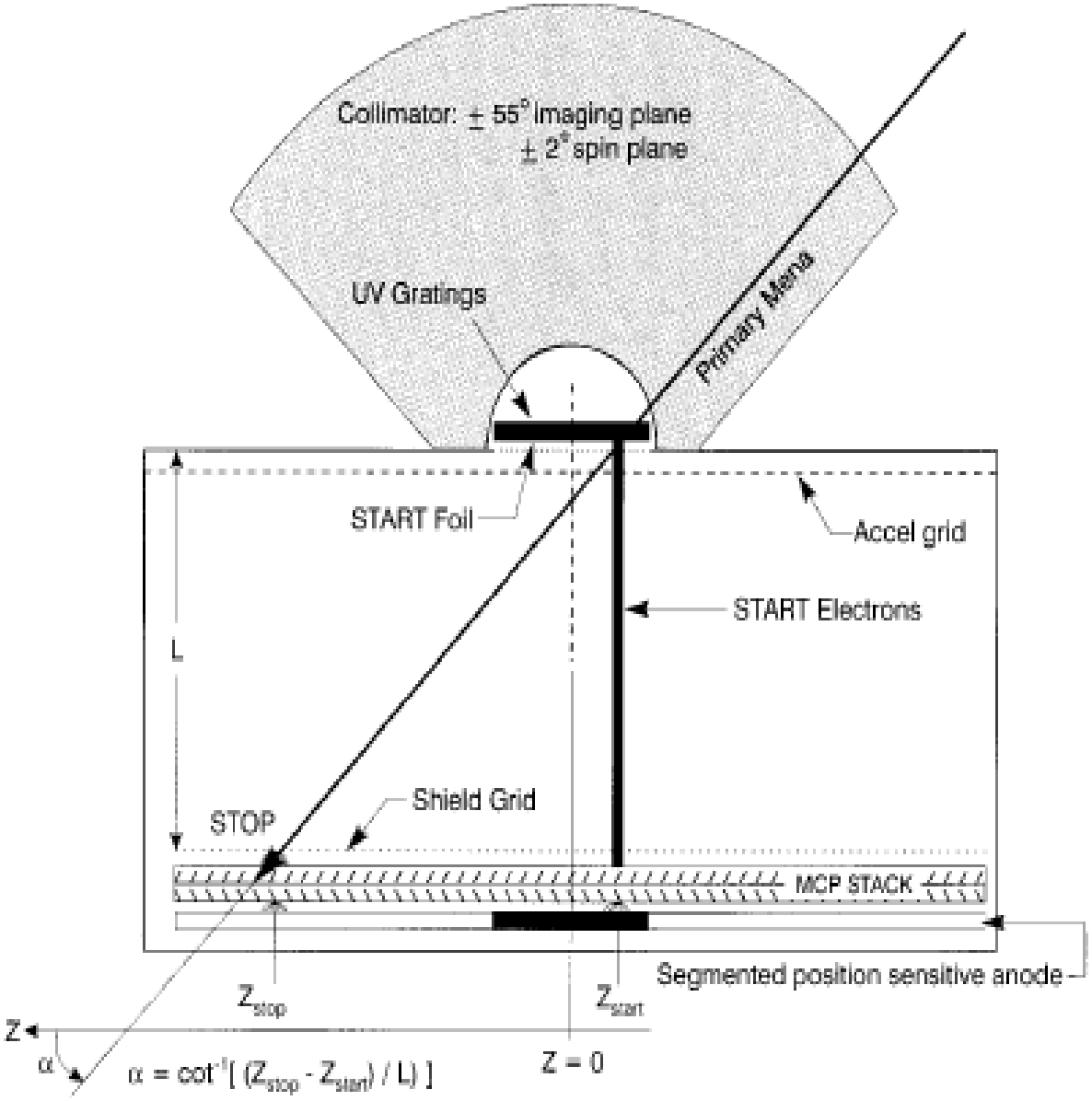

Figure 27: Schematic view of a MENA sensor. A neutral atom passes through the START foil, producing secondary electrons. Secondary electrons are accelerated towards the START segment of the detector, whereas the ENA will impact the detector STOP segment. Particles incident on the START and STOP segment of the detector will provide TOF timing signals, which together with their respective pulse height and ID position on the detector provide the required information for polar incidence angle, energy and species determination of the ENA.

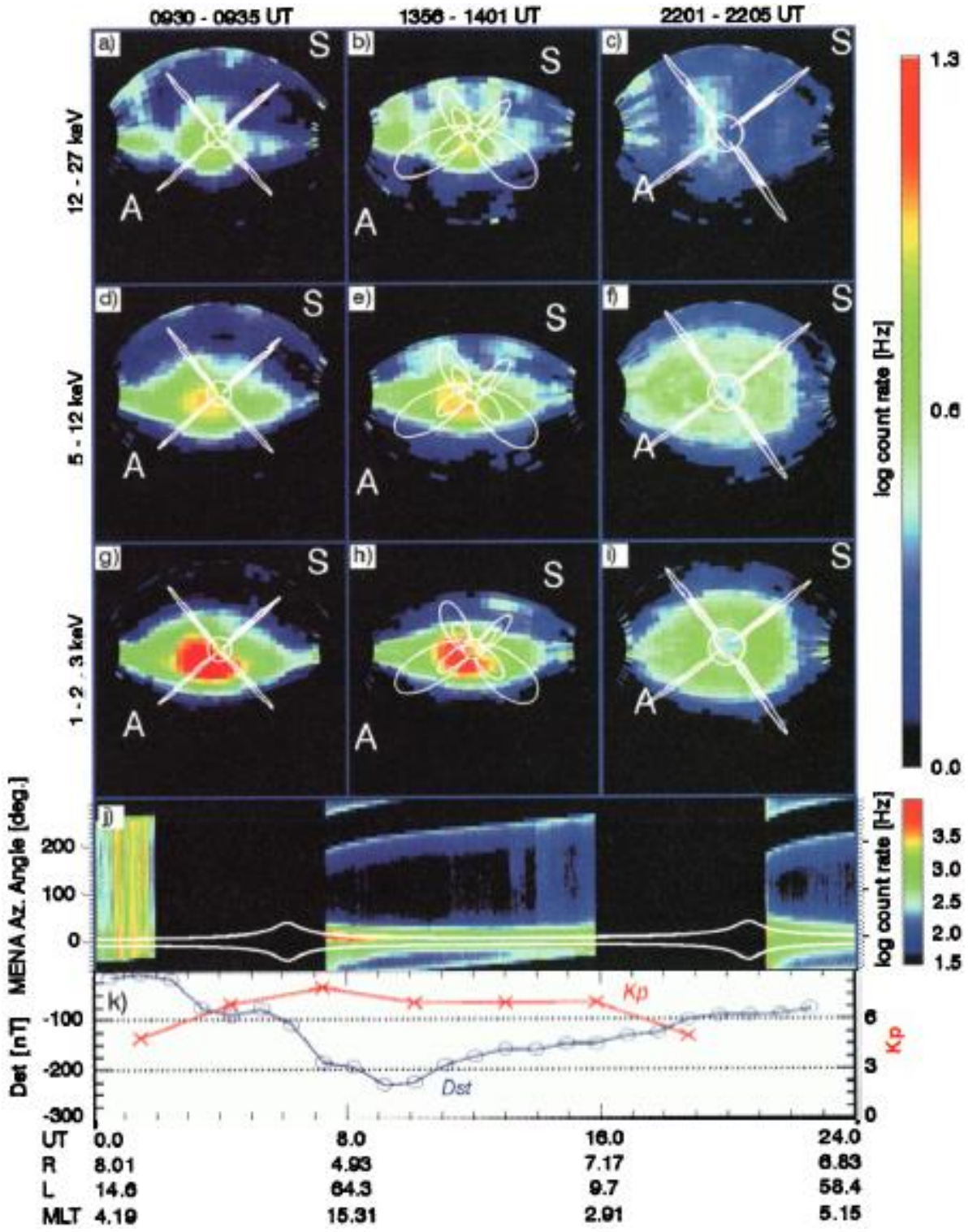

Figure 28: MENA observation and magnetospheric activity indices (D_{st}) from August 12, 2000 (DOY 225). The circle at the center of each image indicates Earth. The images are for three different time periods and three different energy ranges.

3.2.3.2 The Low-Energy Neutral Atom (LENA) Imager for the IMAGE Mission

The low-energy neutral atom (LENA) Imager represents a fundamentally new neutral atom imaging technology, designed for the lowest possible energy range (10 eV to ~1 keV, similar to IBEX-Lo). This is the range of energetic neutrals produced by superthermal ionospheric ions when they charge exchange with atoms in the thermosphere. Figure 29 shows a diagram of the LENA instrument with its different sub-systems labelled as well as an end-to-end simulation of the ion optics of LENA, also showing the TOF optics in a 2D section through the symmetry axis of the instrument.

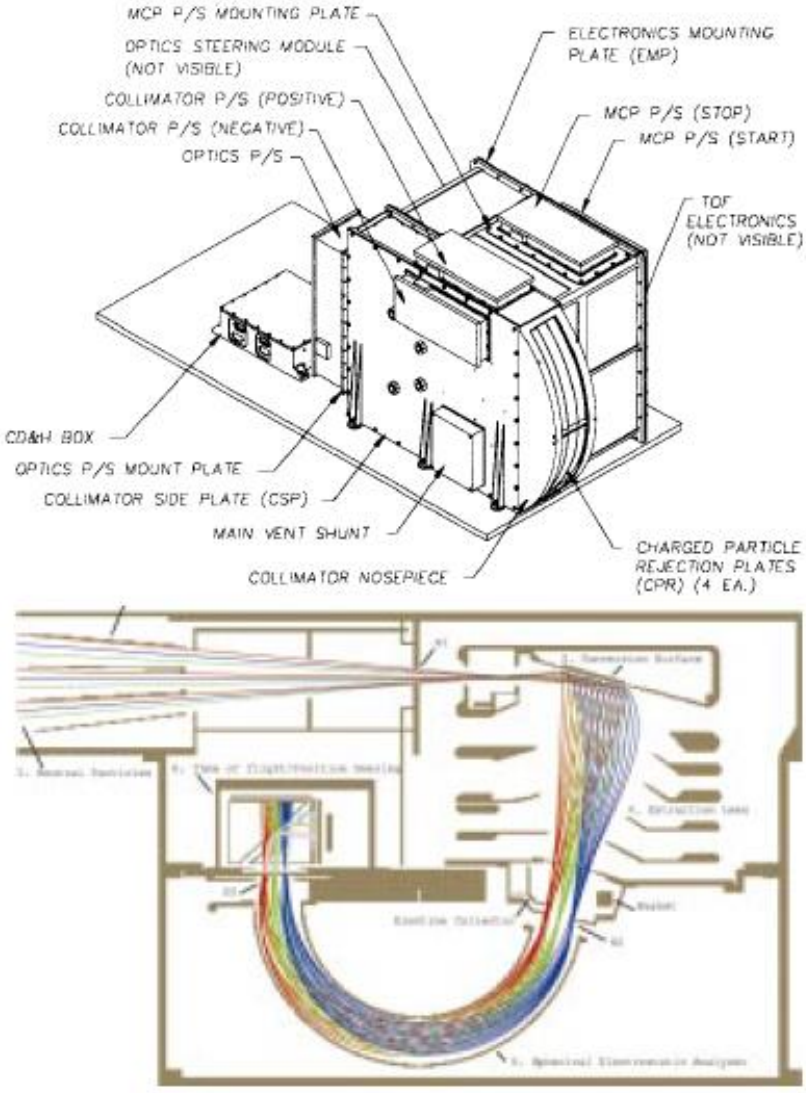

Figure 29: (top) diagram of the LENA instrument on IMAGE, showing the different subsystems and (bottom) an end-to-end simulation of the ion optics of LENA, also showing the TOF optics in a 2D section through the symmetry axis of the instrument.

Similar to IBEX-Lo, LENA has a collimator that rejects charged particles, allowing neutral particles to pass through to the conversion surface which would convert neutrals into negatively charged particles before passing them into an ESA that restricts the energy range of measured particles and are then accelerated before passing into a TOF system similar to IBEX-Lo, in which secondary electrons produced when the ions pass through the start and stop foils and measured by MCPs in order to determine the energy and angular distribution. While the specifics of the design of LENA are different from IBEX-Lo, we can see that the measurement concept is very similar.

Figure 30 shows an example of images taken by LENA early in the IMAGE mission. The images are in some ways similar to those captured by IBEX-Lo in that they are projections of the intensities of measured ENAs onto a 2D map, however the images are also quite different, with LENA observations looking back at the Earth and its magnetosphere "from the outside" whereas IBEX-Lo is able to create maps of the global heliosphere by imaging "from the inside out". The LENA images also are take over much shorter timespans during the course of a day, whereas it takes a full year for IBEX-Lo to create a full-sky map due to its unique measurement concept.

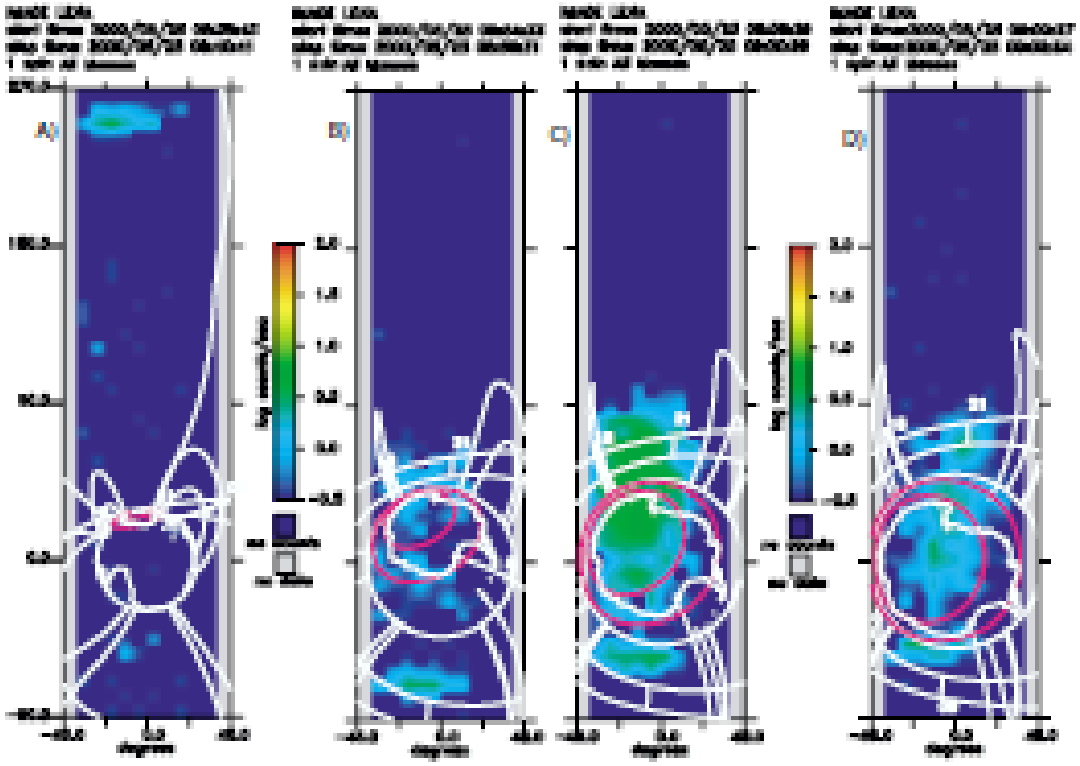

Figure 30: A LENA image sequence from early in the mission (25 May 2000); A) during downleg just past descending node, sun at top; B) approaching passage over the south polar regions, sun at lower left; C) passing over the Antarctica; and D) near perigee, with sun near occultation. Each image contains the Earth with continents, nominal auroral oval in red, and 3 and 6.6 R_E magnetic field lines at the indicated magnetic local times.

4. IBEX Calibration Plan

4.1 Overall Calibration Scheme

This section summarizes the calibration philosophy and methods.

4.2 Pre-flight Calibration Plans

This section details how IBEX-Hi an IBEX-Lo, including all their individual subsystems, were tested and calibrated to verify that they would meet the expected performance parameters prior to placement into orbit.

4.2.1 IBEX-Hi Pre-flight Calibrations

An end-to-end performance model of IBEX-Hi was developed and refined throughout development of the sensor to optimize the sensor design and to simulate and evaluate performance of the subsystems individually and the sensor as a whole. The model is constructed with a combination of analytic modeling, electro-optic simulations, and physics modeling of specific sensor elements. Electro-optic design and simulations were performed using SIMION, a commercially available charged-particle optics simulation package (Dahl 2000).

Testing of IBEX-Hi subsystems and calibration of the fully assembled sensor has been used to validate most components of this model. The calibration results alone do not constitute a complete characterization of IBEX-Hi; in fact, only a limited subset of all possible ion or neutral atom energies, species (H and O), incident angles, and foil locations on the sensor could be tested in the time available. A high-fidelity sensor model allows us to interpolate between these data points to derive an integrated response function and to predict sensor response across the full possible range of operational conditions expected throughout the mission, allowing the flexibility to modify the measurement strategy if needed for discovery science.

4.2.1.1 IBEX-Hi Sensor Model

The end-to-end model includes a geometric ray-tracing of the collimator, an empirical determination of foil transmission and ionization fraction, and 3-D electro-optic SIMION models of the energy analysis and detector subsystems. The end-to-end simulation is performed by propagating a large number ($N \sim 10^6$) of ENAs distributed in energy (E) and angle (θ,φ) through the model for each of the 6 energy settings (j) of the ESA. As the ENAs “fly” through each sensor element (k), they are appropriately propagated in a manner that reflects the physical action of that particular element. At each stage, the transmission efficiency $T_{j,k} = N_{j,k}^{out} / N_{j,k}^{in}$ is determined. Note that T, N^{in}, and N^{out} are all functions of energy, angle, and position. We consider each stage in turn below.

Collimator: As previously described, the IBEX-Hi collimator is composed of a stacked array of hexagonal cells that restrict the FOV to 6.5° FWHM. Because the FOV is based solely on the geometry of a hexagonal channel, the angular dependence of the collimator transmission is accurately modeled using the collimator response function P(θ,φ), which is illustrated in Figure 10 and is indistinguishable from the measured performance. The sensor simulation is initiated here, with virtual ENAs uniformly spread across the cell entrance and uniformly distributed in angle up to ±10° relative to the collimator boresight.

Conversion Foil: Ultrathin carbon foils are used to convert a fraction of the incident ENAs into positive ions that are then energy-analyzed and accelerated into the detector section. Although the desired function of the foil is to simply strip an electron from an ENA, the ENA also undergoes statistical processes of angular scattering, energy loss, and ionization. These are simulated via Monte-Carlo sampling of energy-dependent empirical functions for each of the above factors.

- The scattering angle for a given ENA is determined by sampling a 2-D Lorentziansquared, having an angular width determined by the ENA's initial energy and laboratory measurement of the foil constant k_F. The use of a Lorentzian-squared is based on empirical best fit to the measured laboratory distribution.
- Energy loss of ENAs at energies >1 keV is based on measurements by Allegrini et al. (2006) and uses an asymmetric Gaussian energy distribution having a mean and width that are functions of foil thickness, ion species, and ion energy. These results were extrapolated for ENA energies <1 keV.
- The probability for ENA transmission through the foil τ_{Foil} was derived using SRIM (Ziegler et al. 1985) Monte-Carlo simulations of protons incident on a 1.7 μg cm−2 carbon foil. The results were fit to $\tau_{Foil} = exp(-9.594 \times 10^4/E^2)$, where E is in eV.
- The probability of an ENA exiting the foil as H^+ is determined from the formulas in Figure 15.

Electrostatic Energy Analyzer (ESA) A SIMION electro-optic model of the energy analysis subsystem incorporates the geometry of all relevant electrostatic elements, and the trajectories of H^+ exiting the foil through the ESA are subsequently computed. Figure 31 compares the simulation and calibration (Cal 1) results of the absolute transmission of the combined conversion foil and ESA for each of the six energy steps. The model clearly reproduces the measured behavior, including the energy passband centers and widths, especially for the higher energy passbands. The good correspondence, which is slightly worse at lower energies where the conversion foil behavior is less well known, gives us confidence in our general understanding of the foil physics and ESA electro-optics. We have employed a scaling factor to the modeled transmission values to account for the differences between the simulations and the

calibration data; the scaling factors range from 1.45 at energy step 1 to 0.88 at energy step 6.

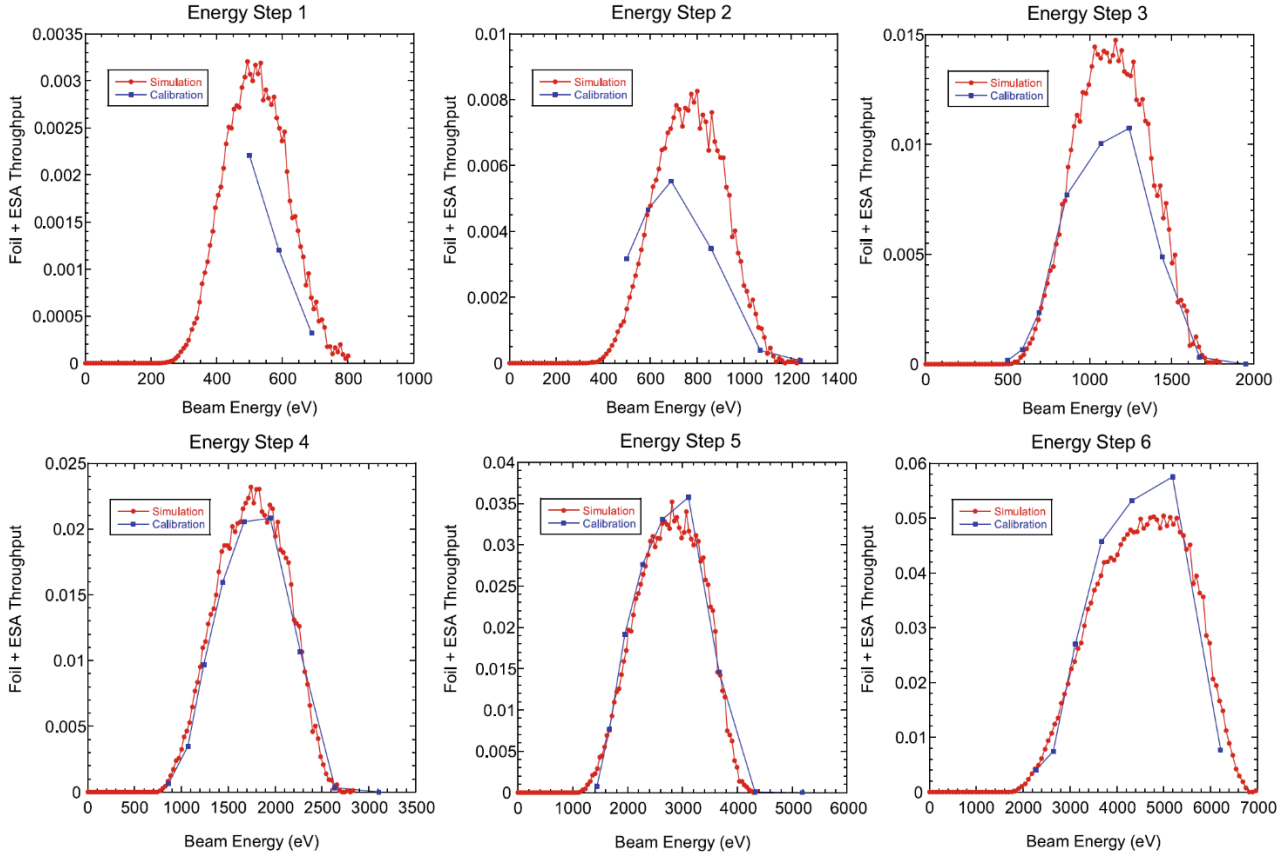

Figure 31: Comparison of simulations and Cal 1 measurements of the absolute transmission of the combined charge conversion and energy analysis subsystems. Agreement is generally good, although slightly worse at lower energies where the conversion foil behavior is less well known

Detector Subsystem: The detector model uses a separate electro-optic model for each chamber and a single carbon foil model for the foils between Chambers A and B and Chambers B and C. Simulated H^+ ions are initially incident at the entrance grid of Chamber A and sequentially propagate through the electro-optic model of Chamber A, the foil model, the electro-optic model of Chamber B, the foil model, and finally the electro-optic model for Chamber C. At the location of ion impact on each foil, the probability for secondary electron emission from each surface is calculated using a Poisson distribution and the measurements of Kozochkina et al. (1993) and Ritzau and Baragiola (1998). These secondary electrons, in turn, are propagated through the appropriate chamber electro-optic model by following their trajectory to the CEM detector, and their detection probability is 0.7. The detector represents the most complex and uncertain component of the end-to-end model, and at the time of the IBEX

launch the sensor response function is primarily based on the empirical, scaled detector response that is discussed in Section 4.2.1.2 (IBEX-Hi Calibration and Performance).

4.2.1.2 IBEX-Hi Calibration and Performance

IBEX-Hi had four phases of calibration: Cal 1, which included calibration without the collimator and photoelectron suppression grids for quantification and electro-optic validation of the integrated performance of the charge conversion and energy analysis subsystems with ion and neutral atom beams; Cal 2, which verified performance for a small subset of energies and foils and was performed between vibration testing and thermal-vacuum testing (Jones and Bernardin 2007); Cal 3, which used the spare CEU that was functionally identical to the flight CEU for detailed, end-to-end performance characterization; and Cal 4, which was cross calibration with IBEX-Lo.

Cals 1, 2, and 3 were performed at Los Alamos National Laboratory (LANL) using a magnetically mass-resolved H^+ beam generated by a microwave ion source having an intrinsic energy spread <2 eV and accelerated to an energy from 0.45 to >10 keV. A neutral hydrogen (H^0) beam was created by charge exchange of the H^+ beam with the residual gas in the beam line between the mass-analyzing magnet and the calibration chamber, and the remaining H^+ in the H^0 beam was magnetically deflected before it could enter the chamber. The beam transited a 2.0-mm-diameter aperture and had a measured diameter at the IBEX-Hi entrance of ~2.2 mm for energies ≥1 keV and 2.8 mm at 450 eV. The wider beam at the sensor entrance was due to angular divergence of the beam. The typical chamber pressure was ≤2×10^{-7} torr, and Residual Gas Analysis (RGA) spectra were obtained at least once each day and every 20 minutes when IBEX was under vacuum but not powered. Cal 4 was performed at SwRI; details of the SwRI calibration facility are provided in McComas et al. (2009).

In all calibrations, the ion or neutral atom beam flux was measured using an absolute beam flux monitor that is schematically illustrated in Figure 32. The monitor utilizes a coincidence scheme (Funsten et al. 2005) in which an ion or neutral atom beam generates secondary electrons at the entrance surface of a foil, and these electrons are accelerated to and detected by detector D_1. A fraction of the beam transits the foil and generates secondary electrons on the back surface of the foil and at the back plate of the monitor; these secondary electrons are accelerated toward and registered by detector D_2. The absolute detection efficiencies for each detector are derived from measurement of the single (non-coincident) count rates C_1 and C_2 of CEM detectors D_1 and D_2, respectively, and the coincidence count rate C_{COIN} between them. The probability (and therefore detection efficiency) that an ion that enters the monitor is detected by D_1 is $\varepsilon_1 = C_{COIN}/(C_{COIN} + C_2)$. Similarly, the D_2 detection efficiency is $\varepsilon_2 = C_{COIN}/(C_{COIN} + C_1)$. Because these detection efficiencies include the secondary electron yields, the fraction of the beam that transits the grid-mounted foil, and the probabilities that secondary electrons are accelerated into the detectors and generate pulses, we do not need to know these quantities individually. The resulting coincidence efficiency is

therefore $\varepsilon_{COIN} = \varepsilon_1\varepsilon_2$, and the incident beam flux is therefore $C_{COIN}/(A_B\varepsilon_{COIN})$, where A_B is the cross-sectional area of the beam.

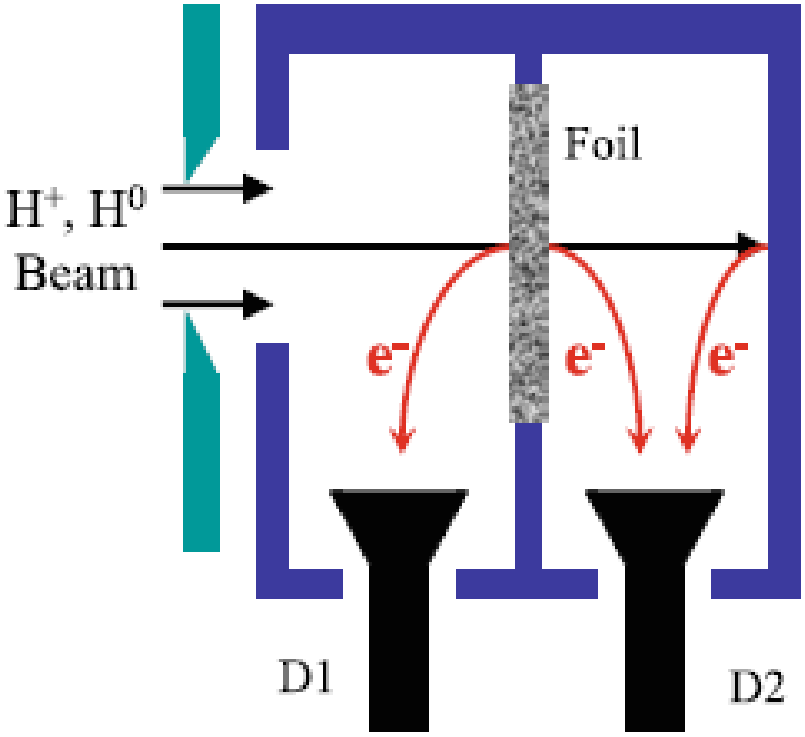

Figure 32: The absolute beam flux monitor was used to measure the H+ or H0 beam flux throughout the IBEX-Hi calibrations

The beam flux and beam stability were measured throughout the calibrations. The stability was typically 1–3% over a single IBEX-Hi measurement. The beam was also monitored for drift over time, and typical drift for >80% of the calibration data was ≤5%. Importantly, the IBEX-Hi sensor telemetry stream reports single (non-coincident) count rates for each of its three detectors as well as all coincidence count rates, enabling *in situ* monitoring of detection efficiencies of each detection chamber throughout the IBEX mission using this method.

The average background count rates, listed in Table 8, were measured over 19.6 hours during Cal 4 (cross calibration) when the sensor was fully operational but had no incident ion or ENA beam. The singles count rates in each CEM detector were <0.2 Hz. While the coincident count rates are higher than expected based on random coincidence of the background singles rates in the detectors, we have found that ambient gamma rays are associated with a majority of the background coincidence events observed in the detector subsystem. This is based on the relative frequency of different coincidence combinations in the detector subsystem from a ^{137}Cs source placed next to the sensor, from a 3.5 keV H^+ beam, and under a quiescent

(unstimulated) condition. We used laboratory TOF electronics to measure the TOF between detected events in all coincidence combinations. While most coincident events from the 3.5 keV H^+ beam involved a first pulse from CEM A and no events in which CEM C registered the first pulse, both the ^{137}Cs source and quiescent background generated approximately an equal number of coincidences in which CEM A and CEM C registered the first pulse. We note that ^{137}Cs also emits 1.175 MeV electrons that have a range of ~2.3 mm in Al, but these were completely blocked by the Al walls of minimum thickness >2.5 mm surrounding the interior of the detector chambers and CEM detectors.

Table 8: Average background count rates for exclusive (non-coincident) single events and a subset of coincidence types measured over 19.6 hours of quiescent operation during cross calibration

Measurement		Background rate
Singles	CEM A	89 mHz
	CEM B	115 mHz
	CEM C	69 mHz
	CEM D	12 mHz
Double coincidences	Long AB	2.8 mHz
	Long BC	4.2 mHz
	Qual(Not_C) AC	0.13 mHz
Triple coincidences	Qual(Not_C) ABC	0.58 mHz
	Long ABC	1.04 mHz

We subsequently measured the background γ -ray environment in the LANL calibration facilities, showing a background flux of 6.3 γ cm^{-2} s^{-1} between 0.2–3 MeV and specific γ - ray lines corresponding to 40K (K is used in concrete) and daughters associated with ^{222}Rn. Therefore, because a majority of coincident counts listed in Table 4 result from the ambient γ -ray environment of the calibration laboratory, the measured background count rates are significant overestimates of the background rates expected in space from this mechanism.

IBEX-Hi was also tested for response to UV light, in particular to study the “ion gun” effect in which photoelectrons generated at the conversion foil are accelerated toward the +10 kV collimator and ionize ambient atoms or molecules, which in turn are accelerated into the conversion foil and can masquerade as ENAs. During Cal 1, an Ar-

purged deuterium lamp, followed by two notch filters used to maximize the fraction of H Ly α (1216 Å) and a MgF_2 window, directly illuminated the conversion foils. The photon rate at the foils was ~4 × 1010 s^{-1} as measured using a calibrated UV photodiode (Korde et al. 2003). The ion gun effect was observed when the collimator was biased to +10 kV and no voltage was applied to the photoelectron suppression grid, yielding individual count rates in CEMs A, B, and C of 17, 12, and 1.6 Hz, respectively; a total double coincidence rate of ~0.1 Hz; and a total triple coincidence rate of <0.05 Hz. The double and triple coincidence rates dropped to background levels when the collimator voltage was switched from +10 kV to 0 V.

The IBEX-Hi FOV alignment was measured during Cals 1 and 3 using a theodolite located at a viewport at the rear of the calibration chamber, collinear with the beam axis, and boresighted with two beam-defining apertures upstream of the chamber. A double-sided mirror was mounted flush to the IBEX-Hi baseplate to an estimated accuracy of <0.1°, and the alignment was measured using autocorrelation. The reproducibility of the autocorrelation and movement of the motion stages was ≤0.02°. Alignment accuracy of the theodolite with the upstream apertures is estimated to be ~0.1°. Finally, angular divergence of the H^0 beam was measured to be 0.2° FWHM. Using this alignment scheme, the angular response of the sensor to a 2.7 keV H0 beam incident on Foil 6a was measured at Energy Passband 5 at several points in the azimuthal and polar directions, and the results are shown in Figure 33. An angular offset of 0.17 ± 0.07° in polar and −0.20 ± 0.07° in azimuth is likely due to a combination of the tolerance errors mentioned above and possibly a slight angular dependence of the overall sensor response. After correcting for beam divergence, the collimator acceptance angle was measured to be 6.5 ± 0.1° FWHM, in agreement with the collimator tests described previously.

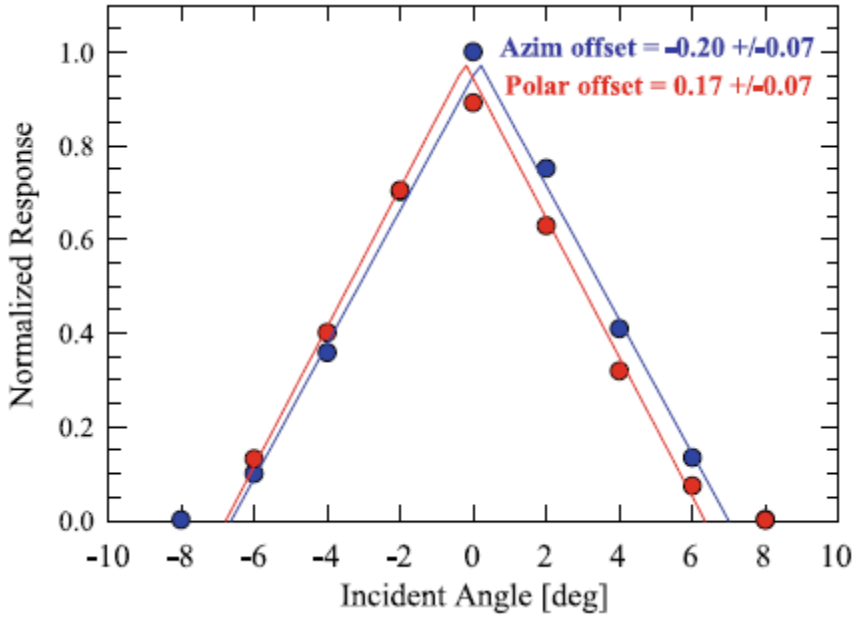

Figure 33: The IBEX-Hi angular response as measured using a 2.7 keV H^0 beam

Using the Cal 1 results of the combined throughput of the conversion foils and energy steps as shown in Figure 31, the central energies and energy resolutions were derived for double and triple coincidence events and are shown in Figure 34. The FWHM energy resolution ranges from approximately 0.45 at the lowest energy passband to about 0.65 at the highest energy passband. Although limited to only the charge conversion and energy analysis subsystems (and therefore not representative of the flight energy passbands or the end-to-end IBEX-Hi energy response), this data was used to validate the physics model of the conversion foil and the electro-optic design of the ESA.

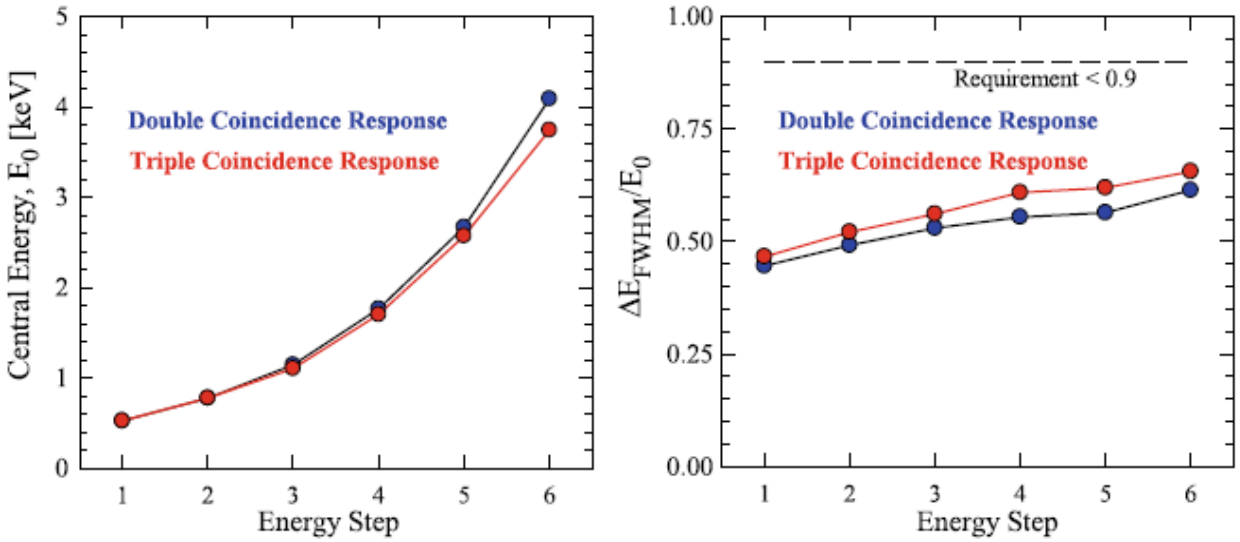

Figure 34: The central energies (left panel) and energy resolutions (right panel) of the combined charge conversion and energy analysis subsystems are shown for each energy step as measured during Cal 1. Double coincidences are the sum of Long AB, Long BC, and Qual(Not_C) AC counts. Triple coincidences are Qual(Not_C) ABC counts

The energy-dependent trajectories through the ESA govern the location and angle at which an ionized ENA enters the detector subsystem. Furthermore, there is a known spatial dependence of the detection efficiency for each detector chamber because the CEM detectors are located on one side of each chamber. However, because ionized ENAs are accelerated by 6 keV into the detector subsystem and because of the scalability of electro-optics, we expect that (1) the response for each energy passband can be generally scaled according to E/E0 where E_0 is the central energy of the passband and E is the initial ENA energy and (2) the detection efficiency for the coincidence combinations are generally independent of energy. Figure 35 shows the detection efficiency for summed double coincidences (defined in the figure caption) as a function of E/E_0 for all passbands and all energies used during Cal 1 and Cal 3. The data for each coincidence combination were fit to $\varepsilon(E/E_0) = c_1 + c_2((E/E_0+c_3)-c_4)^2$ where

c_1, c_2, c_3, and c_4 are fit parameters, and this empirical equation is used as the basis for the detector response in the end-to-end sensor model.

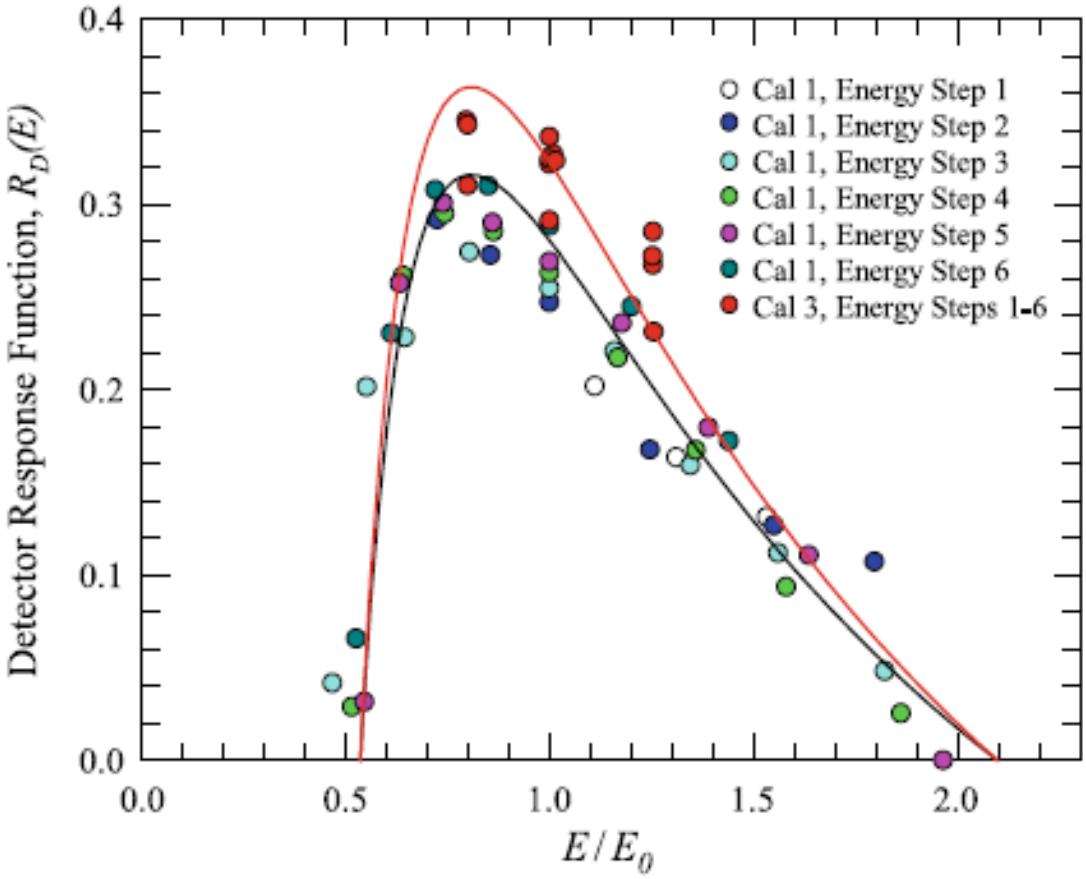

Figure 35: The empirical detector subsystem response for all energy passbands for double coincidence events is approximately represented by a single equation. Cal 1 results are the sum of Long AB, Long BC and Long AC, whereas the Cal 3 results are the sum of Long AB, Long BC, and Qual(Not_C) AC. The black line is an empirical fit to the Cal 1 results, and the red line is the Cal 1 empirical equation scaled by a factor of 1.15 to fit the Cal 3 results

The Cal 3 results show a slightly higher efficiency of the detector subsystem, which likely resulted from new foils installed between Chambers A and B and Chambers B and C. These new foils were mounted using an improved technique and had a higher fraction of coverage over the support grid. To reflect this enhanced detection efficiency, the upper curve in Figure 35 was derived by linear scaling of the empirical Cal 1 equation to the Cal 3 results, which were incorporated into the end-to-end sensor response function.

During Cal 3, a 2.8 keV H^0 beam was directed along a snake-like path at a steady rate of 1 mm/sec along a radial line across a foil and through 0.36° azimuthal steps between the radial lines. The incident beam flux was intermittently re-measured using the

absolute beam current monitor to monitor beam flux drift. The relative singles (non-coincidence) rates, double coincidence rates, and triple coincidence rates over multiple foils is shown in *Figure 36*, in which brighter pixels correspond to higher count rates. The response is observed to change as a function of azimuthal angle (horizontal direction in the figure). This response variation is the direct result of the azimuthal-dependent trajectories through Chambers A, B, and C and, in particular, the location of the CEM within each chamber. The axis of symmetry of the response observed in *Figure 36* and throughout IBEX-Hi calibrations lies along the line between CEM B (corresponding to the middle of Foil 8) and CEMs A and C (located between Foils 1 and 15). *Table 9* shows the relative fraction of double and triple coincidence events averaged over the energy passbands. The most probable triple and double coincidence events are aABC and bBC, respectively.

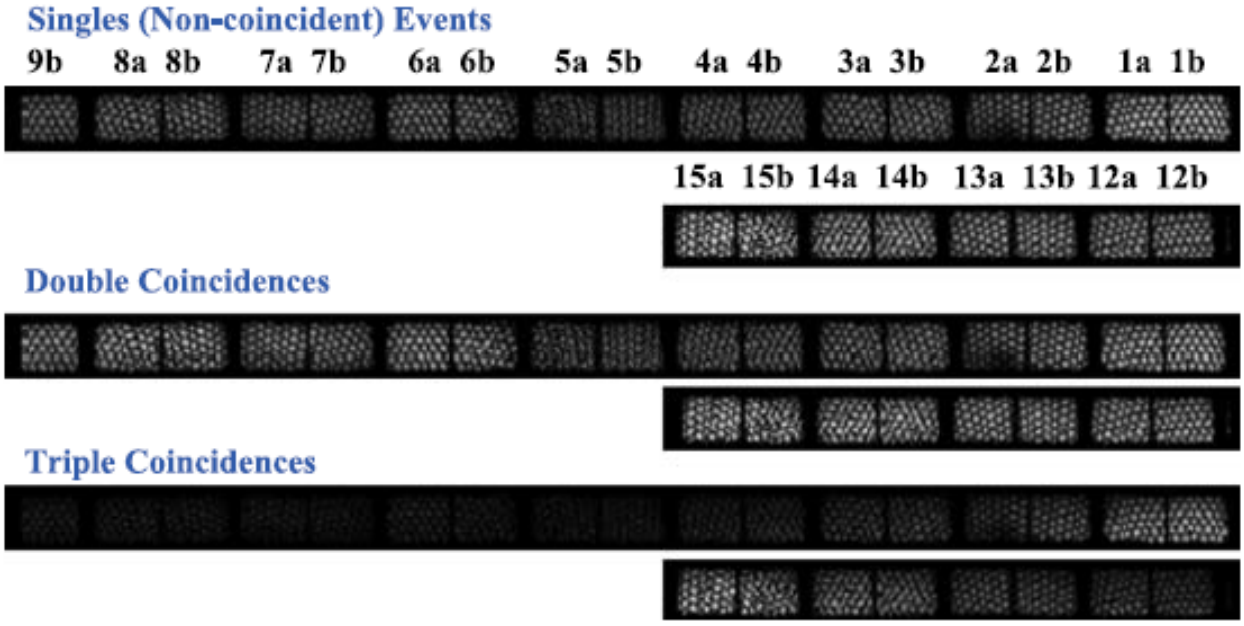

Figure 36: Response of the IBEX-Hi sensor to a beam of 2.8 keV H^0, where the arc-shaped foil apertures have been flattened such that the horizontal direction corresponds to azimuth. Double coincidences are the sum of Long AB, Long BC, and Qual(Not_C) AC counts. Triple coincidences are Qual(Not_C) ABC counts

Table 9: Relative probabilities of occurrence for different double and triple coincidence combinations. Note that coincidence combinations abcABC, acAC, cAC are not included because they are not likely produced by an ENA in the detector subsystem. CEM D is the detector in the IBaM

Triple coincidence event set	Combination	Event probability
Qual(Not_C) ABC	aABC	0.64
	bABC	0.14
	abABC	0.22
Double coincidence event set	**Combination**	**Event probability**
Long AB	aAB	0.18
	bAB	0.03
	abAB	0.06
Qual(Not_C) AC	aAC	0.08
Long BC	bBC	0.49
	cBC	0.07
	bcBC	0.09

Calibration results were used to refine and validate all of the modeled and simulated components of the end-to-end sensor model except for the detector subsystem, which uses the empirical response shown in Figure 35. The model is then used to interpolate the response for energies, foil locations, and incident angles not measured during calibration and derive the integrated response of the whole sensor. The count rate C_i of IBEX-Hi corresponding to an ENA flux of J(E,Ω) cm^{-2} sr^{-1} eV^{-1} s^{-1} at ESA setting i (with central energy E_i) is

$$C_i = \int J(E,\Omega) G_i(E,\Omega) d\Omega dE. \quad (2)$$

The geometric factor G_i is constructed by separating the collimator response P(Ω) from the comprehensive energy-dependent response $R_i(E)$ of the sensor after the collimator:

$$G_i(E,\Omega) = AT_C P(\Omega) R_i(E). \quad (3)$$

In this equation, A is the total aperture area of the charge conversion foils (156.6 cm2) and TC is the fractional area of the collimator consisting of open apertures (0.67). The point spread function P(Ω) describes the angular response of IBEX-Hi, which, to a high degree of accuracy, can be represented solely as the energy-independent collimator response shown in Figure 10. Because the incident ENA flux is expected to be relatively

constant over the solid angle of any single azimuthal pixel, the integrated collimator response corresponds to a solid angle of $\int P(\Omega)d\Omega = 0.0147$ sr.

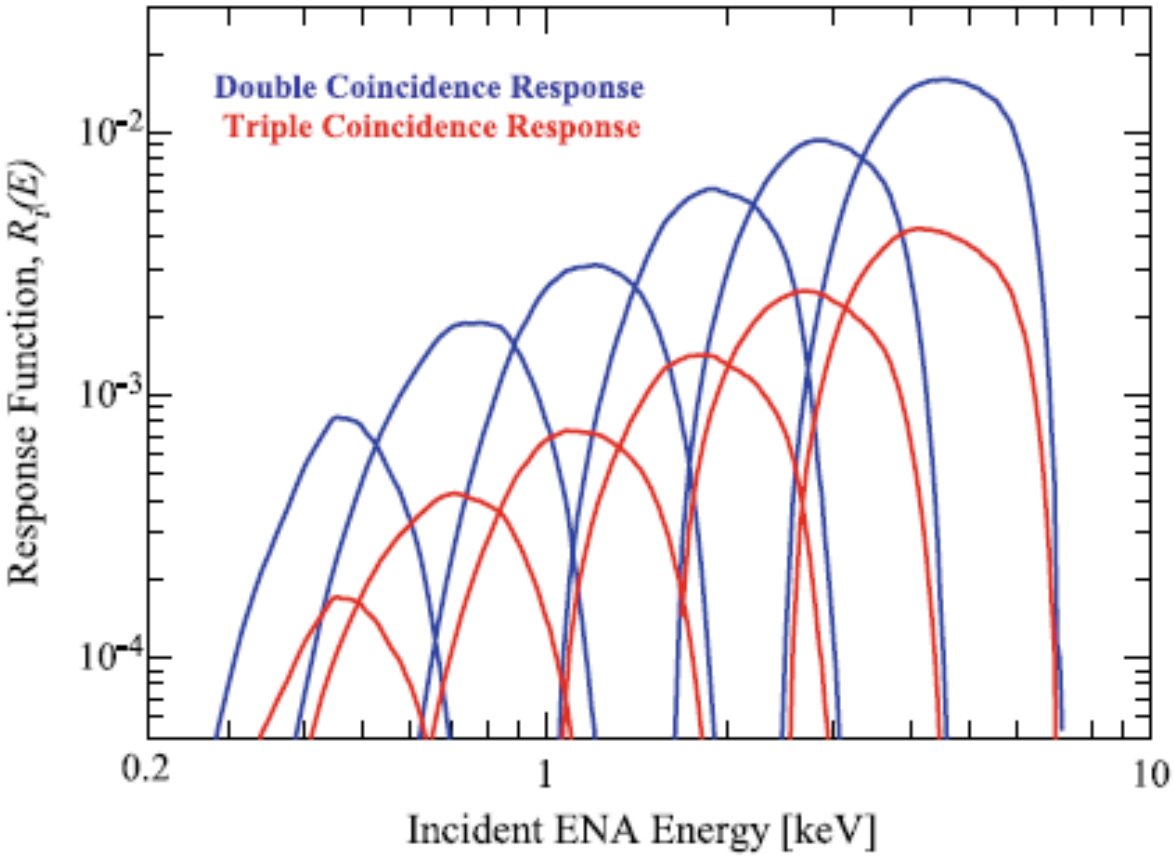

Figure 37: The response function $R_i(E)$ of the IBEX-Hi sensor is shown for each energy passband i. The double coincidence response includes the sum of Long AB, Long BC, and Qual(Not_C) AC events. The triple coincidence response corresponds to Qual(Not_C) ABC events

The sensor response function $R_i(E)$ describes the cumulative, energy-dependent response to ENAs that exit the collimator and are incident within the total area of the charge conversion foils. $R_i(E)$ therefore includes all factors governing transmission and transport through the charge conversion, energy analysis, and detector subsystems, as well as the probability of detection in each CEM chamber. The response function was generated using the end-to-end sensor model, and the results for double and triple coincident events are shown in *Figure 37*. The primary uncertainty of the sensor response function lies in the empirical detector subsystem response function. Using the end-to-end response function, the flight energy passband settings have been defined as shown in *Table 10*.

Table 10: Flight energy passbands for double and triple coincidence events as derived from the sensor end-to-end model for each of the six IBEX-Hi energy steps. The full-

width-at-full-maximum values ($E_{+FW} - E_{-FW}$) represent the 99% level and central energy E_0 represents the energy of the maximum (peak) value of the response function

ESA setting			Double coincidences: Long AB + Long BC + Qual(Not_C) AC					
ESA Step	Outer ESA [kV]	Inner ESA [kV]	E_{-FW} [keV]	E_{-HW} [keV]	E_0 [keV]	E_{+HW} [keV]	E_{-FW} [keV]	$\Delta E/E_0$ [keV]
1	−0.09	−0.78	0.26	0.38	0.45	0.58	0.75	0.20
2	−0.08	−1.28	0.36	0.57	0.78	0.98	1.25	0.41
3	−0.02	−1.85	0.62	0.89	1.21	1.56	1.91	0.68
4	0	−2.88	1.07	1.45	1.92	2.53	3.02	1.08
5	0	−4.46	1.68	2.15	2.80	3.82	4.54	1.67
6	0	−7.00	2.57	3.34	4.51	6.14	6.93	2.80
ESA setting			Triple coincidences: Qual(Not_C) ABC					
ESA Step	Outer ESA [kV]	Inner ESA [kV]	E_{-FW} [keV]	E_{-HW} [keV]	E_0 [keV]	E_{+HW} [keV]	E_{-FW} [keV]	$\Delta E/E_0$ [keV]
1	−0.09	−0.78	0.24	0.38	0.45	0.59	0.75	0.47
2	−0.08	−1.28	0.35	0.52	0.71	0.95	1.23	0.60
3	−0.02	−1.85	0.58	0.84	1.08	1.55	1.93	0.65
4	0	−2.88	1.07	1.36	1.85	2.50	3.02	0.62
5	0	−4.46	1.68	1.99	2.70	3.75	4.54	0.65
6	0	−7.00	2.57	3.13	4.09	6.00	6.93	0.70

Based on simulations and recent estimates of ENA fluxes, the spectral slope of ENAs should sharply decrease with increasing energy above ~1 keV (e.g., Gruntman et al. 2001; Wurz et al. 2008b). Therefore, derivation of the incident ENA flux J(E,Ω) from the sensor count rate C_i through inversion of (2) should be performed using an iterative, forward-modeling method. Nevertheless, the energy geometric factor, defined as

$$G_i^E = \frac{1}{E_i} \int G_i(E, \Omega) \mathrm{d}\Omega \mathrm{d}E, \tag{4}$$

can be used to estimate the ENA flux near energy E_i using $J(E_i) = C_i/E_i G_i^E$. The energy geometric factors for double and triple coincidence events are listed in Table 7 for each of the six IBEX-Hi energy passbands.

Table 11: Values of the energy geometric factor GE (cm^2 sr eV/eV) derived using (4) for the flight ESA passbands

ESA step	G^E, double coincidence: Long AB + Long BC + Qual(Not_C) AC	G^E, triple coincidence: Qual(Not_C) ABC
1	0.00060	0.00013
2	0.0016	0.00041
3	0.0028	0.00075
4	0.0053	0.0013
5	0.0086	0.0024
6	0.015	0.0045

4.2.2 IBEX-Lo Pre-flight Calibrations

This section describes the pre-flight calibration efforts for IBEX-Lo including both the testing of the IBEX-Lo prototype, which had the same basic geometry and design as the flight sensor, and the flight sensor itself, which included separate testing of the entrance and mass analysis subsystems.

4.2.2.1 IBEX-Lo Prototype Tests Prior to Sensor Development

Prior to the IBEX-Lo design phase, a prototype IBEX-Lo sensor was developed and tested using both ions and neutrals (Wieser 2005; Wieser et al. 2007). This prototype had the same basic geometry and design as the flight sensor except that the conversion surface was placed on the outside circumference of the prototype. Also, for initial tests, a single microchannel plate detector was used in place of the TOF mass spectrometer. Test and calibration were performed at the University of Bern MEFISTO calibration facility (Marti et al. 2001). This facility provides a calibrated neutral beam in the energy range from 10 eV to 3 keV. The same facility was used to test and calibrate the IBEX-Lo flight sensor.

The prototype design was somewhat different because one of the tests used a positive ion beam injected at the position and angle of specularly reflected negative ions off the conversion surface. These tests verified the ion optics properties of the ESA. In particular, it verified radial focusing and azimuthal defocusing properties of the ion optics system. Positive ions were used (with the appropriate reversal of ion optics voltages) because ion beam angular width, energy spread, and flux are much better controlled than neutral beam parameters. After these tests, the aperture was replaced

with a DLC conversion surface like the one used in the IBEX-Lo flight sensor, ion optics voltages were reversed, and a neutral beam was used to complete testing.

The neutral beam was produced by surface neutralization (Wieser and Wurz 2005): a 3 kV ion beam (H^+ and O^+ beams were used for the prototype testing, and H^+, O^+, He^+ and C^+ were used in the IBEX-Lo flight sensor calibration) with narrow (about 3 eV) energy spread was injected into the neutralizer unit (Wieser and Wurz 2005). In the neutralizer unit, the ion beam was slowed in an ion deceleration stage by retarding potentials to select a beam energy from 10 eV to a maximum of 3 keV (i.e., no deceleration of the initial beam). The decelerated ion beam was directed onto a highly polished, mono-crystalline tungsten surface at a very shallow angle (10°) where it is very efficiently neutralized. Residual ions in the resulting neutral beam were deflected away from the neutralizer exit slit using a set of electrostatic deflection plates. The neutral beam had a large energy and angle spread caused by the reflection/neutralization process. This large energy and angle spread complicates analysis of the test data. The current off the surface was calibrated prior to prototype tests (and also prior to and after the flight sensor calibration) so that absolute neutral fluxes were known to ~ 20–30%.

Prototype tests using the neutral beam confirmed the energy resolution of the system, verified the ESA transmission function (= 0.4, approximately independent of energy), and demonstrated the overall geometric factor of the sensor. Later, the sensor was upgraded to include “fins” on the outer ESA (like the ones in Figure 18) and to include magnets. The upgrades verified the importance of both the fins in reducing the scattered ion background and the magnets in reducing electron transmission through the ESA.

Upon completion of the tests of the upgraded prototype, the flight sensor design was developed by starting with the prototype geometry and adjusting and optimizing voltages and geometries of the electrodes. This optimization was done in an iterative process using a computer code (Wieser et al. 2008) to maximize sensor throughout and add features that simplify manufacturing and reduce the number of high voltage supplies needed to control the ion optics.

4.2.2.2 IBEX-Lo Flight Sensor Calibration and Performance

For the flight sensor, the entrance and mass analysis subsystems were tested separately. Tests of the entrance system were done to verify collimator performance including transparency, energetic particle rejection, and off axis leakage. In all of these tests, the collimator performed within the specifications. *Figure **38*** shows the solid angle FOV of the low-resolution quadrants of IBEX-Lo as obtained by a Monte-Carlo simulation with maximum manufacturing tolerances on the etched plates that make up the collimator. The simulated leakage over the entire accessible angle space was less than 10^{-6} of the total FOV, (i.e. two orders of magnitude better than the requirement).

Combined effects of leakage through neighboring channels of the collimator and scattering off edges of the collimator plates were investigated using the collimator, a detector, and an intense Argon ion beam. An angular scan across the collimator FOV, with the ion beam intensity increased by a factor of 100 for large angles θ, is shown in Figure 39. The observed particle rate outside the collimator FOV is typically a factor of 10 below the required suppression of 10^{-4}.

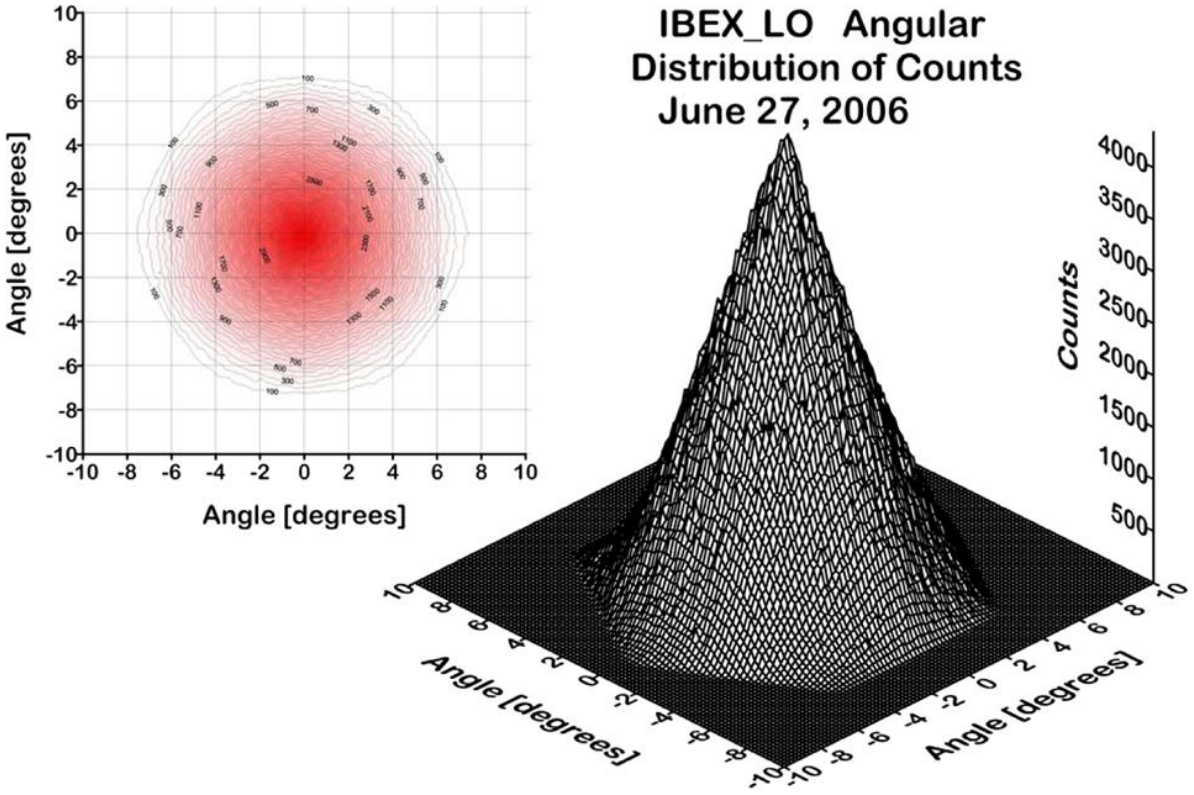

Figure 38: Calibration results. Transmission function of high-resolution sectors of the IBEX-Lo collimator. The transmission is nearly symmetric with a FWHM of ~ 7° ×7°

A positive biased collimator collects plasma electrons from the environment and photoelectrons emitted from the sun-lit side of the spacecraft. In significant numbers, these electrons could be responsible for a substantial background. Thus, electron suppression, especially at low energies, is a critical requirement for the IBEX-Lo sensor. The suppression factor for electrons is shown as a function of electron energy in *Figure 40*. These data are taken from tests with the IBEX-Lo entrance subsystem and an electron beam.

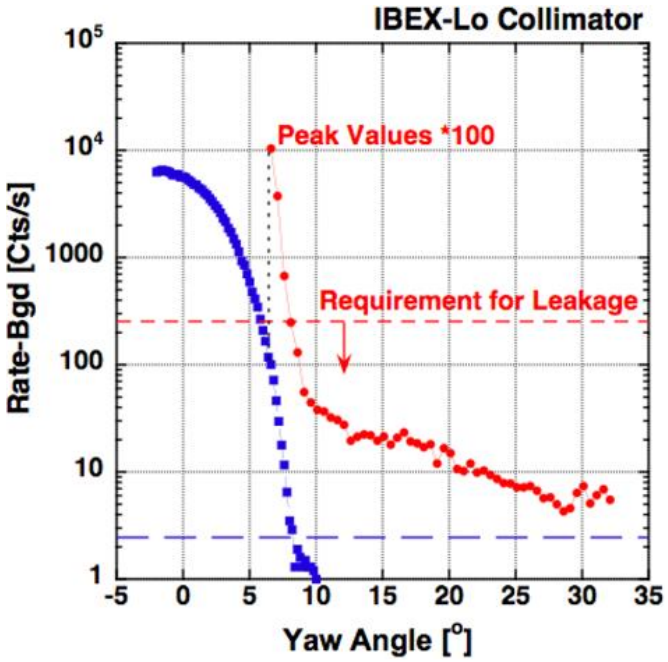

Figure 39: On- and off-axis performance of the IBEX-Lo collimator. The on-axis profile (blue curve) shows the near-gaussian response of the collimator. The off-axis profile (red curve, note the change in scale by a factor of 100), is well below the requirement for leakage outside of ~ 14° yaw angle

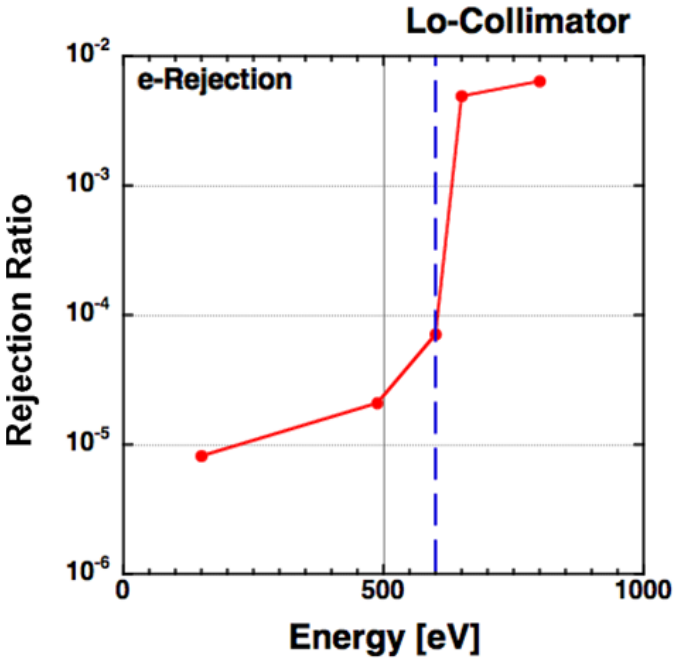

Figure 40: Measured electron rejection properties of the IBEX-Lo collimator. With −3.1 kV on the electron rejection rings (see Figure 18), electron fluxes below 600 eV are reduced by almost 3 orders of magnitude

The mass analysis subsystem was sufficiently complicated that it required separate testing. In addition, a significant simplifying feature of the mass analysis subsystem was that voltages could be reversed and positive ions could be used to verify basic performance, mass resolution, and overall efficiency. These positive ion beam tests were performed at the University of New Hampshire. Similar to the prototype tests, positive ions have the advantage that ion beam angular width, energy spread, and flux are much better controlled than similar neutral beam parameters.

The mass analysis subsystem performed within specifications. Because singles rates and all double coincidence rates are monitored in the TOF and because the triple coincidence rate is determined from these TOF events, the absolute TOF efficiency can be determined independent of whether the TOF is tested with the sensor or tested alone. In particular, because the triple and double coincidence rates can be used to derive detector efficiencies, the IBEX-Lo TOF subsystem is fully self-calibrating, even in flight, without need to correct for any background or sensor inefficiencies. *Figure 41* shows TOF double and triple coincidence efficiencies for hydrogen and oxygen as a function of MCP voltage. These tests were done during final calibration, but they confirm measurements from the University of New Hampshire ion beam tests prior to sensor assembly.

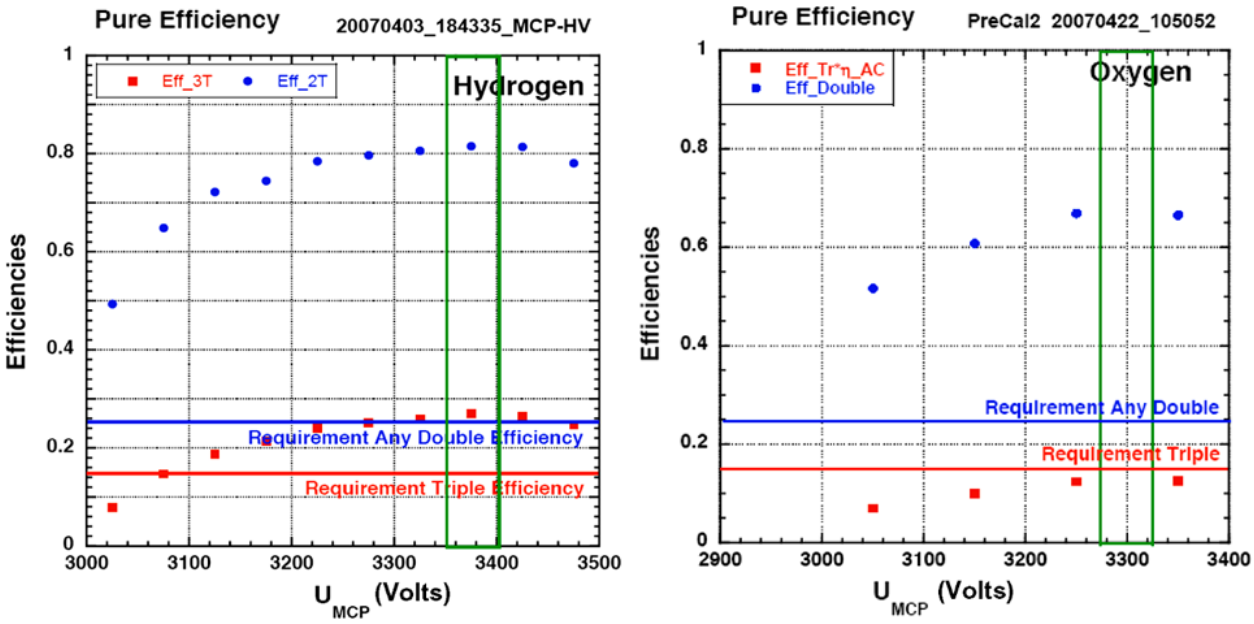

Figure 41: TOF detection efficiencies for hydrogen (left panel) and oxygen (right panel) as a function of the MCP voltage. The MCP voltage will be set so that the detector is run in saturation mode. In this mode, the double and triple coincidence efficiencies are well above the requirements

The sensor was assembled and tested in two stages. First, the ENA to ion conversion subsystem, energy analysis subsystem, and mass analysis subsystems were tested (without the entrance subsystem) using the neutral beam. These initial “pre-cal 1” tests

verified basic sensor performance in a configuration similar to the prototype tests. In particular, the calibration verified that the energy subsystem had an overall throughput of 0.4, essentially independent of energy. After these first tests, the complete sensor was tested and calibrated with the neutral beams. *Figure 42* and *Figure **43*** show the installation of the complete IBEX-Lo sensor into the calibration vacuum chamber and the sensor as installed for the final calibration tests. *Figure 42* provides a good perspective of the sensor size compared to a person. The sensor was installed in a rotation stage that was mounted on a 5-axis motion table. The rotation stage allowed tests of the azimuthal response of the sensor while the motion table was used to test the radial and radial angle response. In *Figure **43***, the neutral beam source is at the left. (The ion beam that feeds this neutralizer source is in a separate beam line that enters the chamber from the left of the picture.)

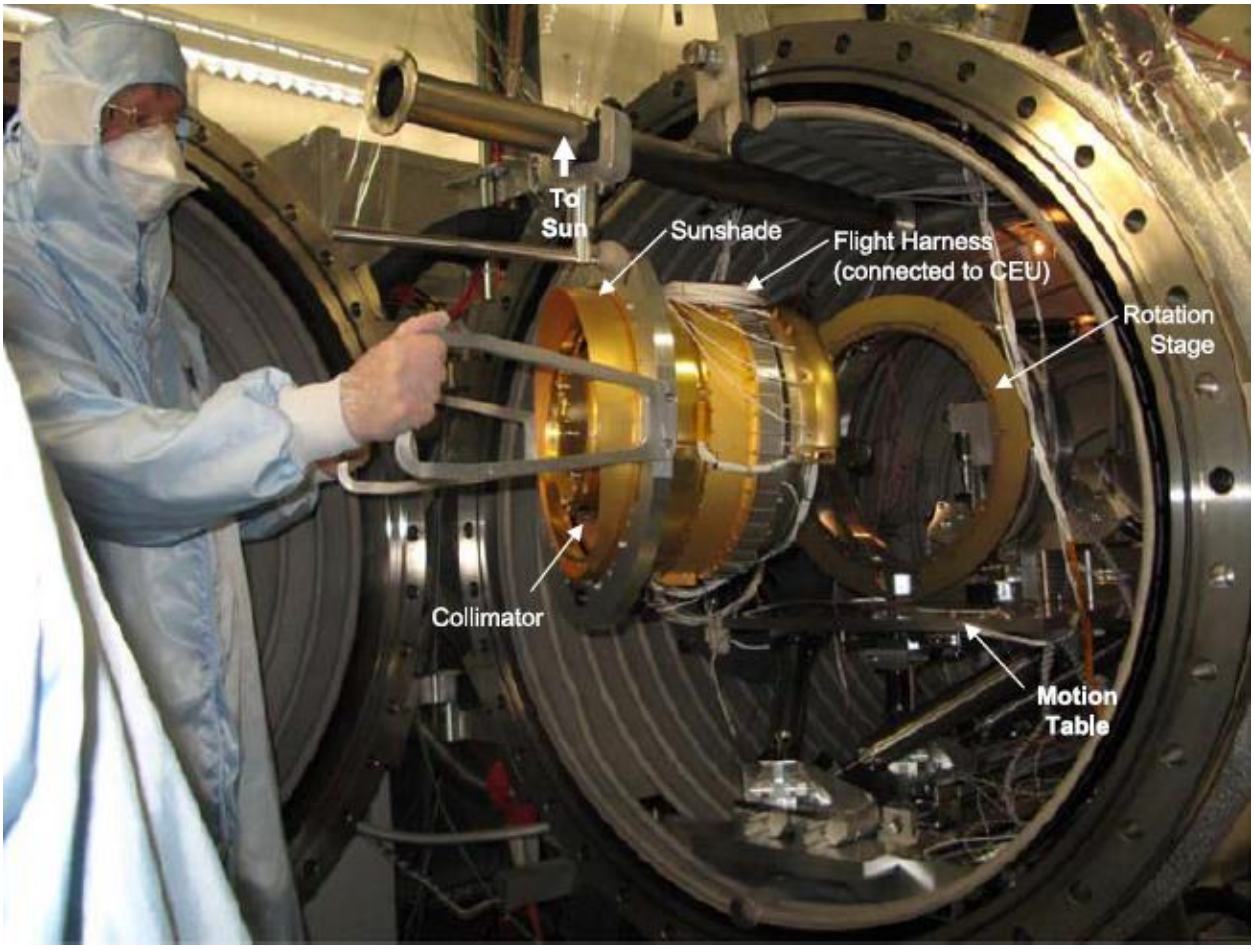

Figure 42: Installation of the IBEX sensor into the calibration vacuum chamber at the University of Bern. The sensor is installed in a rotation stage so that the neutral beam can be directed into different parts of the collimator. The rotation stage is mounted on a motion table that allows vertical and horizontal motion to investigate sensor radial and radial angle responses

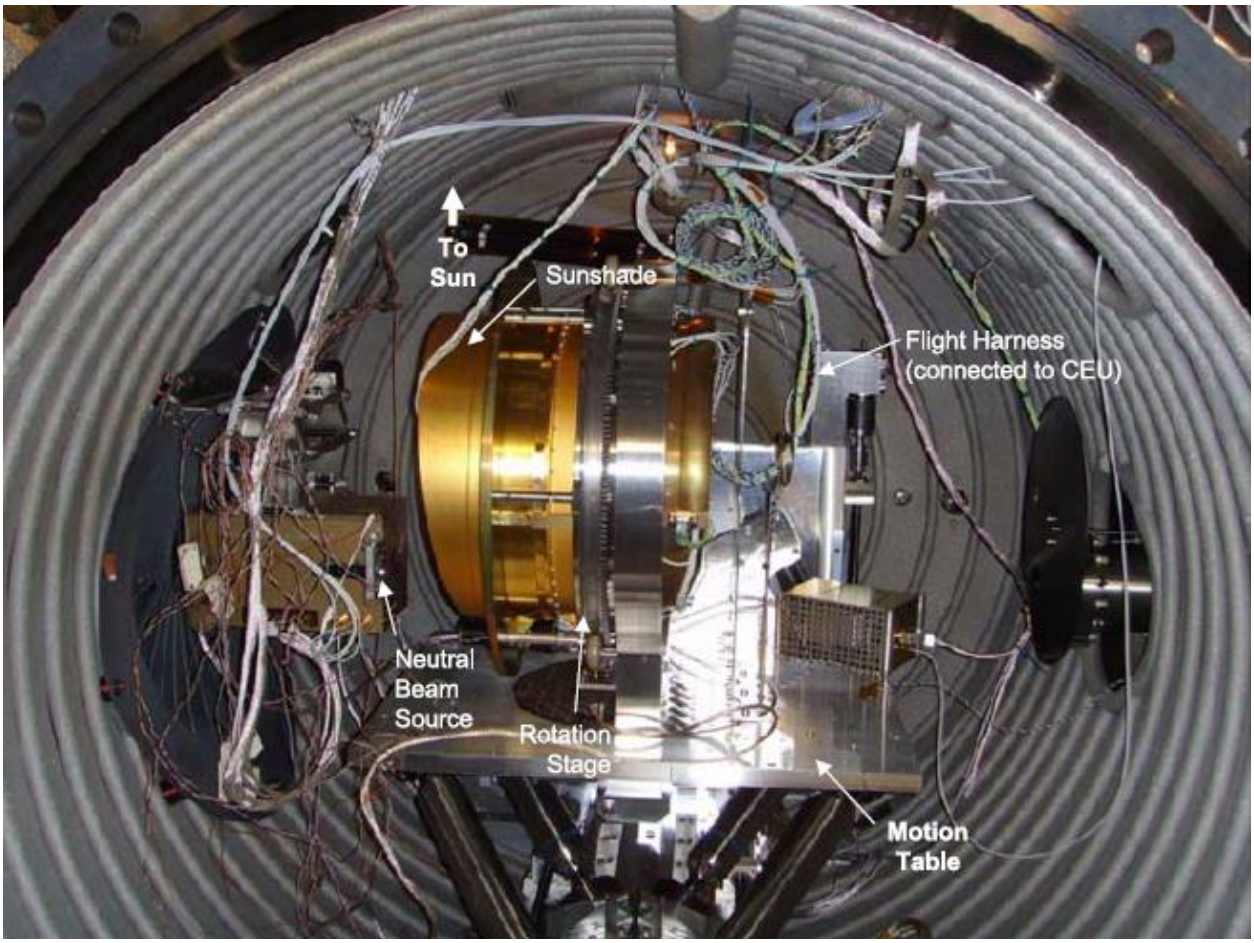

Figure 43: IBEX-Lo installed in the calibration chamber. The neutral beam is mounted on the left and directs neutrals into the lower part of the collimator

Figure 44 shows sample results from the IBEX-Lo calibration. The eight peaks in *Figure 44* correspond to the 8 energy bins of the sensor and show the energy response. These data were obtained by setting the neutral beam to the center energy of a particular energy bin and scanning the sensor energy acceptance over the beam energy. The flux measured at each sensor energy setting was normalized to the flux measured at the nominal center energy of the beam. Although some energy spread is due to the broad energy spread of the incident neutral beam, most of the energy spread in *Figure 44* is due to the broad ΔE/E of the energy analysis subsystem. These data were used to derive the ΔE/E of the sensor. The sensor ΔE/E = 0.8 and is the combined passband of the ESA alone (which is predicted to be ~ 0.67) and the extraction system of the conversion surface. This ΔE/E is constant over the energy range.

Analysis of the calibration data indicated that the peak count rate does not occur when the sensor energy step is the same as the center energy of the beam. At low energies (below several hundred eV), this discrepancy is explained by the difficulty to produce a neutral beam with energies between ten and several hundred eV in the calibration facility. At all energies, the center energy of the beam is difficult to predict because

neutrals lose energy off the tungsten neutralization surface and then lose more energy when they interact with the conversion surface in the sensor. However, measured center energies of the first 5 energy steps correspond reasonably well to the predicted energies. For the last 3 energy steps, energy loss off the IBEX-Lo conversion surface is greater than the predicted value of 15%. *Figure 45* shows the energy loss of hydrogen and oxygen off the conversion surface as a function of incident neutral energy. Since voltages on the ESA were designed to pass negative ions with 15% less than the incident neutral energy, greater loss off the conversion surface translates into a higher incident neutral energy. Thus, in *Table 7*, the center energy of energy steps 6, 7, and 8 are separated from one another and from lower energy steps by greater than a logarithmic spacing (but still without any gaps). For oxygen, energy losses off the conversion surface are even higher as are the corresponding center energies of incident oxygen neutrals. However, the science objectives of the sensor focus on detection of heliospheric hydrogen neutrals. Thus, for normal science operations, ESA voltages and corresponding energy steps are designed to produce a quasi-logarithmically spaced set of energy channels for hydrogen from 10 eV to ~ 2 keV. The energy steps for oxygen are determined from these voltages, but the voltages are set for hydrogen. For the special operations to detect interstellar neutral oxygen in October and January, the sensor energy step is fixed for the center energy of arriving oxygen neutrals. These voltages, using the calibrated higher energy loss off the conversion surface, are shown in Table 7.

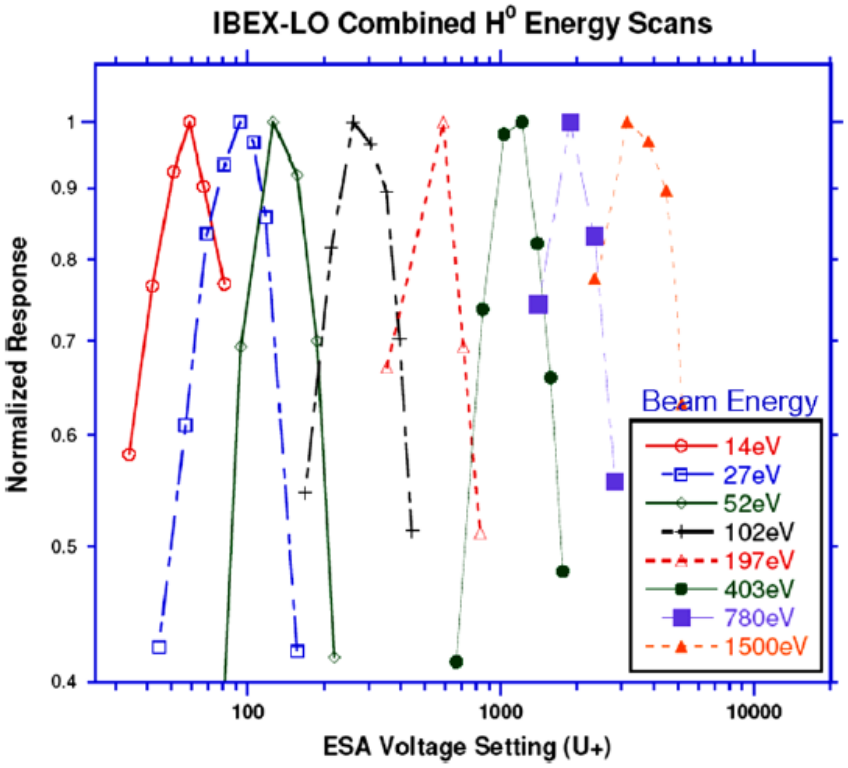

Figure 44: Measured hydrogen fluxes in each of the 8 energy bins as a function of the ESA voltage. In this test, the neutral beam energy was fixed at the values shown in the legend. Energy bins have significant overlap with a ΔE/E of 0.8

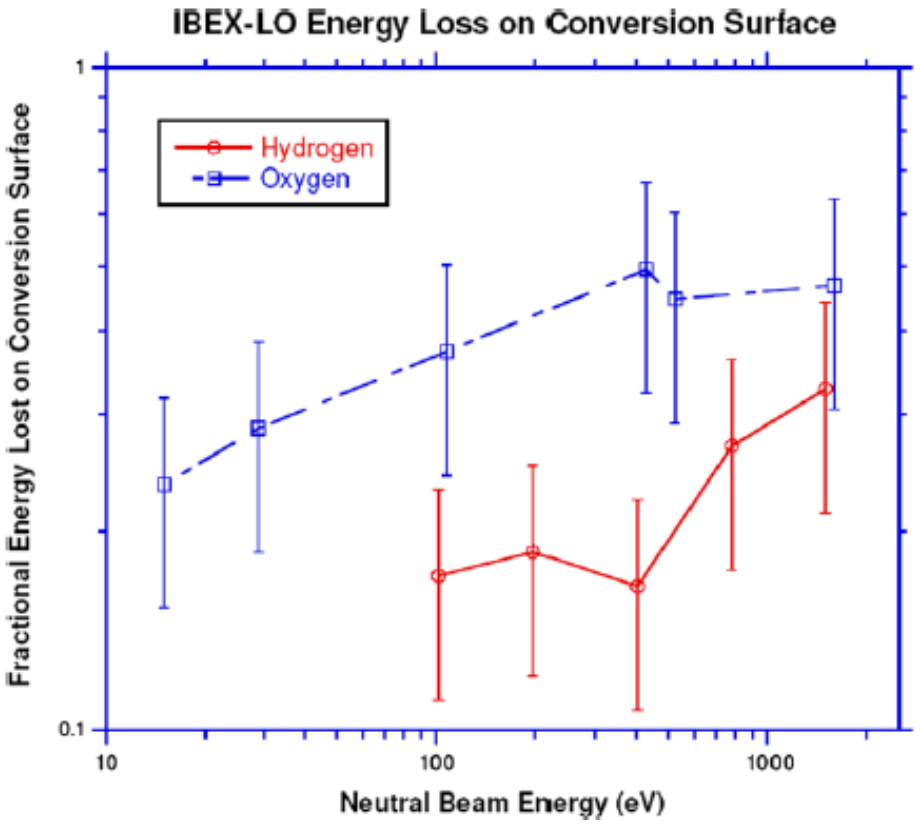

Figure 45: Negative ion energy loss as a function of neutral beam energy. Negative ions lose energy off the conversion surface and this energy loss is species and beam energy dependent. The ESA bandpasses are designed to account for this energy loss

Figure 46 shows a mass spectrum measured by the IBEX-Lo sensor. This figure illustrates important properties of low energy neutral detection using the conversion surface ionization technique. For this test, a 1.5 keV neutral helium beam was directed into the IBEX-Lo sensor. The sensor was set to detect neutrals centered at 1.5 keV, the same energy as the beam. There are several mass peaks in the spectrum. The H, C, and O mass peaks are caused by recoil sputtering of negative ions from the DLC conversion surface by the neutral helium beam. Only the mass peak identified as He is produced by true conversion of neutral helium into He^- on the conversion surface. Unlike neutrals with high electron affinity, He^- is not stable and survives only because of the relatively short flight time from the conversion surface to the TOF entrance (Wurz et al. 2008a). The ionization efficiency for helium is very low ($\sim 10^{-5}$), thus the peak is considerably lower than the recoil sputtered products. For other neutral beams with high electron affinity (i.e., neutral hydrogen or oxygen), nearly 100% of the signal observed at beam energies ~ 1 keV is true conversion to a negative ion. However, all neutrals produce sputtered products at low energies (~ 10's of eV and greater). Thus, analysis of the IBEX-Lo signal at low energies requires knowledge of the flux of high energy (~ 1 keV) neutrals on the surface so that low-energy sputtered products from these neutrals can be subtracted from the observed total flux.

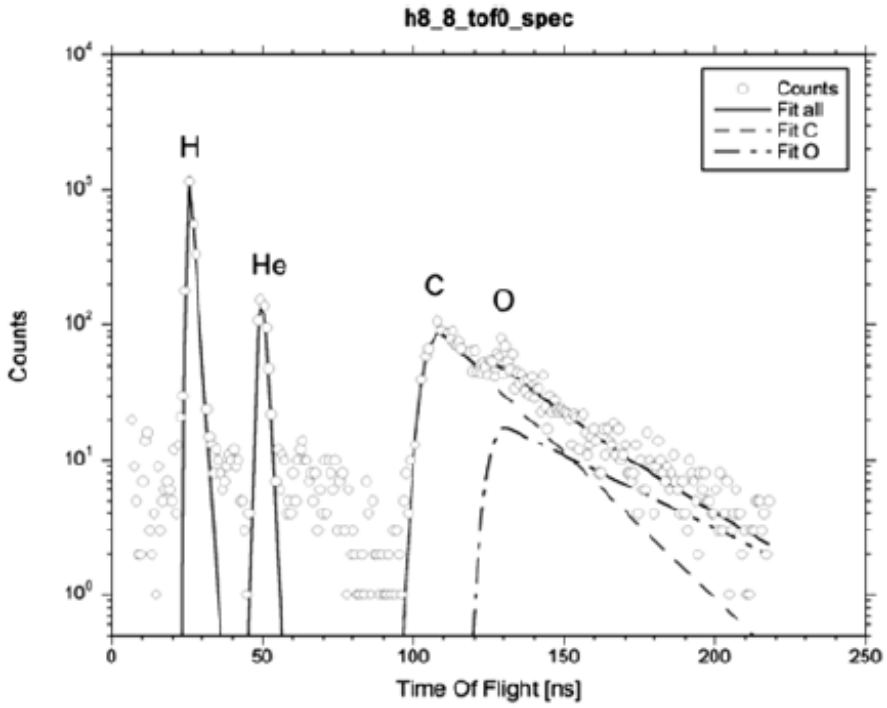

Figure 46: TOF mass spectrum from the IBEX-Lo flight sensor. A neutral helium beam was used in this test. The masses observed include helium (converted to Heat the conversion surface) and H, C, and O sputtered from the conversion surface and from the breakup of water on the conversion surface

Table 12 shows sensor geometric factors for each energy step for double and triple coincidence hydrogen. These factors were determined from the calibration and include the sensor ΔE/E, collimator solid angle FOV, all of the efficiencies of transmission through the collimator, internal grids transmission, effects of the spokes that separate each azimuthal quadrant, the energy dependent conversion efficiency, and TOF efficiencies.

Table 12: GΔE/E for the IBEX-Lo sensor, determined from calibration

Energy Step	Center Energy (eV)	$G\Delta E/E$ for any double coincidence hydrogen (cm^2 sr eV/eV)	$G\Delta E/E$ for triple coincidence hydrogen (cm^2 sr eV/eV)
1	14	7.5×10^{-5}	2.7×10^{-5}
2	27	1.5×10^{-4}	5.3×10^{-5}
3	52	2.2×10^{-4}	8.1×10^{-5}
4	102	2.5×10^{-4}	9.1×10^{-5}
5	197	2.5×10^{-4}	9.0×10^{-5}
6	451	2.9×10^{-4}	1.0×10^{-4}
7	908	5.4×10^{-4}	1.9×10^{-4}
8	1903	7.6×10^{-4}	2.7×10^{-4}

Background suppression is a critical element of the IBEX-Lo design. Suppression of any background that can masquerade as signal neutrals is particularly important because the heliospheric neutral source strength is low. In a separate paper in this volume (Wurz et al. 2009), background sources are discussed in detail. In nearly all instances, background consists of positive ions produced at or behind the collimator exit that are accelerated to high voltage by the collimator positive voltage. This background flux depends on the residual gas pressure in this part of the sensor. To reduce this gas pressure, the sensor has significant vent paths that bypass this critical region (see Figure 18), sensor electronics are vented separately from sensor optics, there are no vent paths to the spacecraft interior, and materials in the optics path were carefully chosen for their low outgassing properties. Based on expected on-orbit electron, ion, and photon fluxes that produce background, a residual gas pressure of $\sim 10^{-8}$–10^{-7} mbar is needed to keep signal to noise > 10 over the full energy range of the sensor.

Estimating residual gas pressure in the region behind the collimator is very difficult. The internal pressure depends strongly on the pumping speed of the sensor, which is determined by the ratio of interior to exterior gas pressures and the amount of pumping area available.

Because the sensor internal pressure drives most of the important background levels, this pressure was measured and compared to the pressure inside the calibration vacuum chamber. The internal pressure was measured using a nude ion gauge installed in the access port at the bottom center of the sensor (see Figure 18). Because this location is deep inside the sensor, the pressure in this region is probably higher there than in the region just in back of the collimator. *Table **13*** shows results of this pressure test. The pressure was measured as the vacuum chamber pressure was decreasing by over an order of magnitude over a few hours. The internal to external pressure ratio is only a factor of ~ 2, presumably because of the extensive measures used to vent the sensor. It is doubtful that this internal to external pressure ratio will remain a factor of two over many more orders of magnitude in pressure. However, these results are encouraging for on-orbit performance, where external pressures are expected to be 10^{-10}–10^{-14} mbar. With these low pressures, the pressure in the critical region behind the collimator is likely to be $<<10^{-8}$ mbar and the background will be correspondingly low.

Table 13: Internal sensor and external vacuum chamber pressures measured during the IBEX-Lo calibration

External (vacuum chamber) pressure (mbar)	Internal (sensor) pressure (mbar)	Ratio internal/external pressure
1.2×10^{-6}	2.5×10^{-6}	2.1
6.0×10^{-7}	1.4×10^{-7}	2.3
1.6×10^{-7}	3.8×10^{-7}	2.4

4.3 In-flight Tracking of Short-Term Changes

This section details periodic operation tests which are used to evaluate the calibration of the instrument over time and to mitigate factors that could result in off-nominal changes to the instruments measurements (such as changes in the radiation environment affecting background levels, degradation of detector components etc.). Some of the tests described are run periodically while others will only be repeated in the event that they are needed (i.e., in response to unexpected changes in instrument response).

4.3.1 IBEX-Hi Background Tests

Penetrating radiation is the primary source of background for IBEX-Hi and background tests are used to infer the amount of background present in the signal (for more details on the background correction applied to IBEX-Hi measurements, see Section 5.3.4). Critical for determining the background levels in IBEX-Hi is determining the ratio of qualified triple coincidence events to unqualified triple coincidence events. Triple coincidence events are defined as events which produces valid triggers in all three channel electron multipliers (CEMs). A qualified triple coincidence event is defined as a triple coincidence event in which electrons are not detected in CEM C—that is to say, the back of the detector— until at least 3 ns after they are first detected in CEM A or B, which are located at the front of the detector, indicating the measurement of a particle that has been ionized on the entrance conversion foil and transited the ESA. In other words, qualified events indicate the measurement of a particle that has been measured according to the measurement concept of the instrument and thus we can determine its energy, etc. Unqualified events do not meet this criteria and are thus indicative of CEM triggers caused by penetrating radiation that penetrates the instrument without passing properly through the ESA.

As detailed in Section 5.3.4, the IBEX-Hi background correction involves using the ratio of qualified to unqualified events. Calculation of this ratio while the instrument is operating in its nominal configuration requires us to know what the ratio is when only background is present. This requires the instrument to be configured in such a way that the ESA rejects particles from passing through it, such that only background is measured by the CEMs.

The ESA settings used during background tests are shown in Table 14. We see that these settings are identical to the nominal ESA settings shown in Table 10, except for the first energy step, which is configured to prevent particles from passing through the ESA. Operating IBEX-Hi in a way that rejects ENA signals allows us both to check this ratio and directly monitor how well our inferred background subtraction rates track actual background.

Background tests are typically run quarterly (4 times per year). This is because quarter-year maps are produced by IBEX-Hi in near-real-time. Otherwise, yearly background

tests would be sufficient for background analysis. One orbit of data taken in this mode provides sufficient statistics to determine the background ratio.

Table 14: ESA voltage settings for background tests

Energy Step	Outer (V)	Inner (V)
0	-45	0
2	-80	-1280
3	-20	-1850
4	0	-2880
5	0	-4460
6	0	-7000

4.3.2 IBEX-Hi CEM Gain Tests

The CEMs within the IBEX-Hi instruments can age over time resulting in degraded performance. In the event of such degradation of the CEMs, their operating voltage would have to be increased in order to maintain the same detector efficiency. The CEM gain test looks at detector response vs operating voltage to determine if the detector is operating in a range where its detection efficiency is at most a weak function of operating voltage.

CEM gain tests are usually run in the solar wind, half a year apart, with the option to add a third test in a year if one of the tests ends up taking place under conditions not amenable to useful analysis (e.g., with rapidly varying backgrounds). CEM tests are run via script-generated STF and take about 4 hours to run. They involve numerous transitions between HVSCI and HVENG.

4.3.3 IBEX-Hi Threshold Tests

IBEX-Hi threshold tests are a processing chain — specifically, if the discriminator thresholds are set correctly. Threshold tests are run infrequently, every few years, unless there is a reason to suspect something has changed. It runs by script-generated STF with the detector voltages low enough not to register valid counts (i.e., in LVENG or perigee HVSTANDBY) and does not affect HVSCI intervals.

4.3.4 IBEX-Hi Negative Collimator Tests

Negative collimator tests were performed around orbits 150-200 to determine the optimal value to run the negative collimator, and there are no plans to run any more tests of this sort. These tests were performed in order to strike a balance between the "ion gun" signal from electrons that are able to enter the instrument if the negative collimator is turned too far down and the deflection of solar wind particles into the instrument from the negative collimator's potential if the voltage is set too high. These tests varied the voltage on the negative collimator in order to determine the optimal setting to minimize overall background from these two sources.

4.3.5 IBEX-Lo Background Tests

Since background subtraction is not used for IBEX-Lo, but rather the primary method of background removal is culling of high-background periods using goodtimes lists, IBEX-Lo background tests are not regularly run, but have only been used once early in the mission in 2010 and again later in the mission in 2020, in order to understand the backgrounds measured by the instrument.

These tests are run by “detuning” the IBEX-Lo ESA to prevent particles from entering into the detector in the usual way through the front of the detector and thus all measurements made while the instrument is in this state can be considered as background. During these periods, the data is analyzed to look for background caused by electronics, penetrating radiation or by so-called “dark counts” which can be stimulated by high electric fields (e.g. such signals can be seen if the MCP voltage is set too high). Table 15 shows the ESA settings for IBEX-Lo background tests (note that the U_POS value is the nominal ESA 1 voltage and the U_NEG value is the nominal ESA 8 voltage).

Table 15: ESA settings for IBEX-Lo background tests. Note that the U_POS value is the nominal ESA 1 voltage and the U_NEG value is the nominal ESA 8 voltage.

Energy Step	U_POS (V)	U_NEG (V)
1	42.04	-1795
2	42.04	-1795
3	42.04	-1795
4	42.04	-1795
5	42.04	-1795
6	42.04	-1795
7	42.04	-1795
8	42.04	-1795

4.3.6 IBEX-Lo MCP Gain Tests

MCP gain tests are run roughly on a yearly basis to evaluate the efficiency of the IBEX-Lo MCPs and determine if the voltage on them needs to be increased in order to compensate for any changes. The efficiency of the MCPs can decrease in response to high particle fluxes which can cause the loss of water in the MCPs and thereby reduce their sensitivity.

The MCP gain tests consist of varying the voltage on the MCPs and analyzing the response of the instrument. The resulting gain curve showing instrument response versus MCP voltage is used to determine if the nominal detector voltage is located in a “plateau” region of the gain curve (called saturation, i.e. increasing the voltage does not increase the measured counts). There is a balance to this as we do not want to increase the MCP voltage to high as this could risk a discharge which would likely damage the MCP.

At this point, 13 years into the IBEX mission, 16 IBEX-Lo MCP gain tests have been run. Thus far, no degradation of the MCPs has been detected by these tests and thus the voltage on the MCPs has not needed to be changed. These tests continue to be performed on a yearly basis in case the MCP efficiency changes and adjustments are needed to compensate.

4.4 Validation

This section describes methods of validating the measurements made by IBEX-Hi and IBEX-Lo.

4.4.1 Cross-Calibration between IBEX-Hi and IBEX-Lo

One important means of validation for IBEX is in-flight cross calibration between the IBEX-Hi and IBEX-Lo instrument. Since Hi and Lo provide independent measurements of ENAs in an overlapping energy region, these data can be used to evaluate the consistency of the two instruments with one another, which lends credibility to their observations. It is important to show that both instruments pick out similar features in their ENA maps and also that their combined spectra are consistent both with each other and with physical expectations of such spectra.

This section provides two examples of in-flight cross-calibration of the Hi and Lo instruments. The first effort was made about a year after the launch of IBEX and showed that both instruments show similar features in their global ENA maps, such as the famous IBEX ribbon, as well as demonstrating the consistency of their respective spectra. The second study was from about five years after the launch of IBEX and goes into greater detail on the spectral comparison between Hi and Lo.

4.4.1.1 Comparison of Hi and Lo Global ENA Maps and Spectra

The IBEX all-sky maps (Figure 47) show that ENA fluxes vary over the ribbon, with maxima 2-3 times brighter than the surrounding regions. The ribbon is variable in width from <15º to >25º FWHM (11), contains fine structure (Figure 47B), and passes ~25º away from the heliospheric nose. The ribbon has brighter emissions from somewhat broader regions Confidential Page 5 9/30/2009 at higher latitudes in both hemispheres (~60º N and ~40º S) with the former having a different spectral shape than the rest of the ribbon (12). While not optimally shown in these projections, the ribbon weakens, but also extends back behind the northern pole, nearly closing a loop on the sky (12).

IBEX-Lo observations independently confirm the ribbon in the overlapping energy range (Figure 47H) and extend them down to ~200 eV (Figure 47G). The ribbon is observed from there up to >6keV, the top of the IBEX-Hi energy range (Figure 47F), with the highest relative intensity at ~1 keV (11). Additional observations from Cassini/INCA (13) indicate that some portions of the ribbon may extend to even higher energies. Finally, although observations of the ribbon collected six months apart (~0º, ~180º ecliptic longitudes) indicate that it remained a largely stable structure, these observations also suggest the possibility of some temporal evolution.

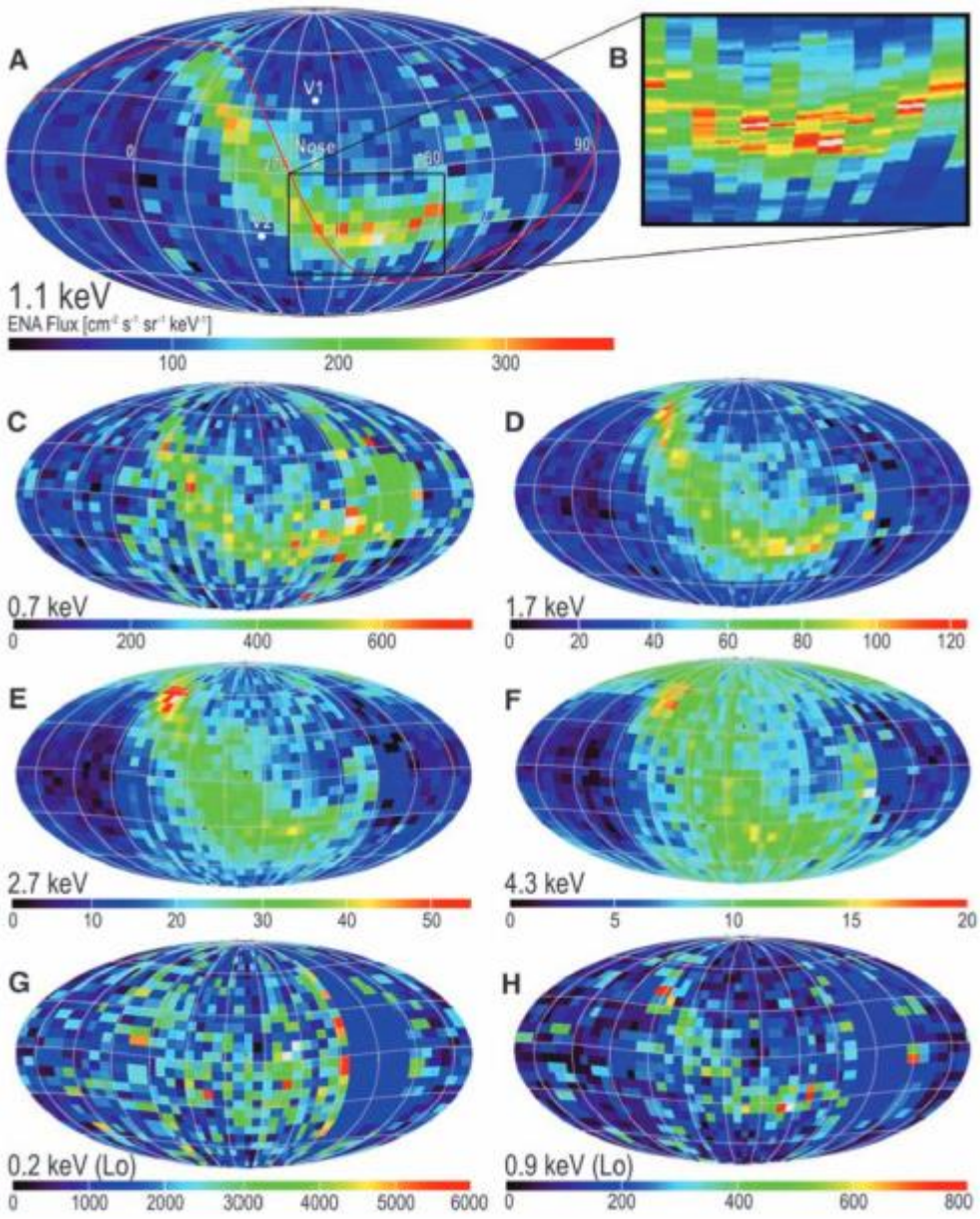

Figure 47: IBEX all-sky maps of measured ENA fluxes in Mollweide projections in ecliptic coordinates (J2000), where the heliospheric nose is near the middle and the tail extends along both sides. The pixels are 6º in spin phase (latitude) with widths (longitude) determined by the spacecraft pointing for different orbits. Maps are shown in the spacecraft frame for passband central energies from IBEX-Hi of (A) 1.1 keV, (C) 0.7 keV, (D) 1.7 keV, (E) 2.7 keV, (F) 4.3 keV, and from IBEX-Lo of (G) 0.2 keV and (H) 0.9 keV. Panel (A) includes the galactic plane (red curve), which clearly does not coincide with the ribbon, and directions toward Voyager 1 (V1; 35º, 255º), Voyager 2 (V2; -32º, 289º), and the Nose (5º, 255º). Inset (B) magnifies a section of the ribbon where each 0.5º in spin phase is averaged with nearest neighbors to reach 100 counts (10 counts standard deviation). Because of contamination of ENAs from Earth's magnetosphere, a small region on the right side of each map was not sampled in the first six months of

data; these regions have been filled in with average values from the adjacent areas and appear unpixelated.

The power law spectral slopes of the ENA flux (κ) display significant, broad variations across the sky (Figure 48) that are ordered by ecliptic latitude and longitude (i.e., the interstellar flow direction). These observations are generally consistent with the concept that ENAs are produced from TS-heated, non-thermal plasma throughout the inner heliosheath. The spectrum is flatter (lower κ) near the poles compared to the equator; this might be caused by the faster solar wind at higher latitudes, which generates and entrains significantly higher-energy PUIs than near the ecliptic. The spectra toward the tail are Confidential Page 8 9/30/2009 significantly steeper (κ>2) than near the nose (κ~1.5), possibly owing to longer line-of sight (LOS) integrations of low-energy ions toward the tail. Remarkably, the ribbon is barely visible in this spectral slope map, even though the fluxes are several times higher.

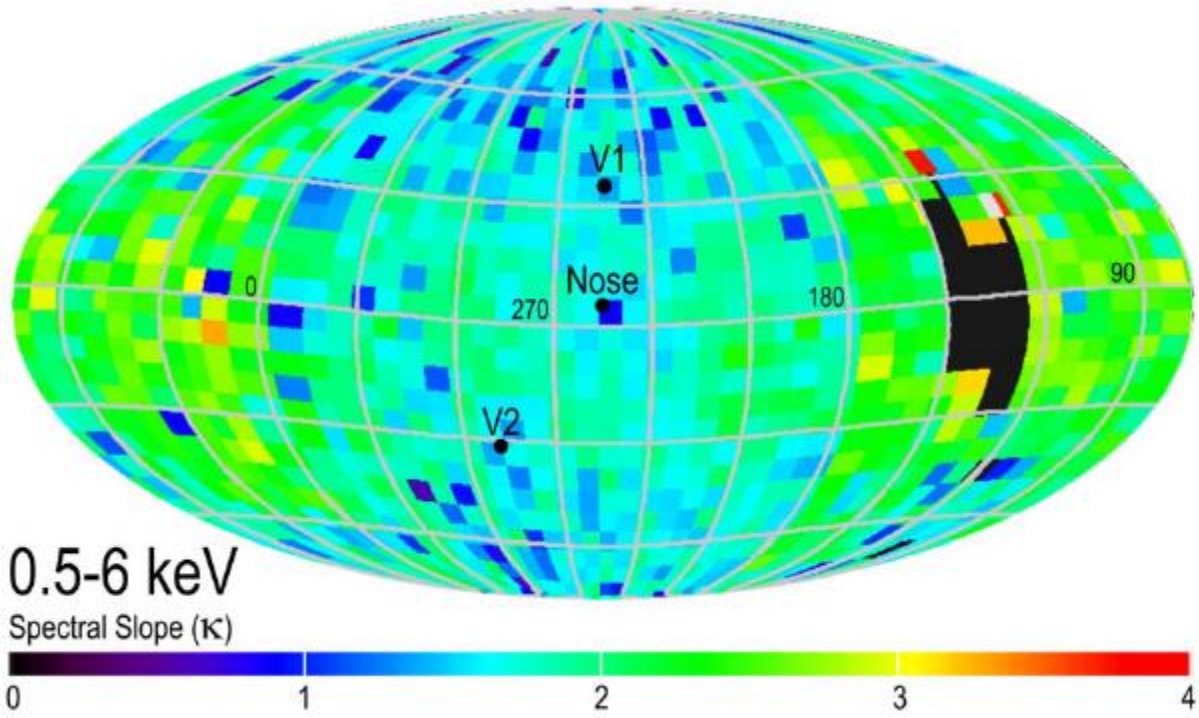

Figure 48: Sky map in ecliptic coordinates of the average power law spectral slope (κ) from ~0.5-6 keV using IBEX-Hi channels 2-6. The measurements were transformed into the rest frame of the Sun; unlike Fig. 1, the unsampled region is left black in this image. While statistical uncertainty remains significant in individual 6º pixels, global variations are clearly evident.

As an example of the detailed spectral information provided by IBEX, Figure 49 shows the ENA energy spectra along LOSs toward the two Voyager spacecraft. These spectra

are Confidential Page 9 9/30/2009 nearly straight power laws with slopes of ~1.5 (V1) and ~1.6 (V2). Globally, spectra generally show simple power laws near the equator with significant enhancements at several keV at higher latitudes (12), again consistent with higher-energy PUIs in the high155 latitude, fast solar wind. IBEX observations are consistent with upper bounds on ENA flux based on Ly-α absorption (14). Claims of heliospheric ENA measurements from ASPERA-3 (15) are inconsistent with IBEX observations.

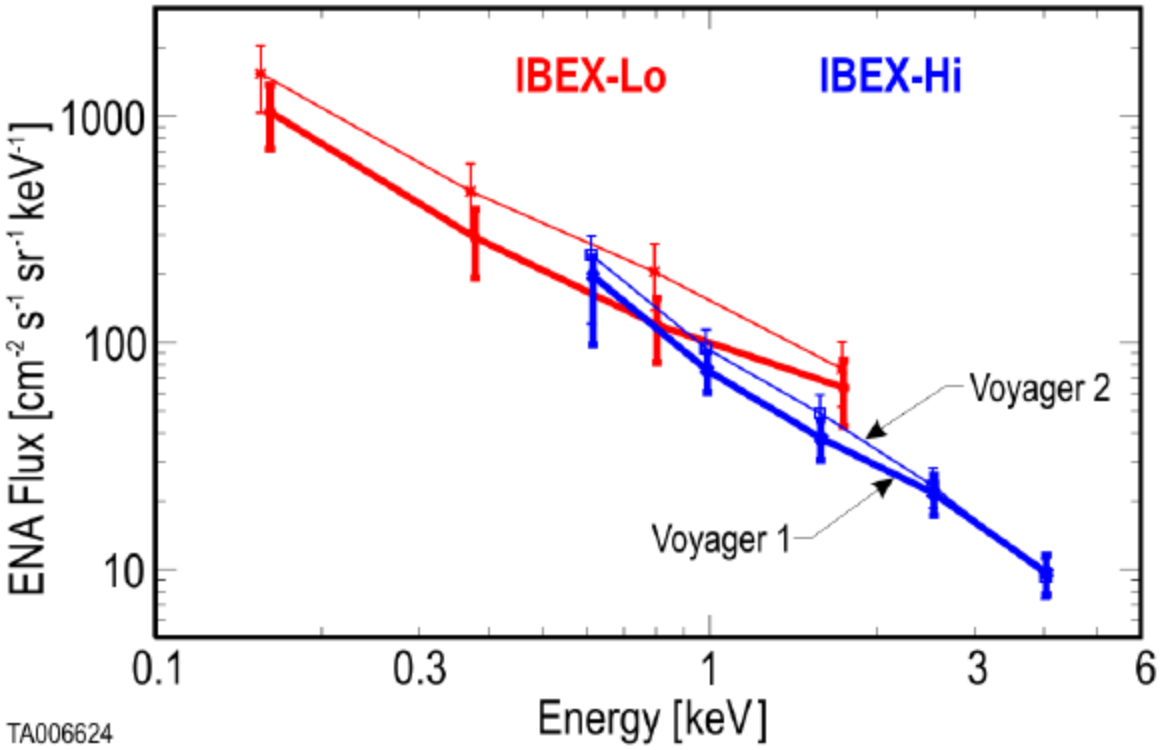

Figure 49: Energy spectra for 20ºx20º regions centered on the V1 (thick lines) and V2 (thin lies) directions. Pre-launch cross-calibration of the IBEX-Lo (red) and –Hi (blue) sensors simultaneously in a single chamber produces quantitative matching between the Confidential Page 10 9/30/2009 spectra. Error bars show counting statistics plus likely systematic errors of +/-20% for IBEX Hi and +/-30% for IBEX-Lo.

4.4.1.2 Combined Spectra from Hi and Lo

Figure 50 shows IBEX-Hi sky map 6 (combining data from orbits 130b to 150a, from 2011 June 21 to December 29) at 1.11 keV. The sky map is a Mollweide projection nearly in ecliptic coordinates (the center of the projection is the new nose direction, which is at approximately 259° (–95°) ecliptic longitude and approximately +5◦ ecliptic latitude (Mobius et al. 2012; McComas et al. 2012a)). Fluxes are in the spacecraft frame at the center passband of IBEX-Hi energy channel 3 (1.11 keV). Most of the measurements for this sky map were made as the spacecraft orbit processed through Earth's magnetotail. All data were culled and corrected for several backgrounds,

including the variable cosmic ray intensity (McComas et al. 2012b). No reference frame corrections have been applied to this sky map, and the fluxes are shown at 1AU (i.e., without correction for survival against reionization as the neutral atoms propagate from ~100 to 1 AU).

Section 5.4.5 provides a detailed discussion of data selection when the spacecraft is in Earth's magnetotail. Data intervals must be selected carefully to avoid regions with high magnetospheric backgrounds and must be selected for specific solar wind conditions that provide favorable magnetotail geometry and plasma conditions. Furthermore, only specific viewing directions of the heliosphere are available for these conditions. Section 5.4.5 identifies two viewing directions or pixels in the sky that meet these stringent criteria. These pixels are shown by the orange rectangles in Figure 50, and they are larger than the 6° × 6° pixels in the sky map. The centers of these pixels are near to the direction to the Voyager 1 spacecraft (labeled "V1" at ecliptic latitude +36°, ecliptic longitude, −115°) and the direction near the downstream (at a longitude opposite the nose) at southern midlatitudes (labeled "downstream" at latitude −42°, longitude +71°).

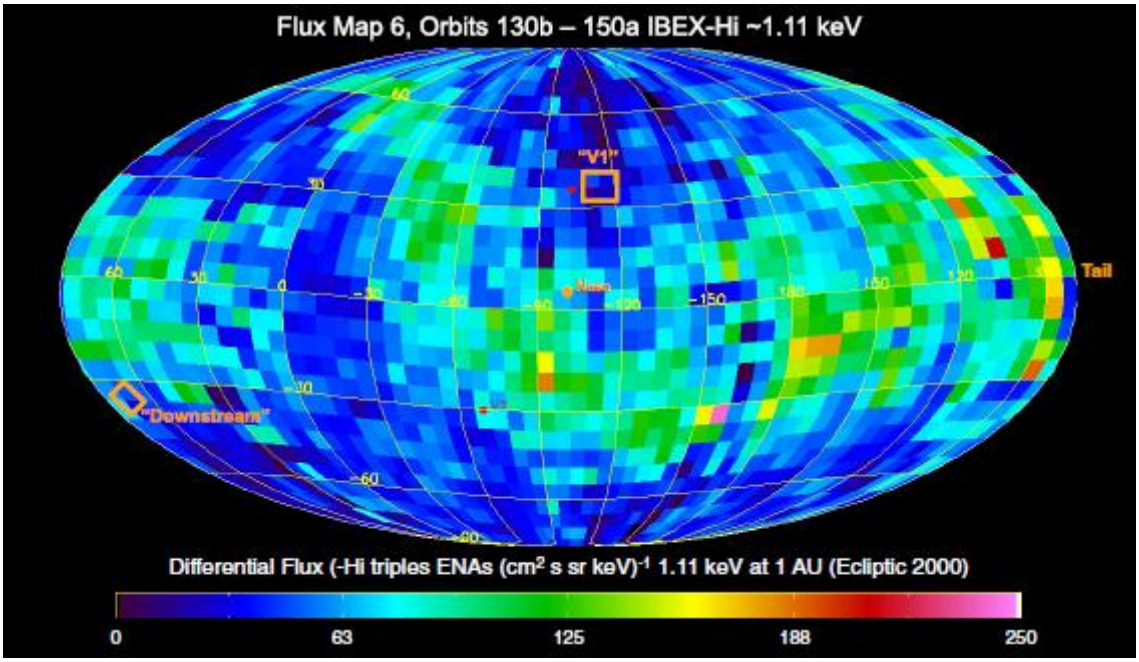

Figure 50: IBEX-Hi sky map 6 (Mollweide projection) at 1.11 keV. The center of the map is the direction of the Sun's motion relative to the local interstellar cloud. The IBEX Ribbon wraps around this direction from high northern latitude in the upper left to southern latitudes in the middle of the map. Two directions or pixels in the sky (orange rectangles) are selected for study. They are centered approximately in the direction of Voyager 1, labeled "V1" and at midlatitudes nearly opposite the nose direction, labeled "Downstream."

Figure 51 shows the ENA energy spectrum in the inertial frame from the V1 pixel and the downstream pixel. In Figure 51 (A), solid lines and filled symbols show fluxes measured when IBEX was in Earth's magnetospheric lobes in 2011 August, while dashed lines connecting open symbols show fluxes measured when IBEX was in the solar wind in 2010 February. Red circles show IBEX-Hi fluxes, and black squares show IBEX-Lo fluxes. Error bars show the larger of either statistical errors or 50% (30%) absolute flux uncertainties for IBEX-Lo at energies greater than (less than) 0.1 keV and 20% absolute flux uncertainties for IBEX-Hi at all energies. For IBEX-Lo, these absolute uncertainties are estimated from the absolute flux uncertainty of the neutral beam used to calibrate the sensor in the laboratory. The absolute flux uncertainty of the low-energy beam that was used is poorly known, and its dependence on energy is likely more complex than assumed here. Therefore, conservative values are used here, consistent with those used previously (Fuselier et al. 2010, 2012). There is an additional, systematic error associated with the frame transformation because the IBEX sensor energy channels are very wide (FWHM, $\Delta E/E \sim 0.7$). Because the error in the approximately Gaussian shaped energy channels is $\Delta E/E/2.354$ (Bevington & Robinson 2003), the resulting uncertainty in the ENA flux is much smaller than the 20%–50% absolute uncertainties. Only five IBEX-Hi energy channels are shown because there is background contamination in the lowest energy channel (Wurz et al. 2009; Fuselier et al. 2012). This background appears to depend on the ambient electron spectrum and is present when IBEX makes measurements both in the solar wind and in the magnetotail.

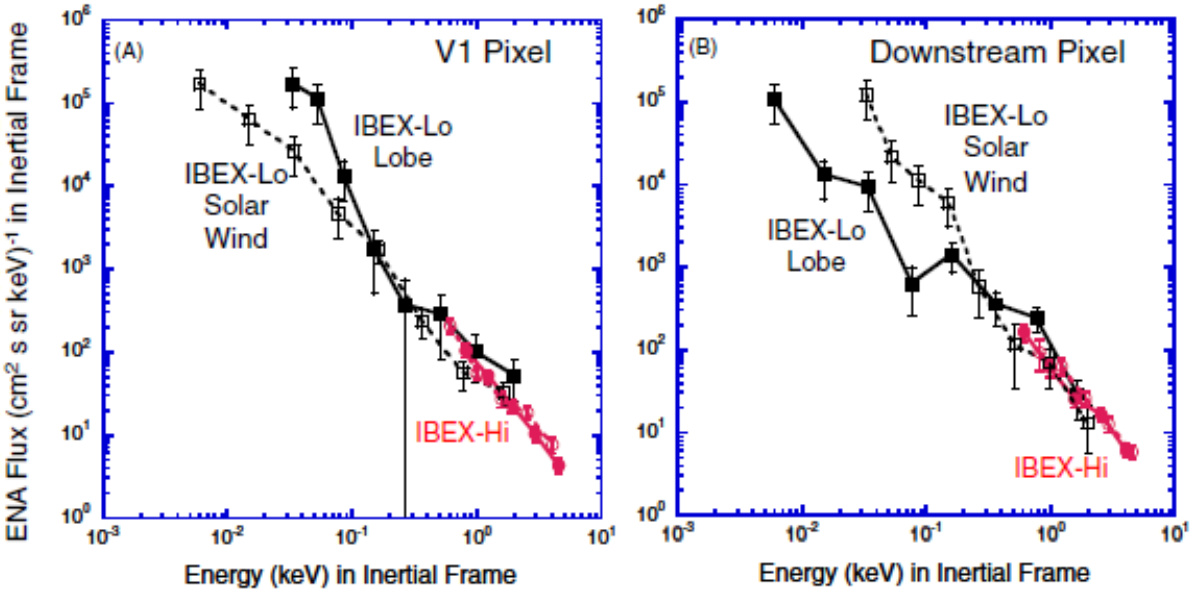

Figure 51: ENA differential energy flux vs. energy in the inertial frame from the V1 pixel (A) and the downstream pixel (B), as indicated in Figure 50. In both pixels, IBEX-Hi and -Lo fluxes agree well at overlapping energies. At fluxes above about 0.1 keV for the V1 pixel and above 0.13 keV for the downstream pixel, the fluxes measured when IBEX was in the solar wind agree well with the fluxes measured when IBEX was in the lobe/magnetotail. Below these energies, the fluxes diverge, indicating that there is a

background in one or both near-Earth locations that is higher than the heliospheric signal.

It is convenient to split up the spectra in Figure 51 into four energy ranges. From lowest to highest these ranges are: less than about 0.1 keV, about 0.1–0.5 keV, 0.5–2 keV, and greater than 2 keV. In these four energy ranges, different tests are applied to identify the heliospheric signal and to understand the nature of the background. In addition, an important assumption (which will be discussed later in Section 4.4.1.2.1) is used to understand the nature of the background in the lowest energy range.

In Figure 51(A), at energies greater than 2 keV, the energy ranges of the two sensors do not overlap. However, IBEX-Hi fluxes measured when the spacecraft was in the lobe and in the solar wind agree very well with each other after the frame transformation. Since absolute flux uncertainties are small, the good agreement in the fluxes after the frame transformation indicates that the heliospheric signal is larger than any local background moving with the spacecraft or the Earth.

At energies between 0.5 and 2 keV, the energy ranges of the two sensors overlap. In this energy range, the IBEX-Lo flux and IBEX-Hi fluxes are in good agreement with one another (certainly within the uncertainties of the measurements). The fluxes measured when the spacecraft was in the lobe and solar wind also agree reasonably well with one another. Similar fluxes in this inter- and intra-instrument comparison are the strongest evidence that the heliospheric ENA signal is larger than any local background in this energy range. As discussed in the introduction, the sensors are susceptible to different local backgrounds and have different measurement techniques, but they were cross-calibrated in the laboratory. Although a background that results in accidental agreement between two sets of flux measurements from the two different sensors (four independent measurements) is possible, it is not likely.

At energies between about 0.1 and 0.5 keV in Figure 51(A), the energy ranges of the two sensors no longer overlap. However, similar to the comparison of IBEX-Hi fluxes at energies greater than 2 keV, IBEX-Lo fluxes at energies between about 0.1 and 0.5 keV agree with each another. This agreement is a good indication that the heliospheric fluxes are larger than any local background. Because of the larger uncertainties at these lower energies (compared with the uncertainties at energies greater than 2 keV), the fluxes could still agree if there was a local background that was up to about half of the total flux.

At energies less than 0.1 keV, IBEX-Lo fluxes from the lobe and solar wind diverge. This divergence indicates that background is larger than the heliospheric signal in one or both of the near-Earth regions where IBEX is making measurements. The nature of this background is revealed in the analysis in Section 4.4.1.2.1.

Figure 51(B) shows the ENA energy spectrum in the inertial frame from the downstream pixel. The format is the same as that for Figure 51(A). The agreement between fluxes in the energy ranges from about 0.1 to 0.5 keV, 0.5 to 2 keV, and greater than 2 keV is also similar to that in Figure 51(A). Thus, the same interpretation applies to the downstream pixel as the V1 pixel. Namely, at energies above about 0.1 keV, the heliospheric signal is larger than the local background. In Figure 51(B), the deviation in the IBEX-Lo fluxes measured when the spacecraft was in the lobe and in the solar wind occurs at a higher energy than in Figure 51(A). This difference is interpreted in the next section as an indication of the background level at energies between 0.1 and 0.5 keV.

4.4.1.2.1 Characteristics of Backgrounds in the IBEX-Lo Measurements at Energies Less than 0.5 keV

As indicated in Figure 51(A), IBEX-Lo fluxes agree at energies between 0.1 and 0.5 keV, but they diverge below 0.1 keV. In Figure 51(B), IBEX-Lo fluxes agree at energies between 0.2 and 0.5 keV, but they diverge below 0.2 keV. Fluxes at and below 0.1 keV are measured in the first four energy channels of IBEX-Lo, with center energies (in the spacecraft frame) of 0.015, 0.029, 0.055, and 0.11 keV, respectively. The flux divergence in Figure 51(A) and Figure 51(B) is indicative of a background in one or both near-Earth regions where IBEX makes measurements. It is most likely that the source or sources of this background are local: (1) neutrals or negative ions generated by some internal process inside the IBEX-Lo sensor, (2) neutrals generated in the near- Earth environment traveling with the Earth or the spacecraft, or (3) neutrals or negative ions generated inside the IBEX-Lo sensor by an external ion or neutral source. By comparing fluxes in the spacecraft frame (i.e., the frame moving with the Earth), possible origins of the background are distinguishable. If background is generated internally in the sensor independent of external conditions, then fluxes measured while IBEX was in the magnetospheric lobe and in the solar wind upstream of Earth’s bow shock should agree. If there is an external, near-Earth origin of the background, then fluxes from the two near-Earth regions should not agree.

Figure 52(A) shows fluxes measured in the spacecraft frame for the first four energy channels for IBEX-Lo and the five energy channels for IBEX-Hi from the V1 pixel. Figure 52(B) shows these fluxes transformed into the inertial frame. The format for the panels in Figure 52 is the same as that for the panels in Figure 51 and Figure 52(B) simply reproduces part of the energy spectrum shown in full in Figure 51(A). IBEX-Lo fluxes for the four energy channels between 0.2 and 2 keV have been removed for clarity.

As shown in Figure 52(A), fluxes in the spacecraft frame do not agree with one another. Fluxes measured when IBEX was in the magnetospheric lobe are consistently lower than those measured when IBEX was in the solar wind upstream of Earth’s bow shock. Higher fluxes are expected when IBEX was in the solar wind because, at the time, the spacecraft was moving toward the ENAs coming from the V1 pixel. Conversely, lower fluxes are expected when IBEX was in the magnetospheric lobe because, at the time,

the spacecraft was moving away from the ENAs from the V1 pixel. In the transformation from the spacecraft frame to the inertial frame, the ENA flux and energy measured when IBEX was in the solar wind decrease. Similarly, in this transformation, the ENA flux and energy measured when IBEX was in the lobe increase.

For IBEX-Hi, the frame-transformed fluxes in Figure 52(B) agree with one another. However, for IBEX-Lo, the transformed fluxes do not agree, and there is a switch from Figure 52(A) to Figure 52(B) such that in Figure 52(B), fluxes measured when the space craft was the solar wind are now lower than those measured when the spacecraft was in the lobe. This switch indicates that there is a background present that is created by a local source (either neutral or non-neutral) moving with the Earth (or with the spacecraft).

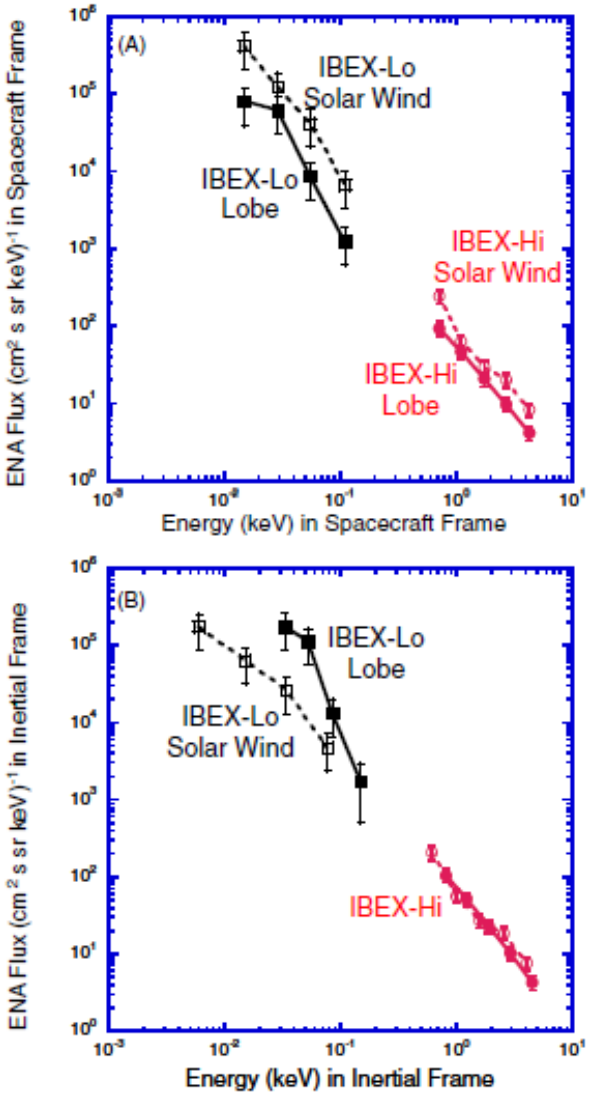

Figure 52: IBEX-Hi and IBEX-Lo (first four energy channels) ENA fluxes from the V1 pixel in the spacecraft frame (A) and in the inertial frame (B). When IBEX was in the solar wind, it measured higher fluxes than when it was in the lobe because the spacecraft was moving in the ENA flow direction when in the solar wind and opposite

the ENA flow direction in the lobe. When transformed into the inertial frame, the IBEX-Hi fluxes agree, while the IBEX-Lo fluxes for the first four energy channels are overcorrected and disagree.

When IBEX was in solar wind and viewing the V1 direction, the first four energy channels are known to contain a sputtered signal primarily from interstellar neutral (ISN) helium (Mobius et al. 2009; Saul et al. 2012; Fuselier et al. 2012). ISN helium sputters low energy negative hydrogen ions from the IBEX-Lo conversion surface. Since these sputtered negative ions do not retain the energy of the incident (helium) neutral, they are created internally in the sensor, and their fluxes should not be transformed from the spacecraft frame. Again, after frame transformation, Figure 5(B) shows that IBEX-Lo fluxes measured when the spacecraft was in the lobe (when no ISN source for sputtered negative ions is present) are higher than fluxes measured when IBEX was in the solar wind. Thus, even in the lobe, there is a background source that is moving with the Earth or the spacecraft that is higher than the heliospheric signal at energies below 0.1 keV.

Figure 53(A) shows ENA fluxes measured in the spacecraft frame for the first four energy channels of IBEX-Lo and the five energy channels of IBEX-Hi from the downstream pixel. Figure 53(B) shows the fluxes in the inertial frame. The format is the same as that for Figure 52.

Similar to Figure 52(A), the ENA fluxes in Figure 53(A) in the spacecraft frame do not agree with one another. However, in Figure 53(A), fluxes measured when IBEX was in the magnetospheric lobe are mostly higher than those measured when IBEX was in the solar wind upstream of Earth’s bow shock. Higher fluxes are expected when IBEX was in the lobe in this case because, at the time, the spacecraft was moving toward the ENAs coming from the downstream pixel. Conversely, lower fluxes are expected when IBEX was in the solar wind because, at the time, the spacecraft was moving away from the ENAs from the downstream pixel.

For IBEX-Hi, the frame-transformed fluxes in Figure 53(B) agree with one another, just as they do in Figure 52(B). However, for the frame-transformed IBEX-Lo fluxes in Figure 53(B), the transformed fluxes do not agree. A switch occurs from Figure 53(A) to Figure 53(B) such that in Figure 53(B), fluxes measured when the spacecraft was the solar wind are now higher than those measured when the spacecraft was in the lobe. This switch is similar to the switch from Figure 52(A) to Figure 52(B) and again indicates that there is a background in IBEX-Lo that is created by a local source (either neutral or non-neutral) that is moving with the Earth (or with the spacecraft).

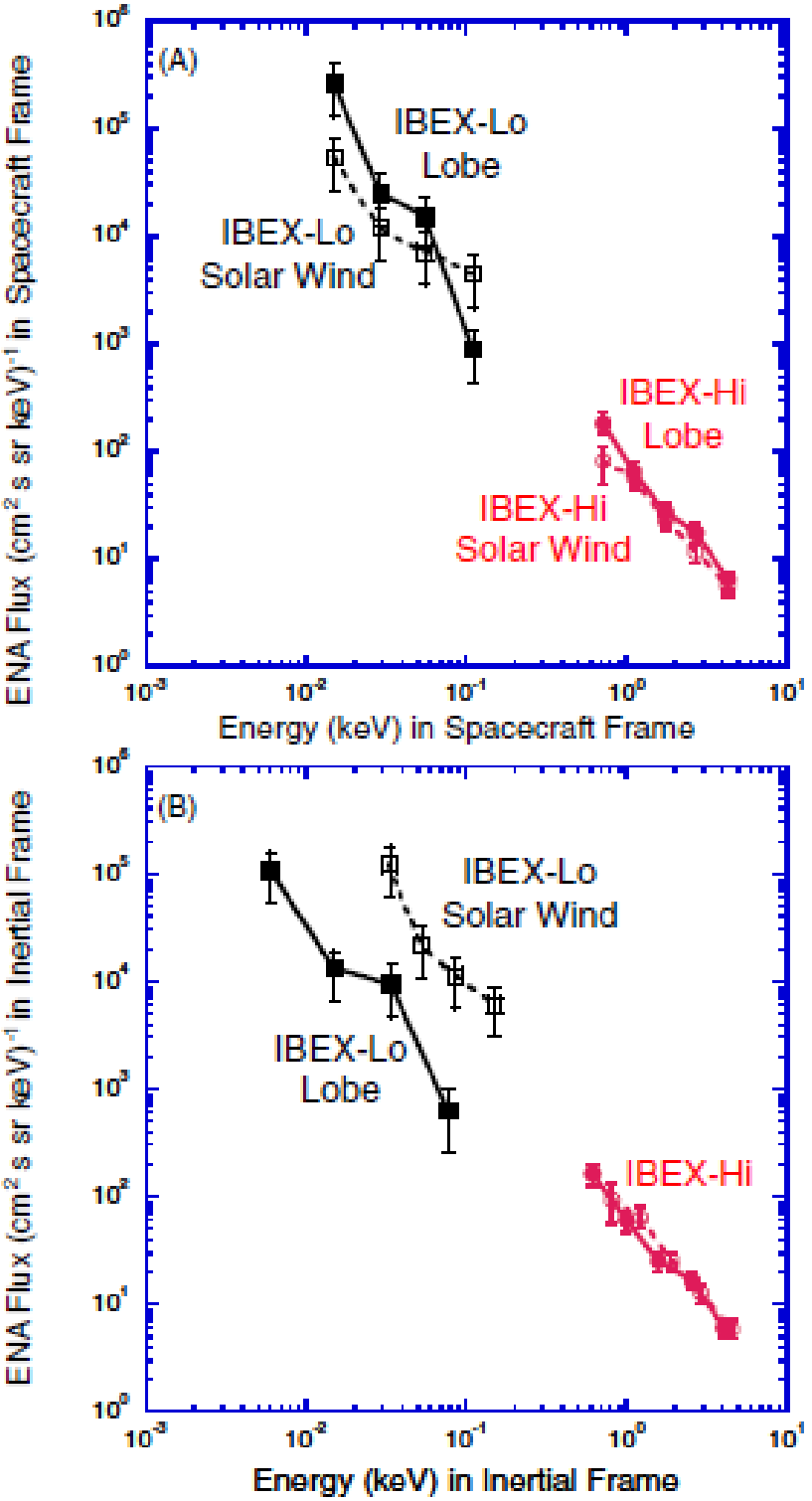

Figure 53: IBEX-Hi and IBEX-Lo (first four energy channels) fluxes from the downstream pixel in the spacecraft frame (A) and in the inertial frame (B). When IBEX was in the lobe, the sensors viewed in the direction of the ENAs from the tail region, and ENA fluxes were generally higher than those measured in the solar wind when IBEX was moving in the opposite direction. When transformed into the inertial frame, the

IBEX-Hi fluxes agree, while the IBEX-Lo fluxes for the first four energy channels are overcorrected and disagree.

While it is clear that the background level in the first four energy channels of IBEX-Lo (up to 0.1 keV) is larger than the heliospheric signal, background levels compared with the heliospheric signal at energies from 0.1 to 0.5 keV are more difficult to determine. To gain some understanding of the background levels at these higher energies, it is assumed here that the background from 0.01 to 0.5 keV is similar in the two-view direction in the sky. Support for this assumption comes from comparison of IBEX-Lo fluxes in Figure 52(A) and Figure 53(A). Fluxes measured in the spacecraft frame from two different directions in the sky should not necessarily agree. However, IBEX-Lo fluxes measured while the spacecraft was in the lobe from the V1 pixel in Figure 52(A) and fluxes from the downstream pixel in Figure 53(A) agree within the uncertainties of the measurements (here the sets of fluxes that were measured when the spacecraft was in the lobe are compared). This agreement suggests that the background (at least in the first four energy channels of IBEX-Lo) can be assumed to be independent of view direction, at least for these two directions in the sky.

With this assumption, fluxes in Figure 51(A) and Figure 51(B) from the V1 and downstream pixels, respectively, can be compared and background levels from 0.1 to 0.5 keV can be estimated. In Figure 51(A), fluxes agree at energies from 0.1 to 0.5 keV, while in Figure 51(B), fluxes agree for energies from 0.2 to 0.5 keV. At 0.15 keV, fluxes in Figure 51(A) are approximately a factor of two to five times higher than at the same energy in Figure 51(B). Therefore, the background could be approximately 50% of the flux at 0.15 keV in Figure 51A) (i.e., the magnitude of the absolute uncertainties in the measurement). At 0.25 keV, the fluxes agree to within about 30%, so the background could be of the order of 30% of the heliospheric ENA flux at that energy.

The results from the approach adopted here suggest that there is a near-Earth background source that is higher than the heliospheric ENA flux below 0.1 keV in the V1 direction and 0.2 keV in the downstream direction. As a consequence, only upper limits of the flux can be specified for these energies. Upper limits are taken to be the lowest fluxes measured in the spacecraft frame. No frame transformation is made to these upper limits because fluxes are dominated by local backgrounds that should not be transformed into the inertial frame. Despite the backgrounds involved, the plots in this section demonstrate that the ENA spectra measured by IBEX-Hi and IBEX0Lo are in reasonable agreement with one another.

4.4.2 Modelling

Due to the novel nature of the measurements made by IBEX, comparable measurements from other missions cannot be used to directly validate the measurements made by IBEX. Therefore, modelling plays an important role in making

sense of the observations of IBEX and showing that the features present in IBEX ENA maps can be explained by physical features. This section shows an example of a modelling effort that attempted to explain the unique and unexpected observations produced by IBEX, such as the famous ribbon, within the context of the Voyager termination shock crossings.

Previous models of energetic neutral atom (ENA) maps (1) provide limits on possible emission patterns depending on the assumed proton distributions in the heliosheath. Models with assumed Maxwellian distributions in the heliosheath show a broad enhanced emission region near the nose where the flow stagnates, whereas highly nonthermal distributions dominated by pickup ions (PUIs) show higher intensities in the sidewind direction and toward the tail where the line-of-sight (LOS) integrations across the heliosheath extended over large distances [hundreds of astronomical units (AU)]. Three-dimensional (3D) models incorporating a k distribution, defined in (2), as a distribution with a Gaussian-like core and a power-law tail, manifest structure influenced by the local interstellar medium (LISM) magnetic field (BLISM) (3). The observed difference inside the termination shock (TS) between interstellar helium flow and the hydrogen flow (4), which interacts more strongly with the outer heliosheath plasma (beyond the heliopause), suggests that BLISM lies in the plane of the two flow vectors (the hydrogen deflection plane), which can push the TS closer to the Sun in the Southern Hemisphere, helping to explain why Voyager 2 (V2; –29° latitude) crossed the TS ~10 AU closer to the Sun than did Voyager 1 (V1; 34° latitude) (5–8). Here, we compare Interstellar Boundary Explorer (IBEX) observations (9–11) with sophisticated models of the heliosphere and outline considerations in the development of new concepts to understand the ribbon.

The ENA flux observed by IBEX derives from the LOS integral over the charge-exchange probability for the differential intensity of protons that move radially inward toward the Earth as they gyrate about the field. ENAs experience charge-exchange and photo-ionization losses as they propagate through the supersonic solar wind and are deflected and shifted in energy by the Sun's gravity and radiation pressure. At the energies considered here (~0.4 to 4 keV), these are small effects (at 0.4 keV, the ionization loss is ~40%, deflection is ~0.5°, and energy shift is ~2%) that decrease with energy. The ENA distribution at 1 AU is sensitive to the LOS path along which emission occurs, the density and bulk motion of the heliosheath plasma, and the energy and pitch-angle distributions of the source proton population.

We simulated ENA maps using different models with different assumptions for the local interstellar conditions. Model 1 (3) uses a magnetohydrodynamic (MHD) model ($B_{LISM} = 1.8\,mG$) (8) incorporating a k distribution (with k =1.6) throughout the heliosheath with the derived MHD plasma parameters, but assumes a uniform density of interstellar hydrogen (0.1 cm−3) a posteriori to generate ENAs and does not treat the interaction between the plasma and neutrals self consistently. Model 2 (Figure 54) (12) uses an MHD model that self-consistently treats the charge exchange interaction between

neutral atoms from the LISM and protons that have a k-function distribution of k =1.6 inside the heliopause but a Maxwellian distribution outside. The model assumes a 450 km/s solar wind emitted inside the TS and a 3 mG B_{LISM} in the hydrogen deflection plane, tilted by 30° to the LISM flow. There are few structural differences at 1.1 and 4.4 keV (Figure 54, A and B), indicating that global heliospheric structure, rather than energy-dependent heating, determines the modeled maps. Other sophisticated models incorporating the self consistent interactions between the heliosheath plasma and LISM neutrals have been run for a range of LISM and solar wind conditions, revealing considerable variability in global structure and dynamics (13).

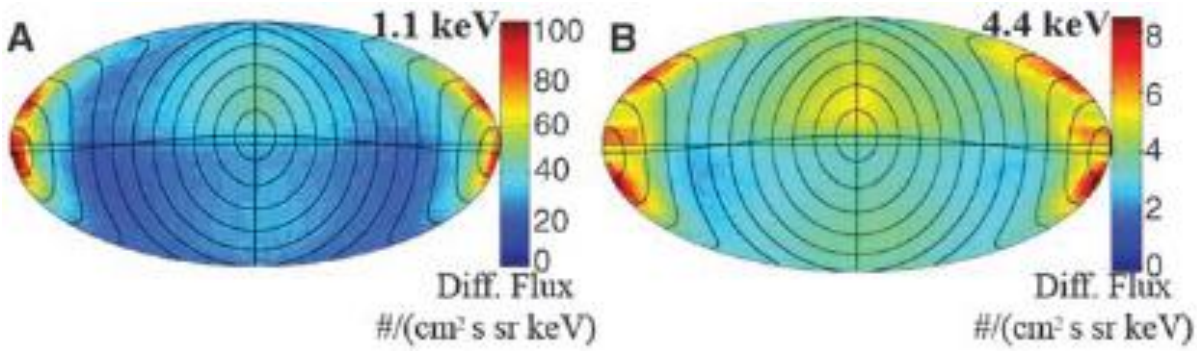

Figure 54: Simulated ENA maps (Mollweide projection) using Model 2 show incident 1 AU ENA fluxes at 1.1 keV (A) and 4.4 keV (B).

The features detected by IBEX may be separated into two parts: the ribbon and distributed emissions outside the ribbon. Models currently miss the ribbon. We compared observations (9–11) with simulated fluxes (Table 16) in ~20° regions outside the ribbon. The IBEX fluxes were interpolated to 0.44, 1, and 4 keV in the Sun-centered inertial reference frame. The model fluxes differ substantially from observations by ~6 to 200%. Models also show that the time-varying latitudinal structure of the solar wind may cause 11-year quasi-periodic variations of ENA fluxes (14) with a local maximum around 60° latitude for 1 keV ENAs (15).

Model 2 shows correlation between the ribbon and the locus of $B \bullet r = 0$, where B denotes the draped field outside the heliopause and r is the radial vector along the LOS (Figure 55). Notwithstanding the assumed direction and strength of B_{LISM}, the correlation with the $B \bullet r = 0$ locus suggests that the ribbon may carry the imprint of BLISM via physical processes not identified in current models.

To quantify the implications of the ribbon for global models, we computed the plasma pressure (P) in the ribbon. Direct analysis of the observed fluxes yields $P \bullet LOS \sim 100\ AU - pdyne/cm^2$ (11). The ribbon's observed width (10) of ~50 AU for a heliopause distance 150 AU from the Sun yields LOS ~ 50 AU, assuming comparable width and depth. This 50 AU LOS suggests P ~ 2 pdyne/cm2, 2.5 times the LISM ram pressure (16). We computed a crude model to estimate the increase in pressure ahead of the heliopause caused by the external J×B force (where J is the current density) and

thermal pressure [approximated by the dynamical pressure for a LISM proton density of 0.07 cm−3 and a flow speed of 26 km/s (16)] (Figure 56). We approximated the heliopause as a perfectly conducting sphere with a slightly flared external magnetic field, conceptually similar to (17) and figure 4C in (9). The crude model compressed |B| to ~4 mG outside the heliopause for BLISM = 2.5 mG. The analytic approach was validated against MHD simulations in other applications (18) and provides the net MHD forces acting on the surface by collapsing current onto the conducting sphere. A ring of high pressure centered on BLISM is associated with magnetic field line draping. If P is comparably high, then the LOS is approximately 60 to 30 AU.

Table 16: Observed and simulated ENA Fluxes at 0.44, 1 and 4 keV, respectively.

Source	IBEX	Model 1 (*3*)	Model 2 (*12*)
	ENAs/(cm2 s sr keV)	ENAs/(cm2 s sr keV) (percent relative to IBEX observations)	
Nose	470	230 (49%)	150 (31%)
	96	60 (63%)	43 (45%)
	9	6 (67%)	5.6 (62%)
Tail	530	30 (6%)	360 (68%)
	120	17 (14%)	100 (83%)
	4	4 (100%)	8 (200%)
North Pole	410	150 (37%)	110 (28%)
	76	45 (59%)	34 (45%)
	9	5 (56%)	4 (48%)
South Pole	360	130 (36%)	89 (25%)
	70	40 (57%)	30 (43%)
	9	5 (56%)	4 (44%)
Right flank (longitude = −165°)	230	190 (83%)	110 (48%)
	70	50 (71%)	35 (50%)
	6	5 (83%)	4.3 (72%)
Left flank (longitude = −45°)	380	170 (45%)	110 (30%)
	86	46 (53%)	33 (38%)
	7	5 (71%)	4.3 (61%)

Field-draping around the heliopause also compresses the heliosheath plasma, which could enhance ENA emission because of density enhancement (the plasma density, n, scales with the field strength, B) and first adiabatic invariance ($v_\perp^2/B = const$, where $v_\perp$ is the velocity of plasma protons perpendicular to the field), provided that some mechanism creates a large suprathermal population beyond the heliopause and there is limited scattering. We assumed a k-distribution (k = 1.6) in the unperturbed LISM, applied n/B and $v_\perp^2/B$ conservation, and integrated along the LOS from the heliopause to 40 AU beyond it in order to estimate ENA emission (Figure 56). The structure of the map is preserved at different energies with only the absolute fluxes changing. If distributions are isotropic because of scattering, adiabatic heating and density

compression could still enhance fluxes, but the emission band broadens because of the lack of pitch-angle dependence.

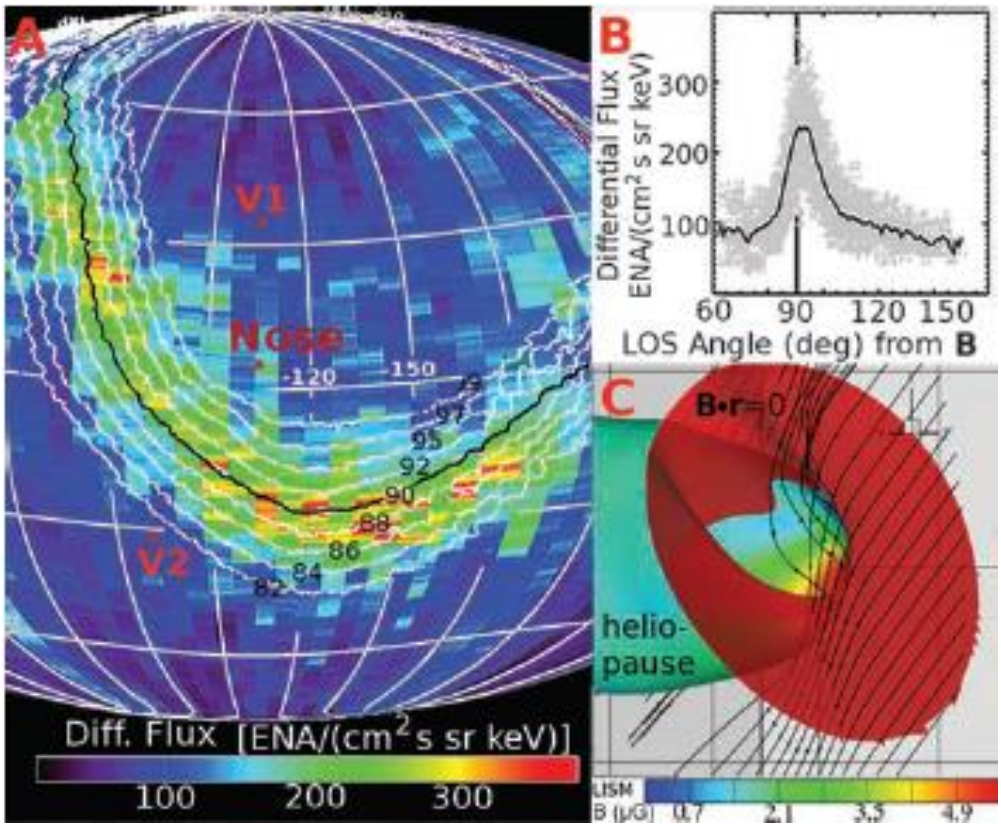

Figure 55: (A) The observed ENA map at 1.1 keV superimposed with contours of the B•r angle (from 82° to 99°, black contour at 90°) between the simulated B (from Model 2 in Table 1) and the LOS, r, averaged over a 10-AU region just outside the heliopause (taken where themodeled plasma temperature is <80,000 K). (B) The overall correlation between ENA fluxes (–180° to 0° ecliptic longitude) and the B•r angle. (C) Global configuration of field lines draped over the heliopause, and the surface where B•r = 0. The black contour in (A) corresponds to the red 3D surface outside the heliopause in (C) where the LISM field is most stressed by draping about the heliopause and B•r = 0. The assumed BLISM direction (ecliptic longitude = –120°, latitude = 31°) is consistent with indirect observational inferences (5, 13, 16).

Our crude model does not explain the origin of the ribbon but supports the notion that the draped LISM magnetic field influences the heliosheath pressures and ENA emission. Our crude model suggests that the flow may stagnate along the ribbon (9). However, the $J \times B$ forces that we isolated are present in all MHD models, and stagnation along the $B \bullet r = 0$ locus is not seen. Therefore, if the $J \times B$ forces lead to an enhanced ribbon pressure, they must do so via mechanisms not currently present in global models. For example, elevated J×B forces could induce an interchange instability near the heliopause, causing the higher-pressure plasma inside the heliopause to displace field lines longitudinally and protrude beyond the heliopause and elevating ENA emission through charge exchange with the higher neutral density beyond the

heliopause (16) and the lengthened LOS. This instability could depend critically on highly mobile ions, effectively enhancing the pressure along the protruding plasma fingers and highlighting the importance of ion-kinetic effects that are not self-consistently included in current models.

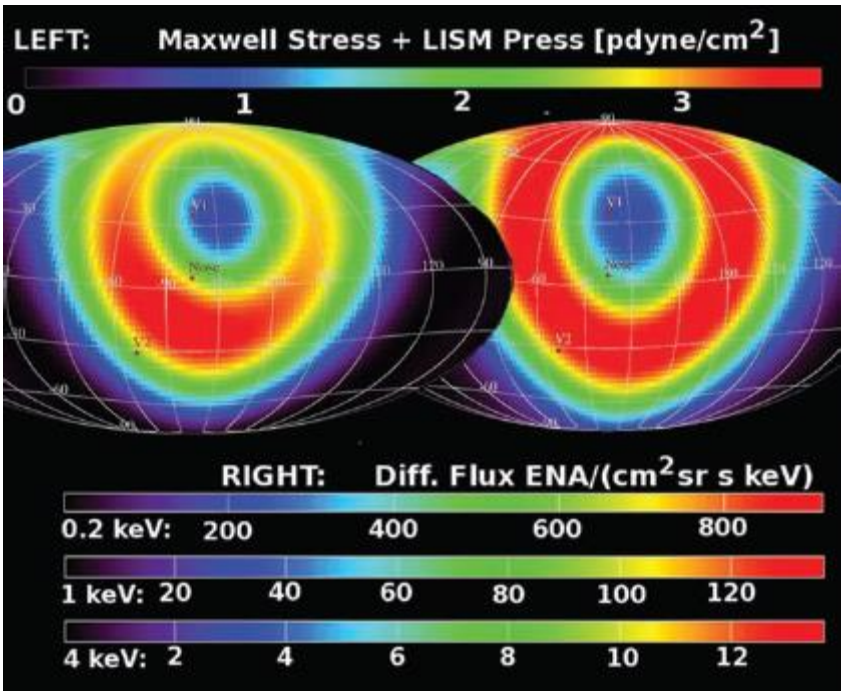

Figure 56: (Left) Results of a crude model for the combined force-per-unit area on the heliopause from external J×B forces (Maxwell stress). (Right) Estimated ENA emission from beyond the heliopause using a crude model of plasma compression.

Model predictions provide mixed agreement with observations, and the ribbon is not predicted. The ribbon suggests a high-pressure region in the heliosheath possibly imprinted by the influence of the LISM magnetic field. However, current models are unable to translate the influence of LISM magnetic field into enhanced ENA fluxes along the ribbon, indicating that an important physical ingredient is missing.

5. IBEX Measurement Algorithm Description

5.1 Theoretical Basis

This section provides context and background information for the measurement of ENA/ISN flux by the IBEX instruments. Descriptions of the algorithms and techniques

used by the IBEX data pipeline to generate science data products from raw instrument data from IBEX-Hi and IBEX Lo are provided.

IBEX analysis can be viewed as a processing pipeline connecting the principle science data products. This pipeline is a part of a larger framework for receiving telemetry, trending the payload, delivering Science Tasking Files when needed, archiving data, and distributing data to the scientific community and public (Fig. 11). Because the raw telemetry (Level 0 data) may contain corrupted, garbled communications, data dropouts or repeats, the first stage of the processing produces a “clean copy” of the science data (Level 0.5) as it was stored in the solid state recorder on orbit. If necessary, commands can be sent to the spacecraft to resend portions of the recorded data until it has all been received on the ground. The CEU flight algorithm encodes the data rather compactly, and for subsequent processing expanded forms of this data (Level 1.0 data products) are needed. The most significant change is the correlation of event times (or spin phase) with the corresponding IBEX attitude to determine the arrival direction of each event.

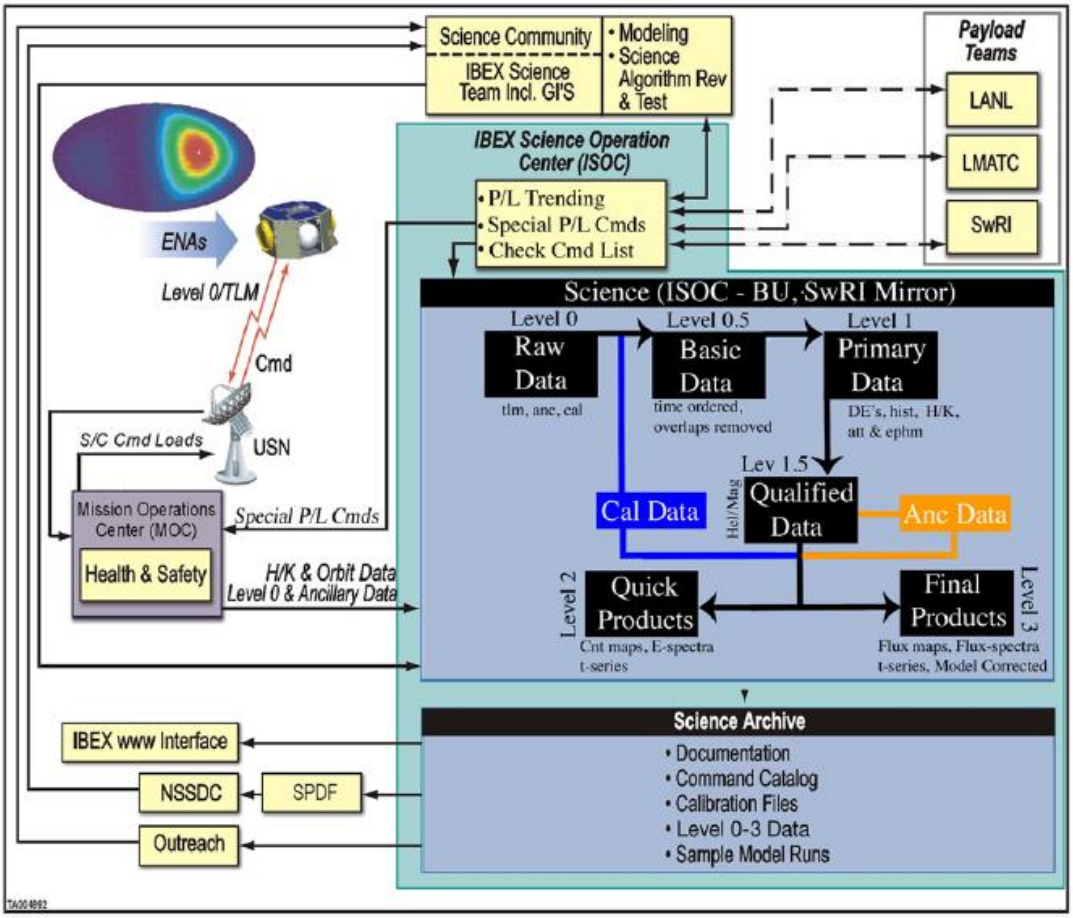

Figure 57: IBEX data flow from the spacecraft and through the ISOC. The IBEX raw telemetry data and ancillary data are received and processed into high-level data products, archived and distributed to the scientific community

At this point in the processing pipeline, with a magnetospheric model and knowledge of background sources, we remove obvious non-heliospheric signal events and perform data quality checking (magnetospheric ENA data are culled and assembled into a separate data set for use by that community). With the resulting data, we construct ENA count maps or simple spectral estimates for various regions of the sky (Level 2.0 data products). A “toolbox” of methods for the selection and display of data along with some degree of human interaction is used at this processing level. At the next level, we include sensor calibration data and produce estimations of the true ENA flux into the sensor from the direct-event counts. Because these calculations require the inclusion of detailed instrument models, the maps and spectra of ENA flux are higher-level (3.0) products.

Level 3 maps include both the incident maps of ENA flux onto the sensors near 1 AU and heliospheric maps of ENA flux from the outer heliosphere. (The ENA flux from an arbitrary outer boundary at 100 AU is used in existing software, but can be easily modified to any closed surface in the outer heliosphere.) An important component in the generation of the heliospheric ENA maps is understanding the transmission of ENAs from their points of origin to observation at the IBEX spacecraft (Bzowski 2008; Roelof and Bzowski 2009). To solve for the ENA transmission, we take into account loss by ionization (predominantly photo-ionization and charge-exchange) and the effects of gravitation and radiation pressure. The final destination of IBEX data products is the SPDF (Space Physics Data Facility) at the National Space Science Data Center in a form suitable for use by the community.

Section 5.2 provides an overview of the IBEX data pipeline. Section 5.3 describes the conversion IBEX-Hi signals to flux, Section 5.4 describes the conversion IBEX-Lo signals to flux, and Section 5.5 describes algorithms and techniques common to both instruments.

5.2 IBEX Data Pipeline

The IBEX data processing system may be viewed as a pipeline with raw data flowing in at one end, and various products flowing out at various stages. Figure 58 was used in the pre-launch planning and provides a useful overview. This figure shows schematically how IBEX raw telemetry data are processed into high level data products. Several intermediate stages of “virtual products” are identified in the figure. Real number designations are used to classify the data products in a fashion suitable for IBEX and to distinguish the levels from those used in other NASA missions. (In standard NASA definitions in which Level 0 denotes raw telemetry, which is calibrated to yield Level 1, &c.) Integral values are used for those that might be usefully exported outside of the processing pipeline. The others are working products that might appear after intermediate processing steps, but are not necessarily viewable objects.

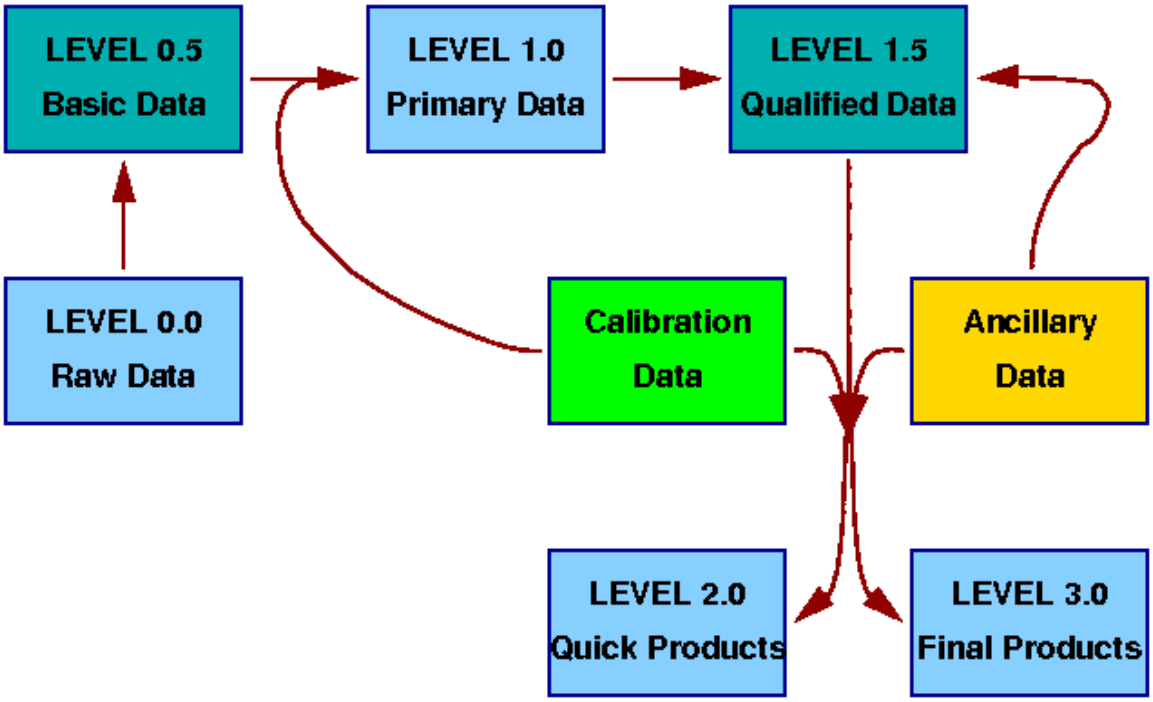

Figure 58: Planned Flow through Automated Pipeline

The raw telemetry (Level 0.0 data) delivered by mission operations may be corrupted garbled communications, data dropouts or repeats &c. Thus the first stage of the processing pipeline is intended to correct for this, producing a "clean" copy of the science data (Level 0.5) as it was stored in the Solid State Recorder (SSR) on IBEX. If necessary, commands can be sent to the spacecraft to reread portions of the recorded data until it has all been received on the ground. There is sufficient space in the SSR to store data for about 4 orbits, so there is roughly a month to request the re-transmission of any missing data. Level 0.0 data products also include other materials (contact logs, ephemerides, &c.) received from the Mission Operation Center (MOC).

It should be noted that the payload firmware (PLFW, an 8051 Microcontroller implemented in an Actel FPGA core with 12 MHz clock) has a sophisticated, table-driven algorithm which guides the selection of individual events to be downlinked (whereas all events are included in downlinked histograms). This algorithm has undergone extensive testing in the development phase; and in early in the science phase of the mission its performance must be verified, and if necessary, adjustments made to its configuration.

The flight algorithm also encodes the data rather compactly, and for subsequent processing, an expanded form of this data (Level 1.0 data products) needs to be created. The most significant change is the correlation of event times (or spin phase) with the corresponding IBEX attitude to determine the arrival direction of each event (or

assigned to each histogram bin). The IBEX attitude control system (ACS) provides the PLFW with (1/3 Hz) attitude updates (quaternions), and samples of these (sufficient to reconstruct attitude to the required accuracy) are included in the telemetry.

At this point in the processing pipeline, with a magnetospheric model and knowledge of background sources, one can remove obvious non-signal events and construct ENA count maps and simple spectral estimates for regions of the sky (Level 2.0 data products). However, the analysis path is not completely straightforward, insofar as there are model-dependent choices which play a role at this point. For example, the magnetosphere is a dynamic entity with a rich phenomenology of its own, so the segregation of the magnetospheric ENAs from the heliospheric ENAs is not always straightforward.

Thus a "toolbox" of methods for the selection and display of results along with some degree of (local or remote) human interaction is implicit at this processing level. Algorithms for this toolbox are provided by the IBEX sensor and science teams. Thus the road to the Level 2.0 data requires intermediate (virtual) data products (shown as Level 1.5 in the figure).

The sensor calibration data also plays a significant role in the processing at this level. It is likely that the actual calibration products will be created by ISOC in conjunction with the sensor designers, either from pre-launch data, or from certain post-launch calibration activities.

The estimation of the true ENA flux into the sensor from the direct event counts is ultimately a model-dependent process. Thus maps and spectra of ENA flux are higher level products (Level 3.0).

The dissection of the physics of heliospheric boundary layer is also a model-dependent process, and interesting science results and interpretations may be expected to come from this (also in product Level 3.0). Some of the modelling requires knowledge of the solar wind and magnetosphere, and so data products from other missions are desired. Depending on what the IBEX sensors themselves produce, the full science analysis may well extend beyond the life of the mission itself.

5.2.1 Automated Data Processing as Implemented

The "as implemented" story is not very different from the preceding plan. The "flow" diagram, shown in Figure 59, is slightly different, as now we can label the action with the scripts doing the work. In this section we'll just present the picture and mention the players. You will want to consult the cron-driven procession section (see Section 3.3

[proc-cron], page 47) where some of this is handled in considerably more detail. And all of the processing scripts here are "tunable" through configuration parameters. There is an entire chapter (see Chapter 4 [config], page 70) discussing those details.

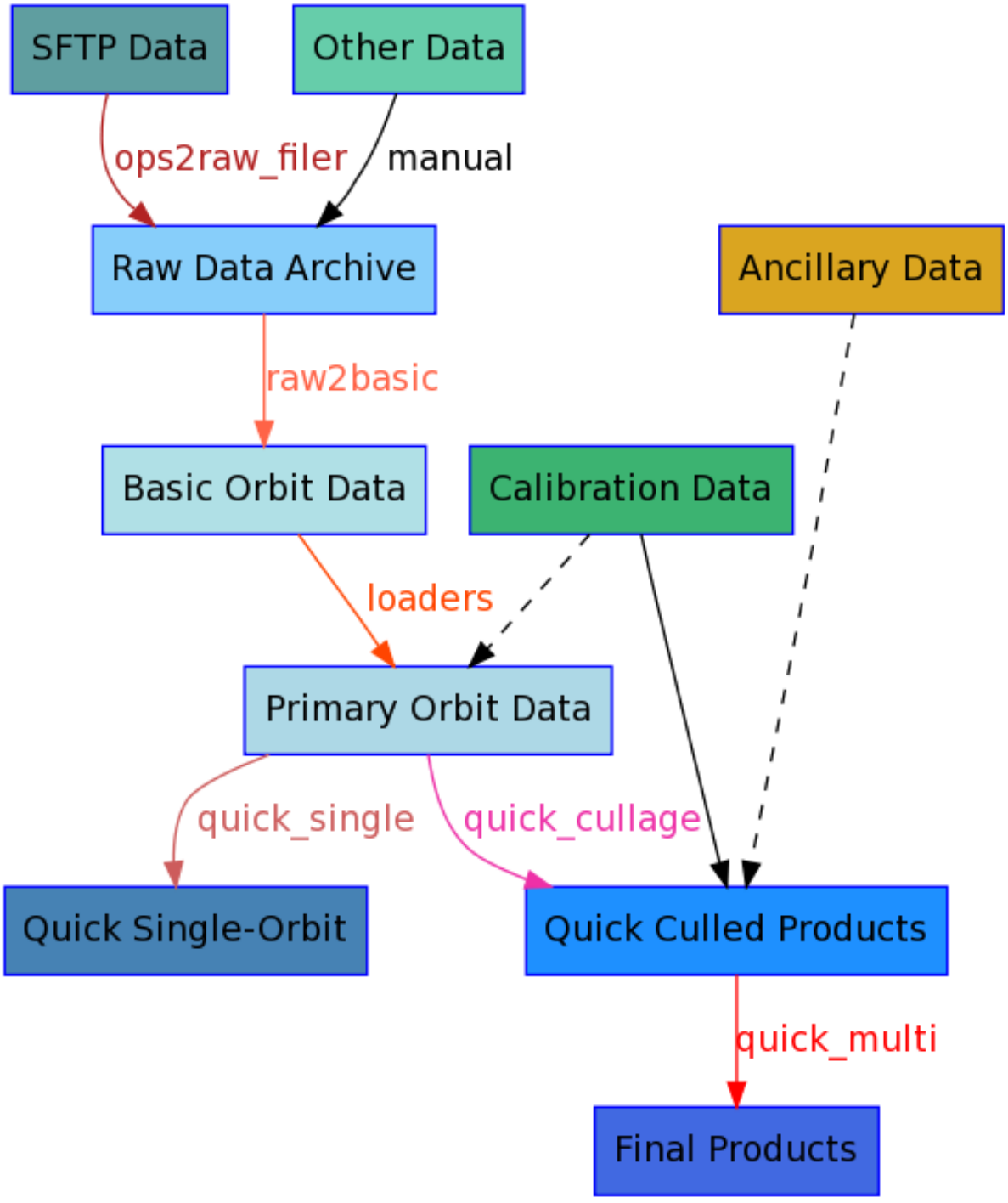

Figure 59: Implemented Flow through Automated Pipeline, see text for explanation.

5.3 Conversion of IBEX-Hi Signals to Flux

This section describes the algorithms and methods used to derive science data from raw instrument signals from IBEX-Hi.

5.3.1 IBEX-Hi Data Binning

Once the cull has been made, the primary choice is an angular resolution, or bin size in which to gather the events for rate estimation. The Hi data has typically been binned at four different angular resolutions (0.5, 2.0, 3.0 or 6.0 degrees, organically and confusingly labelled hd05, hsds, hsd3, hsd6; all corresponding to the "hd" cull).

All subsequent processing steps are similar for all culls. First, count rates and fluxes are calculated in each ESA for both Hi and Lo ("estflux" files). The rate calculation may include some background subtraction. The observed sensor flux response is then used to adjust the flux estimates to create the flux1au files. These may be graphically presented in an orbit-frame, aligned so that the spin-phase direction lies on the equator.

5.3.2 IBEX-Hi Signal Calculation

The number of ENA signal counts $C_{s,i}$ for an individual spin bin *i* is calculated from the total DE counts for that bin C_i as follows:

$$C_{s,i} = C_i - C_{b,i} = C_i - r_{b,i}T_i \tag{5}$$

Where $C_{b,i}$ is the number of background counts, estimated from the product of $r_{b,i}$, the background rate, and T_i, the exposure time, for the spin bin. When building a sky map, for a given pixel in the map, the counts from multiple spin bins are combined. The total number of signal counts for the pixel is:

$$\begin{aligned} C_s &= \sum_{i=1}^{n} (C_i - r_{b,i}T_i) \\ &= \sum_{i=1}^{n} C_i - \sum_{i=1}^{n} r_{b,i}T_i \end{aligned} \tag{6}$$

And the signal rate is

$$r_s = \frac{C_s}{T} = \frac{\sum_{i=1}^{n} C_i}{T} - \frac{\sum_{i=1}^{n} r_{b,i}T_i}{T}, \tag{7}$$

where *n* is the number of spin bins whose centers lie within the pixel, and the total exposure time $T = \sum_{i=1}^{n} T_i$. Note the second term on the RHS of (7) can be interpreted as the time-weighted average background rate.

The total signal rate uncertainty in a map pixel is a combination of uncertainties in the observed counts in a pixel ($\sqrt{\sum C_i}$) and the background rate. In terms of the variance,

$$\sigma_{r_s}^2 = \sigma_{r_{tot}}^2 + \sigma_{r_b}^2 = \frac{\sum_{i=1}^{n} C_i}{T^2} + \frac{\left(\sum_{i=1}^{n} \sigma_{r_b,i} T_i\right)^2}{T^2}$$

(8)

Thus we are assuming the uncertainty of the total count rate and the uncertainty of the average background rate are uncorrelated. This is reasonable since the background rate is determined separately using different data products. Note that for the background variance term in (8), we take it to be the square of the exposure-time-weighted average of the individual background rate uncertainties, *not* a quadrature sum of background rate uncertainties. This is because the background uncertainties are (a) not necessarily independent of each other (i.e., they are correlated), and (b) they contain systematic uncertainties. To see the consequences of this, examine the behavior of (8) if we write the individual spin bin counts in terms of the pixel-averaged total count rate r_{tot} times the bin exposure time, $C_i = r_{tot} T_i$, and we set the background rate uncertainties to all be the same: $\sigma_{r_b,i} = \sigma_{r_b}$. Then, using $T = \sum_{i=1}^{n} T_i$, the signal rate variance is:

$$\sigma_{r_s}^2 = \frac{r_{tot}}{T} + \sigma_{r_b}^2.$$

(9)

Thus, if the background uncertainty is small, the signal rate variance is dominated by the first term, which is typically the dominant term for individual spin bins or even a full 6° x 6° pixel. For large *T* (which can be achieved by making larger pixels or summing over multiple maps), the variance does not vanish, but becomes dominated by the background rate uncertainty; and thus, we see one cannot achieve infinitely better statistics by summing over larger and larger areas of the sky. Rather, we hit a hard limit.

Note that the variance of the number of signal counts (*not* of the signal rate) is Equation (8) times the total exposure time:

$$\sigma_s^2 = \sum_{i=1}^{n} C_i + \left(\sum_{i=1}^{n} \sigma_{r_b,i} T_i\right)^2.$$

(10)

5.3.3 IBEX-Hi Flux Calculation

For a given skymap pixel *k*, the ENA flux for energy step E_j is:

$$j_{ENA,k}(E_j) = \frac{C_{s,j,k}}{T_{j,k} G_j E_j} \tag{11}$$

where the G_j is the geometric factor for energy step *j*, and E_j is the central energy. At the time of writing the geometric factors are given by the following table. Note however that these values will be updated as more information about the flight units is acquired.

[A table of geometric factors and central energies will be inserted here.]

The flux variance is found by replacing $C_{s,j,k}$ in Eq. (11) above with the corresponding signal count variance $\sigma^2_{s,j,k}$.

5.3.4 IBEX-Hi Cosmic Ray Background Removal

Accurate removal of backgrounds and accurate characterization of any trends over time in IBEX-Hi's detection efficiency are both vital to analysis of time evolution of the heliospheric ENA signal. The chief background, always present, is from penetrating radiation. During times of "clean" heliospheric viewing, cosmic rays provide the only penetrating background. By using coincidence and qualification event information inherent in the detailed IBEX-Hi measurements, we are able to quantify and remove the absolute contribution of penetrating radiation over time. In addition, coincidence information provided by the detector section allows precise trending of the detection efficiency of ENAs over time.

5.3.4.1 Initial IBEX-Hi Cosmic Ray Background Removal Methods

The IBEX-Hi detector section consists of three consecutive channel electron multipliers (CEMs) (A, B, and C) collecting electrons from three sequential detector volumes that are separated by ultrathin carbon foils (Funsten et al. 2009b). An ENA which has been ionized on the entrance conversion foil and transited the ESA will then pass through the foils, producing electrons, which are collected by the CEMs. A triple coincidence event is one in which electrons are detected in all three CEMs within a 96 ns ("long") window; a qualified triple coincidence event, or qABC, is a triple coincidence where electrons are not detected in CEM C—that is to say, the back of the detector— until at least 3 ns after they are first detected in CEM A or B, at the front of the detector. Unqualified triples, or unqABC events, are triple coincidences, where CEM C triggers before or within 3 ns (the "short" window) of the first of CEMs A and B.

Cosmic rays produce electrons essentially simultaneously throughout the various surfaces of the detector, on the walls, and on the nickel grids, which support the carbon foils. Ideally, any triple event produced by cosmic rays would be classified as a unqABC event, due to the sub-nanosecond transit time of cosmic rays. However, variation in the electron transit times from various parts of the detector foils and walls to the CEMs is not short compared to the short qualification window, and many of these events appear as qABC.

The enhancement in the qABC rate due to gamma radiation was measured prior to launch, during IBEX-Hi testing and calibration, and the appropriate removal technique is outlined in Wurz et al. (2009). The ratio of unqABC/qABC is different for ENAs ($\eta \sim 1{:}99$, depending on the velocity of the incident ENA) than for cosmic radiation ($\xi \sim 9{:}10$ as measured during on-orbit testing). Consequently, by comparing qABC and unqABC rates, the qABC count rate due to ENAs can be separated from the qABC count rate due to penetrating radiation. In particular, if over some interval of time N_q qABC counts and N_u unqABC counts are observed, the number of qABC counts attributable to cosmic radiation rather than to ENAs is $(Nu - \eta N_q)/(\xi - \eta)$.

The unqABC/qABC ratio for cosmic radiation was determined by on-orbit tests in Orbits 13 and 77, during which the voltages of the ESA were set to prevent any charged particles, either from the space environment or generated by ENAs, from getting to the detector. The uncertainty in the ratio comes from the counting statistics of the tests and is about 3%. The unqABC/qABC ratio for ENAs is different for each energy setting of IBEX-Hi, and depends weakly on the energy spectrum of incoming ENAs. This is true because slower-moving ENAs produce relatively more qualified and fewer unqualified triples. The ratios for each of the six ESA settings were determined by requiring the calculated penetrating background rate for all moderately quiet intervals of Orbits 16–122 be independent of ENA flux. The ratios obtained this way for ENAs are consistent with those determined during calibration, but are considerably more precise.

The penetrating background rates determined this way, which do not include solar energetic particle (SEP) event intervals, corresponds extremely well with cosmic ray monitors. The top panel of Figure 60 shows an orbit-by-orbit comparison of IBEX-Hi penetrating background rate to CRaTER/LRO dose (Spence et al. 2010), with intervals of enhanced solar particles removed. Similarly, the bottom panel of Figure 60 shows a comparison to McMurdo neutron monitor data; note that in this case, in order to achieve agreement, the neutronmonitor data had to be offset in addition to being scaled, due to the atmospheric cutoff around 700 MeV. In both cases the error bars shown for IBEX include both statistical and systematic uncertainties arising from the uncertainty in the unqABC/qABC ratios for ENAs and for penetrating background.

In summary, IBEX-Hi measures a background due to cosmic rays, which is accurately characterized by coincidence ratios in the detector section. After the correction is made

to remove this background from the IBEX-Hi ENA signal, the heliospheric ENA flux is more accurately determined.

A second critical area for providing accurate ENA fluxes and determining if they have changed over time is the overall IBEX-Hi detection efficiency. We monitor the IBEX-Hi's ENA detection efficiency over time in two ways. First, periodic gain tests, roughly every six months, find no apparent difference in behavior between the three CEMs. Overall, there has been a minor shift of only ~60 V on the location of the edge of the gain plateau relative to operating voltage, which has been held constant. Since the total count rates in the IBEXHi detector tend to be below 10 s^{-1} per CEM, and negligible charge has been extracted from them so far in the mission, all three CEMs remain in saturation and well up on their gain cure plateaus.

A more precise check of the entire detector section is made possible by comparing coincidence rates supplied by the spacecraft (Funsten et al. 2005). If the detection efficiency of sections A, B, and C of the IBEX-Hi detector are ε_A, ε_B, and ε_C respectively, then N incident ENAs will produce $N_{ABC} = N\ \varepsilon_A\ \varepsilon_B\ \varepsilon_C$ triple counts, qualified or unqualified. Similarly, the number of times both CEM B and CEM C will register an event, regardless of whether or not CEM A does, is $N_{BC} = N\ \varepsilon_B\ \varepsilon_C$. The efficiency of the first section of the detector is then simply $\varepsilon_A = N_{ABC}/N_{BC}$. Similar derivations supply ε_B and ε_C. These three efficiencies can thus be calculated per orbit and tracked over time. ε_A, ε_B, and ε_C constitute monitors not just of the three CEMs but of the entire detector section, including, for instance, the secondary electron emission properties of the ultrathin carbon foils.

The derivation of efficiencies is exact in the absence of signals other than that produced by a spatially uniform H ENA flux with a time-independent energy spectrum entering IBEX-Hi. In practice, we limit data used to trend efficiency to the cleanest data with the lowest backgrounds, selected for heliospheric analysis in energy steps 2–6, and subtract the penetrating background contribution to the doubles rates (N_{AB}, N_{AC}, and N_{BC}) and triples rate (N_{ABC}), using the previous calculation of triples background rates and scaling by the ratios of coincidence events observed in the background tests of Orbits 13 and 77 (see above).

Penetrating radiation along trajectories not possible by real ENA-produced particles generate additional single and double coincidence events beyond those that can produce triple coincidences. Thus, the fraction of observed double coincidence events due to cosmic radiation is considerably higher compared to their triples than for ENAs. Uncertainty in the penetrating background ratios N_{AB}, N_{AC}, N_{BC}/N_{ABC}, resulting in uncertainty in the background subtraction of the doubles, is the limiting factor in determining the absolute value of ε_A, ε_B, and ε_C. However, this systematic uncertainty does not prevent quite precise trending of any changes in efficiency, as long as the penetrating background ratios do not change over time. If there were any indication of this, we would need to run another on-orbit background test.

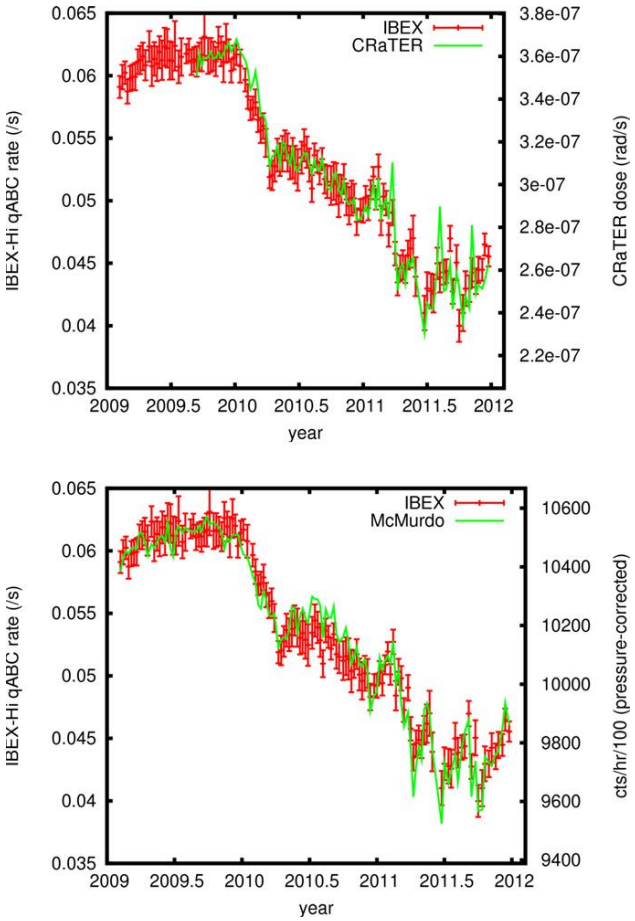

Figure 60: Penetrating background rate for qualified triples, calculated orbitby- orbit excluding SEP events, compared to (top) CRaTER/LRO radiation dose and (bottom) McMurdo neutron monitor rates.

A complication arises with AB coincidences. Heavy species, such as oxygen, generate measurable AB coincidences, but rarely generate triples (or any other count involving CEM C), owing to their difficulty in penetrating even ultrathin carbon foils (e.g., McComas et al. 2004, and references therein). One source of oxygen is water in the IBEX-Hi collimator, which can ionize and become accelerated into the conversion foil at the entrance of the ESA, where it dissociates (Wurz et al 2009). Currently, we do not correct for heavy ion contamination from AB counts, and so the efficiency of CEM C, $\varepsilon_C = N_{ABC}/N_{AB}$, cannot be calculated nearly as accurately as ε_A and ε_B. One motivation behind examining the three detector sections individually and not simply monitoring the overall triples detector section efficiency, $\varepsilon = \varepsilon_A \varepsilon_B \varepsilon_C$, is that ε_A and ε_B are unaffected by this issue.

IBEX-Hi detection efficiency depends slightly on the initial energy of the ENA; thus, the efficiency reported depends weakly on the energy spectrum of the ENA signal. Figure 61 shows the orbit-by-orbit calculated detection efficiencies of the three sections of the

IBEX-Hi detector, along with the linear trend. ε_C shows clear seasonal variation due to contamination in the AB coincidences, which reduce ε_C from its true value. Ground calibration could not directly produce values of ε_A, ε_B, and ε_C to correspond to the not-yet-observed heliospheric ENA energy spectrum, but the closest values are approximately 0.30, 0.78, and 0.49 respectively. Least-squares fits indicate ε_B and ε_C are consistent with no change from 2009 to 2012 at 1σ: the possible changes are 0.005 ± 0.005 and −0.004 ± 0.02, respectively. ε_A has increased, according to this analysis, by approximately 0.02 ± 0.004 over this time. Altogether, there has been essentially no change in efficiency in IBEX-Hi on orbit and the general observed temporal variations reported in this study are real.

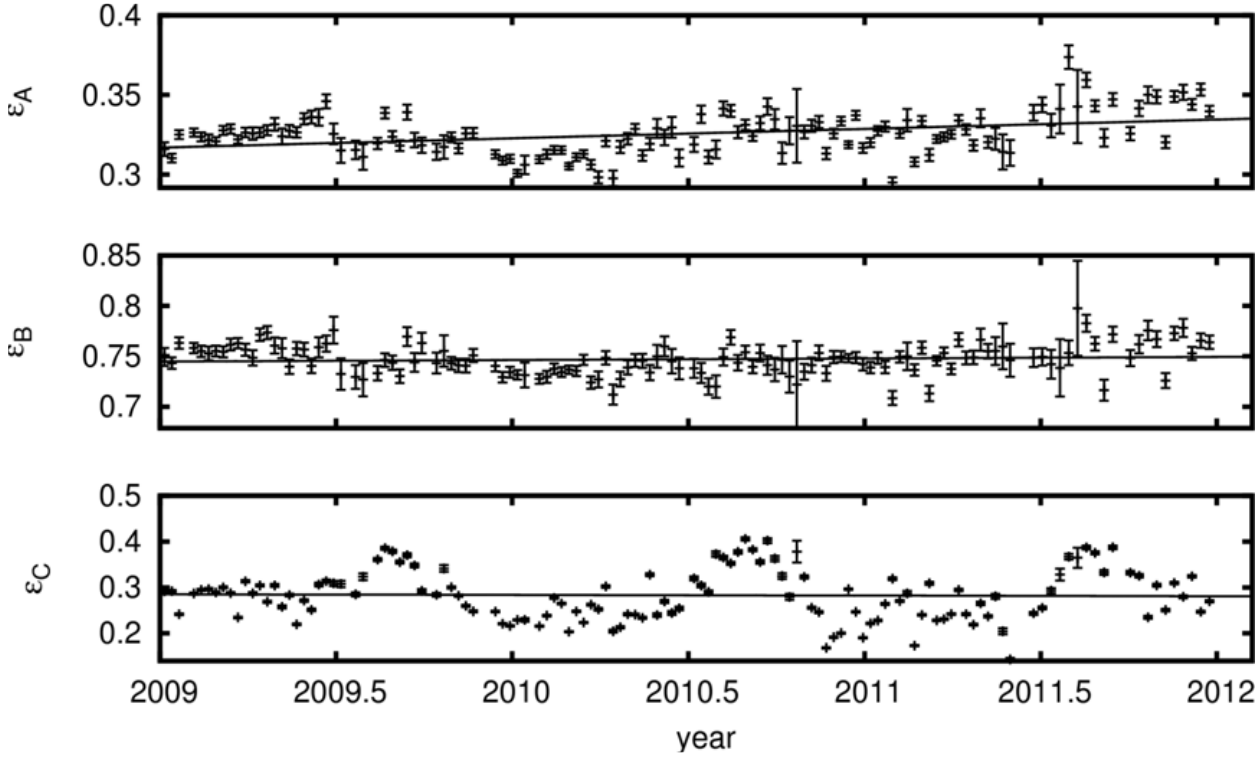

Figure 61: Detection efficiency of the three sections of the IBEX-Hi detector, as determined for each orbit from double and triple coincidence count ratios. Error bars shown are from counting statistics only. ε_C shows yearly variation due to contamination in the AB coincidences. Lines shown are from a linear regression of the data.

5.3.4.2 Time Variable Cosmic Ray Background Correction in IBEX-Hi

IBEX-Hi data is subject to a variety of backgrounds. Some are always present to some degree; some are present only over limited times and at limited angles, such as foreground objects (e.g., Earth magnetosphere and the moon) and deflected solar wind contamination. Data intervals, in angle and time, are sorted into one of three categories: “good,” “loose,” and intervals not currently used for heliospheric science. In “good” periods, the data appears statistically consistent with the quietest intervals of an orbit arc and does not contain any additional intermittent signal. “Loose” periods have at most a small and (nearly) isotropic additional background beyond those in the good times. Loose intervals are selected infrequently, as the data permits, and are treated by

the subtraction of a small offset for a presumed isotropic background (not scaled) to match on average the signal rate observed in the good cull intervals.

Even in the “good” intervals, some always-present backgrounds remain. The principal such background is penetrating background due to cosmic radiation (another: the ion gun background is discussed in Section **Error! Reference source not found.**). As in M cComas et al. (2012b), penetrating background appears in the “qualified” triple-coincidence count rate, which is the cleanest IBEX-Hi data product and the one used in the five-year maps. However, the fraction of qualified triple coincidences, where the event is registered in detector section A (the “front” of the detector) prior to registration in detector section C (the “back”), is different between ions and penetrating background. Nearly all signal ions are detected in section A first, as shown during calibration (Funsten et al. 2009b), whereas only roughly half of penetrating radiation is detected in section A first. This ratio for penetrating background was measured in orbits 13, 77, and 189 (2009 January, 2010 May, and 2012 December) and has not changed over time. Penetrating background is then calculated from the number of qualified triples, the number of unqualified triples, and the predetermined ratios of the two for signal and background (Funsten et al. 2009a).

The penetrating background correction is calculated for each orbit’s worth of data, and thus is approximated as constant over that interval. Times of solar energetic proton events are excluded from this determination as the IBEX-Hi data is generally culled out at such high background times. Uncertainty arises from the counting statistics; systematic uncertainty arises from the calibrated ratio of coincidence types for ENAs (determined in calibration) and for background (determined on-orbit).

Figure 62 shows a comparison of IBEX-Hi calculated penetrating background as a rate of qualified triples (red data points, vertical axis on the left), compared to the McMurdo neutron monitor data (green curve, vertical axis on the right) over the same interval. The error bars shown for IBEX include statistical uncertainty and systematic uncertainty arising from the uncertainty in the unqualified ABC to qualified ABC ratios for ENAs and for penetrating background. A scaling factor is needed to correlate the data types, and an offset is necessary due to the atmospheric low energy cutoff around 700 MeV for the McMurdo measurements. The scaling factors in this figure are identical to those used in McComas et al. (2012b), indicating the long-term stability of IBEX-Hi as well as understanding the causal factors for this background.

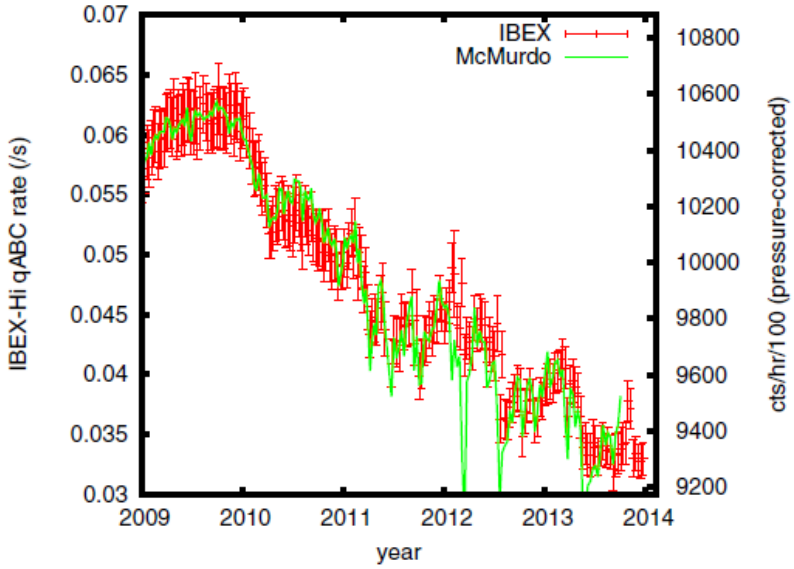

Figure 62: Penetrating background rate for qualified triples, calculated orbit by orbit excluding SEP events, compared to the McMurdo neutron monitor rates.

5.3.5 Removal of ion gun background in IBEX-Hi

We use the term “ion gun” to describe the background generated from ambient neutrals, such as desorbed or outgassing atoms or molecules in the IBEX-Hi instrument, that become ionized within the positive collimator region of IBEX-Hi. From this location, they can be accelerated into the entrance conversion foil and masquerade as ENAs from outside the instrument (Wurz et al. 2009). Ionization is principally due to electrons in the local environment of the spacecraft that manage to get past the negative collimator and are then accelerated onto the positive collimator surfaces. UV light can also produce photoelectrons at the entrance surface of the charge conversion foils, where they are accelerated toward and into the collimator, which is biased at 7 kV. The negative collimator was designed to run at a voltage high enough to prevent electrons with <600 eV from reaching the positive collimator. However, very early in the mission it was observed that the negative collimator voltage potential also pulled solar wind ions around the sunshade and into the edge of the instrument, causing a different and larger background. Once this was established, collimator voltages were reduced, and from the start of science data collection onwards, the negative collimator voltage was set to reject electrons only below 80 eV. Testing in 2011 November to 2012 January determined that no statistically observable additional solar wind contamination could be correlated to an increase in negative collimator voltage which rejected electrons below 120 eV. Starting in 2013 April the negative collimator was increased accordingly, significantly reducing the ion gun signal.

The ion gun background shows up in triple coincidences almost entirely in IBEX-Hi energy pass bands 1, 2, 5, and 6 (see Funsten et al. 2009a, Table 6), and is negligible

in ESAs 3 and 4. The signal in pass bands 1 and 2 arises from $H2O^+$ produced in the positive collimator: the molecular ion dissociates on passing through the entrance foil, creating H^+ at 1/18 of the 7 kV potential between the positive collimator and the entrance foil (i.e., 389 eV) that is slightly reduced by energy lost in transiting the charge conversion foil. The signal in ESAs 5 and 6, which was not predicted in the background paper (Wurz et al. 2009), arrives at very close to half the collimator potential (i.e., 3.5 kV) and is therefore inferred to come from H_2^+ produced in the positive collimator. Additionally, the O^+ from H_2O^+ arrives over a broad range of straggled energies less than 16/18 of the 7 kV acceleration voltage. Its signal is limited almost entirely to coincidences of A and B. The observed ion gun signal that can be associated with hot electrons (e.g., by correlating with WIND 103 eV and 165 eV electron fluxes when IBEX is in the solar wind) is isotropic; the effect of photoelectrons was observed in orbit 114, when spacecraft pointing briefly allowed sunlight onto the collimator for a portion of the spin and produced a bright, anisotropic ion gun signal.

As a result of the oxygen signal in the AB coincidences, the amount of ion gun background in the qualified triples signal can be calculated using the rates of uniquely associated double and triple coincidence combinations, regardless of external information as to the hot electron flux. First, for energy pass bands 3 and 4, which do not see ion gun background in the qualified triples, the count rate is determined for AB coincidences in excess of what would be expected from the penetrating background rate (determined as in Section 5.3.4.1 and scaled to AB based on the on-orbit penetrating background test ratios) and from the ENA signal rate, using the penetrating-background-subtracted qualified ABC rate and an assumed efficiency for detector section C of $\varepsilon_C = 0.465 + (-0.015)$. This efficiency estimate comes from comparing the calibrated efficiencies of detector sections B and C to the on-orbit efficiency of detector section B. Then, over the intervals and observing angles considered to be good heliospheric viewing over the first four and a half years (before the negative collimator voltage was increased), slopes were determined between the minimum isotropic signal observed by IBEX-Hi in energy pass bands 1, 2, and 6, and the excess oxygen signal observed in energy pass bands 3 and 4. The minimum isotropic signal is defined as the minimum qualified triples count rate observed in the quietest contiguous 48 degree portion of spin, over a contiguous hour and a half of data collection, for intervals considered good for heliospheric data for energy pass bands 3 and 4. This correction assumes that all isotropic excess AB counts—that is to say, any heavy ion signal—is entirely due to ion-gun oxygen.

These slopes can then be applied to the good times of any specific orbit arc to correlate the qualified triple coincidence ion gun correction in energy pass bands 1, 2, and 6 from the calculated excess oxygen background. The correction is too small in energy range 5 for a statistically meaningful slope to be extracted by this technique, so for this range, the ESA 6 correction is scaled using the ion gun ratio during two intervals of very high ion gun background—an isotropic period from 2009 December, and the 2011 February orbit when IBEX's pointing allowed sunlight to hit the collimator.

The minimum isotropic background signal in energy pass bands 1 and 2 correlates extremely well with the excess oxygen signal, which is to be expected since it all originates from the same H_2O^+ source. The signal in energy range 6, from H_2^+, also is highly correlated, though not as well as that in energy pass bands 1 and 2. No statistically significant time variation was observed in the correlation between the energy range 6 qualified ABC minimum isotropic background and the excess oxygen background of energy pass bands 3 and 4.

For intervals when IBEX is in the solar wind and WIND data is available, the excess oxygen background correlates well with 103 eV electron flux. Requiring the oxygen background to extrapolate to zero at zero electron flux provides values of ε_C consistent with the value used above, though with larger uncertainty values.

The triple coincidence ion gun count rate for a typical orbit was approximately 0.017 s^{-1} for energy range 6, 0.014 s^{-1} for energy range 2, and 0.01 s^{-1} for energy range 5, before the negative collimator voltage was increased. Energy range 1 is not currently used for heliospheric sky maps, but enabled quantification of this background early in the mission. In comparison, the penetrating background rate over the course of the first five years of data has ranged from about 0.06–0.03 s^{-1}. Ion gun corrections in the future should remain at least a factor of three smaller, owing to the recently increased negative collimator voltage.

5.3.6 Generation of IBEX-Hi Good Times Lists

In addition to the background removal techniques described in Sections 5.3.4 and 5.3.5, background is removed by culling periods of high-background. Periods with data suitable for scientific analysis (i.e. low-background periods) are defined by the Good Times list, which excludes periods when:

1) The instrument field-of-view (FOV) is pointed at the Earth, its magnetosphere or the Moon.
2) The background monitor count rate exceeds a given threshold (this was 50,000 but has been adjusted down to 35,000 due to decreased efficiency of the background monitor).
3) Periods with incorrect spin information or missing data.
4) Periods with enhanced background, which can be due to penetrating background or solar wind intake.

The first three exclusion criteria are trivial given the necessary data, however the third requires manual examination of the data. To do this the data is summed over all angles and over 48 or 96 spins. To check for penetrating background all ESA steps are summed over, whereas for solar wind either steps 1 and 2 or 1, 2, and 3 are summed over. The data are then examined by eye and periods of high background are removed. Optimally, this process is repeated a few days later as a further precaution, potentially with a reversed time axis and rotated angles to remove bias. The optimal

cull will have the smallest error bars for the lowest count rates since the backgrounds are sporadic but the heliospheric signal is constant.

5.3.7 IBEX-Hi Data Efficiency Factor Over Time

The IBEX-Hi ENA detection efficiency is tracked over time in a number of ways. First, the measurement of penetrating background from cosmic radiation (see Section 5.3.4) does not show systematic variation over time as compared to ground-based cosmic-ray neutron monitors; this strongly implies that the efficiency of the channel electron multipliers (CEMs) at detecting secondary electrons is reasonably constant. Additionally, periodic gain tests of the CEMs are performed on orbit to determine if they are aging off of the "gain plateau," the range of operating voltage over which detection efficiency is nearly constant. Over the first five years, all three CEMs remain on the plateau and behave identically: there has been a shift of approximately 80 V on the location of the edge of the gain plateau relative to operating voltage, which has been held constant. Finally, the ratios of various coincidences during data collection allow the tracking of the absolute detection efficiency of each section of the IBEX-Hi detector (Funsten et al. 2005).

The process of determining the efficiency of the detector sections of IBEX-Hi is given above in Section 5.3.4. Briefly, if the detection efficiency of sections A, B, and C of the IBEX-Hi detector are ε_A, ε_B, and ε_C respectively, then N incident ENAs will produce $N_{ABC} = N\ \varepsilon_A\ \varepsilon_B\ \varepsilon_C$ triple counts, qualified or unqualified, and $N_{BC} = N\ \varepsilon_B\ \varepsilon_C$ double counts in detector sections B and C. Thus, the efficiency of the first section of the detector is $\varepsilon_A = N_{ABC}/N_{BC}$; similar ratios supply ε_B and ε_C. The derived efficiency is for not only the CEM but the entire detector section, including, for instance, the secondary electron emission properties of the ultrathin carbon foils.

This derivation of efficiencies is exact in the absence of signals other than that produced by a spatially uniform hydrogen flux of time-independent energy spectrum entering IBEX-Hi. In practice, we limit data used to trend efficiency to the "good times" selected for heliospheric analysis in ESA settings 2–6 (see Section 5.3.4), and subtract the penetrating background contribution to the doubles rates (NAB, NAC, and NBC) and triples rate (NABC). The doubles rates are derived from the calculation of triples background rates from Section 5.3.4 and the doubles coincidence rates based on linearly interpolating and extrapolating the ratios of coincidence events observed in the background tests of orbits 13, 77, and 189. Imprecision in removal of these backgrounds limits the accuracy of the efficiency determination, and, in as much as the background ratios vary over time, the detection of any efficiency trends over time. In particular, the calculated drop in εA and εB over the year 2013 is almost certainly an artifact resulting from the doubles-to-triples background ratios dropping more slowly over time than is extrapolated from the 2009, 2010, and 2012 penetrating background tests, although confirmation awaits the results of the 2014 penetrating background test. Similarly, the initial drop in efficiencies mid-2009 appears only once the background ratios are allowed to vary over time linearly between the 2009 and 2010 background

test, and do not appear in McComas et al. (2012b), which used constant values consistent with the 2009 test.

A further complication arises because heavy species, such as oxygen, generate measurable AB coincidences but rarely generate triples, or any other coincidence involving CEM C, owing to their difficulty in penetrating even ultra-thin foils (e.g., McComas et al. 2004, and references therein) and the limited duration of the coincidence window Allegrini et al. 2008). The main source of excess AB coincidences is related to the “ion gun” background, discussed in Appendix D. In fact, the removal of the ion gun background requires as input an (estimated) efficiency of detector section C. The heavy-ion contamination in the AB counts severely limits the accuracy of ε_C determination, and consequently, coincidence-ratio determinations of detector section efficiencies is really applicable only to ε_A and ε_B. Based on gain tests, it is reasonable to assume that CEMs B and C behave very similarly.

Figure 63 shows the efficiencies of the three detector sections calculated from coincidence ratios, averaged over five orbits or orbit arcs per point. For detector section C, no heavy ion contamination was removed: its presence is evident from the annual variation in ε_C well outside the statistical uncertainty shown, and the jump in calculated efficiency later in 2013, when the negative collimator voltage was increased. Detector sections A and B may have dropped slightly, but not beyond the bounds associated with linearly interpolating and extrapolating from the three background tests. Thus, for this study, efficiency of the IBEX-Hi detector as a whole has been taken to be constant over the first five years. Altogether, no change in efficiency is seen that would account for the general observed decrease in heliospheric ENA emissions.

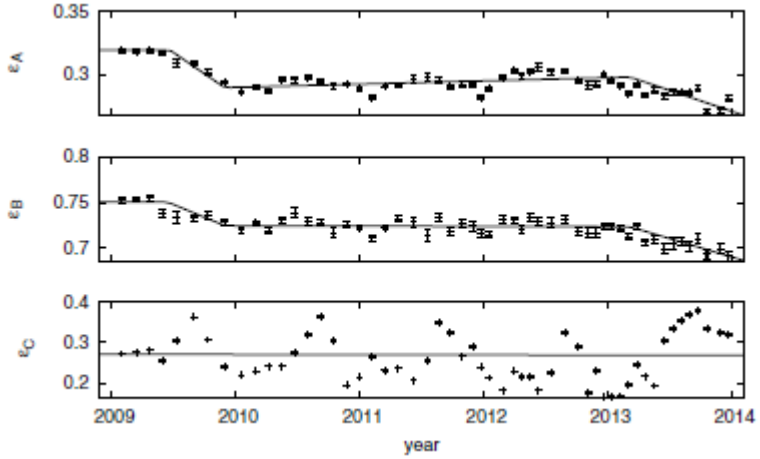

Figure 63: Detection efficiency of the three sections of the IBEX-Hi detector, as determined orbit by orbit from double and triple coincidence count ratios. Points are shown once every five orbit arcs. Error bars shown are predominantly from counting statistics.

5.4 Conversion of IBEX-Lo Signals to Flux

This section describes the algorithms and methods used to derive science data from raw instrument signals from IBEX-Lo.

5.4.1 IBEX-Lo Signal Calculation

Taking the number of ENA signal counts for an individual spin bin *i* and energy *e* to be $C_{s,i,e}$ and the total DE counts for that bin as $C_{i,e}$, the signal rate is computed:

$$R_{s,i,e} = \frac{C_{s,e}}{T} = \frac{\sum_{i=1}^{n} C_{i,e}}{T} \tag{12}$$

Where n is the number of spin bins located within the pixel being generated and T is the total accumulation time for the interval being considered, with deadtime correction applied. The uncertainty is given by:

$$\sigma_{R_s,e}^2 = \sigma_{R_{tot},e}^2 = \frac{\sum_{i=1}^{n} C_{i,e}^2}{T^2} \tag{13}$$

5.4.2 IBEX-Lo Flux Calculation

Rates are converted to differential energy flux for each energy step *e* according to:

$$J_e(E_e) = \frac{R_{s,e}}{G_e \Delta E_e} \tag{14}$$

where G_e is the geometric factor and ΔE_e is the width of energy bin *e*. Similarly, the differential flux uncertainty is given by:

$$\sigma_e(E_e) = \frac{\sigma_{R_s,e}}{G_e \Delta E_e} \tag{15}$$

Tables of values for G_e for different species are provided in Section 5.4.3.

5.4.3 IBEX-Lo Geometric Factors

In this section, we provide geometric factors of IBEX-Lo for four neutral species (H, He, O, and Ne). The geometric factor in Table **17**–Table **24** is the product of the absolute geometric factor, the energy resolution of the ESA, TOF efficiency, the combined grid transparency, the collection efficiency, the combined conversion and reflection efficiency, and the relative probability of detecting an ion of species “X.” The efficiencies and transparencies are explained in detail in the IBEX science operation paper

(Schwadron et al. 2009). Those values are based on various calibration runs with neutral beams of four species during final calibration before flight. In Table **17**–Table **24**, the indices i and k indicate the ESA and incident energy steps, respectively.

Table 17: Geometric Factors of Triple Coincidence Events for $H \rightarrow H^-$

i/k	1	2	3	4	5	6	7	8
1	7.29E-06	4.23E-06	5.70E-06	1.09E-06	1.08E-06	1.29E-06	6.92E-07	5.61E-06
2	0.00E+00	1.41E-05	1.78E-05	2.30E-06	1.33E-06	1.53E-06	1.90E-06	7.19E-07
3	0.00E+00	0.00E+00	2.17E-05	9.48E-06	2.05E-06	1.95E-06	1.95E-06	1.28E-06
4	0.00E+00	0.00E+00	0.00E+00	2.43E-05	8.22E-06	2.13E-06	2.26E-06	1.19E-06
5	0.00E+00	0.00E+00	0.00E+00	0.00E+00	2.41E-05	8.24E-06	3.57E-06	1.15E-06
6	0.00E+00	0.00E+00	0.00E+00	0.00E+00	0.00E+00	2.82E-05	2.72E-05	4.49E-06
7	0.00E+00	0.00E+00	0.00E+00	0.00E+00	0.00E+00	0.00E+00	5.23E-05	5.54E-05
8	0.00E+00	0.00E+00	0.00E+00	0.00E+00	0.00E+00	0.00E+00	0.00E+00	7.41E-05

Table 18: Geometric Factors of Triple Coincidence Events for $H \rightarrow O^-$

i/k	1	2	3	4	5	6	7	8
1	2.09E-08	3.05E-08	4.46E-08	1.72E-07	7.24E-07	3.88E-07	9.89E-08	9.42E-07
2	0.00E+00	5.13E-08	4.03E-08	1.93E-08	5.08E-07	5.24E-07	3.38E-07	1.06E-07
3	0.00E+00	0.00E+00	3.92E-08	3.97E-08	3.65E-08	4.23E-07	5.15E-07	2.50E-07
4	0.00E+00	0.00E+00	0.00E+00	9.44E-08	2.15E-08	5.90E-08	4.36E-07	2.37E-07
5	0.00E+00	0.00E+00	0.00E+00	0.00E+00	6.05E-08	8.67E-09	6.20E-08	1.96E-07
6	0.00E+00	0.00E+00	0.00E+00	0.00E+00	0.00E+00	1.55E-08	2.72E-08	3.35E-08
7	0.00E+00	0.00E+00	0.00E+00	0.00E+00	0.00E+00	0.00E+00	0.00E+00	5.27E-08
8	0.00E+00	0.00E+00	0.00E+00	0.00E+00	0.00E+00	0.00E+00	0.00E+00	0.00E+00

Table 19: Geometric Factors of Triple Coincidence Events for $O \rightarrow O^-$

i/k	1	2	3	4	5	6	7	8
1	3.55E-05	2.31E-05	3.48E-05	3.46E-05	1.04E-05	3.97E-06	4.72E-06	3.73E-06
2	0.00E+00	3.98E-05	5.25E-05	9.10E-05	1.73E-05	1.15E-05	7.68E-06	5.69E-06
3	0.00E+00	0.00E+00	6.36E-05	2.10E-04	4.76E-05	1.42E-05	8.86E-06	4.14E-06
4	0.00E+00	0.00E+00	0.00E+00	7.29E-05	4.74E-05	4.25E-05	1.48E-05	5.11E-06
5	0.00E+00	0.00E+00	0.00E+00	0.00E+00	7.24E-05	9.71E-05	5.13E-05	1.29E-05
6	0.00E+00	0.00E+00	0.00E+00	0.00E+00	0.00E+00	6.89E-05	8.33E-05	5.00E-05
7	0.00E+00	0.00E+00	0.00E+00	0.00E+00	0.00E+00	0.00E+00	8.01E-05	8.11E-05
8	0.00E+00	0.00E+00	0.00E+00	0.00E+00	0.00E+00	0.00E+00	0.00E+00	7.80E-05

Table 20: Geometric Factors of Triple Coincidence Events for O → H^-

i/k	1	2	3	4	5	6	7	8
1	2.15E-06	3.01E-06	1.50E-05	3.01E-05	2.16E-05	1.86E-05	1.57E-05	3.30E-05
2	0.00E+00	2.34E-07	5.96E-07	9.84E-06	1.89E-05	2.34E-05	1.82E-05	3.85E-05
3	0.00E+00	0.00E+00	1.66E-07	1.29E-06	5.31E-06	3.28E-05	2.80E-05	2.08E-05
4	0.00E+00	0.00E+00	0.00E+00	3.96E-07	2.16E-06	7.10E-06	3.34E-05	2.76E-05
5	0.00E+00	0.00E+00	0.00E+00	0.00E+00	4.55E-07	1.19E-06	3.96E-06	2.85E-05
6	0.00E+00	0.00E+00	0.00E+00	0.00E+00	0.00E+00	1.00E-06	1.39E-06	8.16E-06
7	0.00E+00	0.00E+00	0.00E+00	0.00E+00	0.00E+00	0.00E+00	4.71E-07	2.87E-06
8	0.00E+00	0.00E+00	0.00E+00	0.00E+00	0.00E+00	0.00E+00	0.00E+00	9.71E-07

Table 21: Geometric Factors of Triple Coincidence Events for He → H^-

i/k	1	2	3	4	5	6	7	8
1	8.23E-06	2.24E-05	3.63E-05	4.89E-05	2.57E-05	7.70E-06	7.43E-06	7.17E-06
2	0.00E+00	7.79E-06	3.81E-05	6.03E-05	2.60E-05	7.62E-06	6.19E-06	6.58E-06
3	0.00E+00	0.00E+00	1.06E-05	5.22E-05	2.76E-05	7.71E-06	5.49E-06	5.85E-06
4	0.00E+00	0.00E+00	0.00E+00	4.89E-06	1.92E-05	1.19E-06	4.59E-06	4.56E-06
5	0.00E+00	0.00E+00	0.00E+00	0.00E+00	7.00E-07	3.79E-07	1.17E-06	2.84E-06
6	0.00E+00	0.00E+00	0.00E+00	0.00E+00	0.00E+00	3.05E-07	1.50E-06	1.32E-06
7	0.00E+00	0.00E+00	0.00E+00	0.00E+00	0.00E+00	0.00E+00	1.88E-07	2.67E-06
8	0.00E+00	0.00E+00	0.00E+00	0.00E+00	0.00E+00	0.00E+00	0.00E+00	1.23E-07

Table 22: Geometric Factors of Triple Coincidence Events for He → O^-

i/k	1	2	3	4	5	6	7	8
1	2.49E-08	1.48E-07	7.21E-08	1.51E-06	9.77E-07	3.53E-07	5.17E-07	6.76E-07
2	0.00E+00	2.36E-08	7.85E-07	2.04E-06	1.41E-06	4.79E-07	5.33E-07	7.99E-07
3	0.00E+00	0.00E+00	1.31E-07	1.88E-06	2.14E-06	6.51E-07	6.78E-07	1.04E-06
4	0.00E+00	0.00E+00	0.00E+00	1.38E-07	1.29E-06	1.59E-07	7.22E-07	1.21E-06
5	0.00E+00	0.00E+00	0.00E+00	0.00E+00	2.59E-08	4.56E-08	2.05E-07	9.42E-07
6	0.00E+00	0.00E+00	0.00E+00	0.00E+00	0.00E+00	2.02E-08	1.93E-07	4.10E-07
7	0.00E+00	0.00E+00	0.00E+00	0.00E+00	0.00E+00	0.00E+00	1.44E-08	5.27E-07
8	0.00E+00	0.00E+00	0.00E+00	0.00E+00	0.00E+00	0.00E+00	0.00E+00	1.56E-08

Table 23: Geometric Factors of Triple Coincidence Events for Ne → H^-

i/k	1	2	3	4	5	6	7	8
1	0.00E+00	4.07E-06	0.00E+00	1.52E-04	0.00E+00	0.00E+00	0.00E+00	3.12E-05
2	0.00E+00	3.22E-07	0.00E+00	6.20E-05	1.72E-04	1.46E-04	2.92E-05	4.03E-05
3	0.00E+00	0.00E+00	2.04E-07	2.38E-06	4.80E-05	1.85E-04	9.53E-05	4.72E-05
4	0.00E+00	0.00E+00	0.00E+00	2.57E-08	2.59E-06	2.48E-05	1.10E-04	5.42E-05
5	0.00E+00	0.00E+00	0.00E+00	0.00E+00	6.61E-08	5.04E-07	1.16E-05	5.23E-05
6	0.00E+00	0.00E+00	0.00E+00	0.00E+00	0.00E+00	1.21E-07	5.12E-07	2.65E-06
7	0.00E+00	0.00E+00	0.00E+00	0.00E+00	0.00E+00	0.00E+00	9.15E-08	4.72E-07
8	0.00E+00	0.00E+00	0.00E+00	0.00E+00	0.00E+00	0.00E+00	0.00E+00	4.85E-08

Table 24: Geometric Factors of Triple Coincidence Events for Ne → O^-

i/k	1	2	3	4	5	6	7	8
1	0.00E+00	1.72E-06	0.00E+00	7.18E-06	0.00E+00	0.00E+00	0.00E+00	9.53E-06
2	0.00E+00	1.72E-06	0.00E+00	6.50E-06	1.83E-05	1.87E-05	8.52E-06	1.31E-05
3	0.00E+00	0.00E+00	2.15E-06	1.32E-05	2.13E-05	3.33E-05	2.13E-05	2.26E-05
4	0.00E+00	0.00E+00	0.00E+00	2.61E-06	2.80E-05	4.07E-05	3.46E-05	1.92E-05
5	0.00E+00	0.00E+00	0.00E+00	0.00E+00	5.25E-06	4.39E-05	3.59E-05	2.70E-05
6	0.00E+00	0.00E+00	0.00E+00	0.00E+00	0.00E+00	7.89E-06	3.56E-05	2.90E-05
7	0.00E+00	0.00E+00	0.00E+00	0.00E+00	0.00E+00	0.00E+00	9.20E-06	2.72E-05
8	0.00E+00	0.00E+00	0.00E+00	0.00E+00	0.00E+00	0.00E+00	0.00E+00	1.05E-05

5.4.3.1 Geometric factors for IBEX-Lo ISN O

The geometric factor of IBEX-Lo for heavy neutral atoms, such as O, is controlled by the combination of surface conversion and sputtering to negative ions. As a consequence, the peak of the effective response in energy E_{Peak} is always noticeably below the energy of the incoming neutral atom E_{In}, with this energy reduction factor $R = E_{Peak}/E_{In}$ decreasing with the energy E_{In} of the neutral atoms. In addition, the sensor detects these neutral atoms as negative ions over a broad range in energy around the peak energy E_{Peak} due to the large acceptance range $\Delta E/E = 0.7$ of the ESA and the broad range over which sputtered ions are generated. Therefore, the geometric factor that needs to be applied to a given combination of incoming energy E_{In} and IBEX-Lo energy step n (E-Step n = 1 8) depends on the absolute efficiency as a function of E_{In}, the reduction factor R, and where along the energy response function, relative to E_{Peak}, the energy of energy step n E_n lies.

To obtain such a geometric factor calibration, the energy response curve of the sensor is needed, how its peak energy varies with the incoming energy of the neutral atoms, and the absolute geometric factor as a function neutral atom energy. It turns out that based on various calibration runs with an O beam during final calibration before flight, a combined normalized energy response curve $\epsilon(E/E_{Peak})$ could be constructed, normalized to the peak efficiency and the peak energy for each beam energy. The best-fit energy response curve to the combined calibration data set yields

$$\epsilon(E/E_{Peak}) = \exp\left(-\frac{(E/E_{Peak}-1)^2}{2\delta^2}\right). \quad (16)$$

where $\delta = 0.59$. This functional dependence remains constant over the energy range of IBEX-Lo. The reduction factor $R(E_{In})$ as a function of beam energy E_{In} has been derived from a series of energy response measurements as:

$$R(E_{In}) = R_0 - R_1 \log(E_{In}), \quad (17)$$

where $R_0 = 1.04$ and $R_1 = 0.134$. ISN O arrives during the early spring ISN flow observation season in the IBEX frame at 1 au with a bulk energy of ≈540 eV. If

secondary O is included in the analysis, the range of O energies in the IBEX frame falls between 540 and 435 eV, the energy of O atoms arriving on bounding parabolic trajectories starting with 0 eV outside the heliosphere. This energy range is between IBEX-Lo energy E-steps 5 and 6, which are the only steps of interest here. The signals in E-step 4 and the lower steps are completely controlled by ISN He (Möbius et al. 2009, 2012), and the O signal is too weak in E-step 7 to be of much use.

To determine the absolute geometric factor for E-steps 5 and 6, we used calibration results obtained with a neutral O beam E_{In} = 279 and 601 eV, the nominal incoming energies for these two steps, with the IBEX-Lo response taken at the same energy step and all the way down to energy step 1. Using Equations (16) and (17) the energy response curve was then fitted to the set of calibration results for E-step 5 and 6, adopting the same ±35% uncertainty for the absolute efficiency of each calibration point. To get the values for the two bounding energies of ISN O, the geometric factors at E_{Peak} for the two E-steps were linearly interpolated. *Table 25* shows the resulting geometric factors for the ISN bulk flow energy (540 eV) and for ISN O on a parabolic trajectory (435 eV). Listed are the geometric factors at E_{Peak} for these input energies at the top, followed by the geometric factors for observations in E-step 5 and 6.

Table 25: Geometric Factors for ISN O

Parameter	ISN O	ISN O (ISN Traj)
$E_{1\ \mathrm{au}}$ (eV)	540	435
GF at E_{Peak} (cm^2 sr)	$9.6 \pm 3.4\ 10^{-5}$	$8.7 \pm 3.0\ 10^{-5}$
GF at E-Step 5 (cm^2 sr)	$8.8 \pm 3.1\ 10^{-5}$	$8.6 \pm 3.0\ 10^{-5}$
GF at E-Step 6 (cm^2 sr)	$5.6 \pm 2.0\ 10^{-5}$	$2.2 \pm 0.8\ 10^{-5}$

5.4.4 Generation of IBEX-Lo Good Times Lists

The primary method of background removal for IBEX-Lo is the culling of periods of high background. Thus, Good Times lists are generated in order to identify periods of low background which are suitable for scientific analysis of ENAs or ISNs. The process of defining these Good Times is highly manual and is described in this section. For convenience, Good Times lists are generated using histogram data at the same cadence as histograms (15 minutes).

IBEX-Lo Good Times are defined by excluding periods when:

1) The spacecraft was in the bow shock.
2) The IBEX-Lo field-of-view (FOV) was pointed at the Earth's magnetosphere or the count rates was anomalously high over an entire hemisphere or the full 360° over the course of an extended period of time for any reason.

3) Gain or threshold tests were performed.
4) The IBEX-Lo FOV was pointed at the Moon.
5) The spinning and pointing information are incorrect.

Thus, in order to generate the Good Times list for a given orbit the following inputs are needed: 1) Histogram count rates per spin bin, 2) Pointing information, 3) Spacecraft location, 4) Instrument operational information. Using this data it is trivial to remove periods where the spacecraft is in the bow shock, the instrument FOV is pointed at the Moon or magnetosphere, gain or threshold tests were performed, or the spinning/pointing data are incorrect. Thus it remains to manually remove extended periods of high background in one or both hemispheres.

Figure 64 shows an example of histogram data with significant background that is in need of culling. The plot shows a period of high background lasting for a few hours at the start of this period which extends over the full 360° followed by a longer period of more than two days in which significant backgrounds are seen primarily in the hemisphere from 180-360°. Figure 65 shows the resulting good times when the background in Figure 64 has been culled. Some studies call for additional culling beyond the basic Good Times list. In these cases, periods in which the count rate per spin exceeds 4 counts per spin are also excluded. The resulting culled list is called the Super Good Times List. Figure 66 shows an example of the time series of total count rate per spin for both Good Times and Super Good Times.

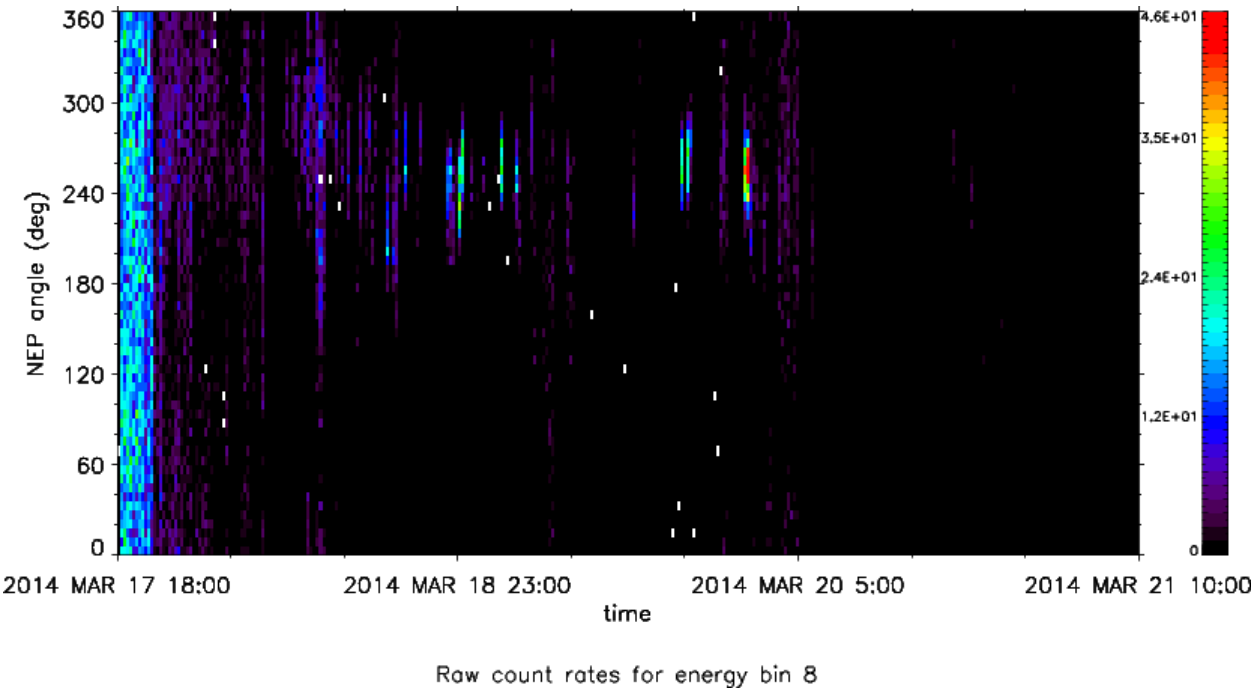

Figure 64: IBEX-Lo raw count rate histogram data for energy bin 8 over a period of almost four days. A high background period is seen extending over the full 360° for the first few

hours in this period, followed by a period in which backgrounds are observed primarily in the hemisphere from 180-360° for an extended period of more than two days.

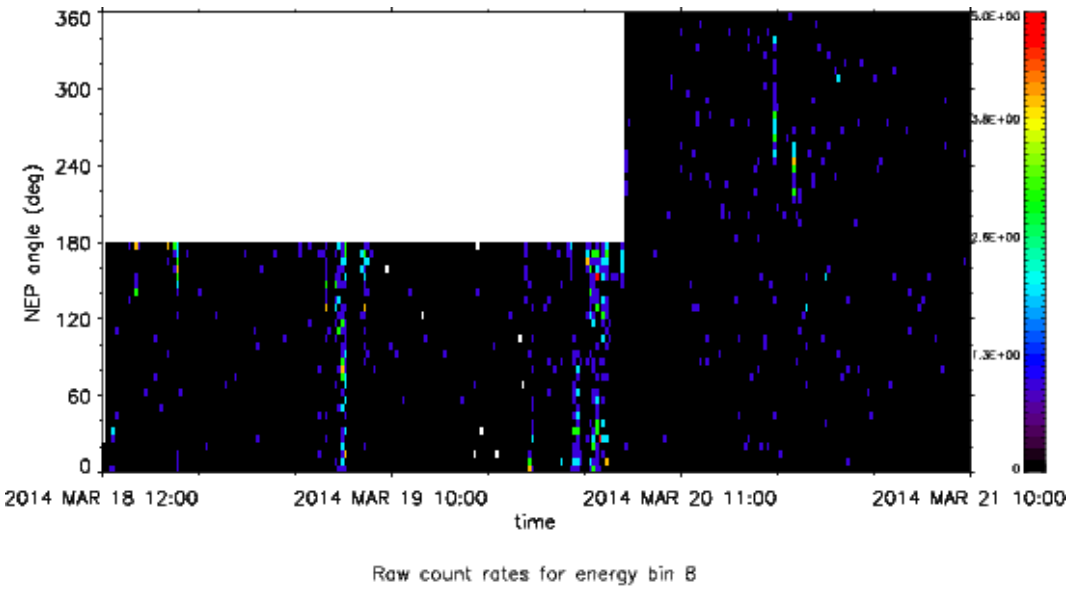

Figure 65: Histogram data showing the resulting Good Times after culling has been performed on the data in (note that the color scale in this figure is different than that of Figure 64).

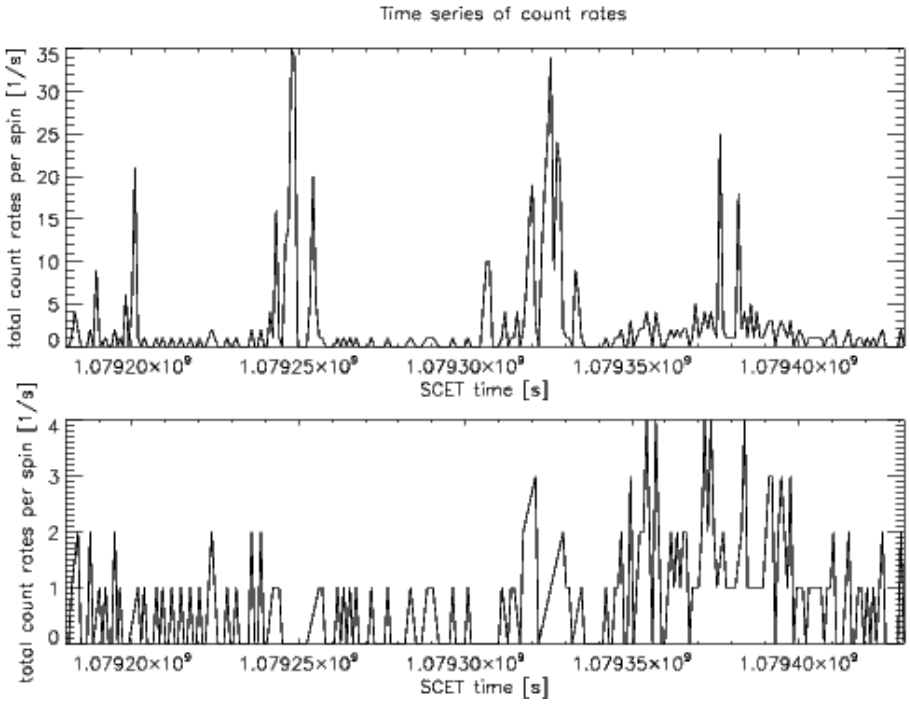

Figure 66: Good Times total count rate data per spin (top panel) and Super Good Times total count rate data per spin (bottom panel).

5.4.5 Removal of Observations with High Magnetospheric Backgrounds when in Magnetotail

This section provides a detailed discussion of data selection when the spacecraft is in Earth's magnetotail. Data intervals must be selected carefully to avoid regions with high magnetospheric backgrounds and must be selected for specific solar wind conditions that provide favorable magnetotail geometry and plasma conditions. Furthermore, only specific viewing directions of the heliosphere are available for these conditions. This section provides an example that identifies two viewing directions or pixels in the sky that meet these stringent criteria.

The lobes of Earth's geomagnetic tail are bounded by Earth's magnetopause and located above and below the plasma sheet. From the standpoint of ENA observations above 1 keV, the lobes are an ideal observing location. They are regions of low plasma beta, which implies low plasma densities and high magnetic fields. Because the magnetic field lines that thread the lobes are either "open" or have been open in the past, they are devoid of energetic plasma ions and electrons. Thus, they are free of any local energetic particle foreground in ENA images. Without this foreground, ENA fluxes from a distant source can be detected. Indeed, the first measurements of ENAs from the near-Earth region were made by an energetic particle instrument on International Sun–Earth Explorer spacecraft that was in the lobes (Roelof 1987).

Magnetic reconnection at Earth's dayside magnetopause has a dominant effect on the structure of the lobes and the properties of the plasma within them. Gosling et al. (1985) noted that plasma densities in the northern and southern lobes differed by a factor of 10 or more. Furthermore, density differences were observed in different quadrants of the lobes, and these differences were correlated with the orientation of the interplanetary magnetic field (IMF). Gosling et al. (1985) were able to associate density differences in the lobe with magnetic reconnection at the dayside magnetopause, convection of reconnected field lines into the tail lobes, and E×B drift of plasma through the open magnetopause and into the lobes.

Figure 67 is a schematic representation of the lobe density structure that results from dayside magnetic reconnection. This cross section of the magnetotail at ~40 Earth Radii (RE) from the Earth splits the lobes into four quadrants. For the average IMF orientation shown in Figure 67, the upper right quadrant of the north lobe and the lower left quadrant of the south lobe are associated with open magnetic field lines. The other two lobes are associated with closed magnetic field lines. In the open quadrants, low energy plasma from Earth's dayside and low energy plasma from the high latitude magnetopause on the nightside can E×B drift into the lobes. This plasma has energies of about 0.3 keV (Hirahara et al. 1997) and, while convecting tailward, can also have a significant drift toward the plasma sheet.

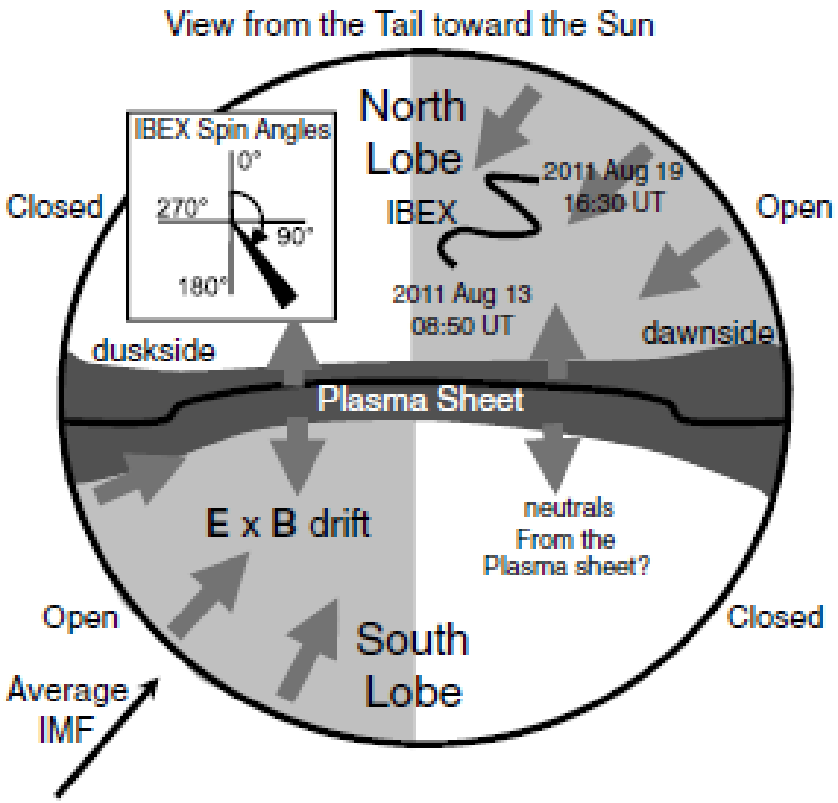

Figure 67: Schematic cross section of Earth's magnetotail about 40 RE from the Earth. The view is toward the Sun. Low energy ions enter the magnetosphere on the dayside and on the flanks of the magnetopause through open field lines. For the average IMF shown, these ions can drift into the lobe in the two quadrants shown. The other two quadrants are devoid of these low energy ions. Possible sources of background in heliospheric ENA measurements include these low energy ions and neutrals created by charge exchange of low energy ions from the lobes or plasma sheet. Careful selection of intervals with stable IMF and careful selection of view directions minimizes these backgrounds.

The presence of this plasma in an otherwise low density, very low energetic particle flux region is a significant complication for heliospheric ENA observations at low energies in the lobes. The difficulties are particularly acute for IBEX-Lo, which does not reject ions above about 0.2 keV from entering the sensor. IBEX-Lo was supposed to have a positive high voltage on its collimator. However, this voltage failed during commissioning. The sensor has an internal deflection voltage for low energy ions (less than about 0.2 keV), but higher energy ions can enter the sensor and sputter low energy negative hydrogen off the conversion surface, creating a background. Above ~15 keV, ion fluxes are detected in the IBEX background monitor (Funsten et al. 2009a; Allegrini et al. 2009). Therefore, for intervals when IBEX is in the plasma sheet (which contains hot, dense plasma with energies up to tens of keV), the background monitor flux is used to eliminate these intervals. However, any ions between 0.2 and 15 keV, like those

encountered in Earth's lobes, create a potential background in IBEX-Lo and are not detected in the IBEX background monitor.

Even if these low energy ions could be rejected, there is also a small flux of neutrals at energies below 0.3 keV that result from charge exchange of low energy ions in the lobe with Earth's geocorona. These neutrals are indistinguishable from neutrals from the heliosphere at the same energies. To reduce background from low energy ions and neutrals in the lobe, data interval and view angles must be carefully chosen. For example, in Figure 9, the apparent IBEX trajectory in the cross section of the magnetotail from 2011 August 13–19 is shown. During this time in orbit 136b, there are long intervals when the IMF orientation (convected from the ACE spacecraft solar wind monitor to the location of IBEX in the magnetotail) was within about 40 degrees of the orientation shown in Figure 67. For that magnetic field orientation, the open lobe quadrants (which are regions with ion distributions E×B drifting into the lobe) should be in the upper right and lower left. The small inset in the magnetotail cross section shows the IBEX sensor spin angles. IBEX views 360◦, essentially normal to the magnetotail axis. For the orientation of the IMF shown, one would expect higher background levels for spin angles from 0◦ to 90◦ and from 180◦ to 270◦. Furthermore, if there are neutrals from charge exchange of plasma sheet ions, they may also appear in spin angles from 90◦ to 180◦. Thus, for this particular IMF orientation and IBEX spacecraft location, only the quadrant from 270◦ to 360◦ is available for viewing heliospheric neutrals at low energies. Similar conditions occurred during orbit 137b. These two orbits combined provided the intervals for observing the near- Voyager 1 direction in Figure 68.

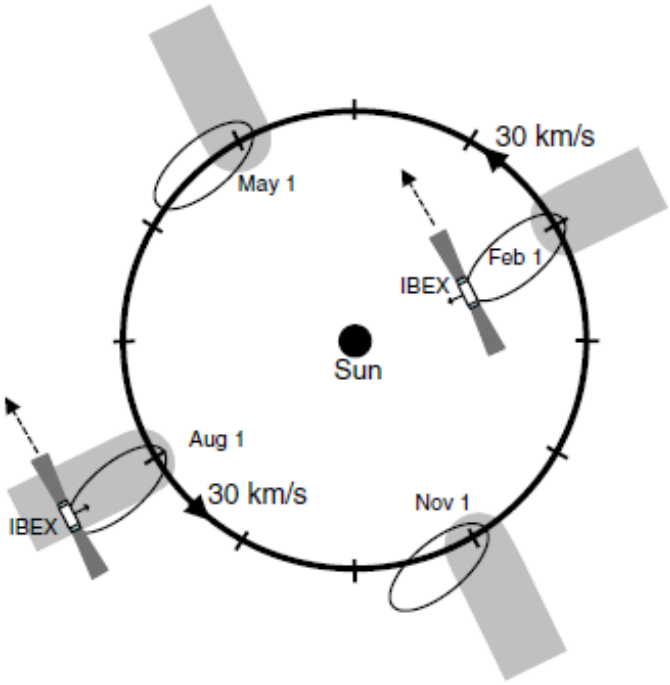

Figure 68: IBEX's orbit around the Sun (not to scale). The spin axis is always directed within about 7° of the Sun, so that the sensors sample the same region of the sky every

6 months. The dashed lines show the view direction in the ecliptic in February and August. In February (August), heliospheric ENAs have the 30 km s^{-1} velocity of the Earth added to (subtracted from) them. ENA signal from the heliosphere should be the same in February and August, after the appropriate frame transformation. However, the ENAmeasurements in February and August are made in very different near-Earth regions and susceptible to different backgrounds. In February (August), ENA measurements are made when the spacecraft is in the solar wind (in Earth's magnetosphere, shown by the shaded regions).

During orbit 44, from 2009 September 6–9, IBEX was in the southern lobe in the lower left hand quadrant of Figure 67. There were long intervals (hours at a time over several days) when the IMF average orientation was the same as shown in Figure 67. For these intervals, the available spin angles for viewing heliospheric neutrals were between 90◦ to 180◦. This orbit provided the intervals for observing the downstream direction in Figure 68.

5.4.6 IBEX-Lo Species Classification and Selection

In IBEX-Lo, measured ENA events may be classified as species of particular elements based on their time-of-flight values. Depending on whether processing occurs in flight code, pipeline map making code, ground based "IDEAS" IDL code, or the Perl based mapping code, the exact set of algorithms varies.

This section reviews the methods of species classification used for IBEX-Lo. Data from various orbits are used as examples, with both 2D, 3D and 4D plots used as tools to perceive both the differences amongst the algorithms as well as the data itself. A common set of plot techniques for visualization will allow the team to understand any changes applied to algorithms for species determination as we move forward.

5.4.6.1 The Use of TOF Factors in Species Determination Thresholds

IBEX-Lo has the capability to distinguish a small set of ions by mass through postacceleration by nominally 16 kV (maximum 20 kV) and subsequent triple time-of-flight (TOF) analysis.

Figure 69 and Figure 70 show a schematic radial cut of the TOF subsystem together with the major electronic blocks. The incoming ions generate secondary electrons at the first carbon-foil that are guided to the outermost section of the microchannel plate (MCP) detector. Similarly, electrons are generated at the second foil and guided to the innermost section of the MCP. The ions are detected in the center section, which is divided into 4 quadrants to allow for a separate background characterization. A single MCP pair is used. The anode pattern that provides for these signals is shown in the upper right of Figure 70. Three TOF values are determined between each of the foils and the MCP (TOF0 and TOF1) and between the two foils (TOF2). Each of these three

TOF measurements is equivalent to the observation with a CODIF-like sensor. The ability to use any of the three measurements provides for very high efficiency.

The quadrant position is derived from a delay line TOF measurement (TOF3). A histogram showing event distribution amongst the possible and primary TOF3 values is shown in Figure 71. It has been suggested that we may want to primarily select events from the primary TOF peak distributions, as they suggest a more certain event has occurred, and ignore the relatively few, perhaps more ambiguous/scatter, events in the valleys. The number of events that would be thrown away using this criteria is being developed. Such thresholds would have to be determined prior to the application of any TOF3 factors (described below). It may be appropriate to apply different criteria per LO energy range.

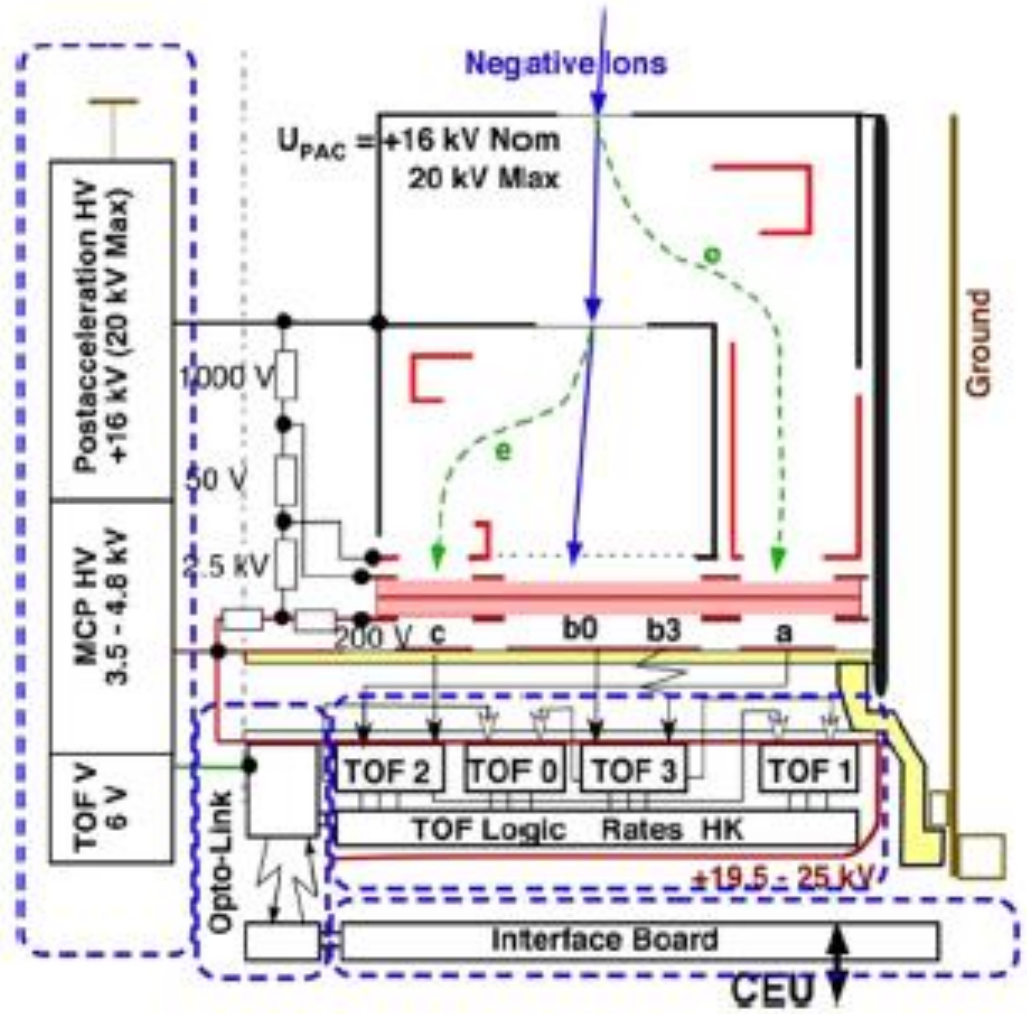

Figure 69: Functional schematics of the IBEX-lo TOF system. A radial cut is shown on the left with a block diagram of the main electronic elements. All 4 TOF measurements are indicated.

The effect of the TOF3 values upon event placement in the TOF 3D data space (or 4D with TOF3 color coding of events) is depicted in Figure 72, Figure 73 and Figure 74. These 3D plots show data from orbit 110 and orbit 20 which has been filtered to contain only triple golden events (0000 or all TOFs present) and no TOF equal to zero. One can see from the particular viewing angle of Figure 71 and Figure 72 that the events tend to fall mostly in one of four planes, each color coded by one of the major peak locations of TOF3 distributions at TOF3 equal to 1, 21, 41 and 71 and inclusive of a range of values around those peaks. However, there are some events that fall in the valleys of the distribution and these are denoted by shades of gray to black. These can be seen in the closeup of the hydrogen events in Figure 73. When viewed from overhead, i.e., looking "downward" onto TOF0 vs TOF1, as in Figure 74, the event planes are harder to perceive.

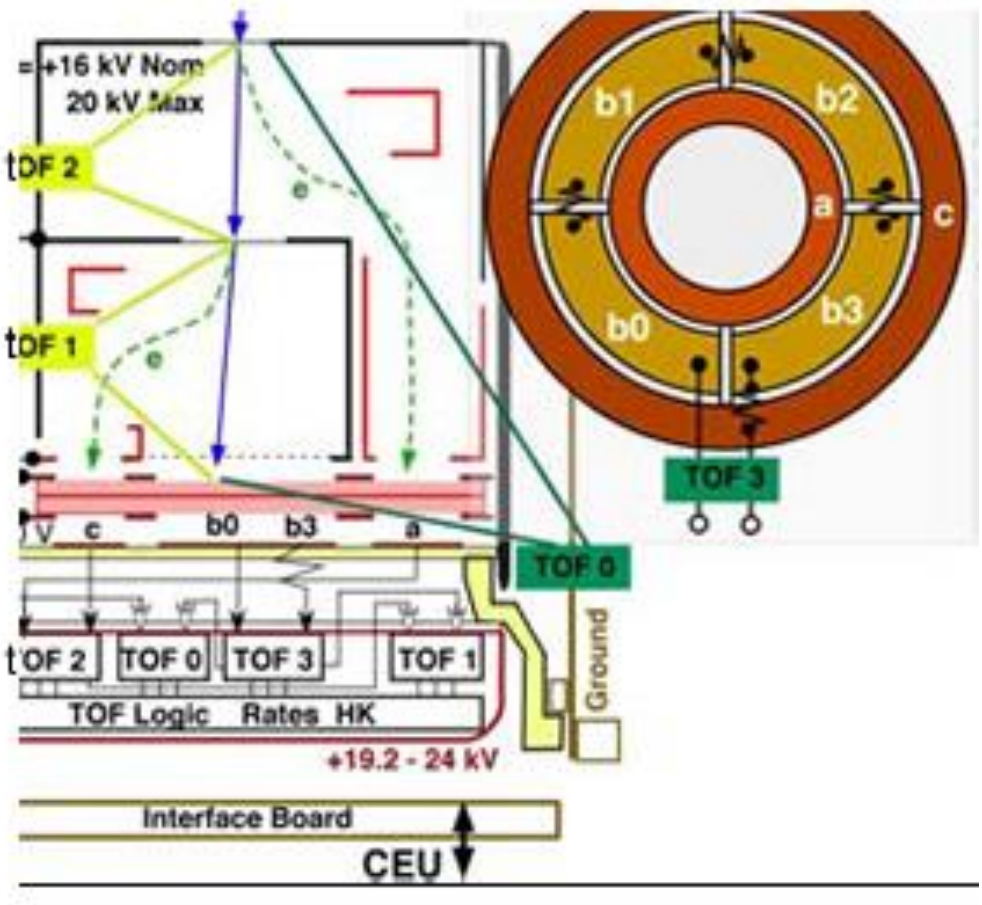

Figure 70: A top view of the signal anodes is shown on the right with the 4 quadrant anodes in the Stop portion of the MCP, which are connected by delay lines. Closeup of the elements from which the 4 TOF measurements are derived.

In subsequent discussions of algorithms below, TOF3 factors are added or subtracted to the other TOF values in order to minimize or nullify the effects of the inclusion of

TOF3 in TOF0 and TOF1's values. To illustrate this, Figure 75 shows the effect of applying the factor of TOF3/2 to TOF0 as TOF0 + TOF3/2 and to TOF1 as TOF1 - TOF3/2 which causes the data events to fall essentially into the same plane (not exactly, but very close). This allows the limits applied as species thresholds to be more tightly specified as well as TOF3 quadrant neutral. The change from Figure 73 to Figure 75 illustrates how the spreading effect of TOF3 is minimized if not eliminated.

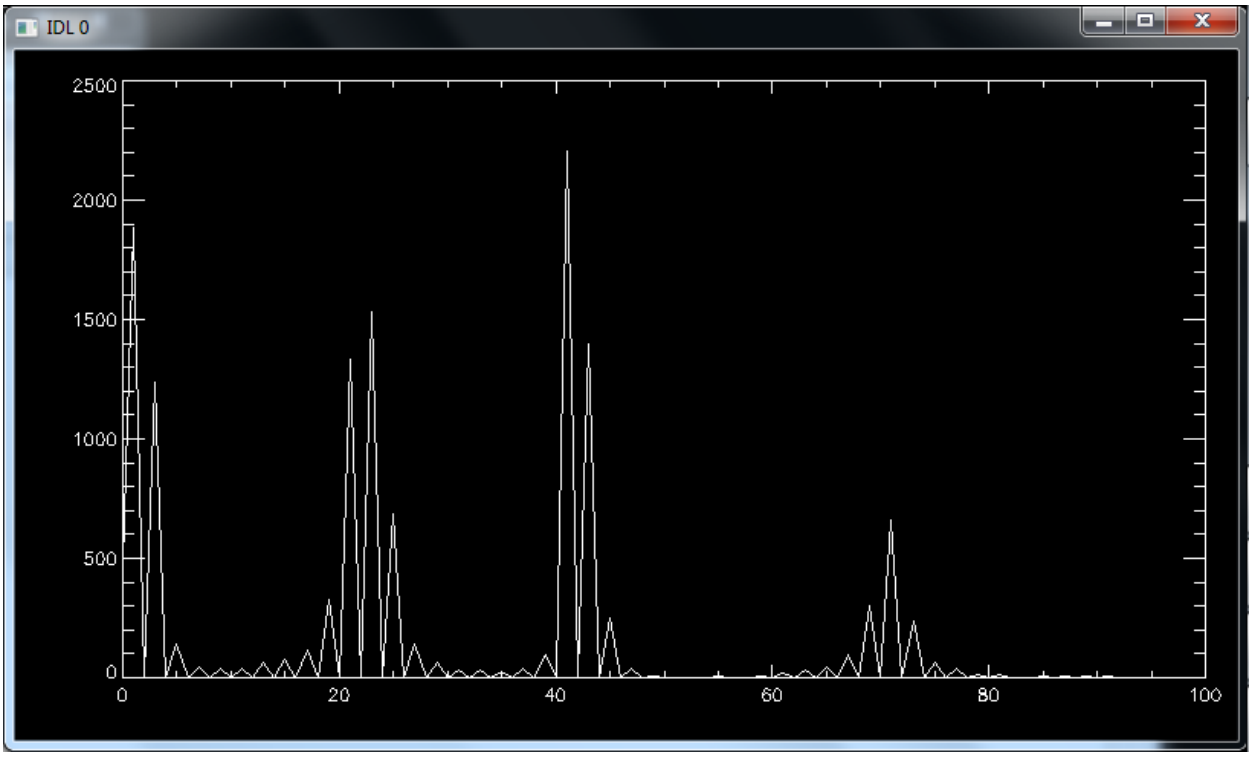

Figure 71: Histogram showing event distribution among possible and primary TOF3 values for orbit 110.

Ion detection with a maximum of background suppression is achieved when all 4 TOF signals are registered. It is clear from the data however, that even though all four TOF signals may be present, some of those may be 0. This is evident in Figure 9.8 showing an unfiltered plot of triple golden events, some of which reside on the 'walls' of the TOF 3D data space. The zero events fall along the axis or are circled in the following plot (not inclusive of all zero TOF valued events).

5.4.6.2 Flight Software Species Determination Algorithm

IBEX Lo collects H and O ENAs in spin angle histograms. In order to perform this action the flight software (ie, the CEU code) identifies these species based on the time-of-flight (TOF) values obtained for each PHA event. The default setting specifies that triple coincidence events are accumulated into the Histograms, with the provision that other

types of PHA events may be selected depending on the functional state of IBEX-Lo and/or considerations derived from data analysis.

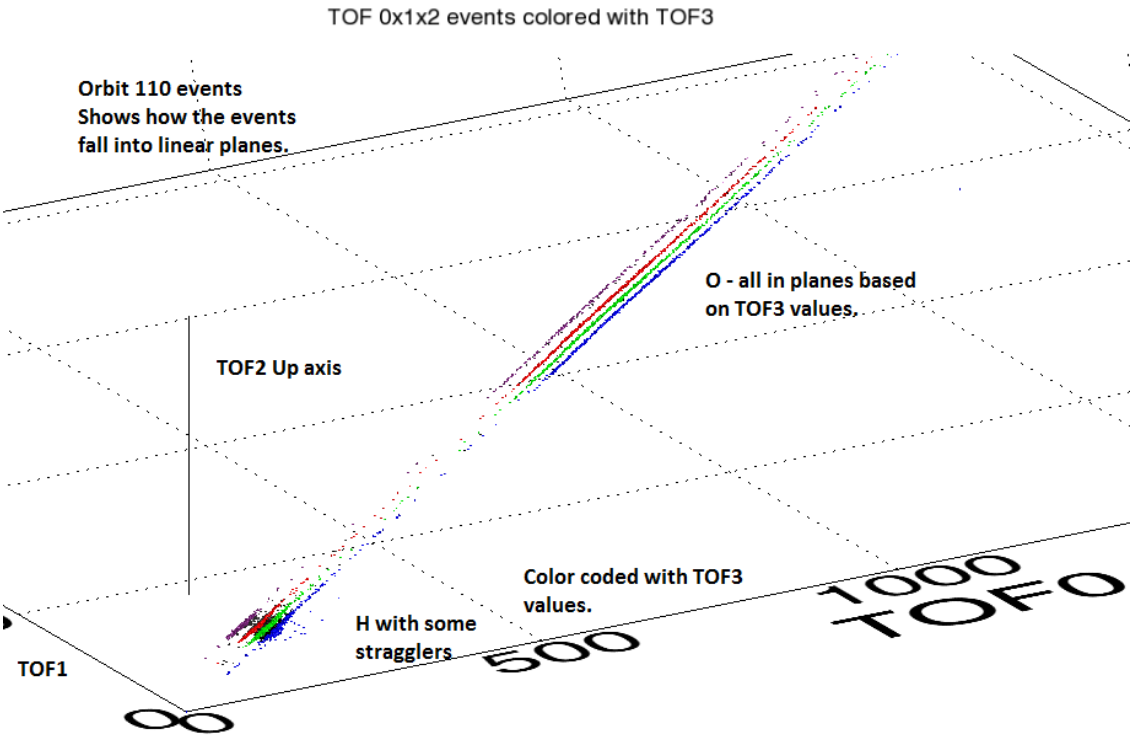

Figure 72: 3D plot showing data from orbit 110 and orbit 20 which has been filtered to contain only triple golden events (all TOFs present) and no TOF equal to zero.

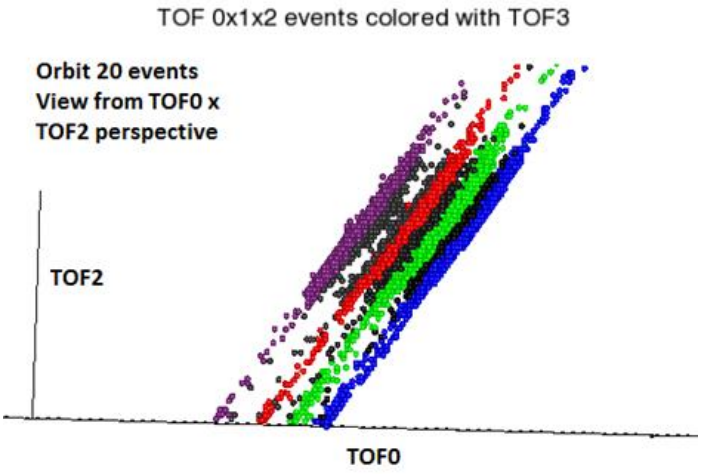

Figure 73: 3D plot showing data from orbit 110 and orbit 20 which has been filtered to contain only triple golden events (all TOFs present) and no TOF equal to zero.

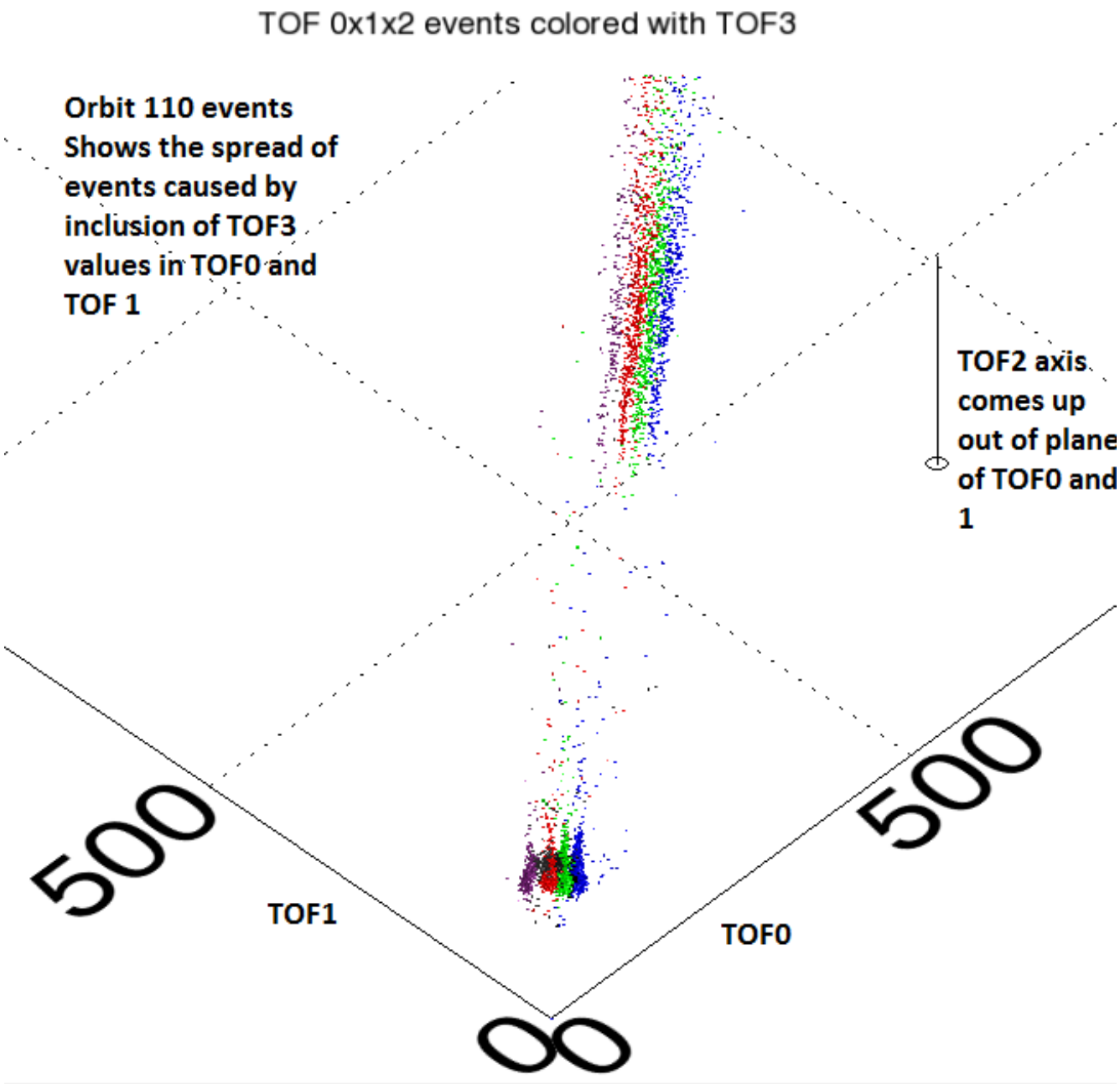

Figure 74: 3D plot showing data from orbit 110 and orbit 20 which has been filtered to contain only triple golden events (all TOFs present) and no TOF equal to zero.

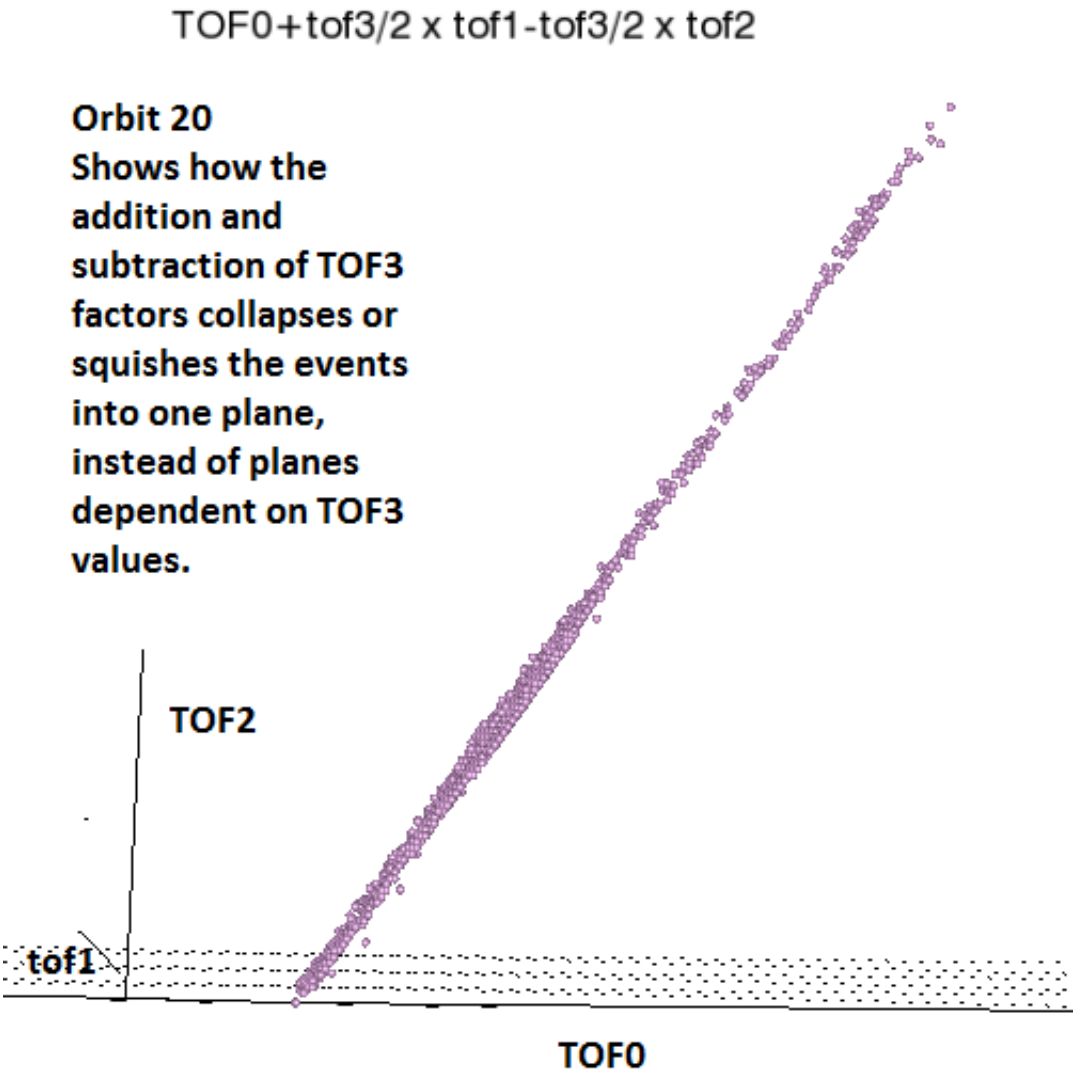

Figure 75: TOF0 + TOF3/2 x TOF1 - TOF3/2 minimizes the effect of TOF3 on placement of events in 3D data space

Triple PHA events contain all TOF values. However, based on Pre-Cal 2 data from the University of Bern tests, it was determined that only TOF2 needed to be evaluated. As designated below, incoming neutral atoms could be identified as either H or O if they fall between a lower and upper TOF limit. These limits depend on the PAC voltage, but only in a negligible way on the particle energy because the original particle energy is small compared to the energy attained by post-acceleration. It was understood that the TOF limits may change with actual PAC setting in orbit and may be subject to update as better calibration analysis was performed. The conversion between raw values in Bits and TOF values in ns is formatted as follows:

$$TOFX(ns) = C_0 + C_1 \cdot RAW(ADC) \quad (18)$$

where TOFX stands for TOF0, 1, 2, or 3 and C0 and C_1 are constants from calibration. For TOF2, C_0 is 0.87, and C1 is 0.1671. (NOTE: The C_1 value equates to a division of the raw ADC value by approximately 6 in all TOF cases and is used instead of .1671 in Perl code. See discussions of the Perl code in following sections)

The flight software was therefore configured to read a look up table (LUT) table to retrieve the min and max TOF values for H and O. The algorithm uses the following set of tests depending on the presence of certain TOF values as outlined below.

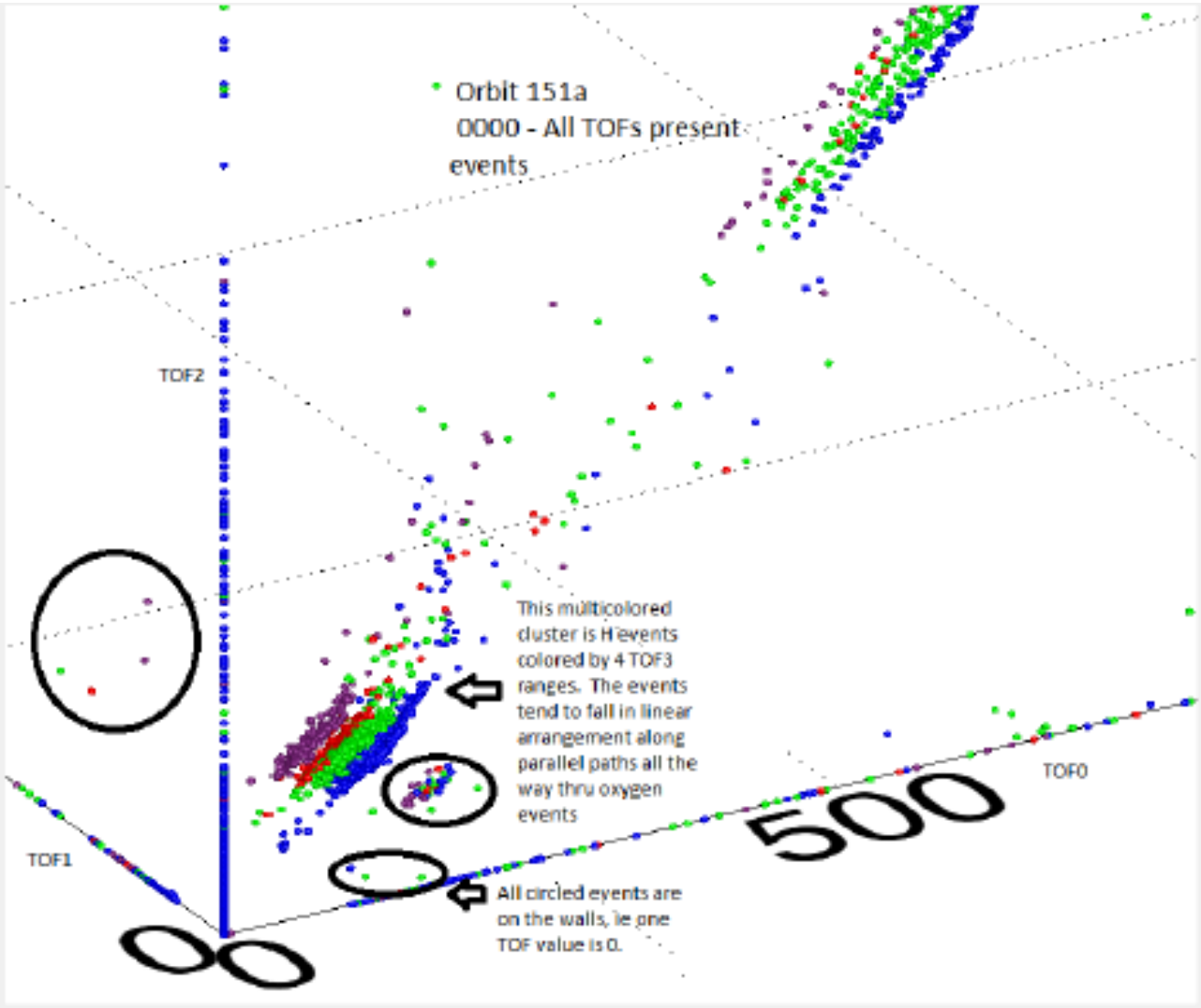

Figure 76: *3D plot showing data from orbit 110 and orbit 20 which has been filtered to contain only triple golden events (all TOFs present) and no TOF equal to zero. This plot shows that some triple golden events have 0 in one or more TOF values.*

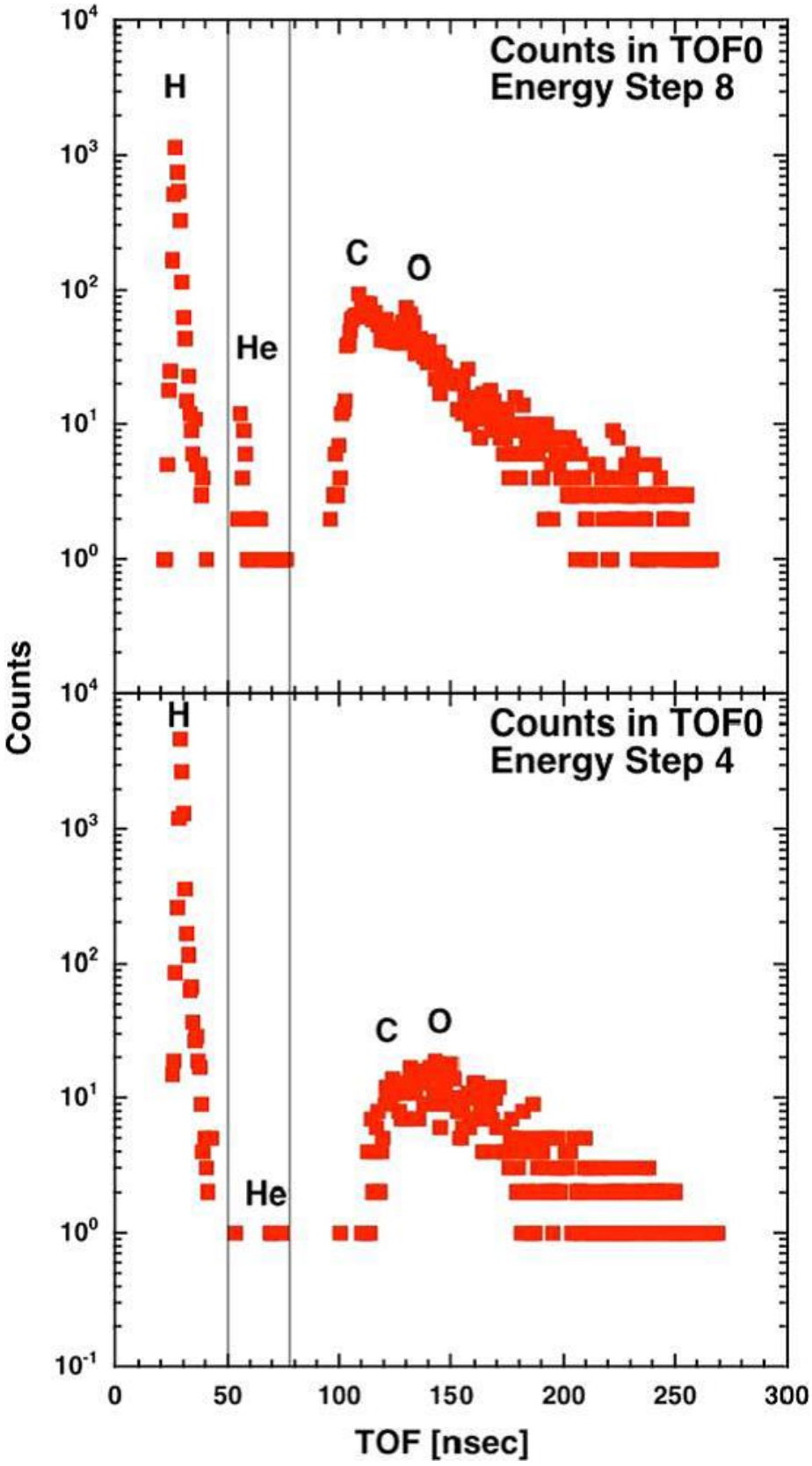

Figure 77: Time-of-flight spectra for various species during calibration

5.4.6.3 TOF2 Present

For golden triples (and all cases where TOF2 is present), the limits shown in Figure 78 determine whether an event is considered H or O.

Figure 78: TOF2 thresholds

5.4.6.4 TOF0 + TOF3/2 when no TOF2

In cases when TOF2 might not be available for any reason, i.e., when it is not considered present in the TOF coincidence quartet, TOF0 is the next best time-of-flight measurement to use. In fact, it is even of better resolution for H than TOF2, but not for O. Because the observation of TOF0 is influenced by the Delay Lines for TOF3 and thus time-of-flight values for each of the 4 quadrants differ, we need to use a corrected value for TOF0 by including a factor based on TOF3. The resulting equation, TOF0 + TOF3/2, adjusts TOF0 appropriately. Preliminary limits for TOF0 + TOF3/2 are given below. For TOF0, C_0 is 1.131, C_1 is 0.1662.

Figure 79: TOF0 + TOF3/2 thresholds

5.4.6.5 TOF1 - TOF3/2 when no TOF2 or TOF0

Additionally, in those cases when both TOF2 and TOF0 are not available for any reason, i.e., when they are not considered present in the TOF coincidence quartet, TOF1 is considered the fallback time-of-flight measurement. Similar to TOF0, the observation of TOF1 is influenced by the Delay Lines for TOF3 and thus time-of-flight values for each of the 4 quadrants differ. Again, we need to use a corrected value of TOF1 - TOF3/2 instead. Appropriate preliminary limits for TOF1 - TOF3/2 are given below. For TOF1, C_0 is 1.2808, and C_1 is 0.1642.

Figure 80: TOF1 - TOF3/2 thresholds

5.4.6.6 Conversion for TOF3

Since TOF3 is used for the correct evaluation of TOF0 and TOF1, the conversion for TOF3 specifies C0 is 0.2385, and C1 is 0.1646 Note that the values for 12 kV PAC voltage have been computed according to the following relation as function of U PAC, which is fairly accurate for the range of $12\ \mathrm{KV} = \mathrm{U\ PAC} = 20\ \mathrm{kV}$: $TOF(PAC) = TOF(16\ kV) \cdot v(16/U\ PAC\ [kV])$

5.4.6.7 Ground Based IDEAS vs PERL Algorithms

In this section we discuss the differences between the pipeline based ground processing used in the IDL IDEAS analysis code versus the Perl code used to generate maps.

5.4.6.8 Perl Algorithm

In the Perl algorithm, H and O events are determined from a sequence of tests using TOF0 combined with TOF2. Prior to these steps, the Perl code selects only golden triple events. In the following discussion, the hard coded numbers (201, 501, and 1000) refer to raw ADC values and the divide by 6 converts values from raw DAC values to ns values.

Perl Algorithm Steps:

1. Checksum Test: $cs = $tof0 + $tof3 - $tof1 - $tof2 is used to confirm the checksum <= 2.0.

   (NOTE: This differs by a test $cs < 1.0 in the IDEAS code

   (ground based IDL code that calls pipeline routines).)

   if(sqrt($cs*$cs) > 2.0) bypass
2. Electron Test (throw out): TOF0+$TOF2 < 201/6 (or < 33.5ns)
3. Hydrogen Test: TOF0+$TOF2 < (501.0/6.0) (or < 83.5ns)
4. Oxygen Test: (TOF0+$TOF2) > (1000.0/6.0) (or >166.7ns)

Put another way, the TOF0+$TOF2 ranges for PAC 16 KeV are:

16 KeV 0--E--<33.5--------H------<83.5------166.7<-----O---max (ns)

There is no accommodation for UPAC 12 KeV in the Perl code.

5.4.6.9 IDL Ideas Code Output (based on ISOC pipeline routines) Compared to Perl Code

The detail lower and upper limits in TOF2 used in flight and Ideas code and the three boundaries of TOF0+TOF2 used by Perl code are listed in Table 9.1.

Table 26: The criteria used to identify ENA species used in CEU and Perl code.

CEU Lower and upper limits in TOF2		Perl code	
U_PAC = 16 keV:			
H: 9 = TOF2 [ns] = 20	-> Io(H.)	TOF0 + TOF2 < 201.0/6.0	-> 'ET'
O: 50= TOF2 [ns] = 100	-> Io(O.)	201.0/6.0 = TOF0 + TOF2 < 501.0/6.0	-> 'HT'
Others	-> Io(Io)	TOF0 + TOF2 > 1000.0/6.0	-> 'OT'

Figure 9.13 shows a scatter plot of TOF0 versus TOF2 for all triple events of orbit 20 at energy step 2. Two horizontal red dashed lines indicate the lower and upper limits in TOF2 for Hydrogen events and two horizontal blue dashed lines represent the lower and upper limits in TOF2 for Oxygen events. Three diagonal green dashed lines indicate the TOF0+TOF2 boundaries to determine ENA species in Perl code.

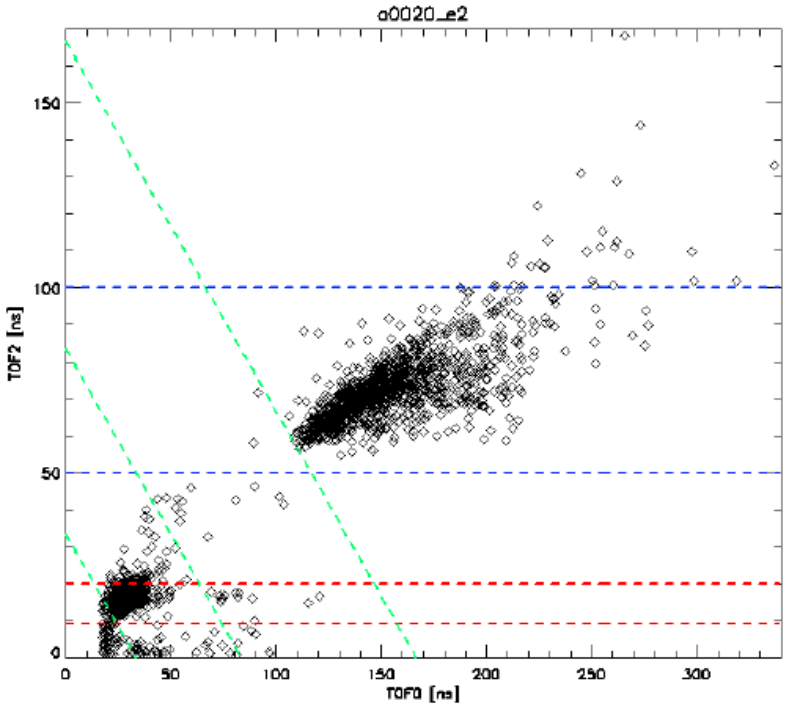

Figure 81: The two criteria delineated by horizontal (flight, pipeline and IDL Ideas) vs vertical (Perl) lines in data space.

5.4.6.10 Discrepancy between the Pipeline and Perl Criteria

Figure 82 and Figure 83 below show the difference between the two approaches. The pipeline plot (Figure 82) shows Hydrogen events (red diamond) selected by TOF2 limits. It also includes a few events which have much longer TOF1 values than TOF2. Approximately 0.5 % of these Hydrogen events do not satisfy the Perl TOF0+TOF2 threshold, i.e. 0.5 % of Hydrogen events are out of the green boundaries (around the regions of TOF0 = 20 ns and TOF0 > 70 ns).

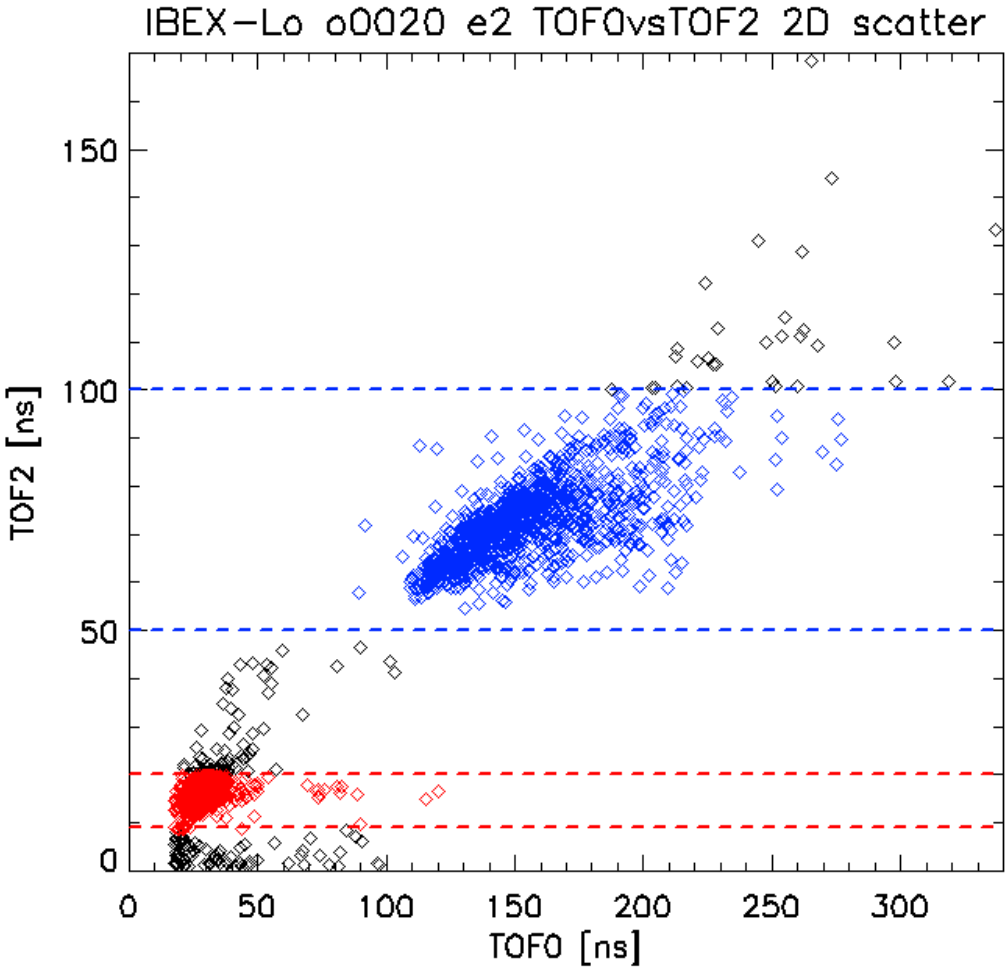

Figure 82: TOF0 versus TOF2 scatter plots showing triple events selected by pipeline upper and lower limits of TOF2. H:red diamond, O:blue diamond, others: black diamond.

The Perl code plot (Figure 83), on the other hand, shows events selected by TOF0+TOF2 boundaries. Approximately 1.8% of events are out of the red boundaries, some of them are above the upper limit and the others are below the lower limit. Therefore, the total discrepancy between two criteria is approximately 2.3%.

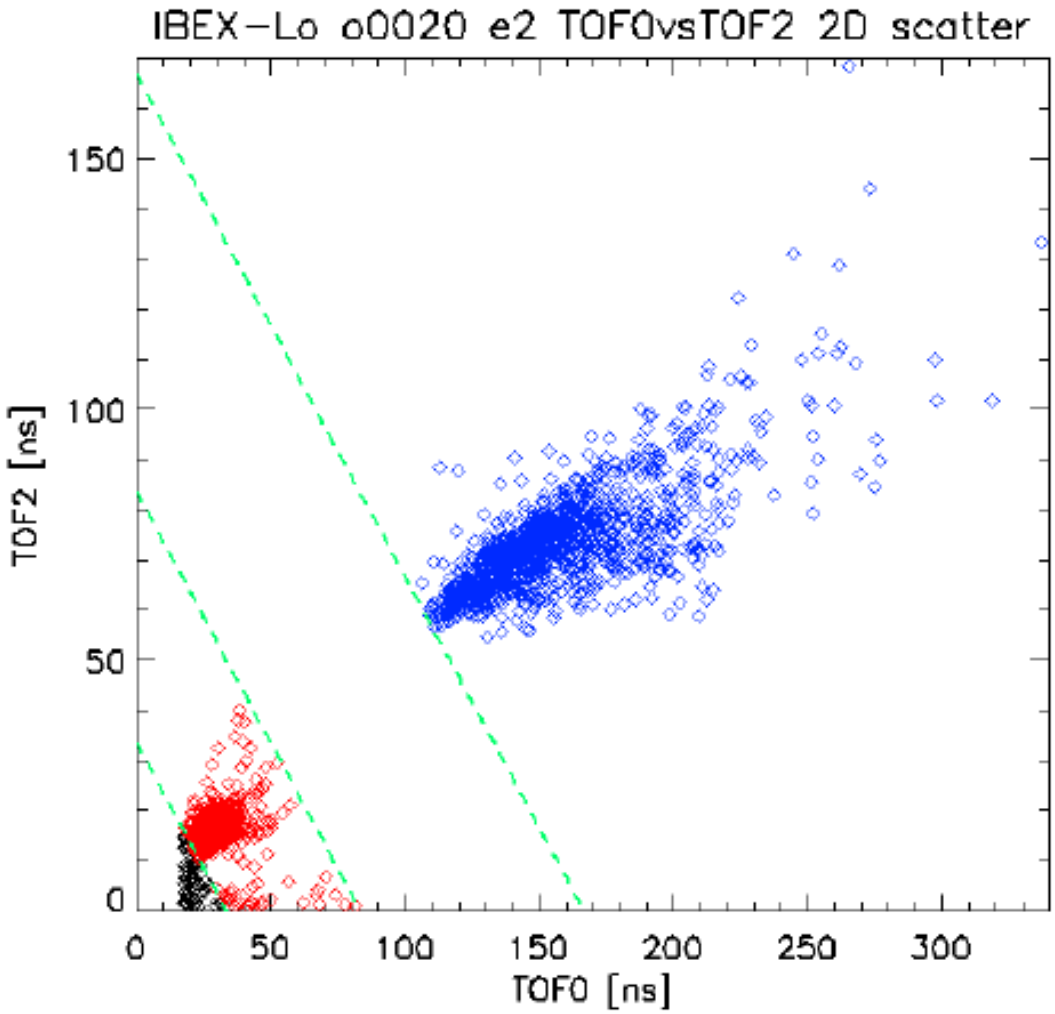

Figure 83: TOF0 versus TOF2 scatter plots showing triple events selected by Perl use of upper and lower limits of TOF0+TOF2 boundaries. H:red diamond, O:blue diamond, others: black diamond.

Figure 9.16 below shows the rate of "out of the red" boundaries when we use TOF0+TOF2 condition as the identifying criterion. In the IDL Ideas code, the textual label assigned to each event is used to select events, not the original TOF data. In a sense, this is post species assignment that occurred either by the spacecraft or by subsequent pipeline reprocessing of events using purify and the program lo de tof (both discussed in a subsequent section). The identifiers are a mix of H, O and 'lo' with a format of one or two characters (assigned before lo de tof) and one or two characters in parenthesis (H.|O.|lo) that are indicative of lo de tof recategorizing the event.

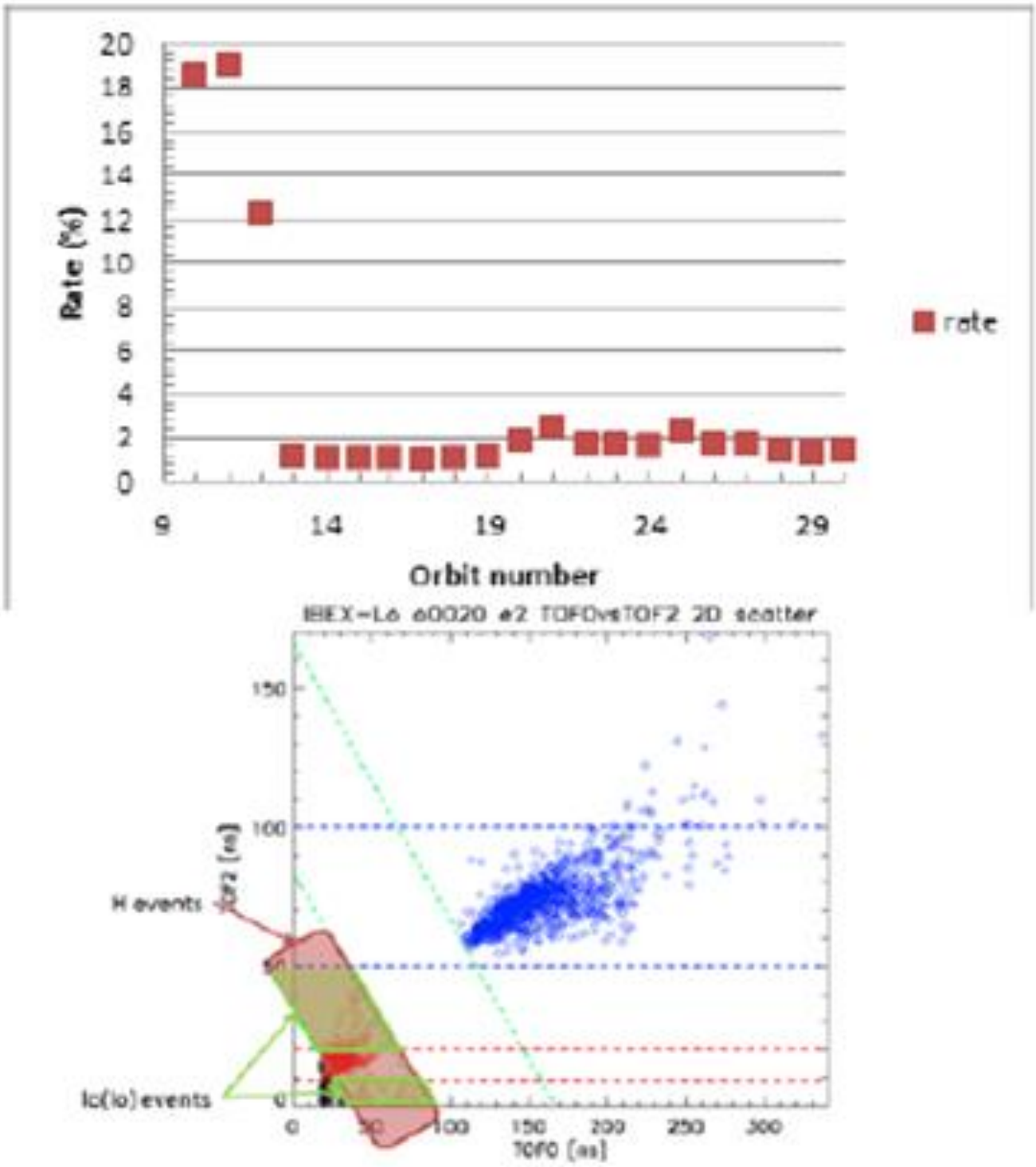

Figure 84: Discrepancy percentage of events satisfying the TOF conditions and including lo (H.) (events in the red box) to events satisfying the TOF conditions and including lo (lo) (events in the green boxes).

The criterion using TOF0+TOF2 boundaries is contaminated by some electron events as we can see in the right side of Figure 83 (events below the lower TOF2 limit, 9 ns) and exclude some events near TOF0 = 20 ns and TOF2 = 12 ns. Considering these errors, it would seem the criterion using the lower and upper limits in TOF2 shown in Figure 82 is more reasonable to determine ENAs species. However, there is another issue in TOF2 limits. We can see in Figure 82 and Figure 85 that TOF2 limit criterion includes some events having long TOF0 values (TOF0 > 65 ns in the reddish shadow in Figure 85, a red tail region). It means that these events have at least three times longer TOF1 values than TOF2, which is physically impossible because the flight distances for TOF1 and TOF2 are the same. In addition, events between the upper limit of TOF2 for H and the lower limit of TOF2 for O (20 ns < TOF2 < 50 ns in the gray shadow in Figure 85, a black tail region) are more reasonable events, from a physical point of view, than the red tail events. Figure 86 shows the number of events located in the red and black tail regions. Table 27 lists the percentages as the number of each tail event over the total number of H events.

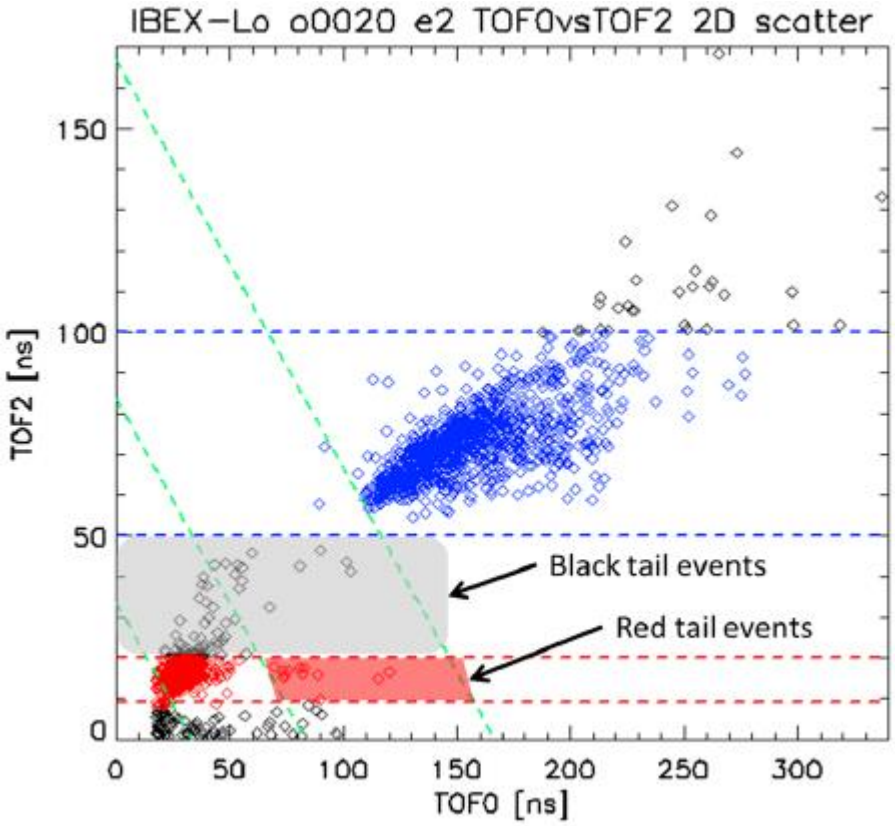

Figure 85: Two tail regions (red and black) are seen in TOF0 versus TOF2 scatter plot. The black tail events are located in the gray shadow region between the upper limit of TOF2 for Hydrogen (20 ns) and the lower limit of TOF2 for Oxygen (50 ns). The red tail events are located in the reddish shadow region which is the overlap region between TOF2 limits for Hydrogen and TOF0+TOF2 limits for others.

Table 27: The number of H events, E events, red tail events and black tail events. The events species is identified by TOF2 limits and the numbers in the parenthesis are the percentages which are the number of red or black events over the number of the H events.

Orbit	H events	E events	Red tail events	Black tail events
18	48,129	841	54 (0.112%)	537 (1.116%)
19	19,234	376	21 (0.109%)	213 (1.107%)
20	6,270	206	13 (0.207%)	96 (1.531%)
21	4117	169	7 (0.170%)	85 (2.064%)
22	4422	154	7 (0.158%)	66 (1.493%)

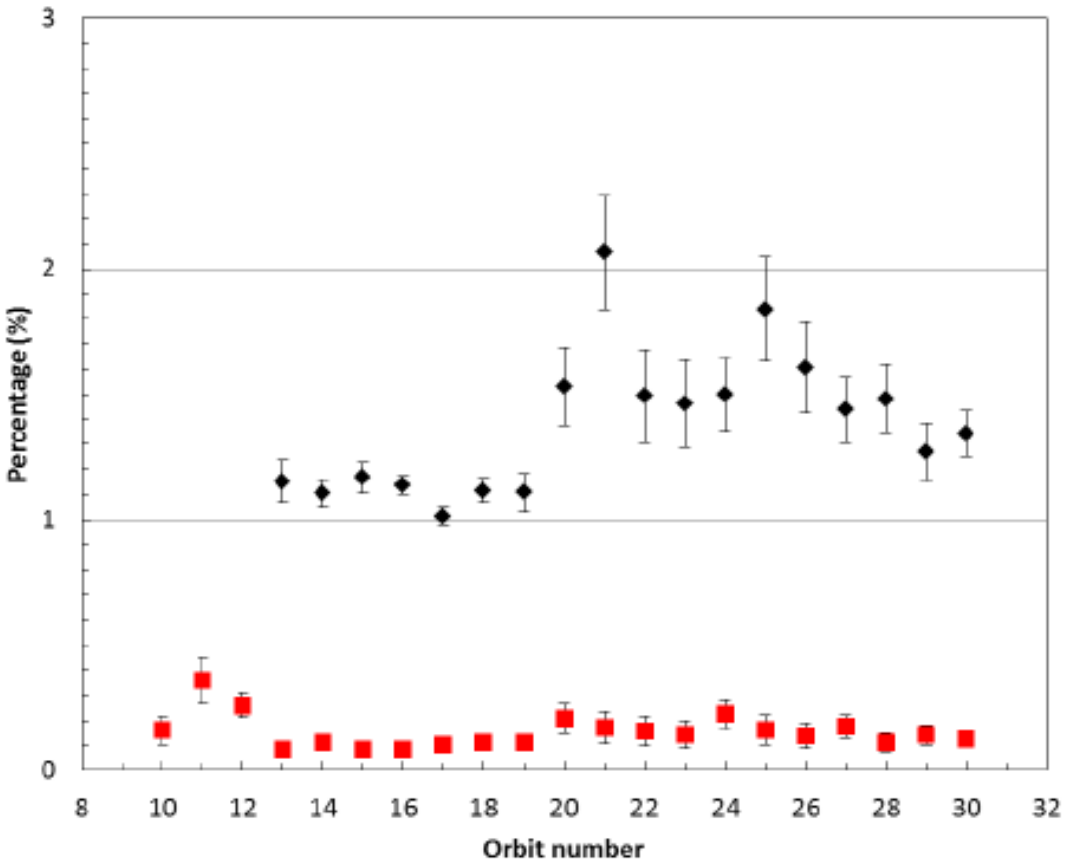

Figure 86: The tail percentages for orbit 10 to 30. The red closed rectangular boxes are the red tail percentages and the black closed diamonds are the black tail percentages. The black tail event percentages for orbit 10 to 12 are 19.5, 18.9, and 13.0%, respectively

orb	H events	E events	red tail	black tail	p1 (%)	p2 (%)
10	5001	15975	8	977	0.159968	19.53609
11	4177	15370	15	789	0.359109	18.88915
12	10801	15428	28	1409	0.259235	13.04509
13	16486	326	14	190	0.084921	1.152493
14	37095	669	41	410	0.110527	1.10527
15	30327	541	26	354	0.085732	1.167277
16	88970	1523	75	1012	0.084298	1.137462
17	79143	1287	81	803	0.102346	1.014619
18	48129	841	54	537	0.112198	1.115751
19	19234	376	21	213	0.109182	1.107414
20	6270	206	13	96	0.207337	1.5311
21	4117	169	7	85	0.170027	2.06461
22	4422	154	7	66	0.158299	1.492537
23	4852	164	7	71	0.14427	1.463314
24	7144	235	16	107	0.223964	1.49776
25	4350	172	7	80	0.16092	1.83908
26	5045	195	7	81	0.138751	1.60555
27	8623	240	15	124	0.173953	1.438015
28	8170	235	9	121	0.110159	1.481028
29	9852	255	14	125	0.142103	1.268778
30	16140	390	20	217	0.123916	1.344486

Figure 87: The tail percentages numbers for orbit 10 to 30.

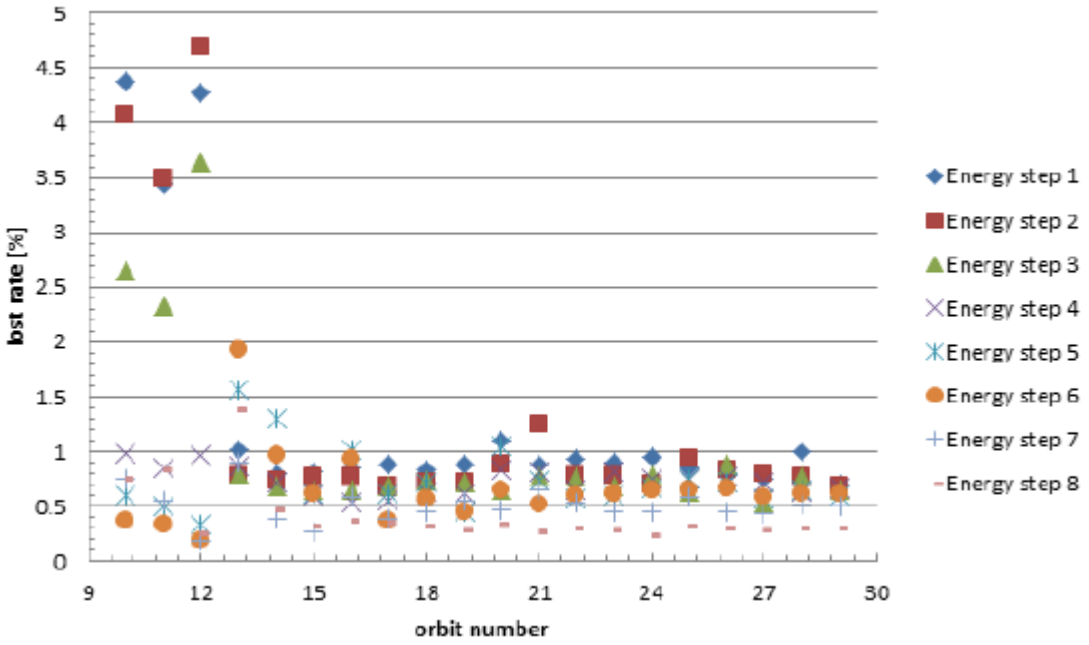

Figure 88: The difference percentages per energy level for orbits 10 to 29 comparing Pipeline to Perl code.

5.4.6.11 Filtering of Data Using the Purify Option in Pipeline Scripts

In the pipeline/ground code, lo de tof is used to filter unwanted events and reclassifies events based on a set of thresholds. It reads AND writes to the .lode file changing any purified events to 4F records, and removes ALL TOF values. The .lode file is normally copied to a work area per script run, so the original file is unaltered.

5.4.6.11.1 LO_DE_TOF Purify Option

There are two sets of thresholds selectable via a one letter suffix (0 or 1) appended to the option named purify. Each set features a slightly different sequence of tests. They are performed in order, and if they filter the event, no further tests are performed in the sequence. The following table lists the default thresholds per option. Thresholds may be changed by using purify0:1,2,3,4,5,6 or purify1:1,2,3,4,5. In this context, 1, 2, 3, 4, 5 or 6 refers to the five or six threshold values that may be specified per type of option.

purify0 (default values are 1, 101, 101, 6, 6, 6)

TOF1 < 1 index 0 in list

TOF0 < 101 && TOF1 < 101 index 1 and 2 in list

|TOF1 TOF0| < 6 index 3 in list

|TOF2 TOF0| < 6 index 4 in list

|TOF2 + 1024 TOF0| < 6 index 5 in list

purify1 (default values are 1, 201, 21, 21, 21)

TOF1 < 1 index 0 in list

TOF0 + TOF1 < 201 index 1 in list

TOF2 < 21 index 2 in list

|TOF2 TOF0| < 21 index 3 in list

|TOF2 + 1024 TOF0| < 21 index 4 in list

5.4.6.11.2 Contour Plots Showing Purify1 Boundaries

The following contour plots (Figures 89-92) of o0161a show the purify1 thresholds as red dashed reference lines. Two sections of the orbit are featured in the following discussion - the first six hours when the spacecraft was requiring TOF2 to be present, and a subsequent 6 hours when the craft was accepting any combination of TOF values (and so was receiving many TOF3 only events).

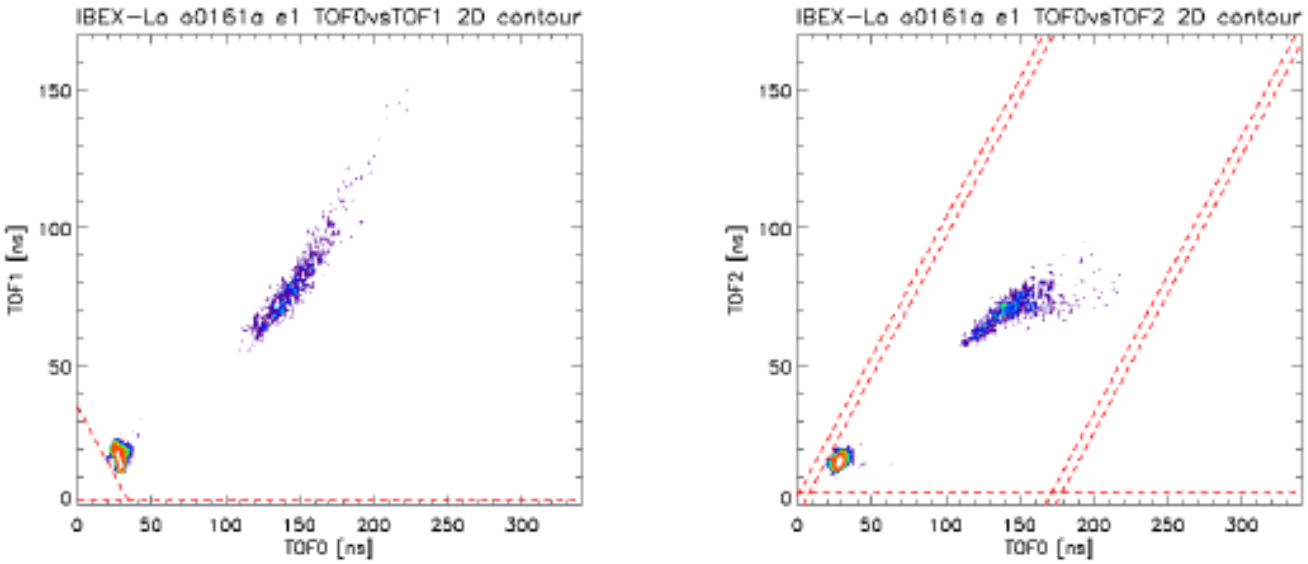

Figure 89: TOF0 vs TOF1 and TOF2 scatter plots (H: red diamond, O: blue diamond, Other: black diamond) with purify1 limits (yellow dashed lines).

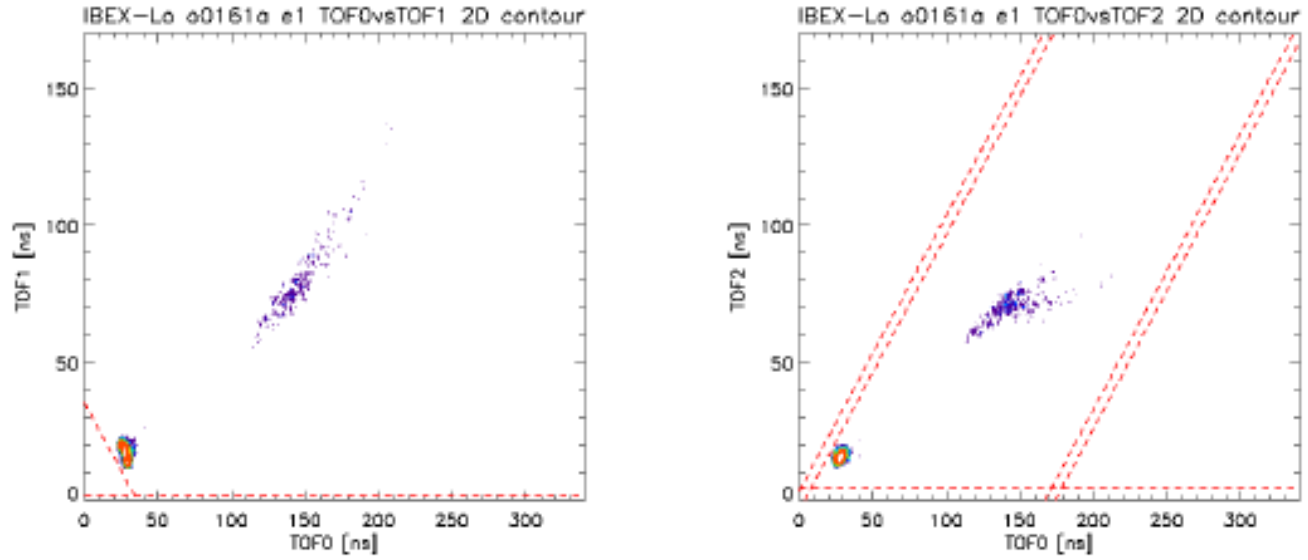

Figure 90: TOF0 vs TOF1 and TOF2 scatter plots (H: red diamond, O: blue diamond, Other: black diamond) with purify1 limits (yellow dashed lines).

In the left plots, we can see H events have a higher slope than other events. This feature is much clearer in this plot than the TOF0 vs TOF1 scatter plot. It also shows that the current purify1 option removes few events below the diagonal lines in the left side. These events are suspected as electrons. Here TOF2 limits have been used to identify event species.

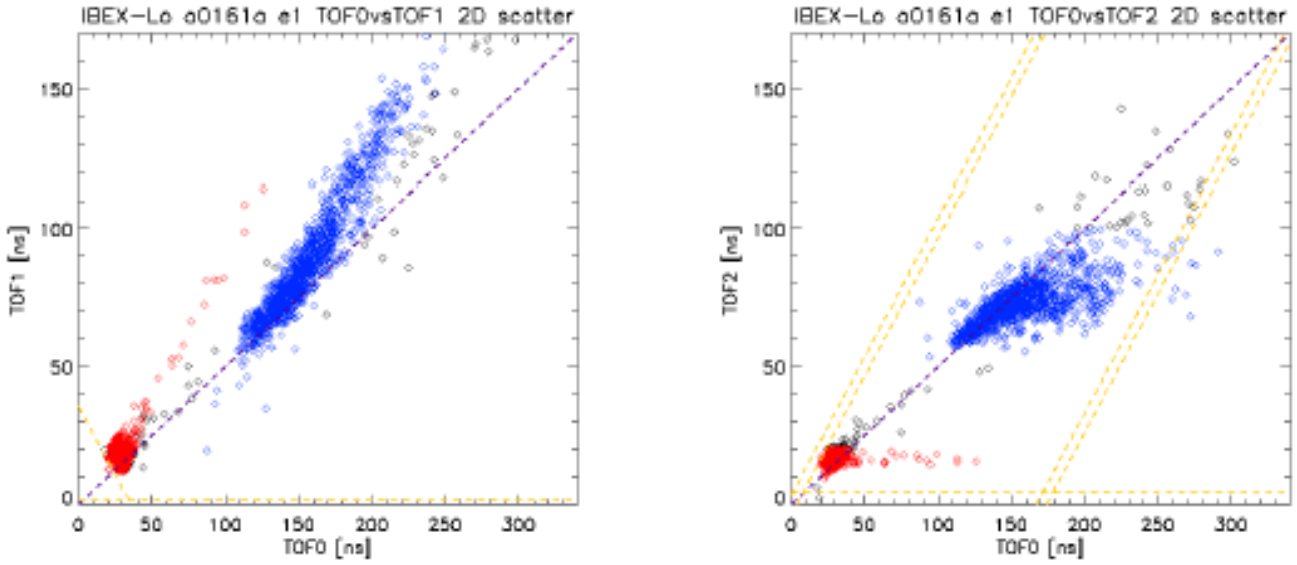

Figure 91: TOF0+TOF3/2 vs TOF1-TOF3/2 scatter plots (H: red diamond, O: blue diamond, Other: black diamond) with purify1 limits (yellow dashed lines).

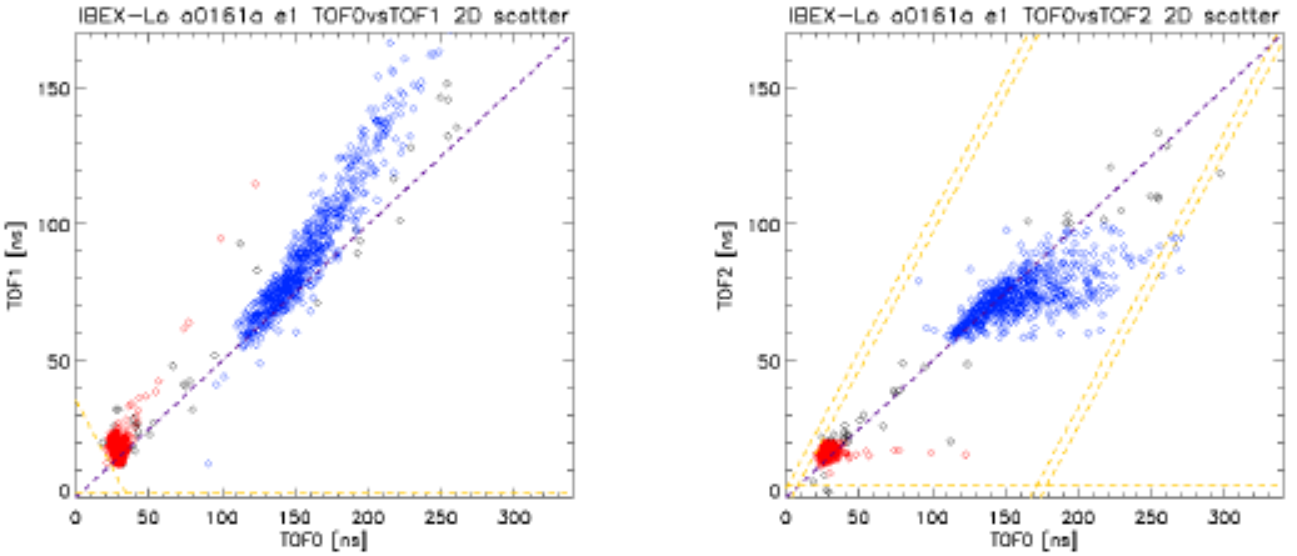

Figure 92: TOF0+TOF3/2 vs TOF1-TOF3/2 scatter plots (H: red diamond, O: blue diamond, Other: black diamond) with purify1 limits (yellow dashed lines).

5.4.7 IBEX-Lo Sputtering Correction

This section documents the original correction process for IBEX-Lo data that includes removing an apparent signal in an energy pass band caused by sputtering from higher energy neutrals. The first step in generating IBEX-Lo ~ 0.2 and ~0.4 keV maps is estimating differential ENA fluxes for H at these energies in the spacecraft frame.

5.4.7.1 IBEX-Lo Sputtering Correction for H Maps

The differential fluxes simply represent the observed rates divided by observed energy times the geometric factor at the observed energy: $J_i = Ri/(E_i G_{ii})$, where J_i is an estimate of the differential energy flux at ESA step i with energy level E_i, the count rate is R_i, and G_{ii} is the geometric factor at this ESA step with units cm^2 sr keV keV^{-1}.

The double index convention for the geometric factor G_{ik} considers the observed ESA step i and the incident flux that contributes from ESA step k where $k \geq i$. Therefore, for an incident flux J_k near the energy level E_k associated with ESA step k, the contribution to the observed rate R_i in ESA step i is $\Delta R_i = E_i G_{ik} J_k$.

The IBEX-Lo H maps show a feature in ESA steps 5 and 6 that are related to the interstellar flow observed in the IBEX-Lo O maps for the corresponding ESA steps. The interstellar neutral species O (and Ne) produce sputtered products, including H, C, and O at energies lower than that of the parent atom causing sputtering.

To determine the amount of sputtered H that needs to be subtracted from the maps, the composition of the interstellar flow in the two ESA steps 5 and 6 is needed. This information was derived from observed TOF spectra. The data was accumulated over one ISM flow season to acquire sufficient statistics. We analyzed ESA steps 5 and 6 separately because the ratio of the sputter product to the actual converted O is substantially different for these two energy pass bands. Because neutral H in the IBEX-Lo data is not only from sputtering, a contribution from the globally distributed ENA H source must be subtracted from the H peak in the TOF spectrum at a given ESA step. After subtraction of the globally distributed flux (Schwadron et al. 2011), we are able to determine the ratio of sputter H to O from the ISM.

In a given pixel of the H map, the O sputtering correction for the H differential flux J^H i is given by $J^H_i = J_i - J^O_i \chi_i$ where J^O_i is the O differential energy flux in ESA step i and χ_i is the correction factor. Our analysis shows that $\chi_5 = 0.15 \pm 0.05$ and $\chi_6 = 0.01 \pm 0.008$.

The next step in solving for differential fluxes at incident particle energies is to correct for sputtering by H at energies above that in the observed ESA step. A bootstrap method was developed by Fuselier et al. (2012) that we adopt here. If we take $\alpha_{ik} = G_{ik}/G_{ii}$ (Table 5) then the estimated differential flux J^H_i at ESA step i is a sum over the sputtering contributions from ESA step i and higher:

$$J_i^H = \sum_{j=i}^{N} \alpha_{ij} J_j \qquad (19)$$

where N = 9 is the highest ESA step (IBEX-Hi flux at 2.73 keV) and we take $J^H_N = J_N$. Equation (**19**) is inverted simply by iterative calculation of the differential flux J_i from ESA step i N − 1 down to step i, with the differential flux at each step given by

$$J_i = J_i^H - \sum_{j=i+1}^{N} \alpha_{ij} J_j.$$

(20)

We have used the fact that $\alpha_{ii} = 1$ by construction.

In producing the IBEX-Lo H maps, we have used the approximation that the geometric factor at each ESA step is constant throughout the mission. In the summer of 2012, the post-acceleration voltage was lowered from 16 to 7 keV, which reduced the time-of-flight efficiencies. However, almost simultaneously the transmission mode between IBEX-Lo and the data system was changed so that previously transmitted unused PHA events are now suppressed. This change has increased the throughput of the PHA events used for the ENA maps, thus roughly compensating for the efficiency reduction. While the team is currently working on accurately quantifying each of these factors, current estimates suggest that the net result of these geometric factor variations will lead to only minor changes to the maps well within statistical uncertainties.

5.4.7.2 Updated IBEX-Lo Sputtering Correction for Maps

In the IBEX-Lo energy range, we expect to observe the ISN gas atoms (H, He, O, and Ne), the secondary ISN He and O populations, and the heliospheric ENAs (mostly H). Based on the combined energy distribution of these populations, the observed H^- rate map in E-step i(- C_i^{H-}) can be written as

$$C_i^{H^-} = G_{ii}^{H^-H} E_i J_i^H + \sum_{k>i} G_{ik}^{H^-H} E_i J_k^H + \sum_{k\geq i} G_{ik}^{H^-He} E_i J_k^{He} + \sum_{k\geq i} G_{ik}^{H^-O} E_i J_k^O + \sum_{k\geq i} G_{ik}^{H^-Ne} E_i J_k^{Ne}$$

(21)

where G_{ik} XS is the geometric factor (in units of cm^2 sr keV keV^{-1}) for the combination of an incoming atom “S” and an observed negative ion “X”. E_i is the center energy of E-step i. The index i represents the E-step of the IBEX-Lo ESA (i = 1–8), and the index k indicates the incident energy step. Even though the incoming atom energy distributions are continuous, we use discrete steps k to represent the incoming energy spectra. The index k can be 1–8 and indicates the center energy of the corresponding ESA energy step (i.e., k = 1–8 and $E_k = E_i$ for i = k). $J_i^S(J_k^S)$is a differential flux (in units of cm^{-2} s^{-1} sr^{-1} keV^{-1}) of the incoming atom “S,” which has an energy corresponding to $E_i(E_k)$. On the right-hand side of Equation (1), the first term represents the count rate of the converted H^- ions due to the incoming H atoms that have the same energy as the ESA E-step i. The second term is the count rate of the sputtered H− due to the H atoms that have higher energies than those in E-step i (k > i). The other terms indicate the count rates of the sputtered H^- ions due to He, O, and Ne atoms, respectively. Here, the

incoming neutral atoms have energies higher than and equal to one corresponding to ESA E-step i (k ≥ i).

Similarly, the observed O^- rate map in E-step i ($C_i^{O^-}$) can also be written as

$$C_i^{O^-} = G_{ii}^{O^-O} E_i J_i^O + \sum_{k>i} G_{ik}^{O^-O} E_i J_k^O + \sum_{k\geq i} G_{ik}^{O^-H} E_i J_k^H + \sum_{k\geq i} G_{ik}^{O^-He} E_i J_k^{He} + \sum_{k\geq i} G_{ik}^{O^-Ne} E_i J_k^{Ne} \quad (22)$$

where E_i is a center energy of E-step i for O^- ions in the ESA (*Figure 93*). On the right-hand side of Equation (**22)**, the first term indicates the count rate of converted O^- ions due to incoming O atoms that have the same energy as E-step i. The second term is the count rate of sputtered O^- due to the O atoms that have higher energies than E-step i. The other terms represent the count rates of sputtered O^- ions due to the H, Ne, and Ne atoms that have energies higher than and equal to E-step i.

In Equations (**21**) and (**22**), there are four terms representing the sputter contributions. In principle, ISN Ne atoms can be observed as "O^-" events in E-steps 5–6 in accordance with the ISN Ne bulk energy. However, it is impossible to unambiguously distinguish the "O−" events caused by ISN Ne atoms from genuine "O^-" events. Only the Ne/O ratio in the primary ISN flow has been studied by Bochsler et al. (2012) and Park et al. (2014). In addition, because of much lower charge exchange cross-sections, the contribution of Ne is expected to be less important for the secondary component. Because we focus on the secondary ISN component, we do not consider the contribution of the ISN Ne atoms here. Therefore, the last terms in Equations (**21**) and (**22**) are neglected in the following equations.

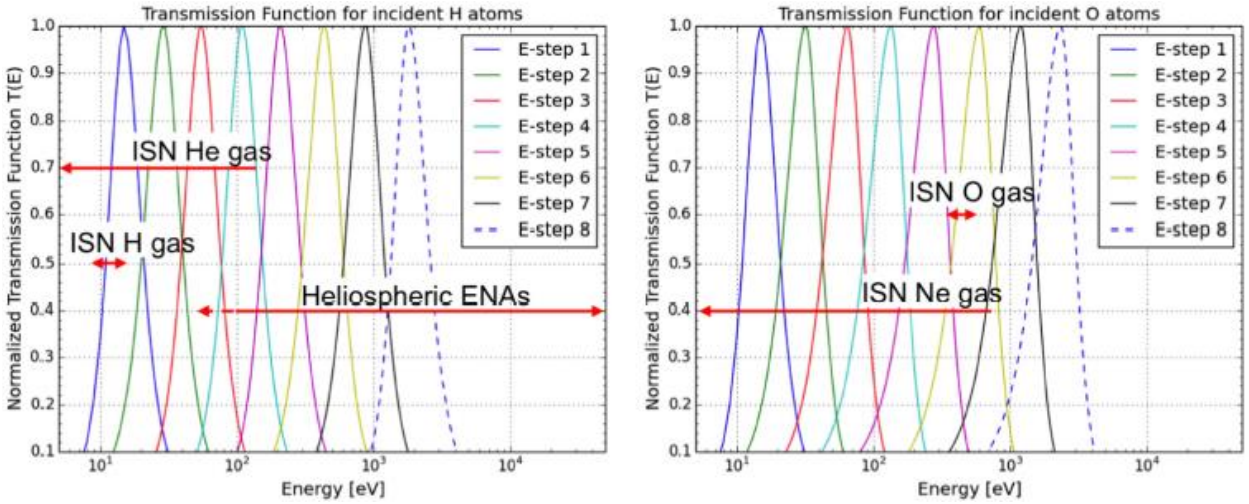

Figure 93: Transmission functions of the eight IBEX-Lo energy steps for "H^-" events (left panel) and "O^-" events (right panel). The normalized energy transmission function is

taken from Schwadron et al. (2013). The energies differ for H and O because the energy loss on the conversion surface of the IBEX-Lo sensor depends on the atom species. The red arrows represent the possible energies of several populations of neutral atoms in the observer frame during the winter–spring season.

In the following, we derive the sputtering correction for the IBEX-Lo maps. As we discuss above, Equation (**21**) represents the measured count rate of negative hydrogen ions at E-step i in terms of flux. In Equation (**21**), the geometric factor G_{ik}^{XS} characterizes the product of effective instrument area, solid-angle acceptance, energy resolution of ESA, and efficiency. The efficiency depends on the incident species "S," the incident energy (in discrete step k), the detected ion species "X," and the ESA-step i. The efficiency is determined by careful analysis of calibration data. Beams of several neutral species were used to study the response of the IBEX-Lo sensor. The energy of these beams ranged 0.01–2 keV. Specific energies have been selected that matched the center energy of the energy steps of the ESA. The ESA allows ions to pass when their individual kinetic energy is within a specific range. For these measurements, we refer to the center energy of the ESA and not to the energy of an individual incoming atom. Through the instrument, we only know the corresponding energy step for the incoming atoms, not their individual energies. Therefore, we use the center energy of the E-step instead of the energy of an incoming atom. In the symbol of the geometric factor, the first letter of the subscript indicates an observed ESA-step and the second letter indicates an energy step associated with the incident energy. The differential fluxes simply represent the observed count rate divided by the observed energy times the geometric factor at the observed energy:

$$J_k^S = \frac{C_i^S}{G_{ik}^{XS} E_i} \tag{23}$$

On the right-hand side of Equation (**21**), the first term indicates a count rate of converted hydrogen ions and the flux Ji H can be replaced with $C_i^H/(G_{ii}^{H\text{-}H}\, E_i)$. Since, however, the other three terms represent contributions due to the sputtering products, the fluxes should correspond to the incident neutral atoms with higher energies than the center energy of the observed ESA step i. Thus, the fluxes J_k^S is replaced with $C_k^S/(G_{kk}^{SS}\, E_k)$ for H and O. For He, the flux J_k^{He} can be written as $C_k^{He}/(G_{kk}^{H\text{-}He}\, E_k)$because helium atoms almost do not produce stable negative helium ions (Wurz et al. 2008). Therefore, we rewrite Equation (**21**) in terms of the count rate:

$$C_i^{H^-} = C_i^H + \sum_{k>i} \frac{G_{ik}^{H^-H} E_i}{G_{kk}^{H^-H} E_k} C_k^H + \sum_{k\geq i} \frac{G_{ik}^{H^-He} E_i}{G_{kk}^{H^-He} E_k} C_k^{He} + \sum_{k\geq i} \frac{G_{ik}^{H^-O} E_i}{G_{kk}^{O^-O} E_k} C_k^O \tag{24}$$

Here we define a sputtering-correction factor α_{ik}^{XS}:

$$\propto_{ik}^{XS} = \frac{G_{ik}^{XS} E_i}{G_{kk}^{SS} E_k}$$

(25)

Extensive testing during the pre-flight instrument calibration with pure neutral hydrogen, helium, and oxygen beams derived the geometric factors. The top two panels in *Figure 94* shows the sputtering-correction factors in the H^- count-rate maps due to the incoming H and O atoms, respectively. For instance, the H^- count rate in E-step 5 (C_5^{H-}, E_5 = 209 eV) is

$$C_5^{H-} = C_5^H + \sum_{k=6}^{8} (\propto_{5k}^{H^-H} C_k^H) + \sum_{k=5}^{8} (\propto_{5k}^{H^-O} C_k^O)$$

(26)

where we ignore the sputtering term due to He atoms because we only expect to observe ISN He atoms with the bulk energy of ~131 eV in the spacecraft frame during the winter–spring season of the ISN He gas. The correction factors for the second and third terms in Equation (**26**) are denoted by the red box in *Figure 94*. The bottom two panels in Figure 10 show the sputtering-correction factors in the O− count-rate maps due to the incoming O and H atoms, respectively. Table 28 shows the actual values of the sputtering-correction factors and the geometric factors that are used.

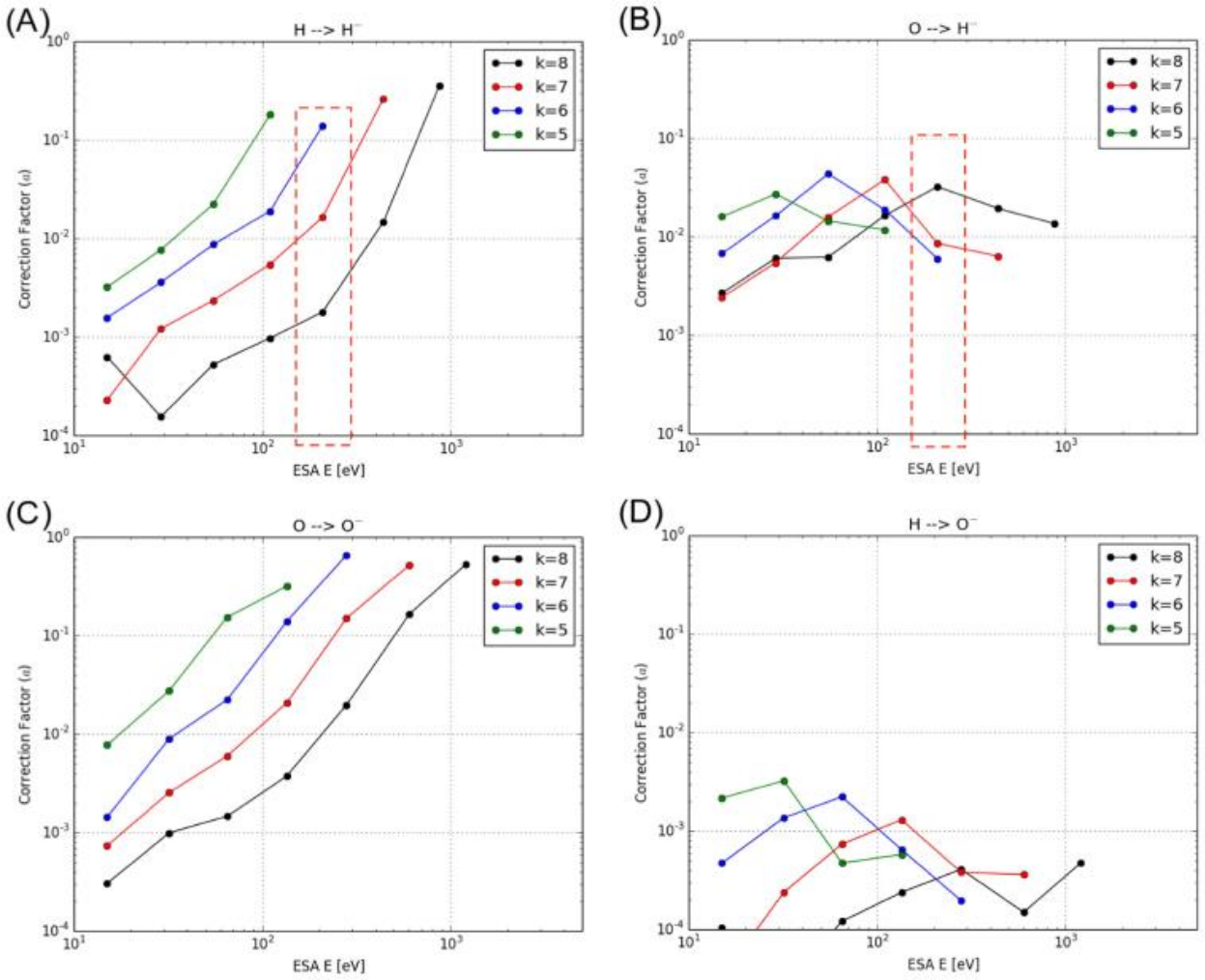

Figure 94: Sputtering-correction factors in the H^- count-rate maps due to the incoming H (panel A) and O (panel B) and in the O^- count-rate maps due to the incoming O (panel C) and H (panel D). "k" is an index of the E-step for the incident energy. The red dashed box represents an example for the H^- count-rate map in E-step 5 (E_5 = 209 eV).

Table 28: Values of the Sputtering-correction Factors (a_{ik}^{XS}) and Geometric Factors (G_{ik}^{XS}, cm² sr keV/keV) that are used

k	i	$G_{ik}^{H^-H}$	$a_{ik}^{H^-H}$	$G_{ik}^{O^-O}$	$a_{ik}^{O^-O}$
8	7	5.538E-05	0.358	8.111E-05	0.531
	6	4.492E-06	0.015	5.001E-05	0.163
	5	1.152E-06	0.002	1.292E-05	0.020
7	6	2.718E-05	0.262	8.326E-05	0.518
	5	3.574E-06	0.016	5.133E-05	0.148
6	5	8.236E-06	0.139	9.715E-05	0.655

5.4.8 IBEX-Lo Bootstrap Correction

5.4.9 Effects of Radiation Pressure on IBEX-Lo Observations

The treatment of neutral H in this paper requires that we take into account the effects of radiation pressure on neutral atoms. Lee et al. (2012) developed an analytical method for solving for the distribution function of neutral atoms that we utilize here (Equations (1)–(8) from Lee et al. 2012). However, the treatment applies for μ < 1 (where μ is the radiation pressure divided by the gravitational force). Here, we develop the specific revisions to the Lee et al. (2012) formulae needed for the solution in the limit μ > 1.

We start by reviewing the formula for an atom's kinetic energy,

$$E = \frac{mV^2}{2} - \frac{k}{R},$$

(27)

where $k = G_m M_s(1 - \mu)$, G is the gravitational constant, m is the atom mass, M_s is the solar mass, and μ describes the ratio of radiation pressure to gravity. The speed of the atom far from the Sun is $V_\infty = (2E/m)^{1/2}$. The angle between **R** and a position vector along the trajectory **R**(t) is θ. The angle θ_∞ corresponds to the position of the particle as it approaches the heliosphere far from the Sun (**R**(t → −∞)) and the angle $\theta = -\theta_0$ is at perihelion, the position closest to the Sun. The angle φ is defined by $\cos\varphi = -\mathbf{R}\cdot\mathbf{V}/(RV)$.

There is one essential revision to the Lee et al. (2012) formulae to account for μ > 1:

$$\frac{1}{R} = \frac{m|k|}{l^2}[\epsilon\cos(\theta + \theta_0) + sgn(k)],$$

(28)

where the sign operator is sgn(k) = 1 for k > 0 and sgn(k) = −1 for k < 0, and is introduced to account for the situation where μ > 1. The angular momentum l is $l = mRV\sin\varphi$ and the eccentricity ϵ is given by

$$\epsilon^2 = 1 + \frac{2l^2E}{mk^2}.$$

(29)

Note that ϵ > 1 in all cases since the energy must be a positive value.

The case of μ = 1 leads to k = 0 in which the trajectories of atoms become perfectly straight and their kinetic energies do not change along the trajectory. The formalism given here and in Lee et al. (2012) does not treat this case explicitly. However, the

formulae in Lee et al. (2012) in the limit that μ → 1 converge to the appropriate limiting solution.

The perihelion angle is found from Equation (22) by setting θ = 0 and may be expressed in a form identical to that in Lee et al. (2012),

$$\theta_0 = \operatorname{acos}\left(\left[\frac{l^2}{m|k|R_0} - 1\right]/\epsilon\right)$$

(30)

where R0 is the perihelion radial distance from the Sun and $\operatorname{sgn}(\theta_0) = \operatorname{sgn}(\pi/2 - \varphi)$. Furthermore, the expression for θ_∞ may also be expressed in a form identical to Lee et al. (2012).

5.4.10 IBEX-Lo Estimation of Parameter Fitting Uncertainties

In this section, we provide the formulae that give the fitting uncertainties in the optimal parameters derived from χ^2 minimization. The fitting of a model to data is achieved through a non-linear least-squares method. This method is applied to a given curve f(x) or data set $\{f_i = f(x_i)\}$ for i = 1 . . . N and a statistical model, V (x; p) or $\{V_i(p) = V(x_i ; p)\}$ for i = 1 . . . N. The fitting involves finding the optimal parameter p = ˜p in a given domain that minimizes χ^2 as follows,

$$\chi^2(p) = \sum_{i=1}^{N} \delta f_i^{-2}[f_i - V_i(p)]^2,$$

(31)

where δf_i^2 is the variance associated with the data f_i. By expanding $\chi^2(p)$ over its local minimum value, we obtain the following positive-definite quadratic form:

$$\chi^2(p) = A_0 + A_2(p - \tilde{p})^2 + O[(p - \tilde{p})^3],$$

(32)

where $A_0 \geq 0$. $A_0 = 0$ corresponds to the optimal fit and$A_2 > 0$ represents the curvature of the fit. These coefficients (A_0, A_2) are analytically given by Livadiotis (2007),

$$A_0 = \chi^2(\tilde{p})$$

(33)

$$A_2 = \sum_{i=1}^{N} \delta f_i^{-2} \left\{ [V_i(\tilde{p}) - f_i] \frac{\partial^2 V_i(\tilde{p})}{\partial p^2} + \left[\frac{\partial V_i(\tilde{p})}{\partial p} \right]^2 \right\}.$$

(34)

The uncertainty may be solved by minimizing the quantity $|p - \tilde{p}| = \sqrt{[\chi^2(p) - \chi^2(\tilde{p})]/A_2}$, which yields

$$\delta\tilde{p} = \sqrt{A_0/(MA_2)}\,,$$

(35)

where M is the number of free parameters in the fit.

In the case that the χ^2 minimum is outside the domain, the χ^2 takes on the following positive-definite linear form:

$$\chi^2(p) = A_0 + A_1(p - \tilde{p}) + O[(p - \tilde{p})^2],$$

(36)

where

$$A_1 = \sum_{i=1}^{N} \delta f_i^{-2} [V_i(\tilde{p}) - f_i] \frac{\partial V_i(\tilde{p})}{\partial p}\,.$$

(37)

Minimization of the deviation, $|p - \tilde{p}|$, yields

$$\delta\tilde{p} = A_0/(M|A_1|)\,.$$

(38)

The formulae above are constructed based on perturbations of one parameter only. The multi-parameter generalization involves treatment of the terms p and ˜p as vectors. The generalization of Equations (35) and (38) is

$$\delta\tilde{p}_l = \sqrt{A_0 (A_2^{-1})_{ll}/M} \sim \sqrt{A_0 \left(M\, A_{2,ll}\right)}$$

(39)

if the parameter $\tilde{p}_l$ is determined at a local χ^2 minimum. $A_{2,ll}$ is the principal curvature of the curve where only p_l varies, at the point $p_l = \tilde{p}_l$. Similarly,

$$\delta\tilde{p}_l = A_0/\left(M\left|A_{1,l}\right|\right),$$

(40)

if the parameter is minimized at the boundary of the domain. In this case, $A_{1,l}$ is the slope of the χ^2 curve where only p_l varies, at the point $p_l = \tilde{p}_l$.

5.4.11 IBEX-Lo Correction for the Throughput Reduction in the Interface Buffer

The IBEX-Lo detector transfers measured events to the Central Electronic Unit (CEU) via an interface buffer in order to adapt the stochastic sequence of the observed events to their intake into the CEU with a certain processing time for each event. To mitigate the smoothing effect, the interface buffer has been designed as a double buffer which temporarily stores up to two events. Only the third consecutive event is lost if it occurs within one processing time window of the CEU. Losses, and thus any reduction of the event rate, are negligible as long as the typical time between successive events is much shorter than the processing time, but they become noticeable as the typical time between successive events approaches this value. In this appendix, we derive an analytical model of the interface buffer (Section 5.4.11.1) to statistically correct for the losses caused by limited throughput. In Section 5.4.11.2, we describe the application of the model to data before orbit 168. Starting with orbit 169, IBEX-Lo was commanded into a new operational mode that requires a TOF2 coincidence, which reduces the total rate to well below 100 events per second. This eliminates the throughput reduction almost entirely.

5.4.11.1 Derivation of IBEX-Lo First In First Out Double Buffer Model

In this section, we derive an analytical model of a First In First Out (FIFO) double buffer designed to compensate for the natural irregularity of the time intervals between successive events. Let $p_2(t)$, $p_1(t)$, and $p_0(t)$ be the probabilities that at time t two, one, and zero events are stored in the buffer. These three states are all possible buffer states, and thus $p_0(t) + p_1(t) + p_2(t) = 1$ at any time. We use this to substitute $p_1(t) = 1 - p_2(t) - p_0(t)$. The buffer processing time, i.e., the time needed to transmit a single event, is t_b. The probabilities of the buffer state at time $t + t_b$ can be expressed as

$$p_2(t_0 + t_b) = \eta_{2\to2} p_2(t_0) + \eta_{1\to2} \times \left(1 - p_2(t_0) - p_0(t_0)\right) + \eta_{0\to2} p_0(t_0), \quad (41)$$

$$p_0(t_0 + t_b) = \eta_{2\to0} p_2(t_0) + \eta_{1\to0} \times \left(1 - p_2(t_0) - p_0(t_0)\right) + \eta_{0\to0} p_0(t_0), \quad (42)$$

where $\eta_{a\to b}$ are the probabilities that during an interval Δt = t_b the buffer changes the number of stored events from a to b. For the FIFO buffer, the probabilities for buffer state changes are as follow:

$$\eta_{2\to 2} = \int_0^{t_b} P_{time,2}(y)[1 - P_{Poiss}(\lambda(t_b - y), 0)]\, dy \tag{43}$$

$$\eta_{1\to 2} = \sum_{n=2}^{\infty} P_{Poiss}(\lambda t_b, n) \times \left(1 - \int_0^{t_b} P_{time,1}(y) \left(\frac{y}{t_b}\right)^n dy\right), \tag{44}$$

$$\eta_{0\to 2} = 1 - P_{Poiss}(\lambda t_b, 0) - P_{Poiss}(\lambda t_b, 1) \tag{45}$$

$$\eta_{2\to 0} = 0, \tag{46}$$

$$\eta_{1\to 0} = P_{Poiss}(\lambda t_b, 0) \tag{47}$$

$$\eta_{0\to 0} = P_{Poiss}(\lambda t_b, 0) \tag{48}$$

where $P_{Poiss}(\alpha, k)$ is the probability of k counts in the Poisson process with parameter α, and λ is the event rate. $P_{time,j}(y)$ is the probability density that the event currently in process will be fully transferred at the time t = t_0 + y if it is known that exactly j events are stored in the buffer at time t = t_0:

$$P_{time,1}(y) = \frac{1}{N_1} P_{Poiss}(\lambda(t_b - y), 0), \tag{49}$$

$$P_{time,2}(y) = \frac{1}{N_2} [1 - P_{Poiss}(\lambda(t_b - y), 0)], \tag{50}$$

N_j are the normalization constants obtained from the condition $\int_0^{t_b} P_{time,j}(y)dy = 1\ for\ j = 1, 2$. The probability density that the transmission of the currently processed event will be finished at time $t = t_0 + y$, if exactly one event is stored in the buffer

time,1(y), is directly proportional to the probability that another event has not been added to the buffer during the interval Δt between the start of the transmission $t = t_0 + y - t_b$ and now $(t = t_0)$: $\Delta t = t_0 - (t0 + y - t_b) = t_b - y$, in other words, the probability of zero counts in the Poisson process with parameter $\lambda\Delta t = \lambda\,(t_b - y)$. Conversely, if it is known that at time $t = t_0$ exactly two events are stored in the buffer, then the probability density for the time of the end of transmission of the first processed event $P_{time,2}(y)$ is proportional to the probability that a non-zero number of events have been added to the buffer from the start of the transmission, i.e., the complementary event to that previously described.

The probabilities given by Equations (**43**)-(**48**) can be inferred based on the following reasoning. The probability $\eta_{2\to2}$ means that after the first processed event was transmitted, at least one additional event has been added. Thus, one needs to integrate the previously described probability density $P_{time,2}(y)$ with the complement probability to the probability of zero events during the interval $(t_0 + y,\ t_0 + t_b)$.

The transition from one event in the buffer to two $\eta_{1\to2}$ implies that at least two events were observed during the interval and at least one of them after the transmission of the first stored event is completed. The probability could be expanded into a series6 of probabilities of different numbers (n) of events (folded with the complementary event) to account for all of the events possibly accumulated in a time shorter than the time needed to complete the transmission of one stored event. Due to the statistical independence of the events, one needs to fold the fraction of y/t_b n times.

The probability $\eta_{0\to2}$ means that at least two new events are added during the interval; this is the complementary event to the sum of zero and one events. If at the time $t = t_0$ two events are stored in the buffer, then both of them cannot be transmitted during the time t_b , and thus $\eta_{2\to0} = 0$. The transition from the state with one $(\eta_{1\to0})$ and zero $(\eta_{1\to0})$ events in the buffer to the empty buffer occurs if new events are not added to the buffer during this interval.

Assuming that the event rate does not change with time, i.e., the stationary Poisson process, we have $p_j(t + t_b) = p_j(t)$, and we can solve Equations (**41**) and (**42**) and express the probabilities p_2, p_1, and p_0 as a function of the probabilities , $\eta_{i\to j}$, defined in Equations (**43**) through (**48**). In the left panel of Figure 95, we present these probabilities as a function of λ for the two values of the buffer transmission time t_b in the IBEX-Lo interface buffer. Hereafter, we treat these probabilities $p_j(\lambda, t_b)$ as a function of λ and t_b, which were assumed to be constant in the above reasoning. The probability that the event is added to the buffer, i.e., that it is transferred to the CEU, is equal to the probability that the buffer is not full: $p_{tr}(\lambda, t_b) = 1 - p_2(\lambda, t_b)$. In the right panel of Figure 95, we compare the transmission probabilities for the cases with and without the double buffer included in the interface.

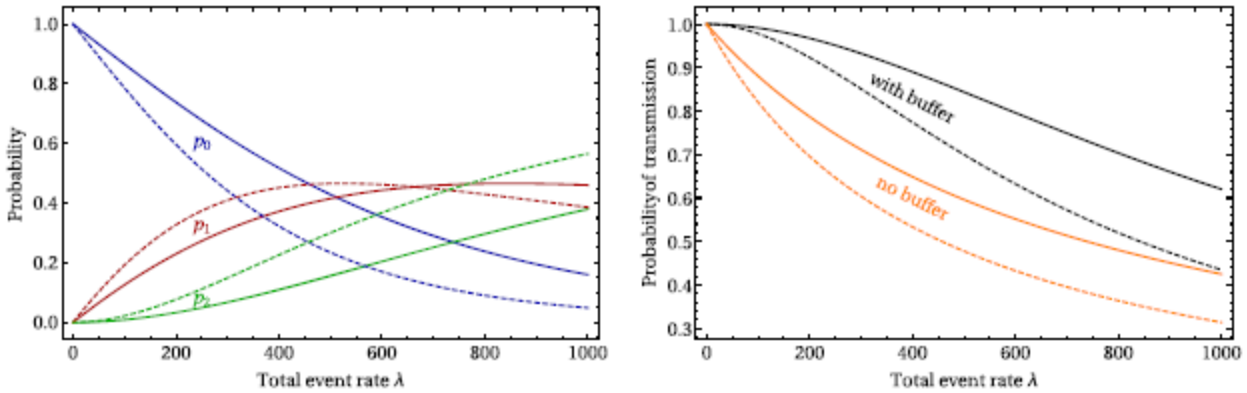

Figure 95: Probabilities of the buffer states (left panel) and probability of event transmission (right panel) as a function of the total event rate (λ). In the right panel, we present probability of event transmission for an interface without a buffer (orange). Solid lines are plotted for $t_b = t_{oHK}$ and dashed for $t_b = t_{wHK}$. Typical values of the total event rates measured by IBEX-Lo are 200–500 s^{-1}.

In addition, at the beginning of each 6° bin, 20 House Keeping and Rate packets must be transferred to the CEU. The transmission of each packet takes t_{HK} = 0.834 ms, whereas t_{event} = 1.354 ms is needed for the transmission of a single event. Each packet is transferred together with the currently processed event, or consecutively, if the interface buffer is empty. During the part of the 6° bin when these packets are transferred, the buffer transmission time is $t_{wHK} = t_{event} + t_{HK}$, whereas outside this part it is $t_{oHK} = t_{event}$. Transmission of the House Keeping and Rate packet right after the event takes an additional time t_{HK}.

The time needed to transfer all of the House Keeping and Rate packets varies depending on the measured event rate. If the buffer is empty during the transfer, it takes 20 × t_{HK} = 16.68 ms, whereas if the buffer is not empty for the whole time, it takes 20 × t_{wHK} = 43.76 ms. For an appropriate estimate of the transfer time for the House Keeping and Rate packets, we perform a linear interpolation of the actually transmitted event rate between the following two values:

$$\boldsymbol{t_{transfer}(\lambda) \approx 16.68\,ms + \frac{p_{tr}(\lambda, t_{wHK})\lambda}{\tilde{\lambda}_{max}} \times (43.76 - 16.68\,ms),}$$

(51)

where $\tilde{\lambda}_{max} = t_{wHK}^{-1}$ is the maximum possible transmission rate during the transfer of House Keeping and Rate packets.

The data are accumulated in 6° bins. The accumulation time for a bin is equal to $t_{bin} = \frac{6}{360} t_{spin}$, where $t_{spin} \gg 14.4\ s$ is the time of one spacecraft rotation. To correct the data

for the limited throughput, we need to estimate the ratio of the total event rate to the rate of transmitted events as a weighted average:

$$\gamma(\lambda) = \frac{\lambda}{\tilde{\lambda}} = \left(\frac{t_{transfer}(\lambda)}{t_{bin}} p_{tr}(\lambda, t_{wHK}) + \frac{t_{bin} - t_{transfer}(\lambda)}{t_{bin}} p_{tr}(\lambda, t_{oHK}) \right)^{-1}.$$

(52)

Equation (52) gives the correction factor for limited throughput as a function of the total event rate (λ). In this derivation, we assume that the total event rate is constant over time. This is not the case in IBEX observations, as the spacecraft rotates and the total event rate varies. However, the timescales of the changes in the total event rate and the time of scanning through one spin-angle bin are much longer than the transmission time tb, and thus we are able to use the stationarity condition as a reasonable assumption.

5.4.11.2 Application of the Model to the IBEX ISN Flow Observations

In this section, we will apply the model for the event reduction across the interface buffer to the ISN flow observations with as much information about the total event rate that arrives at the buffer as is available in the data. The TOF system of the IBEX-Lo sensor can measure up to three TOF values for each incoming particle: TOF0 between the first C-foil and the microchannel plate (MCP) detector, TOF1 between the second C-foil and the MCP, and TOF2 between the two foils. In addition, it records a delay line value TOF3, which indicates the position of incidence on the stop MCP detector which is subdivided into four sectors (for details see Fuselier et al. 2009a). Up to orbit 168, each event with at least one TOF measured (TOF0-TOF3) was transmitted to the interface buffer. The majority were events with only TOF3 present, most of them caused by electrons.

In addition to the full event information, the IBEX-Lo TOF logic generates the monitor rates for each of the individual TOF channels, integrated over 60° wide spin-angle sectors, denoted as S0–S5, at a cadence of 64 spins. The total event rate λ transmitted to the interface buffer is given by the sum of the TOF2 (λ_{TOF2}) and TOF3 (λ_{TOF3}) monitor rates, with the “triple” event rate (λ_{triple}) subtracted. The start and stop signals used in TOF2 and TOF3 are mutually exclusive, except for “triple” events, which involve all detector parts, and thus they are recorded by both the TOF2 and TOF3 monitor rates:

$$\lambda = \lambda_{TOF3} + \lambda_{TOF2} - \lambda_{triple}.$$

(53)

These rates are not reduced by the losses at the interface buffer. Based on this information, we estimate the total event rate λ for each 6° bin separately.

We realize that the contribution of the measured ISN atoms to these rates can be determined separately for each 6° bin based on the histogram events. We sum these

events over the appropriate 60° sectors and subtract them from the total event rate for now to obtain the background for each sector S_j, which can be expressed as

$$\lambda_{bg}(S_j) = \lambda_{TOF3|bg}(Sj) + \lambda_{TOF2|bg}(Sj) = \lambda_{TOF3}(Sj) + \lambda_{TOF2}(Sj) - \sum_{i \in Sj} (\alpha + 1)\lambda_{triples}(i).$$

(54)

The summation is over ten 6° bins i in sector S_j, where $\alpha = 2.56 \pm 0.29$ denotes the ratio of the rate of all possible atom events to the rate of triple atom events. The additional 1 in the brackets accounts for the presence of triple events in both TOF2 and TOF3. In *Figure 96*, we present two examples of the angular distributions of these rates within the 60° sectors. Because the monitor TOF rates only represent averages over the wide sector, the actual rates in each 6° bin cannot be restored unambiguously. Retaining constant values for each 60° sector would lead to discontinuities at the edges. Therefore, we use a quadratic spline S_{bg} with knots at the sector edges, defined so that the integral of the spline over the respective sector is equal to the sector background rate $\lambda_{bg}(Sj)$. Only one unique spline fulfills these conditions. Subsequently, we assess the uncertainties of this approximation. In the last step, we reconstruct the total event rate in each 6° bin i. In the last step, we reconstruct the total event rate in each 6° bin i by adding the previously subtracted counts:

$$\bar{\lambda}(i) = S_{bg}(i) + \alpha\lambda_{triples}(i).$$

(55)

$S_{bg}(i)$ is the value of the spline for each bin i.

The total event rate varies substantially with time during the observations, and therefore the correction factor also varies. Therefore, the procedure to obtain estimates of the total event rate is applied separately for each 512-spin time block, enumerated with q. The number of counts $d_{i,q}$ in each bin i for this time block q is multiplied by the correction factor given by Equation (52) for $\lambda = \bar{\lambda}_q(i)$. The effective TC factor for a given bin i is the ratio of the corrected-to-uncorrected cummulative number of counts:

$$\gamma_i = \frac{\sum_{q=0}^{n} \gamma_{i,q} d_{i,q}}{\sum_{q=0}^{n} d_{i,q}}$$

(56)

where $\gamma_{i,q} = \gamma\left(\bar{\lambda}_q(i)\right)$ is the TC factor for the time block q.

In Figure 97, we show effective TC factors for those bins with a spin-angle in the range (240°, 294°) for orbits 13–19. The maximum in the correction factor around spin-angle 270° in individual orbits is caused by the events due to the ISN flow. A typical value for the correction factor in this range is ~1.1, while the maximum value reaches ~1.15.

These values represent systematic differences in the data from orbit to orbit and over spin-angle for the fitting of the He ISN parameters. This systematic variation is statistically significant at least for the data points with highest statistics.

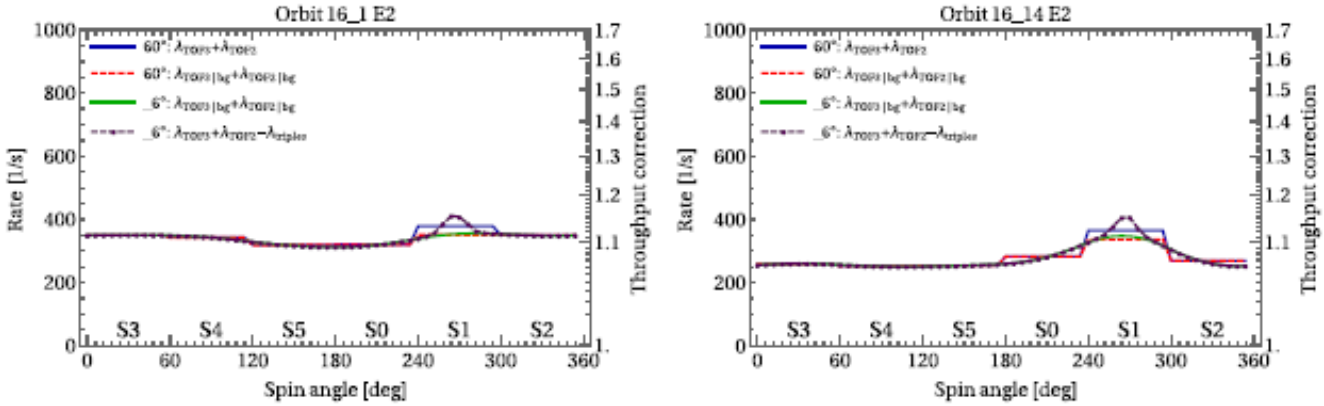

Figure 96: Illustration of the steps of the procesure used to estimate the total event rate for two selected time blocks on orbit 16: sum of the TOF3 and TOF2 event rates for the wide 60° sectors (solid blue line); the sum with a subtracted contribution from the measured atoms (dashed red); determined spline S_{bg} (solid green); the spline with added atom contribution (dashed purple). The scale on the right represents the appropriate correction factor. The two panels illustrate the event rates and the correction factors for two different time blocks during the observations. Note the substantial difference between the values of the correction factor for these two blocks.

Given the statistical nature of the correction and the limited resolution of the data on which the correction is based, it is important to also assess the resulting uncertainties. In the described procedure, we quantify two types of uncertainties. The first one is related to the unknown shape of the background rate λ_{bg} over each 6° bin. The other one is related to the statistical fluctuations of the total event rate during each 512- spin time block.

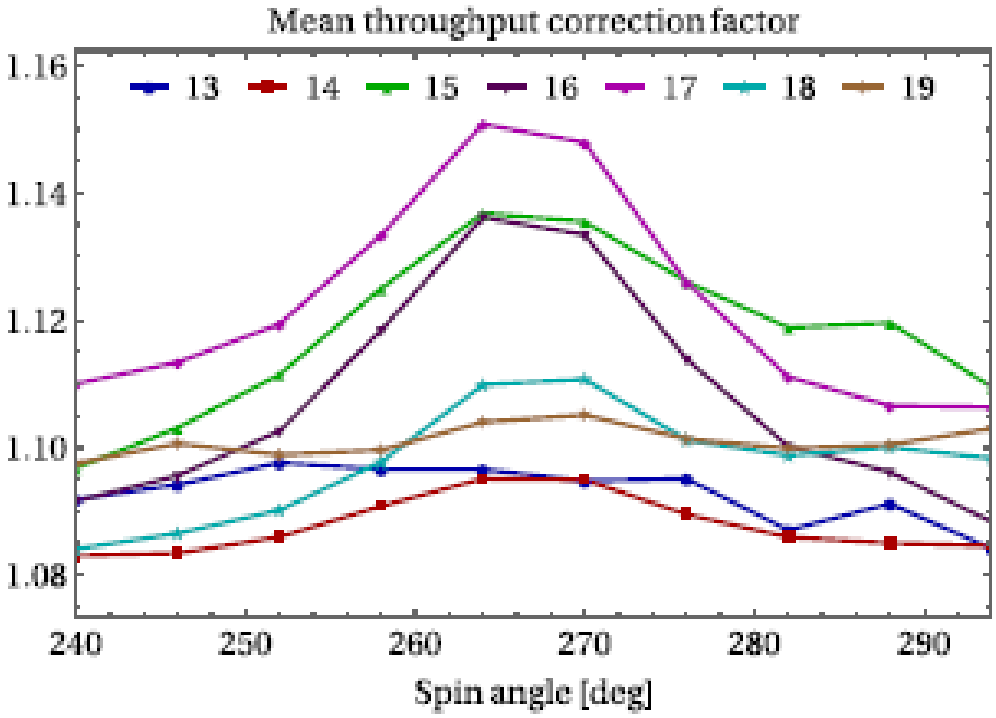

Figure 97: Mean value of the correction factor compensating for the throttling of the interface buffer for the data points around the ISN flow for the orbits used in the analysis.

Determining the structure of the background rate λ_{bg} with a 6° resolution is not possible because the sensor does not store the monitor rates at that resolution. We approximate the uncertainty related to this lack of information based on the previously described spline, and for each bin we take the value

$$\delta_A \bar{\lambda}(i) = \left[\frac{1}{10}\int_{i-5}^{i+5} \left(S_{bg}(x) - S_{bg}(i)\right)^2 dx\right]^{1/2}. \quad (57)$$

We connect the uncertainty for a single bin with the variation of the spline over all 10 bins in the 60° sector. In other words, we assume that if the variation over the sectors is larger, then the uncertainty for a single bin is larger. Variation in the neighboring bins could have different directions and we use this procedure to assess the absolute value of this variation. Thus, despite the integral for each single bin depending on the value in the neighboring bins, we treat the uncertainties for the different bins as independent. Still, we take the correlation over time into account. We assume that a certain sector pattern in the background rate λ_{bg} implies a similar pattern in the 6° bins. Quantitatively, we define this pattern as the following vector:

$$\xi = \left(\lambda_{bg}(S0), \lambda_{bg}(S1), \lambda_{bg}(S2), \lambda_{bg}(S3), \lambda_{bg}(S4), \lambda_{bg}(S5)\right) - \frac{1}{6}\sum_{j=0}^{5} \lambda_{bg}(Sj)(1,1,1,1,1,1).$$

(58)

Then, the correlation coefficient between two 512-spin time blocks q and p is given by

$$a_{q,p} = \frac{\boldsymbol{\xi}_q \cdot \boldsymbol{\xi}_p}{|\boldsymbol{\xi}_q||\boldsymbol{\xi}_p|}.$$

(59)

Each 512-spin time block consists of 8 separate 64-spin blocks, for which the rates λ_{TOF3} and λ_{TOF2} are transmitted. As the statistical uncertainty, we take the standard deviation of the mean of the sum of these rates over the interval. We denote this quantity as $\delta_B\lambda(i)$. The statistical variation of λ_{triple} is small and can be neglected here. These uncertainties are not correlated in time or from bin to bin.

Then, the total uncertainty of the effective TC factor for each bin i is

$$\delta\gamma_i = \left[\frac{1}{\sum_{q=0}^{n} d_{i,q}^2} \sum_{q=0}^{n}\sum_{p=0}^{n} d_{i,q}d_{i,p}\gamma'_{i,q}\gamma'_{i,p} \times \left[\delta_A\bar{\lambda}_q(i)\delta_A\bar{\lambda}_p(i)a_{q,p} + \delta_B\bar{\lambda}_q(i)\delta_B\bar{\lambda}_p(i)\delta_{q,p}\right]\right]^{1/2},$$

(60)

where $\gamma'_{i,q} = d\gamma\left(\bar{\lambda}_q(i)\right)/d\lambda$, and $\delta_{q,p}$ is the Kronecker delta.

Starting from orbit 169, IBEX-Lo was configured into such a mode that the total event rate is equal to the TOF2 rate, which amounts to at most a few tens per second. In this case, the correction factor is at most 1.002, and thus negligible compared to the statistical uncertainties of the measured count rates.

5.4.12 IBEX-Lo: Two Alternative Derivations of Peak Latitude as Function of Longitude

It is instructive to consider two simpler but less complete alternative derivations of the peak latitude ψ_I^0 as a function of observer longitude, which ignore the integration over both energy and the collimator solid angle. The first derivation was in fact used in the analysis presented in Leonard et al. (2015). The derivation is based on the expansion of $A(v, \psi, \zeta)$ not about the peak of the velocity distribution at $(v = v_0, \psi = -\bar{\beta}, \zeta = \zeta_0)$ in inertial-frame velocity coordinates, but rather about $(v = v_l, \psi = -\bar{\beta}, \zeta = 0)$, where v_l is the speed at which $A(v, \psi = -\bar{\beta}, \zeta = 0)$ has its maximum value at the observer

location. The nearly sunward pointing of the IBEX spin-axis, which dictates$\zeta \approx O(\epsilon_z, \epsilon_E) = 1$, motivates the expansion about $\zeta = 0$.

The value of v_l as a function of longitude is given implicitly by Equation (41) or (44) in Lee et al. (2012). If$|\zeta_0| \ll 1$, then v_l may be obtained by differentiating

$$A \simeq -\left(\frac{1}{2}\right) D_v (v - v_0)^2 - \left(\frac{1}{2}\right) D_\psi \left(\psi + \bar{\beta}\right)^2 - \left(\frac{1}{2}\right) D_\zeta (\zeta - \zeta_0)^2 + D_{\zeta v}(v - v_0)(\zeta - \zeta_0).$$

(61)

with respect to v, subject to $\zeta = 0$ and $\psi = -\bar{\beta}$, and setting the result equal to zero. The result is

$$v_l - v_0 = -D_{\zeta v} D_v^{-1} \zeta_0.$$

(62)

It can be shown explicitly that the implicit equations in Lee et al. (2012) reduce to Equation (62) when$|\zeta_0| \ll 1$, or equivalently$|\lambda - \lambda_0| \ll |\lambda_0|$, is satisfied.

The alternative expansion of A yields

$$A \simeq A\left(v_l, -\bar{\beta}, 0\right) + A_\zeta \zeta + A_{vv}(v - v_l)^2/2 + A_{\psi\psi}\left(\psi + \bar{\beta}\right)^2/2 + A_{\zeta\zeta}\zeta^2/2 + A_{\zeta v}\zeta(v - v_l),$$

(63)

where we use the notation $A_\zeta = \partial A/\partial\zeta$ (evaluated at $(v_l, -\bar{\beta}, 0)$) and $A_v = A_\psi = 0$ by construction. The higherorder terms are neglected since they only contribute to ψ_l^0 at $O(\epsilon^3)$ or higher. Using

$$v' = v + 1$$

(64)

$$\zeta' = (v/v')\zeta$$

(65)

$$\psi' = (v/v')\psi,$$

(66)

we transform Equation (63) to IBEX coordinates to obtain

$$A \simeq A\left(v_l, -\bar{\beta}, 0\right) + A_\zeta \left(\frac{v_m'}{v_m}\right)\zeta' + \frac{A_{vv}(v' - v_l')^2}{2} + \frac{A_{\psi\psi}\left(\frac{v_m'}{v_m}\right)^2 + \left[\psi_I + \left(\frac{v_m}{v_m'}\right)\right]^2}{2}$$
$$+ \frac{A_{\zeta\zeta}\left(\frac{v_m'}{v_m}\right)^2 (\zeta')^2}{2} + A_{\zeta v}\left(\frac{v_m'}{v_m}\right)\zeta'(v' - v_l'),$$

(67)

where v_m is the speed at which A is maximized for $\zeta' = \epsilon_z \sin\psi_I - \epsilon_E \cos\psi_I$, which will now be determined. The peak value of A occurs at $v' = v_m'$ and $\psi_I = \psi_I^0$, which are specified by

$$\frac{\partial A}{\partial v'} = 0 = A_{vv}(v_m' - v_l') + A_{\zeta v}(v_m'/v_m)\zeta'$$

(68)

$$\frac{\partial A}{\partial \psi_I} = 0 = A_{\psi\psi}\left(\frac{v_m'}{v_m}\right)^2 \left[\psi_I^0 + (v_m/v_m')\bar{\beta}\right] + A_\zeta \left(\frac{v_m'}{v_m}\right)\left(\frac{\delta\zeta'}{\delta\psi_I}\right) + A_{\zeta\zeta}\left(\frac{v_m'}{v_m}\right)^2 \zeta'\partial\zeta'/\partial\psi_I$$
$$+ A_{\zeta v}\left(\frac{v_m'}{v_m}\right) \times (v_m' - v_l')\partial\zeta'/\partial\psi_I.$$

(69)

Equation (68) yields

$$v_m' - v_l' = -\left(A_{\zeta v}/A_{vv}\right)(v_m'/v_m)\zeta'$$

(70)

Substituting Equation (70) into Equation (69) yields

$$\psi_I^0 + \frac{v_m}{v_m'}\bar{\beta} = \frac{1}{A_{\psi\psi}}\left[\left(A_{\zeta\zeta} - \frac{A_{\zeta v}^2}{A_{vv}}\right)\zeta'\frac{\partial\zeta'}{\partial\psi_I} + A_\zeta \frac{v_m}{v_m'}\frac{\partial\zeta'}{\partial\psi_I}\right].$$

(71)

The factors, A_ζ , ζ' and $\partial\zeta'/\partial\psi_I$ are each of the order of ϵ. Since we are only attempting accuracy to $O(\epsilon^2)$ and both $v_l - v_0$ and $v_m - v_l$ are $O(\epsilon)$, there is no need to distinguish between evaluating A and its derivatives at v_l and at v_0. Accordingly, $A_{vv} = -D_v$, $A_{\psi\psi} = -D_\psi$, $A_{\zeta\zeta} = -D_\zeta$, and $A_{\zeta v} = D_{\zeta v}$, where these values of D may be evaluated at the sweet spot, $\lambda = \lambda_0$. Similarly, the ratio v_m/v_m' following A_ζ in Equation (71) may be replaced by v_0/v_0'. However, A_ζ must retain its dependence on v_l, which is given by Equation (62). After some algebra, Equation (71) then becomes

$$\psi_I^0 + \frac{v_m}{v_m'}\bar{\beta} = \frac{\bar{D}_\zeta}{D_\psi}\epsilon_z\epsilon_E - \frac{(1+v_{ISM}^2)}{V_{ISM}^2}\frac{v_0}{v_0'}\epsilon_z \times [\sin\lambda\cos\theta_\infty^0(v_l) + \cos\lambda\sin\theta_\infty^0(v_l)].$$

(72)

For the expression in square brackets, we must distinguish between v_0 and v_l. Expanding that expression to first order in $v_l - v_0$, Equation (72) becomes

$$\psi_I^0 + \frac{v_m}{v_m'}\bar{\beta} = \frac{\bar{D}_\zeta}{D_\psi}\epsilon_z(\epsilon_E + \zeta_0').$$

(73)

Combining Equations (62) and (70) yields

$$v_m - v_0 = -D_{\zeta v}' D_v^{-1}(\epsilon_E + \zeta_0').$$

(74)

Expanding the term, $v_m(v_m')^{-1}\bar{\beta}$, in Equation (73) to first order in $v_m - v_0$, and substituting Equation (74), yields

$$\psi_I^0 = -\frac{v_0}{(v_0+1)}\frac{\beta}{|\sin\lambda|}\left[1 - \frac{D_{\zeta v}}{D_v}\frac{(\epsilon_E + \zeta_0')}{v_0^2}\right] + \frac{\bar{D}_\zeta}{D_\psi}\epsilon_z(\epsilon_E + \zeta_0'),$$

(75)

which is accurate to $O(\epsilon^2)$. The fact that the two expressions agree implies that to the order of $O(\epsilon^2), \psi_I^0$ is independent of our choice to either integrate over speed or to evaluate the distribution function at the speed at its maximum value. Thus, the intensity integration introduces corrections of the order of $O(\epsilon^3)$.

Equation (75) does not agree with Equation (4) in Leonard et al. (2015) for ψ_I^0, the location of the peak in latitude, even though both are based on expansion about $v = v_l$. The formula in Leonard et al. (2015) took the ϵ_E dependence of ψ_I^0 to arise from the factor $\partial\zeta'/\partial\psi_I$ in the last term in brackets in Equation (**71**). This term, however, is of the order of $O(\epsilon^3)$ and is neglected in Equation (**75**). The second-order terms involving ϵ_E in Equation (**75**) arise from the first term in square brackets in Equation (**71**), which was ignored in the formula in Leonard et al. (2015), and from the choice of v_m (as opposed to v_l) in Equation (**73**) as the speed which controls the Galilean transformation. For $\epsilon_E = 0$, Equation (**75**) is identical with the formula in Leonard et al. (2015). However, Leonard et al. (2015) use the ϵ_E dependence of ψ_I^0 to estimate the value of ψ_I^0 that would be observed had the spin-axis pointed toward the Sun (or $\epsilon_E = 0$). That estimate should be affected by the larger second-order terms that depend on ϵ_E and are evident in Equation (**75**). Figure 98 shows the difference between Equation (**75**) (solid lines) and the expression used for ψ_I^0 in Leonard et al. (2015) (dashed lines) for $\epsilon_z = -4°.2$ and

$\epsilon_E = -6°, -3°, 0°, 3°, 6°$ as a function of ecliptic longitude. It is clear that the dependences on ϵ_E are very different.

The second alternative derivation to determine the spin-angle of maximum intensity as a function of ecliptic longitude, ψ_l^0, while ignoring integration over speed and the entrance aperture, is based on a geometrical approach. We obtain the IBEX spin axis from

$$\frac{\eta}{(2+v_{ISM}^2)^{1/2}}\left[\frac{(2+v_{ISM}^2)\zeta}{(1+v_{ISM}^2)}+\frac{\pi}{2}+\sin^{-1}\left(\frac{1}{1+v_{ISM}^2}\right)\right]-\frac{\eta(2+v_{ISM}^2)^{\frac{1}{2}}}{(1+v_{ISM}^2)}(\zeta-\zeta_0)$$
$$+\frac{\eta}{(2+v_{ISM}^2)}\left[\frac{\pi}{2}+\sin^{-1}\left(\frac{1}{1+v_{ISM}^2}\right)+\frac{2(2+v_{ISM}^2)^{1/2}}{v_{ISM}(1+v_{ISM}^2)}\right]\left[v-(2+v_{ISM}^2)^{1/2}\right].$$

(76)

to $O(\varepsilon)$ as

$$e_s = \epsilon_z e_z + \epsilon_E e_E + e_S = \epsilon_z e_\psi - \epsilon_E e_v - e_\zeta,$$

(77)

where the unit vectors following the last equality are defined according to $v - v_0 = \delta v_v e_v + \delta v_\zeta e_\zeta + \delta v_\psi e_\psi$. In the IBEX frame, the velocity of a helium atom is given by

$$v' = v' e_v + v'_\psi e_\psi + v'_\zeta e_\zeta.$$

(78)

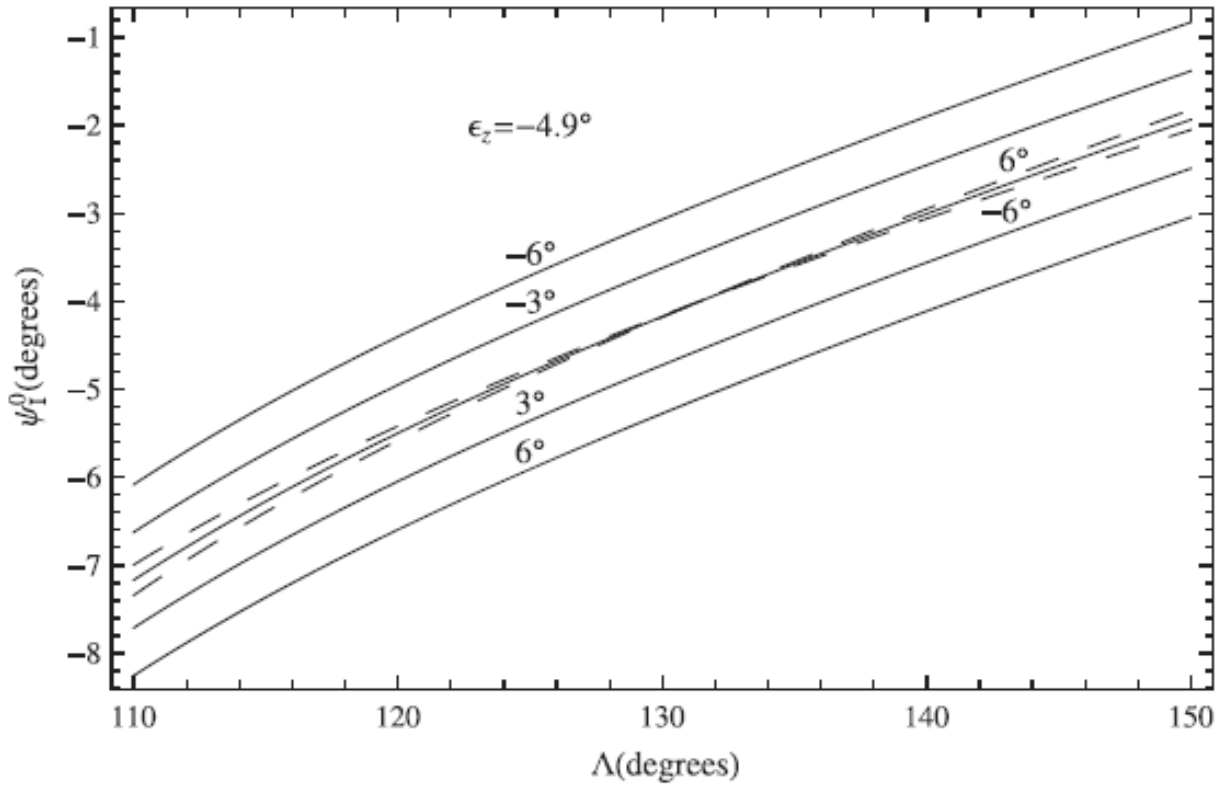

Figure 98: Latitude of the peak count rate, ψ_I^0, as a function of ecliptic longitude, Λ, for our chosen set of representative parameters. The solid curves are based on Equation (**75**). The dashed curves are based on the incorrect expression for ψ_I^0, used by Leonard et al. (2015).

Ignoring the solid angle of the IBEX aperture, IBEX only detects atoms that satisfy $e_s \cdot v' = 0$, which yields the constraint

$$\epsilon_z v'_\psi - \epsilon_E v' - v'_\zeta = 0.$$

(79)

Writing $-A$, which describes the helium atom distribution ellipsoid given by

$$A \simeq -\left(\frac{1}{2}\right) D_v (v - v_0)^2 - \left(\frac{1}{2}\right) D_\psi \left(\psi + \bar{\beta}\right)^2 - \left(\frac{1}{2}\right) D_\zeta (\zeta - \zeta_0)^2 + D_{\zeta v} (v - v_0)(\zeta - \zeta_0),$$

(80)

in IBEX coordinates using

$$v' = v + 1$$

(81)

$$\zeta' = (v/v')\zeta$$

(82)

$$\psi' = (v/v')\psi$$

(83)

we obtain

$$-A = \left(\frac{D_v}{2}\right)(v' - v_0')^2 + \left(\frac{D_\psi}{2}\right)\left(\frac{v'}{v}\right)^2\left(\psi' + \frac{v\bar{\beta}}{v'}\right)^2 + \left(\frac{D_\zeta}{2}\right)\left(\frac{v'}{v}\right)^2(\zeta' - \zeta_0')^2 - D_{\zeta v}(v' - v_0')(v' - 1)^{-1}\left(v_\psi'\epsilon_z - v'\epsilon_E - v\zeta_0\right)$$

(84)

The peak value of the distribution in (v', v_ψ')-space within the plane in velocity space specified by Equation (79) is obtained by differentiating Equation (84) with respect to v' and v_ψ', and setting the two partial derivatives equal to zero. To first order inϵ, we obtain v' at the peak as

$$v' - v_0' = -\left(\frac{D_{\zeta v}}{D_v}\right)(v_0 + 1)v_0^{-1}(\epsilon_E + \zeta_0'),$$

(85)

where v may be replaced by v_0 at this order. Similarly, to second order in ϵ, we obtain v_ψ' at the peak as

$$v_\psi' + v\bar{\beta} = D_\psi^{-1}D_\zeta(v_0 + 1)\epsilon_z(\epsilon_E + \zeta_0') + \left(\frac{D_{\zeta v}}{D_\psi}\right)(v' - v_0')v_0\epsilon_z,$$

(86)

where again v has been replaced by v0 at this order. Substituting Equation (85) into Equation (86), and noting that $D_\zeta \equiv D_\zeta - D_{\zeta v}^2 D_v^{-1}$ and $\frac{v_\psi'}{v'} = \psi' = \psi_I^0$, we obtain

$$\psi_I^0 = -\left(\frac{v}{v'}\right)\bar{\beta} + \left(\frac{\bar{D}_\zeta}{D_\psi}\right)\epsilon_z(\epsilon_E + \zeta_0').$$

(87)

Expanding $v' = v_0' + (v' - v_0')$ and substituting Equation (85), we obtain finally

$$\psi_I^0 = -\frac{v_0}{(v_0 + 1)}\frac{\beta}{|\sin\lambda|}\left[1 - \frac{D_{\zeta v}}{D_v}\frac{(\epsilon_E + \zeta_0')}{v_0^2}\right] + \frac{\bar{D}_\zeta}{D_\psi}\epsilon_z(\epsilon_E + \zeta_0').$$

(88)

Equation (88) is identical to Equation (75). This derivation involves an appealing geometrical analysis to identify the peak of the distribution in the spin plane accessible to the IBEX detector. Figure 99 illustrates approximately the essence of this derivation: where the spin plane is tangent to the helium distribution contour line determines the speed and angle ψ_I^0 of the distribution maximum accessible to measurement by IBEX-Lo for specified values of (ϵ_z, ϵ_E).

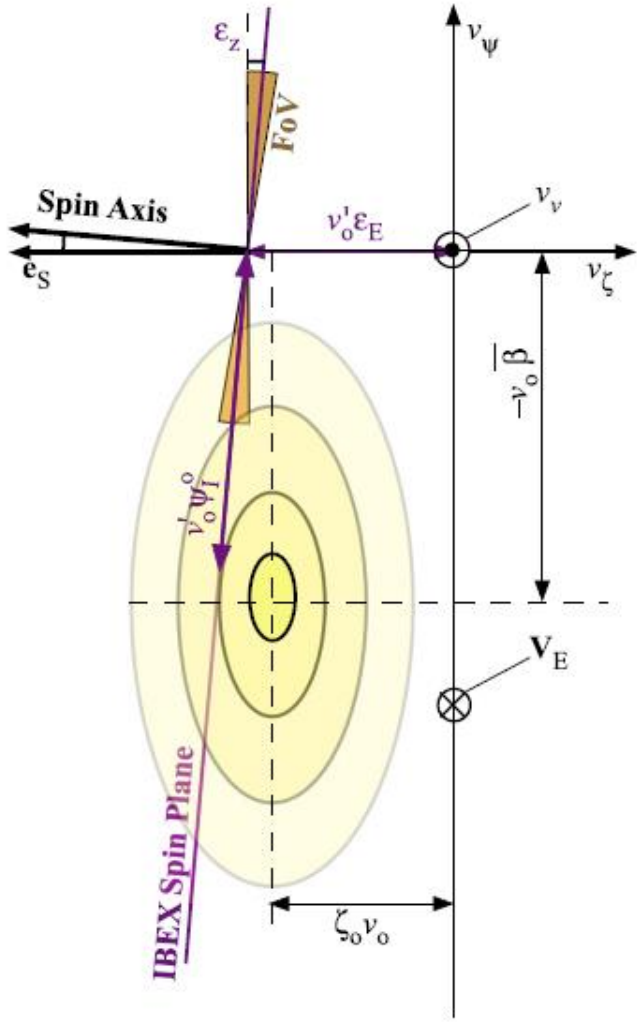

Figure 99: Schematic slice through the peak of the helium velocity distribution in the (v_ζ , v_ψ) plane for a case with $\zeta_0 < 0$. The contours illustrate the elliptical structure of the distribution and the dashed lines show the projection of the principal-axis directions onto the plane. The peak of the distribution has velocity coordinates ($\zeta_0 v_0$, $-v_0\bar{\beta}$). The spin-axis has a tilt ϵ_ζ out of the ecliptic as shown, and a tilt in the ecliptic ϵ_E so that the IBEX spin plane intersects the plane of the figure along the line indicated. The field of view (FoV) of the collimator beyond the spin plane is indicated schematically. The point where the contour is tangent to the spin plane determines the scan latitude ψ_I^0 that results in the maximum count rate as indicated. This schematic representation is approximate since the point of tangency does not precisely occur in the plane of the figure.

5.4.13 Transformation of model fluxes to IBEX-Lo rates

For comparison with the IBEX-Lo data, one needs to convert the fluxes calculated in the model to the count rate (number of counts per second). To do this, we need to integrate the fluxes over a 6° bin of IBEX's lines of sight, acceptance angles of the collimator, and the corresponding energy range. The formula for the count rate in energy bin i and for the NEP angle α_j is the following (this is an analog of Equation 3 from Schwadron et al. 2013):

$$\boldsymbol{C_{i,j} = \frac{1}{\Delta t}\int_{t_0}^{t_1} dt \frac{1}{\Delta \alpha}\int_{\alpha_j-\Delta\alpha/2}^{\alpha_j+\Delta\alpha/2} d\alpha \times \iint \hat{P}(\phi', \psi')\, d\phi' d\psi' \times \int_{V_{i,1}}^{V_{i,2}} f_H(w_H)|w_{rel}|^3 E_{rel} G_i \hat{T}_i(E_{rel}) dw_{rel}.}$$

(89)

Here, $\Delta t = t_1 - t_0$ is the duration of the observations (in seconds) and the NEP angle α determines the direction of a line of sight in the observational plane π. This angle varies over the range of $[\alpha_j - \Delta\alpha/2, a_j + \Delta\alpha/2]$ centered at αj with angular bin-width $\Delta\alpha = 6°$. Integration over the collimator is represented by a collimator transmission function (sometimes it is called the point-spread function) $\hat{P}(\phi', \psi')$ which determines the probability of an atom's detection inside the collimator (see Schwadron et al. 2009, for details). In our calculations, we use a simplified conical shape of the collimator (instead of a realistic hexagonal shape) because numerical tests show that this approximation is appropriate and does not influence the results. In this case, P depends only on one angle ψ' counted from the axis of the collimator. We use $P(\psi')$ found from the ISOC datacenter (the plot is presented in Figure 100). In Equation (89), f_H is the velocity distribution function of the ISH atoms at the point of observation, w_{rel} is the atom velocity relative to the spacecraft, w_H is the absolute atom's velocity vector (i.e., $\boldsymbol{w_H = w_{rel} + V_{SC}}$, where $\boldsymbol{V_{SC}}$ is the spacecraft velocity and the direction of $\boldsymbol{w_{rel}}$ is determined by the local line of sight inside the collimator); $E_{rel} = m_H\, w_{rel}/2$, = $V_{i,1}$ and $V_{i,2}$ determine the boundaries of energy bin i; $E_{min,i} = m_H V_{i,1}^2/2$ and $E_{max,i} = m_H\, V_{i.2}^2/2$, m_H is the mass of an H atom; the boundaries of the energy ranges for bin 1 and bin 2 are taken from Schwadron et al. (2013) and listed in Table 1. G_i is the geometrical factor (constant for each energy bin) and the magnitudes of G_i for i = 1, 2 are also listed in Table 29. Let us emphasize that G_2 is larger than G_1 almost by a factor of two. Hence, the same hydrogen fluxes in the two energy bins will give a two times larger count rate in energy bin 2 than in energy bin 1. Integration over the energy bin is performed with the normalized energy transmission function $\hat{T}_i(E)$ taken from Schwadron et al. (2013):

$$T_i(E) = exp\left(-4\ln 2\frac{\left(\frac{E}{E_{c,i}}-1\right)^2}{\Delta_1^2}\right) \quad for\ E \le E_{c,i}$$
$$= \exp\left(4\ln 2\frac{\left(\frac{E}{E_{c,i}}-1\right)^2}{\Delta_2^2}\right) \quad for\ E > E_{c,i},$$

(90)

where $E_{c,i}$ is the central energy of a given energy bin (see Table 29) and $\Delta_1 = 2\left(1 - E_{min,i}/E_{c,i}\right)$, $\Delta_2 = 2\left(1 - E_{c,i}/E_{min,i}\right)$. Functions $\hat{P}$ and $\hat{T}$ in Equation (89) are normalized by the following:

$$\hat{P}\left(\acute{\phi},\acute{\psi}\right) = \frac{P\left(\acute{\phi},\acute{\psi}\right)}{\iint P\left(\acute{\phi},\acute{\psi}\right)d\acute{\phi}d\acute{\psi}}$$
$$\hat{T}_i(E) = \frac{T_i(E)}{\int_{E_{min,i}}^{E_{max,i}} T_i(E)dE},$$

(91)

where integrations are performed over the acceptance angles inside the collimator and the energy range, respectively.

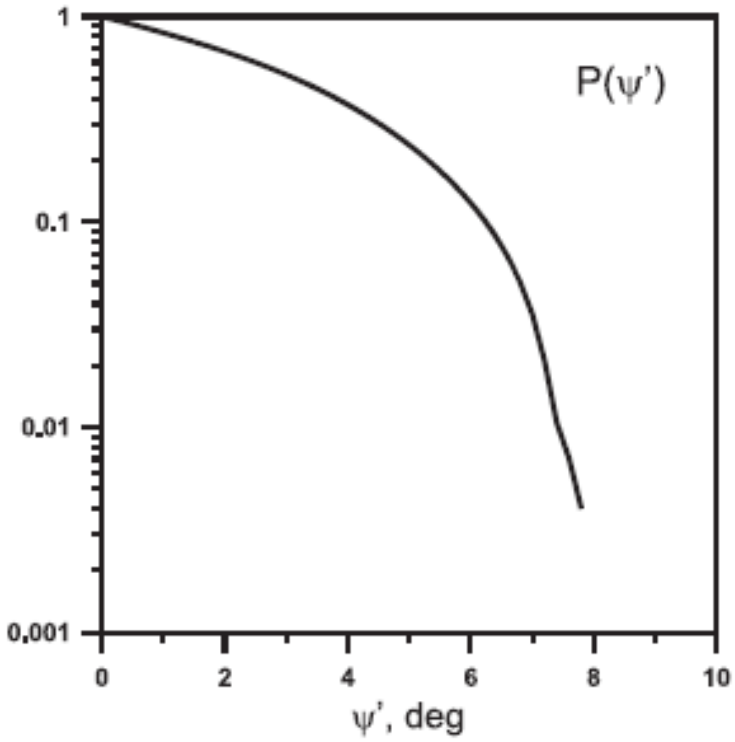

Figure 100: Collimator transmission (or point-spread) function; ψ' is an angle from the axis of the collimator.

Table 29: Central Energies (E_c), Energy Ranges (E_min and E_max), and Geometrical Factors (G) for Energy Bin 1 and Bin 2 of the IBEX-Lo Sensor

Energy Bin	E_c (eV)	E_{min} (eV)	E_{max} (eV)	G (cm^2 sr keV/keV)
1	15	11	21	$7.29 \cdot 10^{-6}$
2	29	20	41	$1.41 \cdot 10^{-5}$

5.4.14 IBEX-Lo Analysis of χ^2 and calculations of uncertainties

Figure 101 shows the obtained χ^2 as a function of the parameters μ_0, $\beta_{E,0}$, and γ. For each plot, two of the three parameters are fixed and correspond to the determined best-fit magnitudes and the third parameter is varied. We see that for μ_0 and $\beta_{E,0}$, the minimum of χ^2 is quite deep, while for γ the minimum almost disappears (χ^2 is almost constant for $\gamma > 1.5$). Therefore, γ cannot be determined precisely from the fitting of the data and only a lower limit of γ can be provided. The standard method for calculations of uncertainties for the determined best-fit parameters in the least-square method is to take $\chi_o^2 = \chi_{min}^2 + 1$ and find the range of parameters corresponding to $\chi^2 \leq \chi_0^2$However, this procedure is valid if the χ_{min}^2 obtained is close to 1. This is not our case because we found $\chi_{min}^2 = 6.82$. Theoretically, this means that either IBEX data

uncertainties ($\sigma_{i,j}^{data}$) are underestimated, or that we need to add some uncertainty connected to our numerical model. We introduce artificial model uncertainties $\sigma_{i,j}^{m} = \alpha \cdot \sigma_{i,j}^{data}$ such that the minimum χ_1^2 would be equal to 1, i.e.,

$$\chi_1^2(a) = \frac{1}{N-M}\sum_{i=1}^{2}\sum_{j=1}^{10}\frac{\left(C_{i,j}(\boldsymbol{a}) - C_{i,j}^{data}\right)^2}{\left(\sigma_{i,j}^{data}\right)^2 \cdot (1+\alpha^2)} = \frac{1}{1+\alpha^2}\cdot\chi^2(\boldsymbol{a}),$$

(92)

and α is chosen such that

$$1 = \chi_{1,min} = \frac{1}{1+\alpha^2}\cdot\chi_{min}^2.$$

(93)

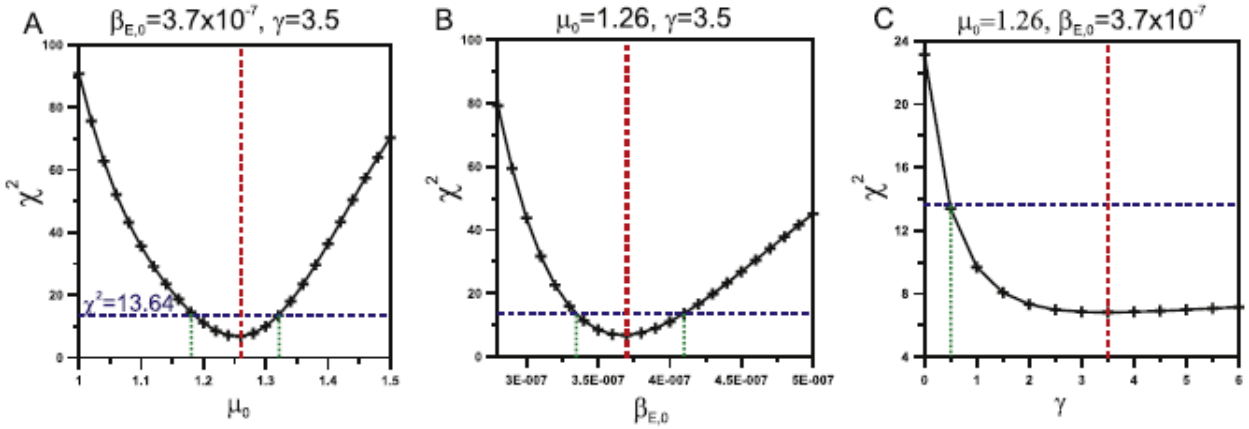

Figure 101: Obtained χ^2 in the fitting procedure as a function of μ_0, $\beta_{E,0}$, and γ. Red vertical lines in each plot correspond to the minimum χ^2. Blue horizontal lines show $\chi^2 = 13.64$ that is found as a level of error bars. Green dotted lines show corresponding ranges of the model parameters (for $\chi^2 \leq 13.64$).

Therefore, $1 + \alpha^2 = \chi_{min}^2 = 6.82$. Next, we consider the condition $\chi_1^2 < \chi_{1,min}^2 + 1 = 2$, which gives $\chi^2 < 2(1+\alpha^2) = 2 \cdot \chi_{min}^2 = 13.64$. From this condition and plots A-B in Figure 101, we can find uncertainties for the obtained best-fit parameters. Namely, $\mu_0 = 1.26^{+0.06}_{-0.076}$, $\beta_{E,0} = 3.7^{+0.39}_{-0.35} \times 10^{-7}\ s^{-1}$, $\gamma = 3.5^{+?}_{-3.02}$. The upper bound for γ can not be determined because the results are not sensitive to the magnitude of γ for any $\gamma > 0.5$.

5.4.15 IBEX-Lo approach to analysis of interstellar O parameters

There are five parameters that can be determined through analysis of IBEX interstellar O neutrals: the bulk flow speed, $V_{ISNO\infty}$, the temperature, $T_{ISNO\infty}$, the flow longitude, $\lambda_{ISNO\infty}$, the flow latitude, $\beta_{ISNO\infty}$, and the survival probability times the flow density, $n_{ISNO\infty} \times S_p$. The survival probability S_p of O atoms from the termination shock to the point of observation at 1 au depends primarily on the ionization rate $\beta^{ion} = \beta_1^{ion}(R_1^2/r^2)$,

which is referenced at $R_1 = 1$ au by β_1^{ion} and scales as $1/r^2$ where r is radial distance from the Sun. This scaling with radial distance neglects electron impact ionization, which makes a small contribution.

As detailed later in Sections 5.4.17 and 5.4.18, in the fitting performed we solve for a scaling constant, A_k, in each interstellar season, k. The scaling constant is proportional to $n_{ISNO\infty} \times S_p$. The survival probability is related to the ionization rate at 1 au,

$$S_p = \exp\left(\frac{mR_1^2\beta_1^{ion}}{l}[\theta - \theta_\infty]\right), \tag{94}$$

where θ is the position angle at the time of observation and θ_∞ is the position angle when the neutral was far from the Sun (at $t = -\infty$), as defined by Lee et al. (2012). The angular momentum is given by l. The model integrates precisely along neutral trajectories, accurately taking into account the variation in the gravitational force, ionization rate, and survival probability with distance from the Sun. The model remains linearly proportional to the scaling constant A_k that varies with the ionization rate at 1 au and the interstellar density near the termination shock. We discuss how the scaling constant A_k is solved in Sections 5.4.17 and 5.4.18.

All parameters other than β_1^{ion} apply at or near the termination shock since we neglect charge-exchange processes that occur within the heliosheath. In particular, filtration of O due to charge-exchange causes the ionization of neutral O atoms predominantly in the outer heliosheath, constituting a loss process for neutrals that modifies the neutral distribution function. Therefore, it is important to take filtration into account when determining the interstellar parameters in the LISM beyond the heliosphere.

The procedure for finding interstellar parameters starts with a comparison between observed rate distributions as a function of spin-phase and corresponding modeled rate distributions. The rate distributions are accumulated over the good times for a given orbit. The modeled rate distributions are also determined at a series of points in time separated by a maximum of 0.8 days (this time interval was chosen as a compromise between efficiency and convergence; smaller time intervals gave almost precisely the same answer as the chosen 0.8 day interval). The modeled distributions are then compared to observed rate distributions to yield a χ^2 difference or a likelihood. We vary interstellar parameters to minimize the χ^2 and maximize the likelihood, therefore finding the parameters that optimize the fits to observations.

Section 5.4.16 details our general approach to fitting and solving for uncertainties in fit parameters. Section 5.4.17 derives an analytical method for minimizing the χ^2 and thereby solving for background rates in each orbit and solving for a scaling factor, the interstellar O density at the termination shock times the ionization rate at a reference

distance (1 au). This scaling factor is treated as an unknown with which all modeled rates scale linearly.

The other four parameters used in the fit are the bulk speed, temperature, longitude, and latitude of the interstellar O flow ($V_{ISNO\infty}$, $T_{ISNO\infty}$, $l_{ISNO\infty}$, and $b_{ISNO\infty}$). In searching these four parameter values to minimize the χ^2 or maximize likelihood, it is important to recognize that there is an underlying dependency between the parameters that influences the 4D dependence of the χ^2 and likelihood functions. These interdependencies between parameters should be understood in order to do an accurate and efficient search for the global χ^2 minimum.

The hyperbolic trajectory equation, along with the IBEX observation at perihelion, leads to a strict relationship between the speed at infinity $V_{ISN\infty}$ and the flow angle $\lambda_{ISN\infty}$ in ecliptic longitude. The relation is governed by the motion of neutrals in the Sun's gravity, which has one parameter, the ecliptic longitude λ_{Peak} where the interstellar bulk flow hits perihelion (referred to hereafter as the peak longitude). We assume a small angle between the ecliptic plane and the trajectory plane (Lee et al. 2012), which is appropriate given that the upstream direction of the interstellar flow is ~5° above the ecliptic based on measurements of neutral He. The bulk flow velocity is defined as follows:

$$V_{ISN\infty} = \sqrt{\frac{GM_s}{R_1}\left(\frac{-1}{\cos(\lambda_{ISN\infty} + 180° - \lambda_{Peak})} - 1\right)} \ . \tag{95}$$

where R_1 denotes 1 au and M_s denotes the mass of the Sun. Equation (95) is strictly exact if the trajectory plane is identical to the ecliptic plane. Equation (95) applies for all species provided that they are acted upon only by gravity and ionization. (Radiation pressure can also be factored in; we have neglected it here for simplicity since we are primarily focused on interstellar O, which is not strongly affected by radiation pressure.)

One of the remarkable properties of the trajectory relation between interstellar speed and the peak longitude is that it naturally allows for a separation between primary and secondary components of ISN atoms. The charge-exchange process in the heliosheath renders secondary interstellar atoms much slower than the primary neutral atoms that come directly from the interstellar medium. In the case of interstellar O, primary atoms should have flow speed of ~26 km s^{-1}, similar to the flow speed of primary He. However, the secondary component is slowed and heated relative to the primary component. The average flow speed of secondary O has not been estimated.

The flow of O is analogous in some ways to He. The primary neutral component of He has a flow speed of 25.4 ± 1.1 km s^{-1} while the secondary component has a flow speed of ~11.3 km s^{-1}. The large speed differential shifts the peak longitude by ~26°. The Sun

acts as a “gravitational lens” that separates the primary from secondary components. This same effect leads to the separation of the secondary O component from the primary component (Park et al. 2015). Further, the secondary O neutrals come from the hot plasma flow in the outer heliosheath that is highly asymmetric relative to the primary flow direction (see Kubiak et al. 2016). This leads to a significant observed offset of the apparent secondary flow at the heliospheric boundary in both flow longitude and flow latitude. Finally, the O secondary component is much better separated from the O primary flow than for He and H because O has a much lower thermal speed (due to its higher atomic mass, the thermal speed of O is ~1/2 the thermal speed of He and ~1/4 the thermal speed of H). The lower thermal speed of O creates a much more sharply peaked velocity distribution function than for the He and H species.

The angular width of the ISN flow distribution as a function of spin-angle ψ observed at IBEX is controlled solely by the thermal speed (expressed through the temperature) and the ISN bulk flow speed $V_{ISN\infty}$ at infinity. Consequently, the width σ_ψ of the spin-angle distribution at the location of the bulk flow intercept at 1 au is defined by

$$\sigma_\psi^2 = \frac{k_B T_{ISN}}{m V_{ISN\infty}^2} \frac{(1 + w_{ISN\infty}^2)^2}{w_{ISN\infty}^2 (2 + w_{ISN\infty}^2)},$$

(96)

where T_{ISN} is the temperature of the ISN and m is the mass. Here $w_{ISN\infty} = V_{ISN\infty}/V_E$ is the dimensionless ISN flow speed normalized to the average speed of the Earth at 1 au, $V_E = \sqrt{GM_s/R_1}$ (Lee et al. 2012).

Note that the computation of the ISN temperature from the width of the observed flow distributions requires the mass of the species. The heavy ISN flow distribution is mostly O but also contains a sizable fraction of Ne (Bochsler et al. 2012; Park et al. 2014). Using the Ne/O ratio derived by Park et al. (2014) and factoring in the IBEX-Lo efficiencies for O and Ne from calibration, the observed Ne/O ratio has been translated into an effective mass of $m_O = 16.85 \pm 0.3$ for the combined O and Ne distribution. This effective mass value was used for the determination of the O temperature, which represents a combined O and Ne temperature.

We begin the process of searching for interstellar parameters by choosing a guess for $T_{ISNO\infty}$: 0, $\lambda_{ISNO\infty:0}$, and $\beta_{ISNO\infty:0}$. We then vary $V_{ISNO\infty}$ and find the minimum χ^2 in this dimension, $V_{ISNO\infty:1}$. Our initial guess for $T_{ISNO\infty:0}$, $\lambda_{ISNO\infty:0}$, and $\beta_{ISNO\infty:0}$ is based on the results for interstellar He (Schwadron et al. 2015). With the initial minimum for $V_{ISNO\infty:1}$, and the guesses for $\lambda_{ISNO\infty:0}$ and $\beta_{ISNO\infty:0}$, we vary $T_{ISNO\infty}$ to find the χ^2 minimum or maximum likelihood in this dimension, $T_{ISNO\infty:1}$.

The next step is to find the χ^2 minimum or maximum likelihood while varying $\lambda_{ISNO\infty}$. The relations previously specified (95) and (96) provide the means to consistently vary

$V_{ISNO\infty}$ ($\lambda_{ISNO\infty}$) and $T_{ISNO\infty}$ ($\lambda_{ISNO\infty}$) as a function of the flow longitude. We specify the peak longitude $\lambda_{Peak:1}$ based on the initial χ^2 minimum for bulk speed:

$$\lambda_{Peak:1} = \lambda_{ISNO\infty:1} + 180° - \cos^{-1}\left(\frac{-1}{1 + R_1(V_{ISNO\infty:1})^2/(GM_s)}\right).$$

(97)

With this value for the peak longitude, Equation (95) provides specification for determining $V_{ISNO\infty}$ ($\lambda_{ISNO\infty}$). Solutions are highly degenerate along the parameter tube. In other words, variation in longitude $\lambda_{ISNO\infty}$ with covariation in $V_{ISNO\infty}$ ($\lambda_{ISNO\infty}$) and $T_{ISNO\infty}$ ($\lambda_{ISNO\infty}$) leads to only small changes in the χ^2 or likelihood. Therefore, the search for a global minimum in the χ^2 or a global maximum in likelihood most strongly depends on where in longitude along the parameter tube that solutions best match observations.

We use Equation (96) to provide a reference angular width $\sigma_{\psi:1}$ based on the initial determinations of χ^2 minima from $V_{ISNO\infty:1}$ and $T_{ISNO\infty:1}$. The temperature as a function of $\lambda_{ISNO\infty}$ follows

$$T_{ISNO\infty}(\lambda_{ISNO\infty}) = \frac{m_O\sigma_{\psi:1}^2}{k_B}[V_{ISNO\infty}(\lambda_{ISNO\infty})]^4 \times \frac{2V_E^2 + [V_{ISNO\infty}(\lambda_{ISN\infty})]^2}{\{V_E^2 + [V_{ISNO\infty}(\lambda_{ISN\infty})]^2\}^2}.$$

(98)

By varying the interstellar temperature and interstellar speed as indicated here we break the underlying degeneracy in the parameter dependence. This greatly increases the efficiency of finding the global χ^2 minimum or the maximum likelihood.

When we find a χ^2 minimum or a maximum likelihood in the search in interstellar longitude, $\lambda_{ISNO\infty:2}$, we update the estimates for the interstellar speed and temperature: $V_{ISNO\infty:2} = V_{ISNO\infty}$ ($\lambda_{ISNO\infty:2}$) and $T_{ISNO\infty:2} = T_{ISNO\infty}(\lambda_{ISNO\infty:2})$. Using these values for the longitude, $\lambda_{ISNO\infty:2}$, the speed, $V_{ISNO\infty:2}$, and the temperature, $T_{ISNO\infty:2}$, we perform a search in latitude to find the corresponding χ^2 minimum or maximum likelihood at $\beta_{ISNO\infty:2}$.

As a final step in the analysis, we vary all parameters about the optimal fit. This serves both to guarantee that we have found an optimal fit, and allows us to map out the multidimensional shape of the χ^2 and likelihood functions of interstellar parameters. From the shape of χ^2 and likelihood functions, we derive curvatures in various parameter dimensions, from which fit and propagation uncertainties are determined (see Sections 5.4.16, 5.4.19, and 5.4.20).

The method described above represents an iterative process whereby initial guesses for the four interstellar parameters, the scale factor (which determines the interstellar

density and the ionization rate at 1 au) and background rates are successfully improved. This scheme converges rapidly. In our case we found convergence to less than 5% of uncertainties in three iterations.

The behavior of the χ^2 function and the maximum likelihood function are also used to ascertain uncertainties in the derived parameters. The uncertainty in the scaling factor δA_k is detailed in Sections 5.4.17 and 5.4.18. We describe here the approach to finding the uncertainties in the other four interstellar parameters ($V_{ISNO\infty}$, $T_{ISNO\infty}$, $\lambda_{ISNO\infty}$, $\beta_{ISNO\infty}$). The implicit parameters are the background rates $B_i = 1 \,..\, N$ where $N = 12$ is the number of orbits, and the linear scaling factors $A_{k=1\ldots Q}$ where $Q = 2$ is the number of interstellar seasons. These parameters are implicit because, as detailed in Sections 5.4.17 and 5.4.18, in every search through parameter space we solve directly for the background rates and scaling factors.

After specifying a guess for interstellar parameters, we then perform a search through parameter space by sweeping first the interstellar speed and then the interstellar temperature. For example, we may represent the one-dimensional (1D) sweep in speed x as $\chi^2 = \chi^2(x, T_{ISNO\infty}, \lambda_{ISNO\infty}, \beta_{ISNO\infty})$. This represents a 1D cut in parameter space. And because the interstellar longitude is frozen, this 1D cut determines the width of the parameter tube for the interstellar speed, $\delta V_{ISNO\infty}$, based on the curvature of χ^2 dependence on interstellar speed (see Section 5.4.19):

$$\chi^2(x) = \chi^2_{est} + C_2(x - V_{ISNO\infty:1})^2,$$

(99)

where C_2 is the curvature of the fit. Similarly, the curvature of likelihood function is used to derive the uncertainty $\delta V_{ISNO\infty:1}$ (see Section 5.4.20).

We approach uncertainties using the method outlined in Section 5.4.19 and 5.4.20, which is an extension of the approach discussed by Schwadron et al. (2013). There are two independent sources of uncertainty (see Section 5.4.16): (1) the propagation of measurement uncertainties associated with the observed rates, and (2) the statistical uncertainty associated with the χ^2 fit. For specificity, we consider the derivation of the uncertainty of the bulk speed, although a similar approach is employed also for the other interstellar parameters. The propagation uncertainty is found by inverting the curvature matrix (one half times the Hessian matrix, Press et al. 1992). The propagation uncertainty is given by

$$\left(\delta V^{pr}_{ISNO\infty:1}\right)^2 = C_2^{-1}.$$

(100)

The statistical uncertainty is

$$(\delta V_{ISNO\infty:1}^{st})^2 = (\delta V_{ISNO\infty:1})^2 \chi_{red}^2,$$

(101)

where χ_{red}^2 is the reduced χ^2 at the global minimum χ_{est}^2. The quantity ν is the number of degrees of freedom: $\nu = N - N_o - g$ where N is the total number of data points and N_o is the total number of orbits. In addition to the No background rates, we have $\gamma = 6$ additional parameters: the four interstellar parameters and two linear scaling factors (one scaling factor for each of the two interstellar seasons in 2009 and 2010). Combining the two forms of uncertainty, we have a total uncertainty given by

$$\delta V_{ISNO\infty:1} = \delta V_{ISNO\infty:1}^{pr} \sqrt{1 + \chi_{red}^2}.$$

(102)

Note that the speed uncertainty $\delta V_{ISNO\infty:1}$ applies *across* the parameter tube and combines the propagation and statistical uncertainties. There is also a covariant uncertainty along the parameter tube (in longitude), $\delta V_{ISNO\infty}^{cov}$, that is the largest source of uncertainty for the interstellar speed of oxygen. The 1σ upper and lower limits of the speed, $V_{ISNO\infty:1} \pm \delta V_{ISNO\infty:1}$, determine the corresponding upper and lower limits of the peak longitude, $\lambda_{Peak\pm\sigma}$, through Equation (97). Analogous solutions are found for uncertainties based on the curvature of the inverse likelihood function (Section 5.4.20).

A similar procedure is used to define the 1σ limits on the temperature parameter tube. We determine the χ^2 dependence or likelihood dependence on temperature, varying only the temperature and leaving the other three parameters fixed. The statistical and propagation uncertainties apply across the parameter tube, $\delta T_{ISNO\infty}$. Another source of uncertainty for the temperature arises from its dependence on interstellar speed in Equation (98).

The statistical and propagation uncertainties in flow longitude $\delta\lambda_{ISNO\infty}$ and flow latitude $\delta\beta_{ISNO\infty}$ are also determined. However, as already discussed, the variation in longitude is done while also varying speed and temperature along the parameter tubes. Therefore, the uncertainty in longitude is understood to apply along the parameter tube.

5.4.16 IBEX-Lo Statistical and propagation uncertainties

We examine the fitting of the M-parameter statistical model $V\ (x;\ p_1, p_2\ , \ldots, p_M)$ to the given data set $\{x_i, y_i\ \pm \sigma_{yi}\}_{i=1}^{N}$, by minimizing the χ^2

$$\chi^2(p_1, p_2, \ldots, p_M) = \sum_{i=1}^{N} \sigma_{yi}^{-2} [y_i - V(x_i; p_1, p_2, \ldots, p_M)]^2.$$

(103)

Here y_i is the number of counts. The global minimum of the χ^2 give the parameter optimal values, $(p_1^*, p_2^*, \dots, p_M^*)$, by solving the system of equations,

$$\begin{aligned}
\frac{\delta\chi^2(p_1, p_2, \dots, p_M)}{\delta p_1} &= 0, \\
\frac{\delta\chi^2(p_1, p_2, \dots, p_M)}{\delta p_2} &= 0, \\
&\dots, \\
\frac{\delta\chi^2(p_1, p_2, \dots, p_M)}{\delta p_M} &= 0.
\end{aligned}$$

(104)

After solving the system of these M equations, we derive the parameter optimal values as functions of data points,

$$\begin{aligned}
p_1^* &= p_1^*(y_1, y_2, \dots, y_N), \\
p_2^* &= p_2^*(y_1, y_2, \dots, y_N), \\
&\dots, \\
p_M^* &= p_M^*(y_1, y_2, \dots, y_N).
\end{aligned}$$

(105)

For simplicity, we have indicated only dependence on data (y) values.

The statistical error (also called the curvature error) of the optimal value p_m^* is given by

$$\delta p_{m,st}^* = \sqrt{\chi_{red}^2 \cdot 2H_{mm}^{-1}},$$

(106)

for $m = 1, 2, \dots, M$ and H is the Hessian matrix of the χ^2 at the global minimum. The quantity H_{mm}^{-1} is the mth diagonal element of the Hessian inverse matrix (Livadiotis 2007). The estimated χ^2 value is

$$\chi_{est}^2 = \chi^2(p_1^*, p_2^*, \dots, p_M^*),$$

(107)

and $\chi_{red}^2 = \chi_{est}^2/(N - M)$ is the reduced χ^2 value (the degrees of freedom are $N - M$).

We generalize the statistical error for use in maximum likelihood fitting techniques. Consider an arbitrary distribution function $P_i = f(y_i, V_i)$. The joint probability distribution over the set $\{y_i\}_{i=1}^N$ is $\Gamma = \Pi_{i=1}^N P_i$, or, by taking its logarithm,

$$\ln \Gamma = \sum_{i}^{N} \ln P_i = \sum_{i=1}^{N} \ln f\left(y_y, V_i\right).$$

(108)

The likelihood is defined by this joint probability, but it is more often used with the inverse function and its logarithm,

$$\ell = -c \sum_{i=1}^{N} \ln[f(y_i,\, V_i)]\,,$$

(109)

where c is an arbitrary constant (typically taken to be c = 2). The inverse likelihood ℓ is a function of the fitting parameters, $\ell(p_1, p_2, \ldots, p_M)$ and needs to be minimized, corresponding to the minimization of the χ^2 in the case of normally distributed data. The Taylor expansion of $\ell(p_1, p_2\,, \ldots, p_M)$ around its minimum value, $\ell^*(p_1^*, p_2^*, \ldots, p_M^*)$, gives

$$\begin{aligned}\ell(p_1, p_2, \ldots, p_M) &= \ell^*(p_1^*, p_2^*, \ldots, p_M^*) \\ &+ \sum_{i=1}^{N} \left(\frac{\delta \ell}{\delta p_i}\right)_{p=p^*} (p_i - p_i^*) + \frac{1}{2} \sum_{i=1}^{N} \sum_{j=1}^{N} \left(\frac{\delta^2 \ell}{\delta p_i \delta p_j}\right)_{p=p^*} \times (p_i - p_i^*)\left(p_j - p_j^*\right).\end{aligned}$$

(110)

Since this expansion is performed about an extremum, the second term in the expansion drops out, resulting in the following:

$$\ell(p_1, p_2, \ldots, p_M) = \ell^*(p_1^*, p_2^*, \ldots, p_M^*) + \sum_{i=1}^{N} \sum_{j=1}^{N} A_{ij}(p_i - p_i^*)\left(p_j - p_j^*\right),$$

(111)

where the curvature matrix A is half the Hessian,

$$A_{ij} = \frac{1}{2} H_{ij} = \frac{1}{2}\left(\frac{\delta^2 \ell}{\delta p_i \delta p_j}\right)_{p=p^*}.$$

(112)

The statistical independent uncertainty in this case is given by

$$\delta p_{i,st} \approx \sqrt{\frac{2\ell^*}{N - M} H_{ii}^{-1}},$$

(113)

There is another type of error that characterizes the uncertainty in parameter optimal values and involves the propagation of the measurement uncertainties $\{\sigma_{yi}\}_{i=1}^{N}$. This propagation uncertainty is given by

$$\delta p_{m,pr}^{*} = \sqrt{\sum_{i=1}^{N} \left(\frac{\delta p_{m}^{*}}{\delta y}\right)^{2} \sigma_{yi}^{2}}$$

(114)

for $m = 1, 2, K, M$.

The two types of uncertainty are fundamentally distinct: the curvature error is not strongly dependent on the measurement uncertainties $\{\sigma_{yi}\}_{i=1}^{N}$. In contrast, the propagation error is based directly on a weighted sum of the squares of measurement uncertainties. For example, if all measurement uncertainties are equal to σ, the propagation error becomes directly proportional to the common measurement uncertainty, $\delta p_{m,pr}^{*} \propto \sigma$. Because both uncertainties are distinct, they must both be included in the final uncertainty estimation. A rough approximation for the total uncertainty (see, for example, Schwadron et al. 2013) is given by

$$\delta p^{*} = \sqrt{(\delta p_{st}^{*})^{2} + \left(\delta p_{pr}^{*}\right)^{2}}.$$

(115)

5.4.17 IBEX-Lo Minimization of χ^2 for derivation of background rates and a model scaling factor

In this section we discuss how minimization of χ^2 can be used to derive orbit-by-orbit background rates and the scaling factor that multiplies the spin-phase distribution. Observed rate distributions as a function of spin-phase are represented by ψ_{ij}^{0} where the first index i corresponds to the orbit number, and the second index j refers to the spin-phase. These rate distributions are accumulated over the good times for a specific orbit. The model has dependencies on the instantaneous velocity and pointing of the spacecraft, and the instantaneous pointing of the IBEX-Lo instrument. As a result, the model simulations must also accumulate rates over the good time periods, and over the angles swept out over a given spin-phase bin. Therefore, the rate distribution modeled ψ_{ij}^{m} simulates the actual instrument response precisely.

The modeled rate distributions scale linearly with a factor that depends on the density times the survival probability, $n_{ISNO\infty} \times S_p$. Therefore, it is convenient to define an overall scaling factor $A_k = \left(n_{ISNO\infty}/n_{ref}\right) \times \left(S_p/S_{p-ref}\right)$ for the modeled rates. Here n_{ref} and S_{p-ref} are a reference density and a reference survival probability. The scaling

factor A_k should be roughly fixed in each interstellar season, but could vary from season to season. The scaling factor therefore depends on the year of observation, indexed by k. The model distribution is expressed:

$$\psi_{ij(k)}^{m} = A_k \psi_{ij}^{m'}.$$

(116)

Only specific orbits i exist in a given year and we treat the index (k) as an implicit value. The quantity $\psi_{ij}^{m'}$ represents simply the unnormalized modeled rate,

$$\psi_{ij}^{m'} = \frac{\psi_{ij(k)}^{m}}{n_{ref} S_{p-ref}}.$$

(117)

This unnormalized model distribution incorporates the effects of survival probability, integration through the instrument response, and all the factors involved in translating fluxes from the outer heliosphere to IBEX at 1 au.

There is also a background rate, B_i, that typically varies from orbit to orbit. We treat this background rate as a constant rate in the spin-phase distribution in a given orbit, which is added to the rate derived from interstellar atoms. Therefore the modeled spin-phase distribution in a given orbit is defined by

$$M_{ij(k)} = A_k \psi_{ij}^{m'} + B_i$$

(118)

and the corresponding χ^2 is given by and the corresponding χ^2 is given by

$$\chi^2 = \sum_{i=orbits} \sum_{j=spinphases} \left(A_k \psi_{ij}^{m'} + B_i - \psi_{ij}^{0}\right)^2 / \sigma_{ij}^2.$$

(119)

where σ_{ij} is the uncertainty in the observed rate.

We solve for the background rate and scaling factor by minimizing the χ^2 explicitly. We solve $\delta\chi^2/\delta B_i = 0$, which yields

$$B_i = \bar{O}_i - A_k \bar{M}_i$$

(120)

where the effective observed rate $\bar{O}_i$ is

$$\bar{O}_i = \frac{\sum_{j=spinphases} \psi_{ij}^0/\sigma_{ij}^2}{\sum_{j=spinphases} 1/\sigma_{ij}^2}$$

(121)

and the effective model rate $\bar{M}_i$ is

$$\bar{M}_i = \frac{\sum_{j=spinphases} \psi_{ij}^{m'}/\sigma_{ij}^2}{\sum_{j=spinphases} 1/\sigma_{ij}^2}.$$

(122)

In order to solve for the scaling factor A_k and its uncertainty δA_k^*, we express the χ^2 as a quadratic function of A_k with a minimum at A_k^*:

$$\chi^2 = C_0 + C_2(A_k - A_k^*)^2.$$

(123)

By setting Equation (123) equal to Equation (119) we may solve for the coefficients C_0, A_k^*, and C_2 :

$$C_2 = \sum_{i=orbits} \sum_{j=spinphases} \left(\psi_{ij}^{m'}\right)^2/\sigma_{ij}^2$$

(124)

$$A_k^* = C_2^{-1} \sum_{i=orbits} \sum_{j=spinphases} \left(\psi_{ij}^O - B_i\right)\psi_{ij}^{m'}/\sigma_{ij}^2$$

(125)

$$C_0 = \sum_{i=orbits} \sum_{j=spinphases} \frac{\left(\psi_{ij}^O - B_i\right)^2}{\sigma_{ij}^2} - C_2(A_k^*)^2.$$

(126)

This formulation is similar to that used by Schwadron et al. (2013), where it is shown that the statistical uncertainty of the χ^2 minimum from a quadratic form is

$$\delta A_{k,st}^* = \sqrt{C_0/(\nu C_2)},$$

(127)

where ν is the number of degrees of freedom.

The propagation uncertainty $\delta A^*_{k,pr}$ follows from the traditional treatment of error propagation

$$\delta A^*_{k,pr} = \sqrt{\sum_{i=orbits} \sum_{j=spinphases} \left(\frac{\delta A^*_k}{\delta \psi^o_{ij}}\right)^2 \sigma^2_{ij}} = 1/\sqrt{C_2}\,.$$

(128)

We note further that C_0 is the minimum of the χ^2 and that the reduced χ^2 (denoted χ^2_{red}) at the global minimum is given by,

$$\chi^2_{red} = C_0/v.$$

(129)

Therefore, the statistical uncertainty is directly related to the propagation uncertainty,

$$\left(\delta A^*_{k,st}\right)^2 = \left(\delta A^*_{k,pr}\right)^2 \chi^2_{red},$$

(130)

which results in a total uncertainty given by

$$(\delta A^*_k)^2 = (1 + \chi^2_{red})\left(\delta A^*_{k,pr}\right)^2.$$

(131)

This result can be readily interpreted. The minimum reduced χ^2 amplifies the propagation uncertainty. A poor fit results in a large value of χ^2_{red} and thereby increases the total uncertainty. The propagation uncertainty represents the minimum possible uncertainty in the presence of a particularly good fit. A statistically likely fit with $\chi^2_{red} \sim 1$ results in a total uncertainty that is $\sqrt{2}$ larger than the propagation uncertainty.

In this case, there are two sets of variables to determine from explicit χ^2 minimization: the background rate B_i determined on an orbit-by-orbit basis; and the scaling factor A_k determined for each interstellar season in a given year. The task is to find a χ^2 minimum as a function of both the background rates and the scaling factor. We find this two-dimensional (2D) χ^2 minimum through successive iterations: we find the background rates, then use those background rates in the solution for the amplitude, and then solve again for the background rates, and so forth. This scheme converges quite quickly (typically within three steps) to the 2D χ^2 minimum.

5.4.18 IBEX-Lo maximum likelihood for deriving background rates and a model scaling factor

We use maximum likelihood to calculate background rates and a model scaling factor in a manner similar to the derivation in Section 5.4.17. Specifically, the model is specified as

$$M_{ij(k)} = A_k \psi_{ij}^{m'} + B_i,$$

(132)

where A_k is the scaling factor and B_i is the background rate. In this case, we must specify the expected counts $m_{ij(k)}$,

$$m_{ij(k)} = \left(A_k \psi_{ij}^{m'} + B_i\right) \Delta t_{ij(k)}$$

(133)

where $\Delta t_{ij(k)}$ is the exposure time. Using this expectation value, the probability of observing counts $o_{ij(k)}$ is

$$P_{ij(k)} = \frac{m_{ij(k)}^{o_{ij(k)}} \exp\left(-m_{ij(k)}\right)}{o_{ij(k)}!}.$$

(134)

The inverse likelihood is expressed as

$$\begin{aligned} \ell_k &= -2 \sum_{ij(k)} \ln\left(P_{ij(k)}\right) \Big) \\ &= -2 \sum_{ij(k)} \left[o_{ij(k)} \ln m_{ij(k)} - m_{ij(k)} - \ln\left(o_{ij(k)}!\right)\right], \end{aligned}$$

(135)

where the summation extends over only those orbits associated with a given season k.

The minimization of ℓ_k with respect to the background rate B_i, $\ell_k / B_i = 0$, leads to the relation

$$\sum_j \frac{\sigma_{ij(k)}}{A_k \psi_{ij}^{m'} + B_i} = \sum_j \Delta t_{ij(k)}.$$

(136)

The constant B_i is varied using a search algorithm to find the optimal value. We minimize the inverse likelihood with respect to the amplitude, A_k, $\delta \ell_k / A_k = 0$, leading to

$$\sum_{ij} \frac{\sigma_{ij(k)} \psi_{ij}^{m'} \Delta t_{ij(k)}}{A_k \psi_{ij}^{m'} + B_i} = \sum_{ij} \psi_{ij}^{m'} \Delta t_{ij(k)} \,.$$

(137)

where the summation extends over only those orbits associated with a given season k. A search algorithm is used to find the optimal amplitude.

5.4.19 IBEX-Lo statistical and propagation uncertainties in nonlinear forward models using χ^2 minimization

As discussed in Section 5.4.16, there are two forms of uncertainty included in our calculations: the statistical and propagation uncertainty. In a previous section (Section 5.4.16), because we are able to solve for the model scaling factor analytically, it is relatively straightforward to directly solve for both the statistical and propagation uncertainties. The difficulty arises however in nonlinear forward models where there is no closed form analytic solution to determine best χ^2 fits for model parameters. In this case, we must find alternative solutions to derive the best-fit parameters and their uncertainties. This section develops a relatively straightforward and robust technique for deriving these uncertainties.

The χ^2 analysis used here is five dimensional. It is useful here to consider a nonlinear forward model with one parameter, p. The $\chi^2 = \chi^2(p)$ is minimized to find a best-fit at $p = p^*$. We consider a series of N measurements $\{O_i\}_{i=1}^N$ with uncertainties $\{\sigma_i\}_{i=1}^N$ and corresponding simulated values $\{M_i\}_{i=1}^N$. The χ^2 is defined:

$$\chi^2 = \sum_{i=1}^{N} \left(\frac{M_i - O_i}{\sigma_i} \right)^2 .$$

(138)

Because the χ^2 has a minimum, its dependence on p can be approximated as a quadratic:

$$\chi^2 = C_0 + C_2 (p - p^*)^2$$

(139)

The statistical uncertainty is then

$$(\delta p_{st}^*)^2 = \frac{C_0}{v C_2},$$

(140)

where v is the number of degrees of freedom: $v = N - M$ and the number of model parameters is $M = 1$.

The propagation uncertainty is calculated as follows:

$$\left(\delta p_{pr}^{*}\right)^{2} = \sum_{i=1}^{N} \left(\frac{\partial p^{*}}{\partial O_i}\right)^{2} \sigma_i^2.$$

(141)

The difficulty in this case is that there is no closed-form solution for $p^{*}(O_i)$, which makes it cumbersome to solve Equation (141).

One option for solution is to approach the problem numerically. We go through each measurement and vary the measured value through $O_i \pm \sigma_i$. As we perform this variation, we solve for the χ^2 and find how variation in O_i causes variation in the χ^2 minimum. This allows us to solve for $\delta p^{*}/\delta O_i$. We then move to the next data point $i + 1$, vary the data point $O_{i+1} \pm \sigma_{i+1}$ find the change in p^{*}, and solve for $\delta p^{*}/\delta O_{i+1}$.

There are two problems with this solution. First, if the number of measurements N is large, which is typical, then the calculation becomes extremely costly to compute. The second problem is that finding the χ^2 minimum often involves interpolation. Therefore, finding the effects of extremely small changes to χ^2 and the resulting small changes in p^{*} is likely to be difficult to compute accurately.

There is another way to approximate the changes to p^{*}, that is far more straightforward to implement and interpret. We consider the solution for p^{*} as a weighted average of individual terms p_i, which represent the model parameter based on a given observation O_i. The average for p^{*} is weighted by the inverse of parameter variances σ_{pi}^{-2} (to be detailed as follows):

$$p^{*} = \left(\sum_{i=1}^{N} \sigma_{pi}^{-2}\right)^{-1} \sum_{i=1}^{N} \sigma_{pi}^{-2} p_i.$$

(142)

In formulating this solution, we use the model to estimate how individual terms in the summation, pi, change based on variations in the observed data O_i. Specifically, we use partial derivative $\delta M_i/p$ to estimate how a change in a given observation ΔO_i leads to a change in the model parameter Δp_i:

$$\Delta p_i = \left(\frac{\partial M_i}{\partial p}\right)^{-1} \Delta O_i.$$

(143)

In order to turn this estimate of Δp_i into an estimate of p_i itself we must simply include a constant $\bar{O}_i$, such that

$$p_i \approx \left(\frac{\partial M_i}{\partial p}\right)^{-1} (O_i + \bar{O}_i).$$

(144)

Since we are concerned only with small changes in pi resulting from changes in O_i, it is important only that the constant $\bar{O}_i$ is fixed while O_i is varied.

Similar reasoning is applied to find the variance of the parameter σ_{pi}^2 based on the variance observed σ_i^2 using $\delta M_i/\delta p$ to convert observed variances into parameter variances:

$$\sigma_{pi}^2 = \left(\frac{\partial M_i}{\partial p}\right)^{-2} \sigma_i^2.$$

(145)

By substituting Equations (144) and (145) into (142), we recover the following solution for p^*

$$p^* \approx \left(\sum_{i=1}^{N} \sigma_i^{-2} \left[\frac{\partial M_i}{\partial p}\right]^2\right)^{-1} \times \sum_{i=1}^{N} \sigma_i^{-2} \left(\frac{\partial M_i}{\partial p}\right) (O_i + \bar{O}_i).$$

(146)

Equation (146) is now substituted into (141) to find the variance in p^*:

$$\left(\partial p_{pr}^*\right)^2 = \left(\sum_{i=1}^{N} \sigma_i^{-2} \left[\frac{\partial M_i}{\partial p}\right]^2\right)^{-1}.$$

(147)

This solution for the propagation uncertainty may be used directly. There is a further simplification when we consider the original form of the χ^2 minimum. We treat the model solutions as a second-order expansion about the optimal solution:

$$M_i \approx M_i^* + \left(\frac{\partial M_i}{\partial p}\right)^* (p - p^*) + \frac{1}{2}\left(\frac{\partial^2 M_i}{\partial p^2}\right)^* (p - p^*)^2.$$

(148)

Substitution of this second-order expansion into the χ^2, Equation (138), results in the following when we retain terms up to the second order in $(p - p^*)$:

$$\chi^2 = \sum_{i=1}^{N} \frac{(M_i^* - O_i)^2}{\sigma_i^2} + 2(p - p^*) \sum_{i=1}^{N} \left(\frac{\partial M_i}{\partial p}\right)^* \frac{(M_i^* - O_i)}{\sigma_i^2} + (p - p^*)^2 \sum_{i=1}^{N} \sigma_i^{-2} \left[\left(\frac{\partial M_i}{\partial p}\right)^{*2} + \left(\frac{\partial^2 M_i}{\partial p^2}\right)^* (M_i^* - O_i)\right].$$

(149)

Because the solution exists at the minimum of the χ^2, the term that is the first order in $(p - p^*)$ must vanish:

$$\sum_{i=1}^{N} \left(\frac{\partial M_i}{\partial p}\right)^* \frac{(M_i^* - O_i)}{\sigma_i^2} = 0.$$

(150)

Notice also that we may now relate the constants in Equation (139) to the terms in the expansion:

$$C_0 = \sum_{i=1}^{N} \frac{(M_i^* - O_i)^2}{\sigma_i^2},$$

(151)

$$C_2 \approx \sum_{i=1}^{N} \sigma_i^{-2} \left(\frac{\partial M_i}{\partial p}\right)^{*2},$$

(152)

where we have neglected the second-order derivative $(\partial^2 M_i/\partial p^2)^*$ from C2. This approximation, which is commonly used, simplifies the analysis and, in practice, does not substantially change the amplitude of the second order term. This association, when applied to Equation (147) implies that

$$\left(\delta p_{pr}^*\right)^2 \approx C_2^{-1}.$$

(153)

As in Section 5.4.16, this then implies that

$$(\delta p_{st}^*)^2 \approx \chi_{red}^2 \left(\delta p_{pr}^*\right)^2$$

(154)

where $\chi_{red}^2 = \chi_{est}^2/(N-M)$ is the minimum value of the reduced χ^2. The total uncertainty is

$$(\delta p^*)^2 = (1+\chi_{red}^2)\left(\delta p_{pr}^*\right)^2.$$

(155)

As was found previously in Section 5.4.16, the statistical uncertainty is an amplification of the propagation uncertainty where the term χ_{red}^2 serves as an amplification factor.

The propagation uncertainty is related to the covariance. For example, in Press et al. (1992), the curvature matrix (one half times the Hessian matrix) is found to be

$$\alpha_{kl} = \sum_{i=1}^{N} \frac{1}{\sigma_i^2}\left(\frac{\partial M_i}{\partial p_k}\frac{\partial M_i}{\partial p_l}\right)^*,$$

(156)

where p_k is a given parameter in a multidimensional fit. The covariance matrix $\boldsymbol{C}$ is the inverse of the matrix $[\alpha]$:

$$\boldsymbol{C} = |\alpha|^{-1}$$

(157)

and the diagonal elements of the covariance matrix constitute the variances of the parameters involved in the fit, which we show are in fact the propagation uncertainties,

$$\left(\delta p_{k,pr}^*\right)^2 = C_{kk},$$

(158)

When applied to a single-dimensional fit, we find that the curvature matrix reduces to the following constant

$$\alpha = \sum_{i=1}^{N} \frac{1}{\sigma_i^2}\left(\frac{\partial M_i}{\partial p}\right)^{*2},$$

(159)

which is identically equal to C2. And the inverse of α is identically equal to the variance of the propagation uncertainty, $\left(\delta p_{pr}\right)^2 = 1/\alpha$, as found previously, Equation (153). Substitution of Equation (153) into (154) therefore yields

$$(\delta p_{st}^{*})^2 = \chi_{red}^2/\alpha$$
$$= \chi_{red}^2 \cdot 2H^{-1}$$

(160)

where H is the Hessian. The derivation comes full-circle, revealing the consistency of the derived terms for the statistical and propagation uncertainties.

The discussion in Section 5.4.15 applies to the derivation of the parameter tube for interstellar parameters, which exists in 4D parameter space. This constitutes a multi-parameter fit using χ^2 minimization. The parameter tube is itself an expression of the underlying relationship between interstellar parameters. And because the interstellar speed and interstellar temperature are varied along the parameter tube when finding the χ^2 minimum in the interstellar longitude, the covariance between parameters is handled explicitly. As a result, it is appropriate to treat uncertainties using the 1D equations for the propagation and statistical uncertainties: Equations (153) and (154). It must be appreciated however that the uncertainty in interstellar speed and interstellar temperature define the width of the parameter tube in their respective dimensions. The uncertainty in the interstellar longitude applies along the parameter tube and provides the most significant covariant uncertainty in determining the interstellar speed and temperature.

It is also apparent that utilization of the covariance alone determines only the propagation uncertainty. The statistical uncertainty is an additional and independent contribution that inflates the total uncertainty.

5.4.20 IBEX-Lo statistical and propagation uncertainties in nonlinear forward models using maximum likelihood

The main difference between χ^2 minimization and maximum likelihood is the approach to metric used to relate observations and model predictions. We consider bin i of the number of counts observed oi or modeled mi. Note that there is an important distinction between the counts within bins used here and the rates used in Sections 5.4.16 and 5.4.17. The exposure time Δt_i is used to relate rates to observed or modeled counts:

$$o_i = O_i \Delta t_i$$

(161)

$$m_i = M_i \Delta t_i.$$

(162)

We treat the observed events within each bin o_i as a random Poisson distribution with expectation value m_i,

$$P_i(m_i) = \frac{m_i^{o_i} \exp(-m_i)}{o_i!}.$$

(163)

The χ^2 is related to the joint probability associated with a Gaussian distribution, P_{Gi}, $\chi^2 = -2\sum_i \ln(P_{Gi})$. The corresponding quantity in the case of Poisson distribution is

$$\ell = -2\sum_i \ln(P_i) = -2\sum_i (o_i \ln(m_i) - m_i - \ln[o_i!]).$$

(164)

The maximum likelihood is found by minimizing ℓ with respect to a parameter p:

$$\frac{\partial \ell}{\partial p} = 0$$
$$= 2\sum_i \left(\frac{m_i - o_i}{m_i}\right)\frac{\partial m_i}{\partial p}.$$

(165)

The counterpart for solving for an extremum in the minimization of χ^2 is

$$\frac{\partial \chi^2}{\partial p} = 0$$
$$= 2\sum_i \left(\frac{m_i - o_i}{\sigma_i^2 \Delta t_i^2}\right)\frac{\partial m_i}{\partial p}.$$

(166)

The variance can be derived precisely based on the curvature of $ln(P_i)$:

$$\frac{1}{\sigma_i^2} = \frac{\partial^2(-\ln P_i)}{\partial M_i^2}.$$

(167)

It should be noted in this relation that the inverse variance is related to the curvature with respect to variation in the model, as opposed to the curvature with respect to variation in observation. The reason for basing the uncertainty on model variation is that the model is a continuous variable, and, as a result, the curvature can be defined accurately even when the observed counts are low. Applying the relation in Equation (167) to the Poisson distribution, we find the following definition for the inverse variance:

$$\frac{1}{\sigma_i^2} = \frac{o_i}{M_i^2}.$$

(168)

We apply the same approach as that in Section 5.4.17 to derive the propagation uncertainty,

$$\left(\delta p_{pr}^*\right)^2 = \left(\sum_{i=1}^{N} \sigma_i^{-2} \left[\frac{\partial M_i}{\partial p}\right]^2\right)^{-1}$$
$$= \left(\sum_{i=1}^{N} \frac{\sigma_i}{m_i^2} \left[\frac{\partial m_i}{\partial p}\right]^2\right)^{-1},$$

(169)

where we have used Equation (168) to relate the variance to expected counts in a bin. We expand the ℓ to the second order in $(p - p^*)$:

$$\ell = \ell^* + 2(p - p^*) \sum_i \left(\frac{\partial m_i}{\partial p}\right)^*$$
$$+ (p - p^*)^2 \sum_i \left(\frac{\partial^2 m_i}{\partial p^2}\right)^* \left(\frac{m_i - o_i}{m_i}\right)^* + (p - p^*)^2 \sum_i \left(\frac{\partial m_i}{\partial p}\right)^{*2} \left(\frac{o_i}{m_i^2}\right)^*,$$

(170)

where $\ell * = \ell\,(p *)$. We neglect terms involving second derivatives of mi and the first-order term vanishes since we are at an extremum. With these simplifications, we find the following quadratic form for ℓ:

$$\ell = C_0 + C_2(p - p^*)^2$$

(171)

$$C_0 = \ell^*$$

(172)

$$C_2 = \sum_i \left(\frac{\partial m_i}{\partial p}\right)^{*2} \left(\frac{o_i}{m_i^2}\right)^*$$
$$= \sum_i \sigma_i^{-2} \left(\frac{\partial m_i}{\partial p}\right)^{*2}.$$

(173)

Therefore, we find that the propagation and statistical uncertainties are

$$\left(\delta p_{pr}^{*}\right)^{2} = C_{2}^{-1}$$

(174)

$$(\delta p_{st}^{*})^{2} = \frac{\ell^{*}}{(N-M)C_{2}}.$$

5.5 Conversion of IBEX-Hi and IBEX-Lo Signals to Flux

This section describes the algorithms and methods common to both IBEX-Hi and IBEX-Lo used to derive science data from raw instrument signals.

5.5.1 Instructions for combining IBEX ENA maps

Combining different maps is done by accounting for the statistical uncertainties and time exposure weighting. In this section, we provide an example of combining three different maps. We consider three different ENA maps and define the following parameters associated with each map:

1) ENA Exposure times for the three ENA maps: τ_1 , τ_2, τ_3;

2) ENA fluxes for the three ENA maps: F_1, F_2, F_3;

3) ENA flux variances for the three ENA maps: σ_1, σ_2, σ_3;

We now calculate the weights from the exposure times as,

$$w_1 = \frac{\tau_1}{\tau_1 + \tau_2 + \tau_3}$$
$$w_2 = \frac{\tau_2}{\tau_1 + \tau_2 + \tau_3}$$
$$w_3 = \frac{\tau_3}{\tau_1 + \tau_2 + \tau_3}$$

(175)

We then determine the combined flux using:

$$F_C = F_1 w_1 \; + \; F_2 * w_2 \; + \; F_3 * w_3 \, ,$$

and the combined variance is given by:

$$\sigma_C = \sigma_1 (w_1)^2 \; + \; \sigma 2 (w t_2)^2 + \sigma_3 (w t_3)^2 \, .$$

5.5.2 IBEX Compton-Getting Correction

The IBEX spacecraft moves around the Sun with a velocity that is a measurable fraction of the velocity of the ENAs being measured. Therefore, a Compton-Getting correction is needed to quantitatively compare measurements taken at different parts of the year. The first two 6-month maps are transformed from the spacecraft reference frame into the inertial reference frame at the central energy of each of the highest five IBEX-Hi energy steps (0.71, 1.11, 1.74, 2.73, and 4.29 keV). The Earth's orbital velocity is ~30 km s^{-1}, which is nearly 7% of the velocity of a 1 keV H atom (the orbital velocity of IBEX around the Earth is ~1 km s^{-1} and will be neglected here). Figure 102 shows the change in angle and energy for the transformation of an ENA from a fixed energy in the spacecraft frame to the inertial reference frame. The change in angle and energy depend on the central look direction of the sensor as it rotates about the spin axis directed approximately toward the Sun. In general, the effects associated with the change in reference frame become most important at the lowest energy steps observed by IBEX, and the corrections are relatively small (<5° change in angle, and <15% change in energy) at the energies analyzed here (>0.7 keV).

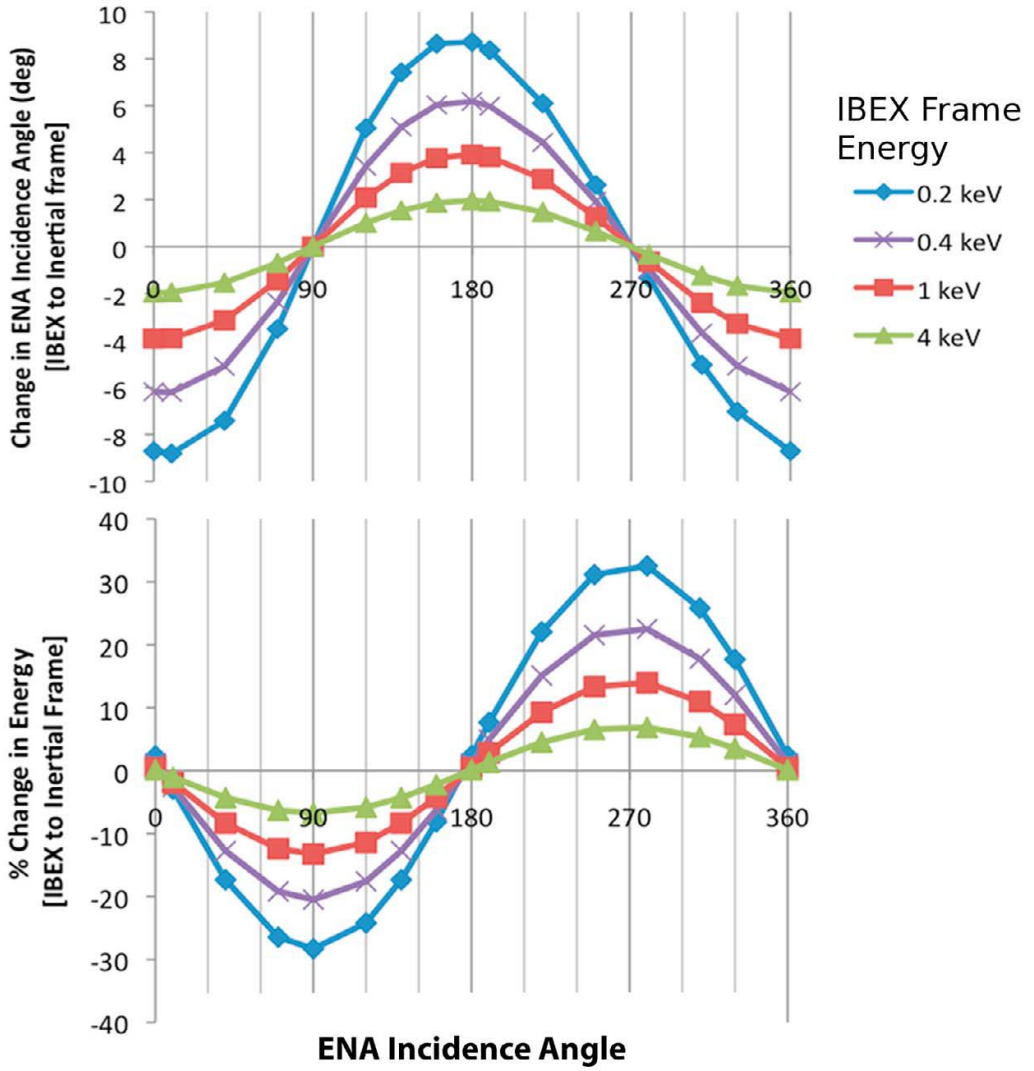

Figure 102: The change in (top) ENA incidence angle and (bottom) energy from the IBEX reference frame to the inertial frame as a function of the ENA incidence angle measured from the North Ecliptic Pole in the spacecraft frame. The spacecraft rotates about the spin axis directed approximately toward the Sun, with each of the sensors directed approximately perpendicular to the spin axis. A sensor measures an ENA incidence angle of 0° where the sensor bore sight points to the NEP (see Figure 104). Since the spacecraft spins in a right-handed sense, an ENA incidence angle of 90° is measured where the sensor bore sight is directed roughly along the vector of Earth's motion about the Sun. An ENA incidence angle of 180° is measured where the bore sight is directed along the South Ecliptic Pole, and an incidence angle of 270° is measured where the bore sight is directed opposite to Earth's motion.

The reference frame changes in energy and angle are particularly important when comparing sky maps obtained 6 months apart, since each map is derived from opposite halves of the year, and thus opposing orbital velocity directions. For example, in Figure 103 we see that the nose of the heliosphere is imaged in March. Since the orbital velocity and actual velocity of the particle are added in the observation, the apparent

velocity of the ENAs from the nose direction is larger in the IBEX spacecraft's frame of reference. That is, IBEX will effectively sample lower energy heliospheric ENAs from the nose. Six months later, in September, the nose is again imaged, but this time in the wake direction (opposed to the velocity vector), so IBEX effectively samples higher energy heliospheric ENAs at the same energy step. In order to compare maps taken 6 months apart we must correct for the difference in effective sampling energy in the two maps. This appendix describes the correction implemented in the IBEX data analysis. It is worth noting that this particular correction methodology was vetted through a consensus process with the IBEX science team, which included significant testing and validation.

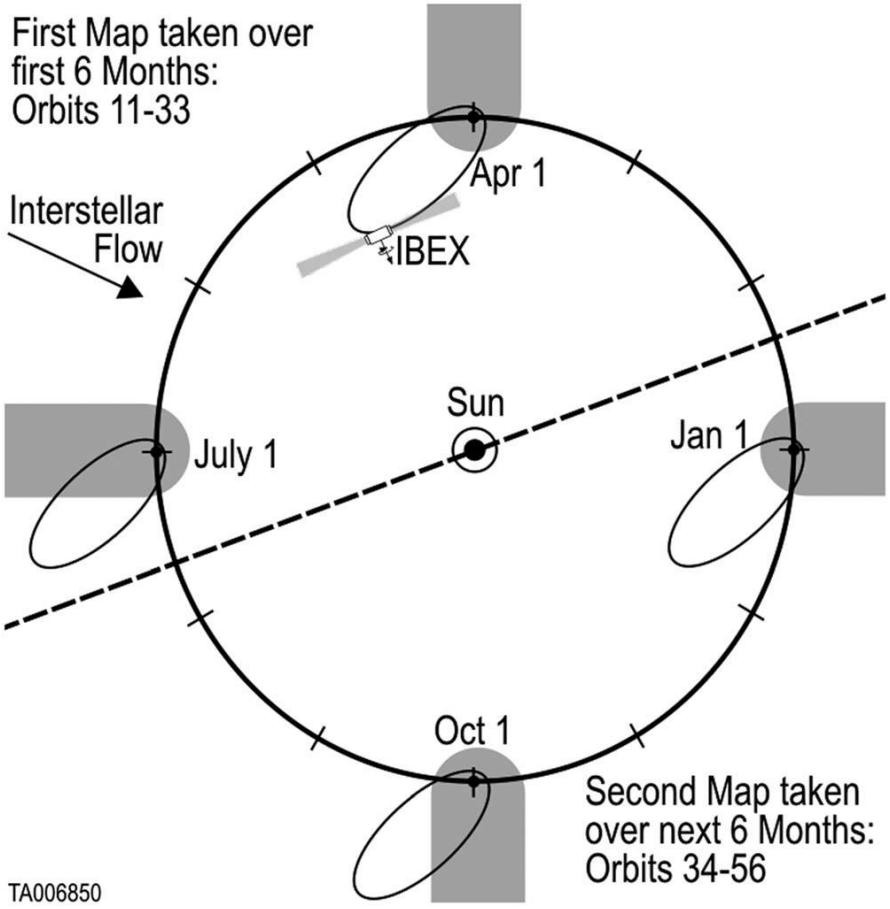

Figure 103: Schematic diagram of IBEX orbital geometry showing the inertially fixed IBEX orbit with respect to the Earth and magnetosphere (gray) over the year. The IBEX spacecraft is repointed once each orbit and views perpendicular to its Sun-pointing spin axis. The first and second maps were taken over separate halves of the Earth's orbit, with IBEX's apogee being mostly sunward of the Earth for the first maps and tailward for the second.

Let v be the velocity vector of an ENA in the IBEX frame (Figure 104). The IBEX spacecraft moves with the velocity u_{SC} with respect to the solar inertial frame. The velocity vector of the ENA in the solar inertial frame, vi, is therefore $vi = v + u_{SC}$. IBEX

measures ENAs in a plane nearly perpendicular to the direction of the Sun, and the ENA incidence velocity angle, θ, is the incoming velocity angle of the ENA referenced to Ecliptic North in right-handed rotation about the sunward axis (Z). Note that the incidence velocity angle, θ, represents the angle between the vector, −v, and the North Ecliptic Pole (NEP). We represent vectors in a coordinate system where the x axis points toward the NEP, the y axis points in the direction of Earth's motion about the Sun (these are Z_{GSE} and $-Y_{GSE}$), and the Z axis is directed toward the Sun. With this representation, Galilean transformations are explicitly

$$v \begin{vmatrix} cos\ \theta \\ \sin\theta \end{vmatrix} = v_i \begin{vmatrix} cos\ \theta_i \\ \sin\theta_i \end{vmatrix} + \begin{vmatrix} 0 \\ u_{SC} \end{vmatrix}.$$

(176)

The magnitude of the velocity in the inertial frame is therefore

$$v_i = v\sqrt{1 - 2\left(\frac{u_{SC}}{v}\right)\sin\theta + \left(\frac{u_{SC}}{v}\right)^2}$$

(177)

the angular aberration between the systems is

$$cos\theta_i = \frac{v}{v_i}\cos\theta$$
$$\sin\theta_i = \frac{v}{v_i}\sin\theta - \frac{u_{SC}}{v_i}$$

(178)

and the ratio of energies is

$$\frac{E_i}{E} = \frac{\boldsymbol{v_i}\cdot\boldsymbol{v_i}}{\boldsymbol{v}\cdot\boldsymbol{v}} = 1 - \frac{2u_{SC}}{v}\sin\theta + \left(\frac{u_{SC}}{v}\right)^2.$$

(179)

The invariance of phase-space density requires that the ENA flux in the solar inertial frame, $j_i(\theta_i, E_i)$, be related to the ENA flux in the IBEX spacecraft frame, $j(\theta, E)$, as

$$j_i(\theta_i, E_i) = \frac{E_i}{E} j(\theta, E),$$

(180)

which along with the equations above, allows us to express the ENA flux in the solar inertial frame given measured fluxes in the IBEX frame. It is important to note, however, that for measurements at a fixed energy and a regular angle grid, the resulting fluxes in the solar inertial frame will be given at multiple energies on an irregular angular grid. This is rather awkward for producing maps and makes comparison of maps taken 6

months apart difficult. We therefore develop a method that allows us to produce estimates of the flux in the solar inertial frame at fixed energies and on a regular angle grid.

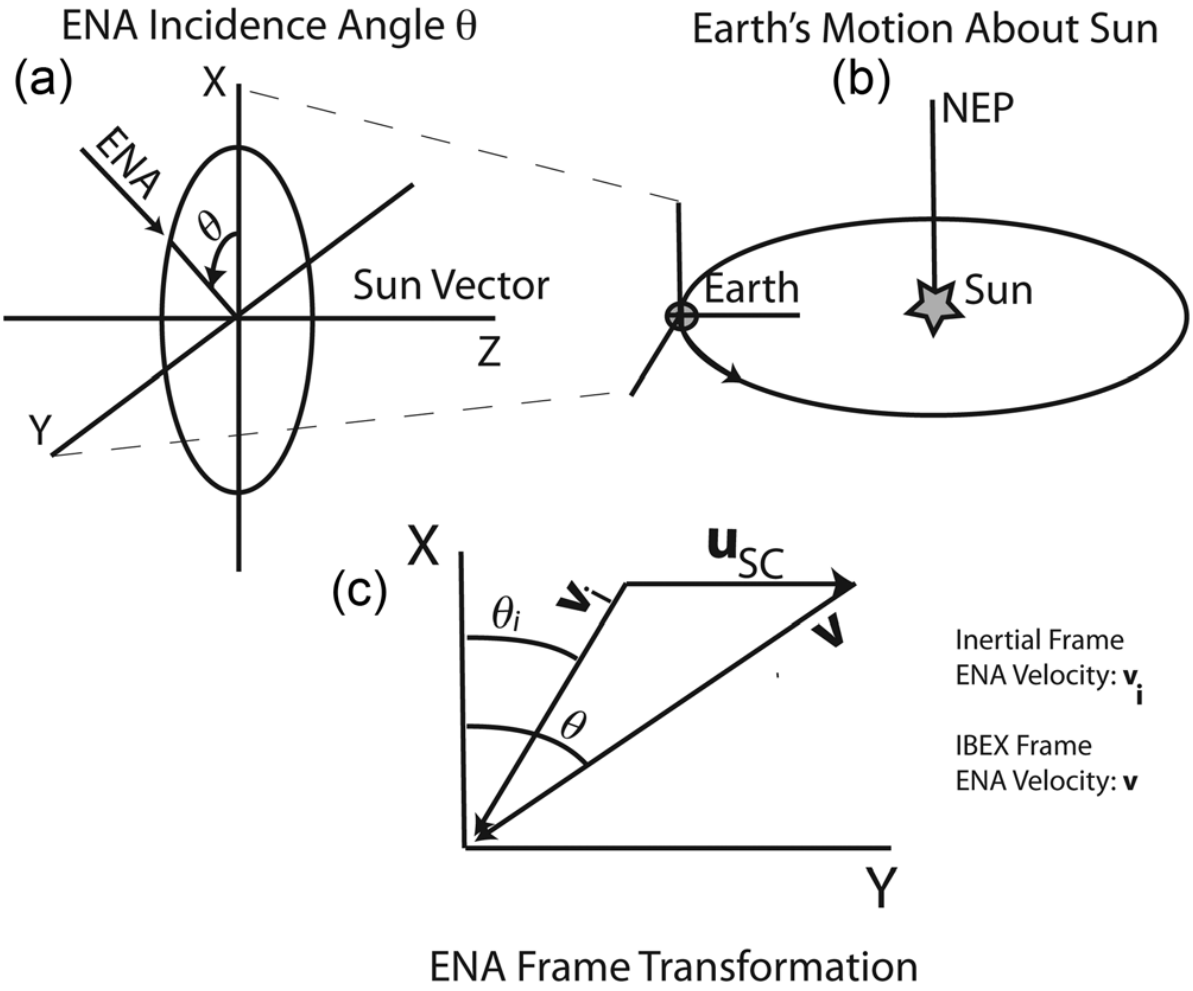

Figure 104: The motion of Earth about the Sun makes it necessary to transform ENA measurements from the IBEX reference frame to an inertial reference frame fixed with the Sun. The geometry of this frame transformation is illustrated here. The IBEX spacecraft has an approximately Sunpointed spin axis, and we measure incident ENAs in the spin plane roughly perpendicular to the spin axis. (a) The incident ENA velocity angle, θ, is measured relative to the NEP (x axis) in the spin plane as a right-handed rotation about the Z axis. (b) The y axis is directed along the vector of Earth's motion around the Sun. (c) In the spin plane, the inertial frame ENA velocity, v_i, is the sum of the spacecraft velocity, u_{SC}, and the measured ENA velocity, v.

Fluxes at a fixed energy in the solar inertial frame will require us to estimate fluxes in the IBEX frame at various energies. Given a spectrum of measured fluxes at the

nominal IBEX channel energies, $j_n = j(\theta, E_n)$, we can estimate the flux at nearby energies using the log-log Taylor expansion from

$$\ln j_{est}(\theta, E) = \ln j_n + k_n \ln \frac{E}{E_n} + \frac{a_n}{2}\left(\ln \frac{E}{E_n}\right)^2 + O\left[\left(\ln \frac{E}{E_n}\right)^3\right],$$

(181)

$$k_n = \left.\frac{\partial \ln j}{\partial \ln E}\right|_{E_n}, a_n = \left.\frac{\partial^2 \ln j}{\partial (\ln E)^2}\right|_{E_n}$$

(182)

are determined numerically from the measured spectrum. For convenience, we calculate the fluxes in the solar inertial frame at the nominal channel energies, En, and therefore write

$$j_i(\theta_i, E_n) = \frac{E_n}{E} j_{est}(\theta, E),$$

(183)

where the variable energy, E, is determined by the ratios of the energies written above (Eq. (**179**)).

In practice, we first calculate the required energy in the IBEX frame using (179), then determine the fluxes in the solar inertial frame using (181) and (183). Note that (183) is given on the irregular angular grid, θ_i. We then use a simple linear interpolation to re-grid these results back to the measurement grid, θ. We have therefore transformed measurements of fluxes in the IBEX measurement frame into the solar inertial frame at fixed energies on a regular angle grid, the results of which allow us to compare maps taken 6 months apart. A more complete development and discussion of how we correct for the CG effect in IBEX data are given by DeMajistre et al. (manuscript in preparation, 2010).

5.5.3 IBEX Survival Probability Corrections

This section describes the determination of survival probabilities for ENAs. Survival probabilities refer to the probability of an ENA of a given species and energy to propagate from the heliosphere and make it to 1 AU where it can be measured by IBEX. The survival probabilities are important because they enable us to use ENA measurements made by IBEX to estimate the ENA environment at the termination shock. Theoretical aspects of the survival probabilities of ENAs in the heliosphere, both in general and in the context of IBEX observations, were extensively discussed by Bzowski (2008) and Bzowski & Tarnopolski (2006).

5.5.3.1 Calculation of Survival Probabilities of Individual ENAs

The survival probability of an ENA is calculated by integrating the ionization rate β(t) (i.e., the ionization probability per unit time) over the duration of the ENA exposure to ionizing factors during its travel from the origin at a time t_{start} down to the detector at a time t_{stop}:

$$w_{sur} = \exp\left[-\int_{t_{start}}^{t_{stop}} \beta(t)dt\right] \tag{184}$$

The total ionization rate is calculated as a sum of the ionization rates due to all relevant ionization processes. These were recently reviewed by Bzowski et al. (2012b). The ionization processes of IBEX H ENAs include charge exchange between the H ENA and solar wind ions (mostly protons), and photoionization by solar EUV radiation. Another potential process is ionization by impact of solar wind electrons, but, as shown by Bzowski et al. (2012b), its intensity outside 1 AU is on the order of the uncertainty of the total ionization rate. Thus, to calculate the survival probabilities of IBEX ENAs we adopt the total ionization rate as a sum of the charge-exchange and photoionization rates:

$$\beta(t) = \beta_{cx}(t) + \beta_{ph}(t) \tag{185}$$

Equation (**184**) says that the survival probability of each atom depends on the history of its exposure to ionization processes during its travel. Therefore, the calculation of survival probability of an ENA requires solving the equation of motion.

The trajectories of IBEX H ENA are governed by the joint action of solar gravity and solar resonant radiation pressure from the solar Lyα photons. Since the inner heliosphere can be regarded as optically thin for solar photons, the flux of solar photons at all wavelengths decreases with the square of heliocentric distance, just as solar gravity force does. Thus, the solar radiation force is conveniently expressed as a ratio μ of the force of radiation pressure divided by solar gravity and the equation of motion takes the form:

$$\frac{d^2\boldsymbol{r}}{dt^2} = -\frac{(1-\mu)GM}{r^2}\frac{\boldsymbol{r}}{r}, \tag{186}$$

where r(t) is the radius vector of the ENA at a time t, M is the solar mass, G is the gravitational constant, and r = |**r**| is heliocentric distance.

If the solar flux in the Lyα line could be regarded as invariant in time and independent of the wavelength, Equation (**186**) would yield a purely Keplerian hyperbolic trajectory. In reality, however, none of these prerequisites is fulfilled. As measured by Lemaire et al.

(2005), the spectral profile of the solar Lyα line is self-reversed, with a central trough and two horns (see the lefthand panel in

Figure 105). Hence, due to the Doppler effect, the radiation pressure force acting on a HENA is a function of radial velocity v_r of this atom relative to the Sun: $\mu = \mu(v_r)$, where $v_r = (d\mathbf{r}/dt) \cdot (\mathbf{r}/r)$. In addition, the total flux in the solar Lyα line varies in time (see the right-hand panel in

Figure 105), so the radiation pressure force is also a function of time: $\mu = \mu(t, v_r)$. Consequently, Equation (**186**) must be solved numerically.

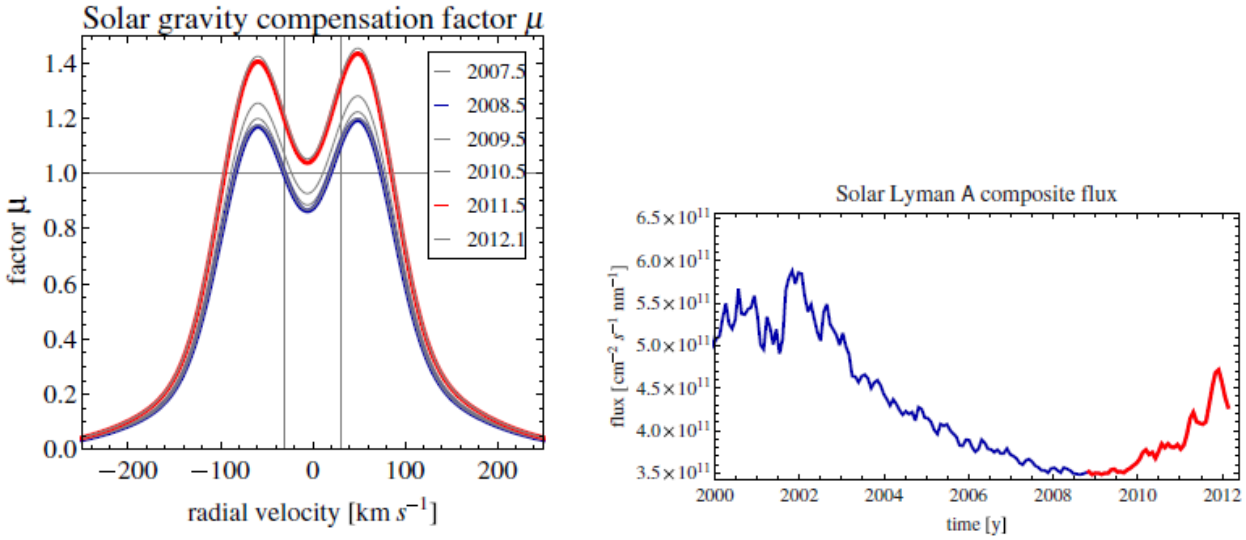

Figure 105: Solar gravity compensation factor μ shown as a function of the radial velocity v_r for selected epochs relevant for IBEX ENAs (left-hand panel) and Carrington period-averaged total flux in the solar Lyα line (right-hand panel). Red in the right-hand panel marks the time interval after IBEX launch. The horizontal line in the left-hand panel marks the level of perfect compensation of solar gravity by the resonance Lyα radiation pressure. The vertical bars mark ±30 km s^{-1} of the Doppler shift.

The complex dynamics is especially important in the case of lower-energy ENAs, i.e., those that travel at ~150 km s−1 (115 eV for H) and less. Their radial velocities are always within the spectral range of the solar Lyα line and radiation pressure affects their trajectories at all times. On the other hand, the highest-energy ENAs are Doppler-shifted outside the spectral range of the solar Lyα line and during most of their travel they are only sensitive to solar gravity. Radiation pressure switches on for them only during their approach to the detector, which at IBEX is always near the perihelion. Even though the absolute velocities of these ENAs remain high, the radial component rapidly decreases, moving into the spectral range of the Lyα line. Nevertheless, such atoms move so fast that the Sun does not significantly modify their motions and their trajectories are close to straight lines.

The instantaneous ionization rate in Equation (184) is in fact a function of both r(t) and t. Since the photoionization rate decreases with the square of heliocentric distance and is practically independent of heliolatitude (see Bzowski 2008 for a discussion of small deviations), it can be expressed as

$$\beta_{ph} = \beta_{ph}(t)\left(\frac{r_E}{r(t)}\right)^2 \tag{187}$$

where r_E = 1 AU.

The charge-exchange rate is, however, a more complex function. It depends on the local density of solar wind ions, n_p, and on the magnitude of relative velocity v_{rel} between the ENA, traveling at a velocity $\mathbf{v}_{ENA} = d\mathbf{r}/dt$, and solar wind, radially expanding at $\mathbf{v}_{sw}$:

$$v_{rel}(\boldsymbol{r}, t) = |\boldsymbol{v}_{rel}| = |\boldsymbol{v}_{SW}(\boldsymbol{r}, t) - \boldsymbol{v}_{ENA}(\boldsymbol{r})|, \tag{188}$$

where the magnitude of solar wind speed is a function of both time and heliolatitude. For ENAs in the supersonic solar wind (i.e., inside the termination shock) the local charge-exchange rate is then given by the formula:

$$\beta_{cx}(\boldsymbol{r}, t) = n_p(\boldsymbol{r}, t) v_{rel}(\boldsymbol{r}, t) \sigma_{cx}(v_{rel}), \tag{189}$$

where σ_{cx} is the charge-exchange cross section (Lindsay & Stebbings 2005) for the collision speed $v_{rel} = |\mathbf{v}_{sw} - \mathbf{v}_{ENA}|$ and the density of solar wind protons is, similar to solar wind velocity, a function of time and heliolatitude and on average, unlike solar wind speed, quadratically decreases with heliocentric distance. Thus, the instantaneous charge-exchange rate is a fairly complex function of the solar wind conditions and of the trajectory of a given ENA. To a first approximation, however, it can be regarded as decreasing with the square of heliocentric distance because $n_p = n_{p,E}(\phi, t)(r_E/r)^2$, where $n_{p,E}$ is the density at r_E = 1 AU and ϕ is heliolatitude. The quality of this approximation was shown by Bzowski et al. (2012b) to be valid to approximately 5%. A schematic illustration of the charge-exchange geometry is presented in Figure 34.

To calculate the survival probability of a single H ENA, one has to specify the time t_{stop} and location $\mathbf{r}_{stop}$ of the detection at IBEX and to select its velocity $\mathbf{v}_{stop}$ (magnitude and direction) as it approaches the detector. Both $\mathbf{r}_{stop}$ and $\mathbf{v}_{stop}$ must be taken relative to the Sun. Then one must choose one of the following two schemes to calculate survival probabilities: either (1) the calculation is for the detection velocity $\mathbf{v}'_{stop}$ in the IBEX inertial reference frame, which is defined by the instantaneous IBEX velocity relative to the Sun $\mathbf{v}_{IBEX}(t_{stop})$ or (2) in the solar-inertial reference frame. In the first of these two

cases, $\mathbf{v}_{stop} = \mathbf{v}'_{stop} - \mathbf{v}_{IBEX}(t_{stop})$, in the second case $\mathbf{v}'_{stop} = \mathbf{v}_{stop}$. Here, we select option (2).

To calculate the survival probability, with the parameters r_{stop}, v_{stop}, t_{stop} selected, one solves the equation of motion (B3), simultaneously integrating the survival probability using Equations (**184**), (**185**), and (**187)**–(**189)**, as extensively discussed by Tarnopolski & Bzowski (2009, see also their Equation 3). To carry out this calculation, one needs to know the evolution in time and heliolatitude of the solar wind speed and density as well as the evolution in time of the H photoionization rate and of the total flux of the solar Lyα radiation. The solution of the equation of motion is performed in the heliographic inertial reference system, proposed by Burlaga (1984) and modified by Franz & Harper (2002) for the J2000 epoch (HCI).

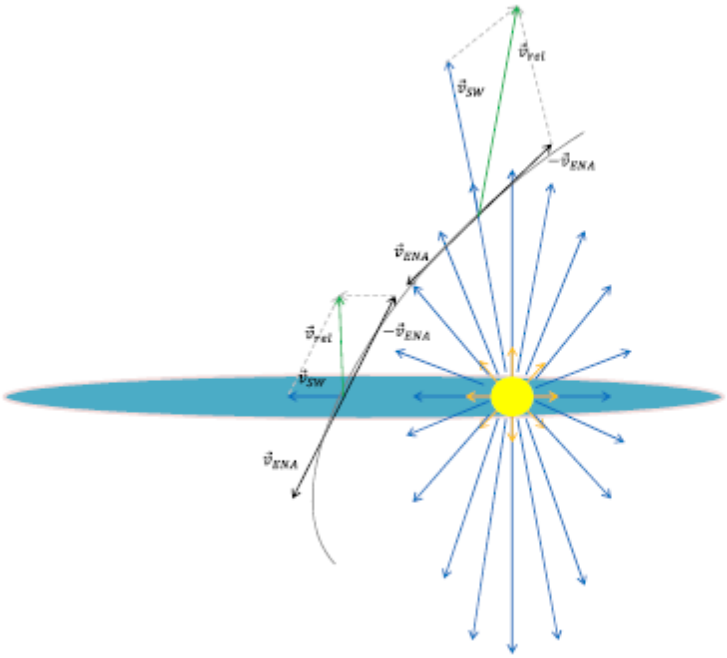

Figure 106: Schematic diagram of the variation of relative velocity $\mathbf{v}_{rel}$ between an ENA that is traveling at a velocity $\mathbf{v}_{ENA}$ along the curved trajectory in the solar neighborhood, and the solar wind, whose radial expansion velocity $\mathbf{v}_{sw}$ is a function of heliolatitude. The yellow circle is the Sun and the blue plane (seen almost edge-on) is the solar equator.

The radiation pressure term μ in Equation (**186**) is calculated using the model of the solar Lyα line profile defined in Equation 5 in Tarnopolski & Bzowski (2009), with the numerical values of the parameters defined therein. Plots of the model profiles for the years since IBEX launch are presented in Figure 105. For the total Lyα flux, needed in Tarnopolski & Bzowski's model, we use the Carrington-period-averaged daily composite flux (Woods et al. 2000), as calculated by Bzowski et al. (2012b) and shown in the right-hand panel of Figure 105. The total Lyα flux is almost spherically symmetric. The small

deviations from perfect symmetry (Auchere 2005; Pryor et al. 1992) are adopted from Bzowski (2008, see Equation 3 therein).

The solar wind parameter evolution was determined by Sokoł et al. (2012) based on the OMNI-2 in-ecliptic solar wind data collection (King & Papitashvili 2005), Ulysses SWOOPS in situ measurements (Bame et al. 1992; McComas et al. 2000; McComas et al. 2002, 2006, 2008) and interplanetary scintillation observations (Tokumaru et al. 2010). The in-ecliptic density and velocity of solar wind, obtained for 1 AU from the OMNI-2 collection as hourly averages and averaged by Carrington rotation period, are presented in Figure 107, with the interval after IBEX launch marked with a vertical line. It is worth noting that the solar wind flux in the ecliptic after IBEX launch was rather stable, but before that it featured a distinct drop that started in the first half of 1990s, which was also likely present at all heliolatitudes (McComas et al. 2008).

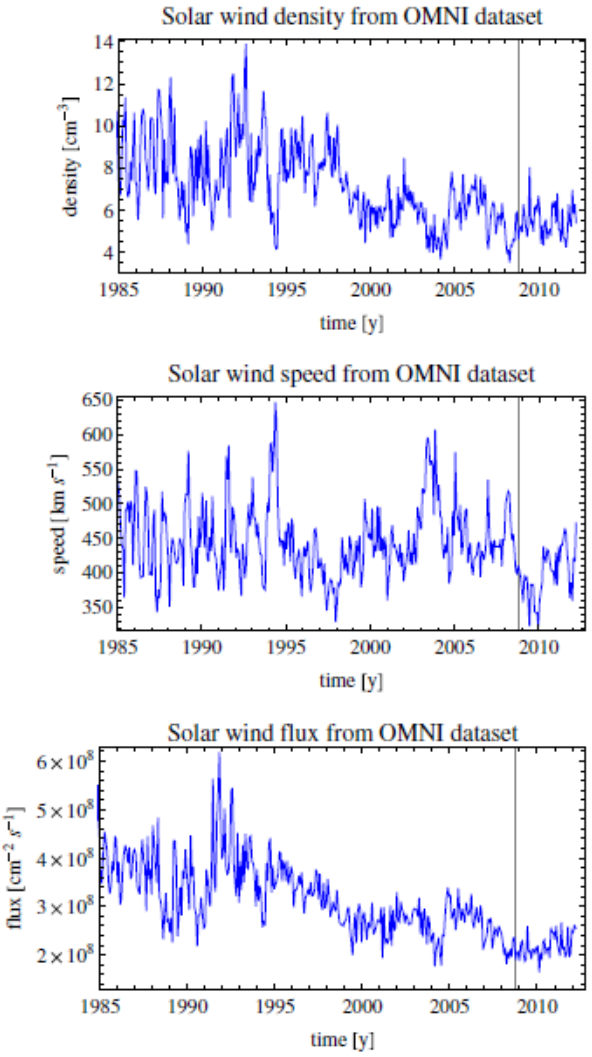

Figure 107: Carrington-period-averaged solar wind density (upper panel), speed (middle panel), and flux (lower panel), calculated based on the OMNI-2 hourly data collection (King & Papitashvili 2005). The density and flux are scaled to 1 AU by the square of

heliocentric distance. The vertical bar marks the time of IBEX launch. The data stop at the end of IBEX Map 6.

The yearly averages of the solar wind velocity and density heliolatitudinal profiles used in the construction of the model are shown in Figures 14 and 19, respectively, in Sokoł et al. (2012). The heliolatitude versus time maps of interpolated solar wind speed and density actually used in the calculations are presented in Figure 20 in Sokoł et al. (2012). The values from these maps, bilinearly interpolated in time and heliolatitude, are fed into Equations (188) and (189) to yield the local instantaneous charge exchange rate $\beta_{cx}(r, t)$. To better illustrate the evolution of the latitudinal structure of solar wind during the time interval of IBEX observations reported in this paper, in Figure 108 we replot the heliolatitude versus time contour map from the Sokoł et al. (2012) model, cut precisely to the time intervals corresponding to IBEX Maps 1–6.

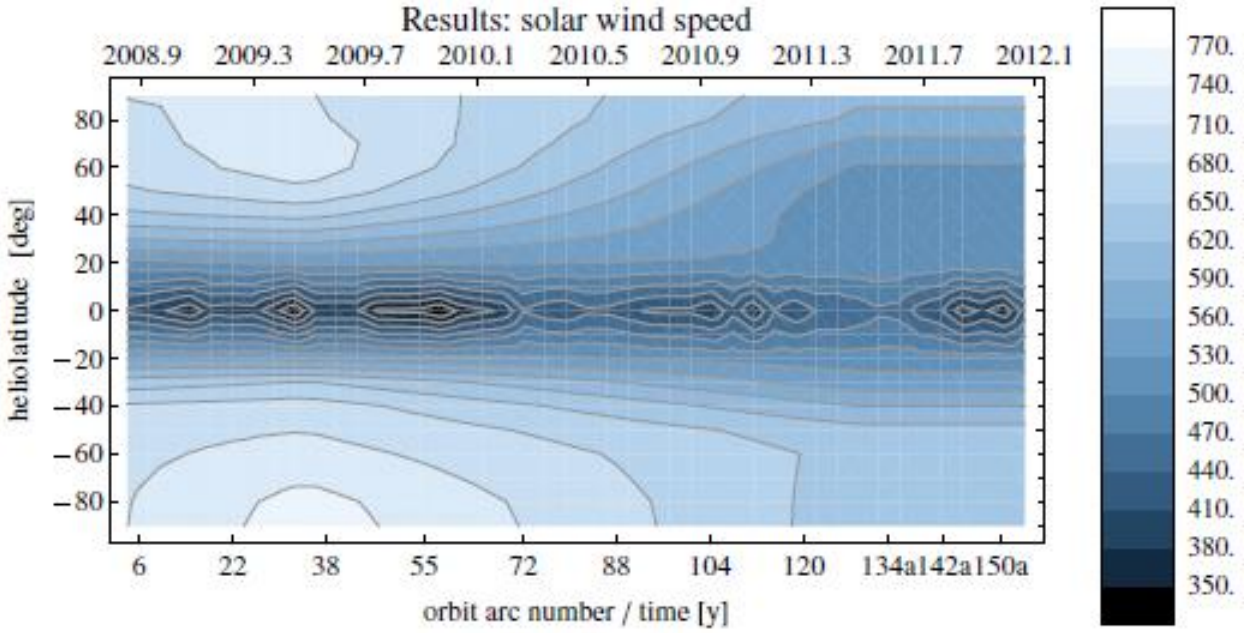

Figure 108: Solar wind speed as a function of time and heliolatitude for the time interval of IBEX observations, obtained from the model by Sokoł et al. (2012). Note the north–south asymmetry in the speed structure, with the onset of the expansion of the slow wind region in the north hemisphere preceding the expansion in the south hemisphere. The equatorial band is composed of Carrington period averages of the OMNI-2 hourly solar wind speed, while latitudes outside the ±20° band are bilinearly interpolated between the yearly averaged solar wind speed profiles obtained from interplanetary scintillation observations. Also note that the structure after ~2011.5 outside the equatorial band taken from the OMNI-2 collection is a simple extrapolation because the scintillation observations needed to extend the model into this time interval are still being collected. For details see Sokoł et al. (2012).

The photoionization rate of H ENAs at 1 AU is adopted from Bzowski et al. (2012b, see their Figure 2.9). Those authors obtained a Carrington period-averaged time series based on direct measurements of solar spectrum by TIMED/SEE (Woods et al. 2005) and a system of proxies detailed in their Equations 2.20–2.22. The proxies are based on well-defined and routinely measured quantities: the CELIAS/SEM double-channel EUV flux time series (Hovestadt et al. 1995; Judge et al. 1998), the F10.7 solar radio flux (Covington 1969; Tapping 1987), and MgIIcw index (Viereck & Puga 1999; Viereck et al. 2004).

The solar wind and solar EUV radiation parameters used in the calculations make a synchronized system based on actual measurements (Bzowski et al. 2012b). The system is based on a uniform time grid centered at halves of Carrington rotations and on a fixed grid of 10° heliolatitudinal bins. The parameters are normalized to 1 AU. All quantities used in this system are assumed to follow the $1/r^2$ dependence on heliocentric distance r except solar wind speed, which is assumed to be solar-distance-independent. The numerical tracking of the atoms is carried out until a given test atom exceeds a preselected limiting distance from the Sun, typically 90 AU. When this is accomplished, the exposure of the ENA to the ionizing factors, calculated from the integral under the exponent in Equation (**184**), is registered and the survival probability w_{sur} for this given atom is obtained from Equation (**184**).

5.5.3.2 Survival Probability for a Given Orbit and Energy

The baseline survival probability product is a series of survival probabilities of H ENAs observed at a given IBEX orbit at a selected energy as a function of spin angle. The calculation is performed for the middle of the observation time interval for a given IBEX orbit or orbital arc. We have verified that the small changes in the probabilities during the time interval corresponding to the orbit are almost linear in time and thus taking the middle point of the time interval is equivalent to averaging over time.

The calculation starts with the selection of the strip on the sky from which the ENAs come into the detector. The strip is defined by the pointing of the IBEX spin axis, which changes from orbit to orbit (and now per orbit arc), and by the field of view of the collimator.

The visibility strip defined for a given orbit is first covered with survival probabilities of individual ENAs calculated on a uniform grid (the HEALPix tessellation; Gorski et al. 2005), which is defined in the heliographic reference system and for each orbit transformed into the IBEX coordinates (ψ, φ), where spin phase ψ runs along the visibility strip from 0 to 2π. The angle φ is in the perpendicular direction to the spin phase line and spans ($\pm\rho_{lim}$), where ρ_{lim} is the outer radius of the collimator field of view equal to ~8°. Then, a virtual collimator is stepped along this strip with the boresight sliding along the centerline. For each step along the visibility strip, the survival probabilities are integrated over the collimator field of view, multiplied with the

transmission function of the collimator T(ρ, θ). This procedure returns an effective survival probability w_{eff} (t,E,ψ) for a given moment of time t, energy E, and spin phase ψ:

$$w_{eff}(t,E,\psi) = \int_0^{2\pi\rho} \int_0^{lim} w_{sur}\left(t,E,\psi'(\psi,\rho,\theta) \times \phi'(\psi,\rho,\theta)\right) T(\rho,\theta)\sin(\rho)\, d\rho d\theta \quad (190)$$

The coordinates ψ'(ψ, ρ, θ), φ'(ψ, ρ, θ), for which the integrand function w_{sur} is evaluated, are calculated separately for each value of spin phase ψ. Thus, the members of the set of individual survival probabilities w_{sur} pre-calculated for the visibility strip for each orbit can be used in the calculation of the effective survival probability for each given spin phase value ψ, which means they can be efficiently re-used for different values of ψ. An illustration of the visibility strip and an orientation of the collimator field of view is sketched in Figure 3 and the transmission function in Figure 2 in Bzowski et al. (2012a). The calibration of the transmission functions for the collimators of the IBEX-Hi and IBEX-Lo instruments were presented in Funsten et al. (2009b) and Fuselier et al. (2009b), respectively.

For this study, we scanned the visibility strips for each of the IBEX orbits and orbit arcs with a 1° cadence and calculated average probabilities for 6° bins in spin phase. In this way, the effective survival probabilities correspond to the IBEX 6° pixels available for each orbit and for each spin phase we have a time series of the effective survival probabilities for the entire duration of IBEX observations.

The values of effective survival probabilities are sensitive to solar wind and solar EUV radiation conditions and in addition, they show some sensitivity to a number of second-order effects, including (1) the mean inclination of the visibility strip to the Earth–Sun line, (2) the distance and velocity of the Earth relative to the Sun, (3) the distance and velocity of the IBEX spacecraft relative to the Earth, and (4) Earth's heliolatitude. An illustration of the scale of these effects is best seen in a time series of effective survival probabilities for selected pixels. Such an illustration is presented in *Figure 109*, which shows time series of survival probabilities in the solar-inertial frame for two selected energies for the north and south ecliptic pole lines of sight (upper panel) and for the ecliptic ram and anti-ram lines of sight.

The magnitude of survival probabilities in the ecliptic plane changes very little on a multi-year timescale because during the IBEX operation such long-term changes were practically absent in the equatorial solar wind (cf. Figure 107). This is illustrated in the lower panel of *Figure 109*, where the survival probabilities vary on both monthly and yearly scales but do not show a clear trend. This is not the case for the polar lines of sight, which show a systematic decrease in time. This decrease, seen for all energies, is related to the change in the global solar wind structure, related to the increasing solar activity. The solar activity began to increase in the second half of 2009, which resulted in an expansion of the slow and variable equatorial solar wind to higher heliolatitudes.

The expansion of the slow wind band was north–south asymmetric, being faster in the north hemisphere than in the south.

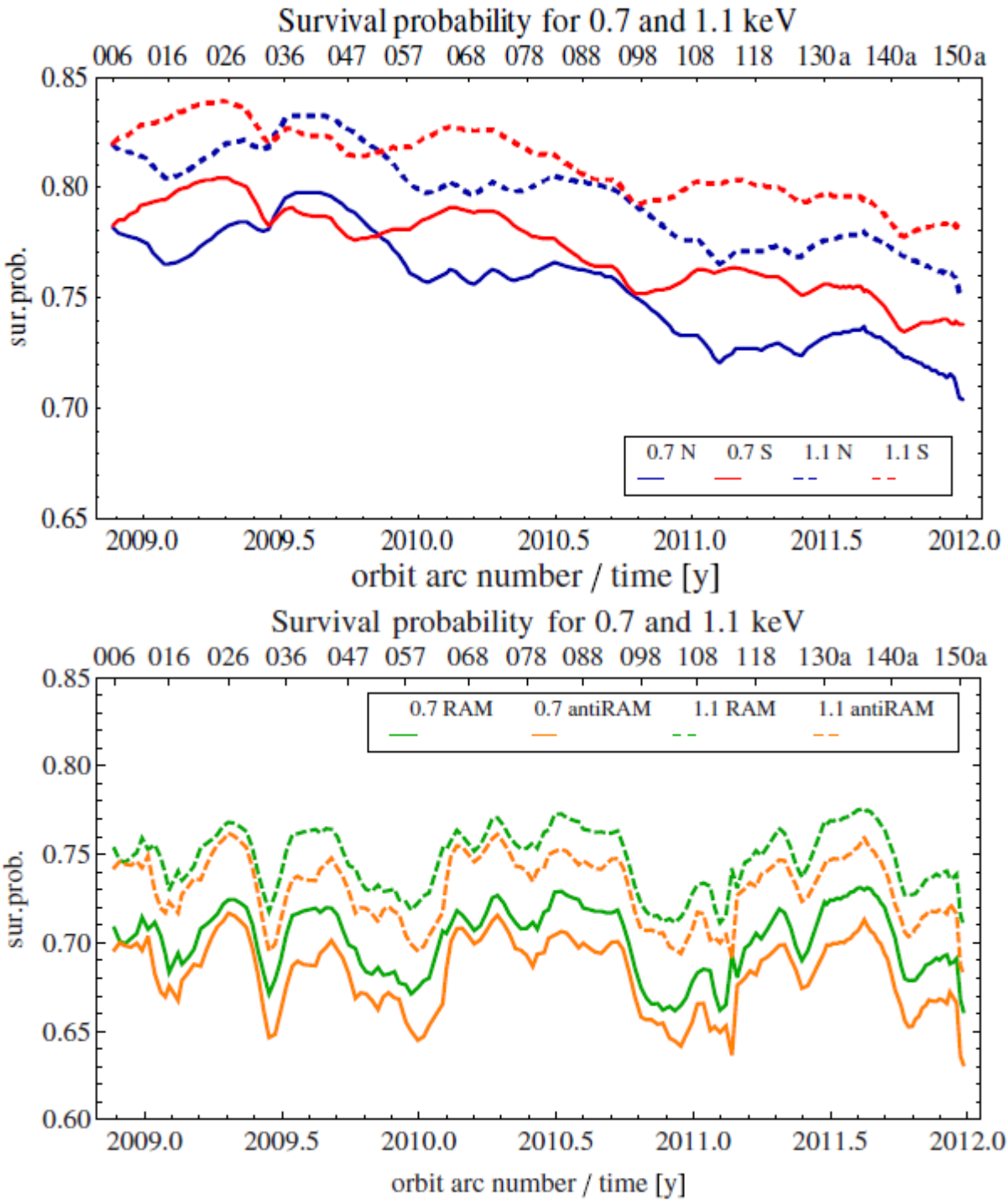

Figure 109: Effective survival probabilities for the north and south ecliptic pole pixels (upper panel) and the ram and anti-ram in-ecliptic pixels (lower panel) for two selected ENA energies in the solar-inertial frame: 0.7 keV and 1.1 keV, shown as a time series from the start of science operations until the end of Map 6.

For ENAs approaching the detector from the direction of the ecliptic poles, the expansion of the slow wind band in heliolatitude results in increasing the portions of their trajectories immersed in the slow/variable wind, where the ionization rate is greater and consequently the survival probabilities of such atoms are lower. The change in the solar wind structure shown by Sok´oł et al. (2012) is visible in the ENA survival probabilities almost immediately (i.e., almost without a time lag) because of the viewing geometry. The atoms cover the last few AU of their flight at trajectories inclined at almost right angle to the radius vector of the detector relative to the Sun, and thus most of the losses due to ionization occur within the last few weeks or months before the detection.

Since the heliographic latitude of the Earth varies periodically during the year (see *Figure 110*) and thus the thickness of the layer of enhanced ionization rate also varies in sync, the north and south time series of survival probabilities show a yearly anti-phase modulation. This effect exists for ENAs at all IBEX energies; however, the magnitude of the modulation decreases with an increase in energy.

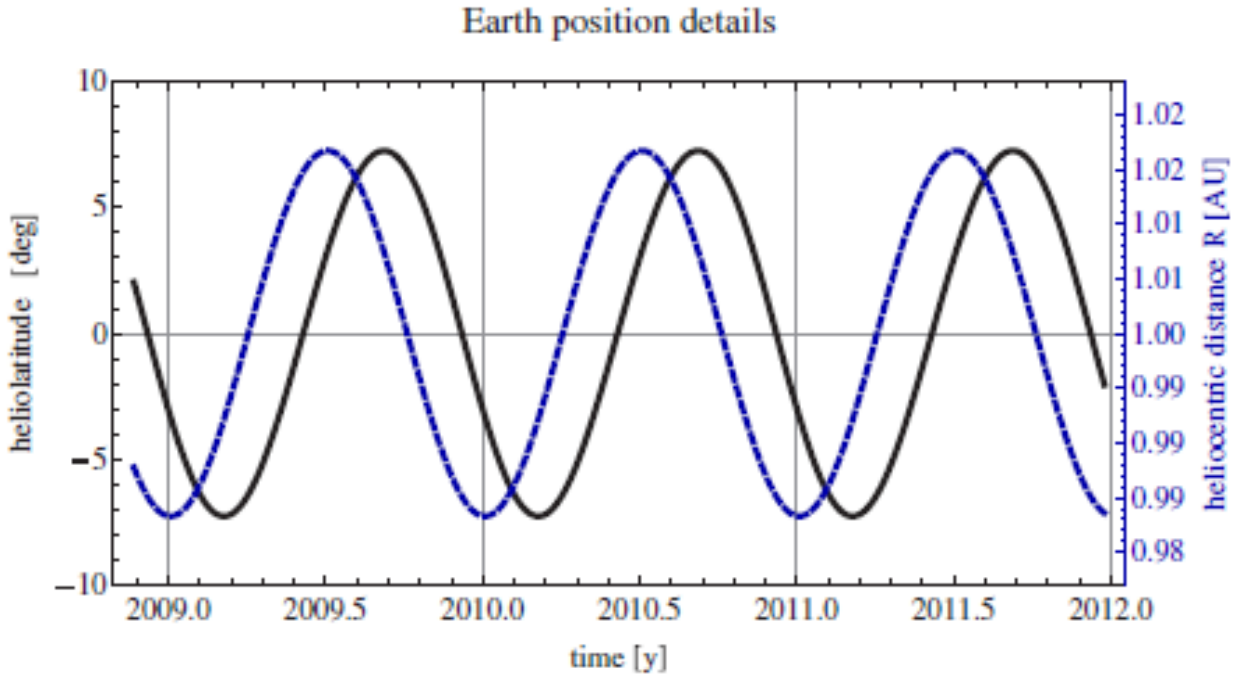

Figure 110: Yearly variations of Earth's (and IBEX's) heliolatitude (black line, left-hand scale) and solar distance (blue line, right-hand scale) show only a small phase shift.

The survival probabilities in the pixels close to the ecliptic plane do not show the modulation due to the periodic changes in IBEX's heliolatitude because the atoms observed near the ecliptic spend their whole time traveling close to the ecliptic plane, where the ionization rate is higher than in the polar regions. Hence, the values of survival probabilities in the ecliptic are lower, but almost do not systematically vary with

time. On the other hand, the yearly modulation of the survival probabilities has an even slightly larger amplitude than that of polar lines of sight. This modulation is due to the variations of the Earth distance from the Sun during the year (see *Figure 110*). This effect is similar in magnitude for the ram and anti-ram lines of sight. Of course, this also affects the polar lines of sight, but because of the small phase shift between the distance and heliolatitude it only seems to reduce the scale of the heliolatitude-related variation of the polar probabilities.

The survival probabilities presented in *Figure 109* were calculated in the solar-inertial frame and thus, to a first approximation, one does not expect any ram versus anti-ram direction effects. However, inspection of the lower panel of *Figure 109* shows that such an asymmetry does in fact exist. This is because the mean angle between the Earth–Sun line and the scan plane of IBEX is not exactly 90◦. Due to this small deviation the atoms approaching the detector from the ram direction have not passed the perihelia of their orbits, while those approaching from the anti-ram direction have already passed them. This results in a small but noticeable difference between their survival probabilities. The magnitude of the differences decreases with the increase of ENA energy.

Additional short-scale “jitter” in the survival probabilities is caused by the monthly variation in the solar wind. Since the solar wind model used in the calculations has a resolution of one Carrington rotation close to the ecliptic plane, but only one year out of the ecliptic plane, the effect of the short-scale fluctuations of solar wind on the survival probabilities is most pronounced for the in-ecliptic pixels. On the other hand, during low solar activity solar wind at high ecliptic latitudes is generally much less variable than in the equatorial band, so less “jitter” in survival probabilities for high-latitude ENAs during a low solar activity interval should be expected.

5.5.3.3 Survival Probability Maps

To examine systematic effects and the evolution of survival probabilities with time, we first average the probabilities over the time intervals corresponding to the times of acquisition of IBEX yearly maps (the “ram” and “anti-ram” maps). By doing so we eliminate all effects related to the Earth’s motion around the Sun and to Earth’s travel in heliolatitude and are better able to study the time variation of global effective survival probability spectra.

The survival probabilities increase with the increasing H ENA energy in the solar inertial frame, as illustrated in Figure 39, which presents spectra of the effective survival probabilities of H ENA for the lines of sight toward the north and south ecliptic poles and in the ram and anti-ram directions for the time interval of IBEX Maps 2009 and 2011, as well as the ratios of these spectra.

The ecliptic spectra vary very little with time, which is understandable given their weak dependence on radiation pressure and the relatively small change in the overall ionization rate in the equatorial band of heliolatitudes. The differences between the 2009 and 2011 polar spectra are much more pronounced. They are related to the expansion of the slow wind region into higher heliolatitudes, which is somewhat asymmetric, with the north hemisphere preceding south.

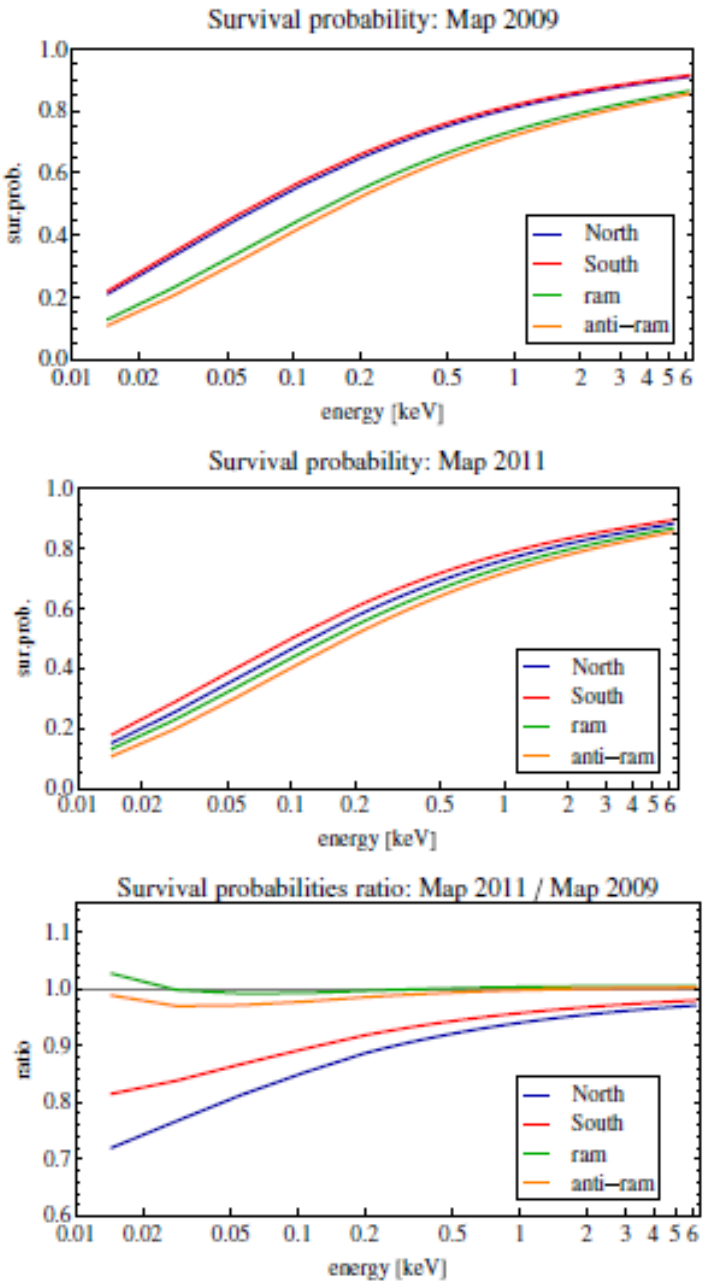

Figure 111: Spectra of effective survival probabilities of H ENAs for the north and south ecliptic pole pixels and for the ram and anti-ram pixels in the ecliptic plane, calculated in the solar-inertial frame and averaged over the time interval corresponding to IBEX Map

2009 (upper panel) and 2011 (middle panel). The lower panel presents a relative change in the spectra (the ratios of the corresponding spectra from 2011 to the spectra from 2009).

Survival probabilities show some small but noticeable systematic differences between the odd- and even-numbered halfyear maps. Plots of the effective survival probabilities averaged over the time intervals of IBEX Maps 1–6 are shown in *Figure 112*. These differences are related to the orientation of the spacecraft relative to the solar equator plane. Generally, IBEX is below the solar equator plane during the first half of each year (cf. *Figure 109*) and above it during the second half. This, together with the north–south asymmetry of solar wind, results in some small systematic differences between the effective survival probabilities.

To correct the IBEX-inertial maps of H ENA flux for survival probabilities, we start from survival probabilities calculated on a grid of energies and spin angles in the solar-inertial frame separately for each orbit, as detailed in the preceding section. These probabilities are applied to the calculated fluxes during the construction of the full sky ENA flux images.

As part of the standard processing of the IBEX data, fluxes are first calculated for each orbit as a function of angle and energy step in the spacecraft frame. A mapping procedure considers each angular element from each energy step and orbit separately for placement on the full sky maps. The fluxes from each element are then transformed into the solar-inertial frame. This transform results in a shift in the apparent ENA energy and a slight change in the apparent direction. Next, we interpolate the appropriate survival probability for the element using the survival probability grid (in energy and direction) for the orbit being considered. This is a two-dimensional interpolation that is linear in spin angle and logarithmic in energy. The flux in the element is finally corrected for this probability and placed on the map via the standard algorithms.

5.5.3.4 Updated Heliolatitudinal Structure of the Solar Wind Speed

The survival probabilities used in this paper are an update and extension of the survival probability system used by McComas et al. (2012b). The heliolatitude-dependent evolution of solar wind speed comes from the Computer Assisted Tomography of the interplanetary scintillations (IPS) observed by the Solar- Terrestrial Environment Laboratory at Nagoya University, Japan (Tokumaru et al. 2012), and the in-ecliptic variation is obtained from the OMNI-2 time series, compiled from in situ observations (King & Papitashvili 2005). The IPS data are released once per year, after the observations are completed before the yearly winter break (Tokumaru et al. 2012). The IPS observations provide Carrington maps of solar wind speed, which we process to obtain yearly averages (Sokoł et al. 2013) and form the basis for our model of solar wind speed and density. The OMNI-2 data are released with approximately 1 month delay in a preliminary form, and the final time series is released sometime later.

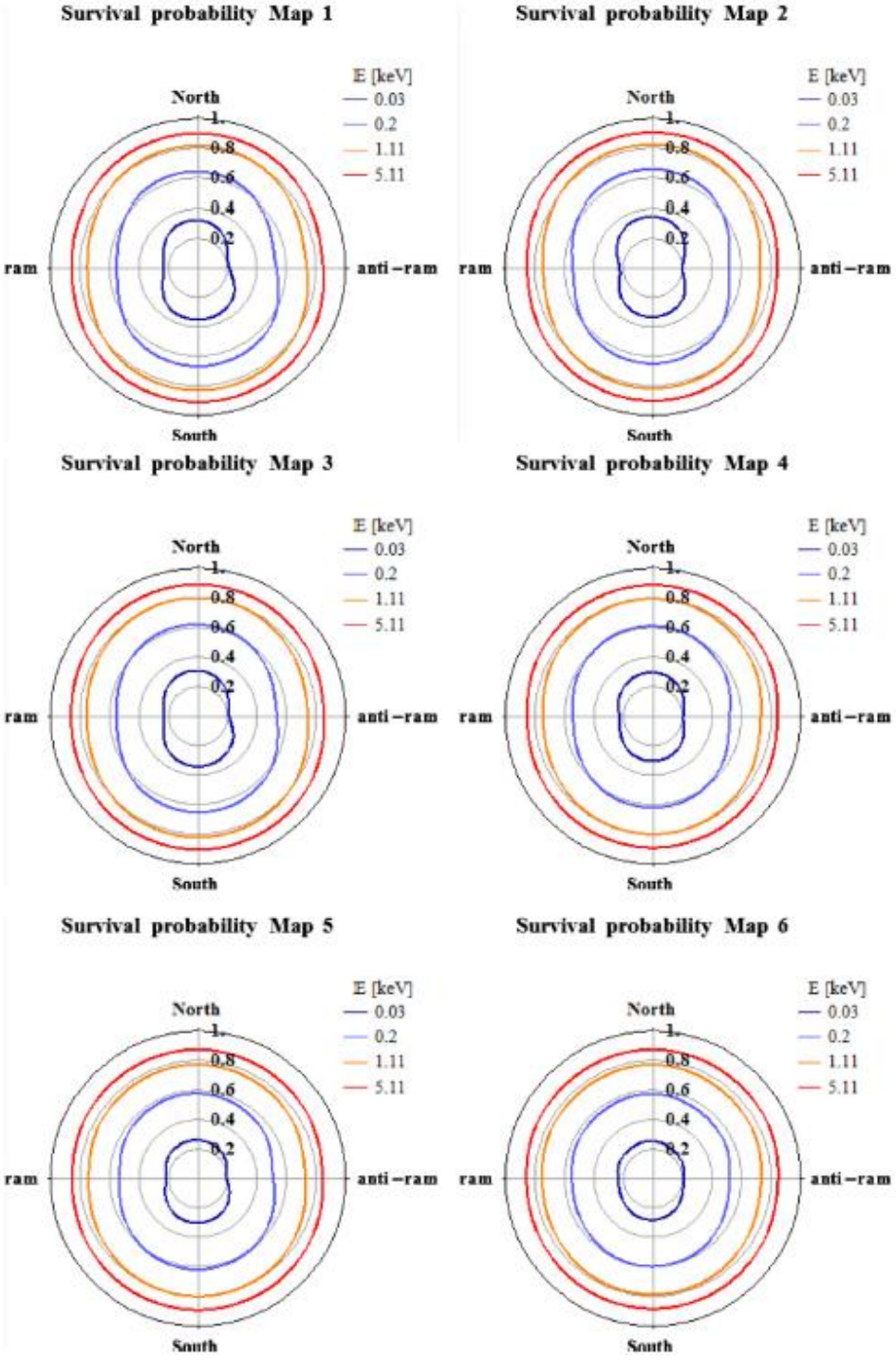

Figure 112: Polar plots of the effective survival probabilities of H ENA, calculated in the solar-inertial frame for the whole range of the IBEX spin phase for selected H ENA energies, averaged over the time interval of IBEX Maps 1–6 for each spin phase. The magnitude of probability is indicated at the vertical axes of the plots. Spin phase increases counterclockwise from 0 at the north pole through 90° in the in-ecliptic ram direction, south pole at 180° and anti-ram at 270°. Note the symmetry between the odd and even maps.

Because of this delay in data availability, McComas et al. (2012b) applied an extrapolation of the solar wind evolution model for the interval after the data were available. This was after middle of 2011, or Orbit 130. Starting from that orbit, those authors “froze” the 3D solar wind structure, but the inecliptic variation of solar wind andEUVradiationwas continued through the later available data. As a result of this necessary procedure, the survival probabilities calculated for Map 6 were not fully accurate. In the present paper, they were recalculated based on solar wind heliolatitude data that became available since that time.

The freezing of the heliolatitudinal structure of the solar wind speed in this study starts from the end of May 2013 (Orbit 207b). The in-ecliptic time series was frozen after orbit 225b. The solar wind velocity structure used in this study is shown in *Figure 113*.

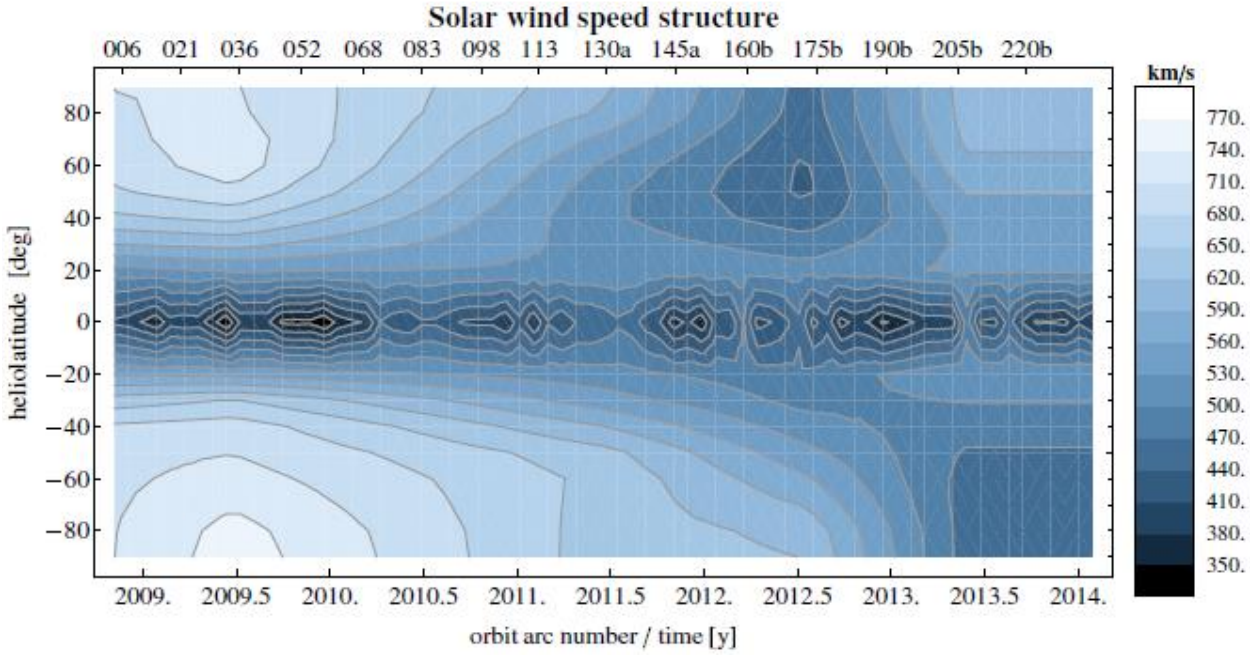

Figure 113: Solar wind speed evolution as a function of time and heliolatitude. The vertical axis is heliolatitude, the lower horizontal axis is time in calendar years, and the upper horizontal axis presents the corresponding intervals for IBEX orbital arcs.

5.5.3.5 Change of the Calculation of the Solar Wind Density as a Function of Heliolatitude

Unlike the solar wind speed, solar wind density outside the ecliptic plane is not easily available from measurements. Sok´oł et al. (2013) used a phenomenological relation between solar wind density and speed based on the density and speed data from three fast latitude scans of Ulysses and noticed that each Ulysses orbit required a different correlation formula. Since solar wind shows a clear secular evolution (McComas et al. 2013), we felt it was no longer best to use the relations obtained from measurements completed during the previous solar cycle. Instead, to infer solar wind density as a

function of heliolatitude for the current study, we use the relation of Le Chat et al. (2012) based on Ulysses data that the solar wind energy flux

$$W = n_p\left(m_p + \xi_\alpha m_\alpha\right)v_{SW}\left(\frac{1}{2v_{SW}^2} + G\ M_{Sun}/R_{Sun}\right)$$

(191)

varies very little with heliolatitude (is quasi-invariant) and thus could potentially be used to infer density if speed is known. Knowing the value of the solar wind energy flux in the ecliptic plane and the solar wind speed as a function of heliolatitude we can calculate the solar wind density at a given heliolatitude following the formula:

$$n_p(\phi) = 10^{-6}\frac{W}{v_p(\phi)\left(0.5v_p^2(\phi) + C\right)\left(m_p + \xi_\alpha m_\alpha\right)}$$

(192)

Where m_p is amass of the proton,m_α is mass of the alpha particle, ξ_α abundance of alpha particles in the solar wind, assumed to be 4% (e.g., Kasper et al. 2007), $v_p(\varphi)$ solar wind speed as a function of heliolatitude φ, W solar wind energy flux, and C = ($M_{Sun}G/R_{Sun}$) (R_{Sun}: the radius of the Sun, M_{Sun}: the mass of the Sun, and G: gravity constant).

The total energy flux of solar wind is nearly constant after ~2008 (W = 0.00124 W m2). In the present version of survival probability calculations, we switched from the previously used formula for solar wind density to the formula defined in Equation (**192)** starting at the second half of 2012 (orbit 174a), when the solar maximum at the north hemisphere was observed. For the solar wind total energy flux value we adopted the mean obtained from averaging over the interval marked in *Figure 114*.

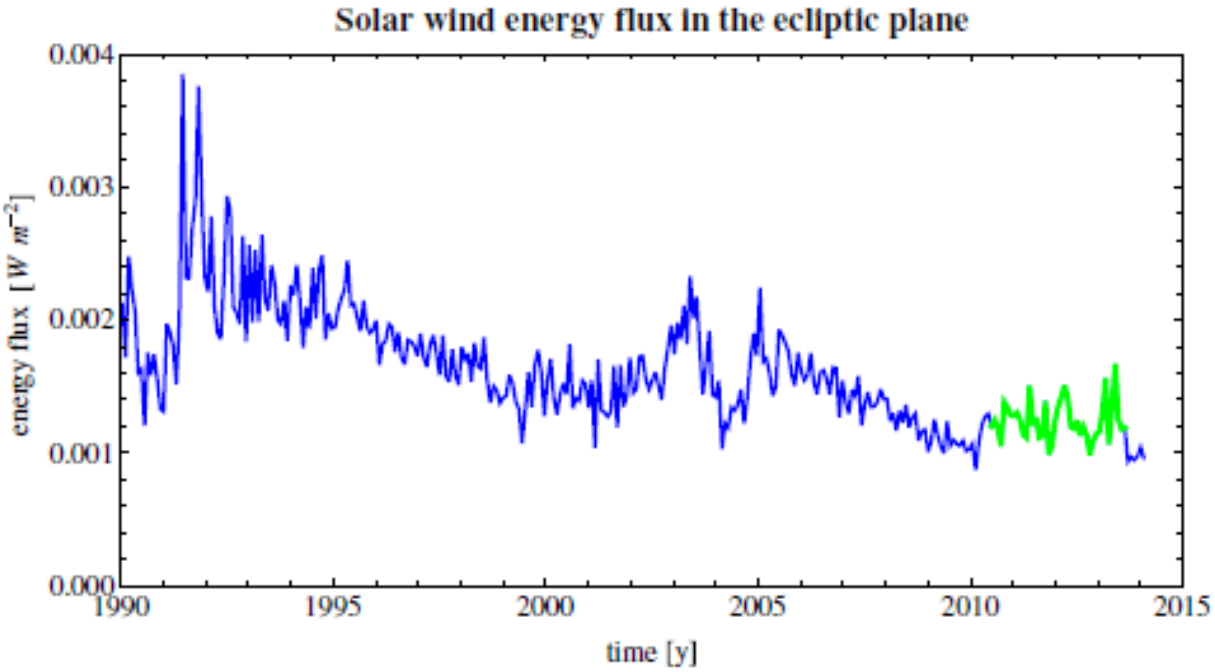

*Figure 114: Energy flux of solar wind based on OMNI-2 Carrington rotation-averaged solar wind parameters, calculated from Equation (**191**). The value adopted to compute the solar wind density as a function of heliolatitude from Equation (**192**) is the average from the interval marked in green (W = 0.00124 W m2).*

In 2013 February, OMNI2 released a new version of the in ecliptic solar wind data, with various changes and modifications. The changes affect data since 1995. Their magnitude was only ~1% in the Carrington rotation-averaged solar wind speed, and up to about 10% in Carrington rotation-averaged solar wind number density, which resulted in such small changes in survival probabilities (much less than the overall uncertainty) that we decided to not recalculate the first five IBEX ENA maps.

In 2011, the 3D structure of the solar wind still generally resembled the structure typical for solar minimum conditions. Since that time, the Sun transitioned into the maximum activity phase, with a profound modification of the solar wind latitudinal structure. In this paper we take into account the evolution of the latitudinal structure of solar wind from ~2011.5 to ~2013.5. During this interval, the solar wind speed structure was characterized by a solar activity peak, with mixed speed solar wind in the northern hemisphere (see *Figure 113*). This means that the solar wind structure as a function of heliolatitude shows a distinct north–south asymmetry. This asymmetry was also indicated by, e.g., Chowdhury et al. (2013) based on a study of sunspot distribution. This asymmetry is clearly reflected in survival probabilities of H ENAs as illustrated in *Figure 115* and *Figure 116*.The north and south polar survival probabilities for two selected energies clearly show yearly modulations superimposed on a solar cycle trend related to the evolution of the latitudinal variation of the solar wind speed. The ecliptic probabilities, shown for the same energies for ram and anti-ram directions reflect their own yearly modulations, but the solar cycle-related trend is absent.

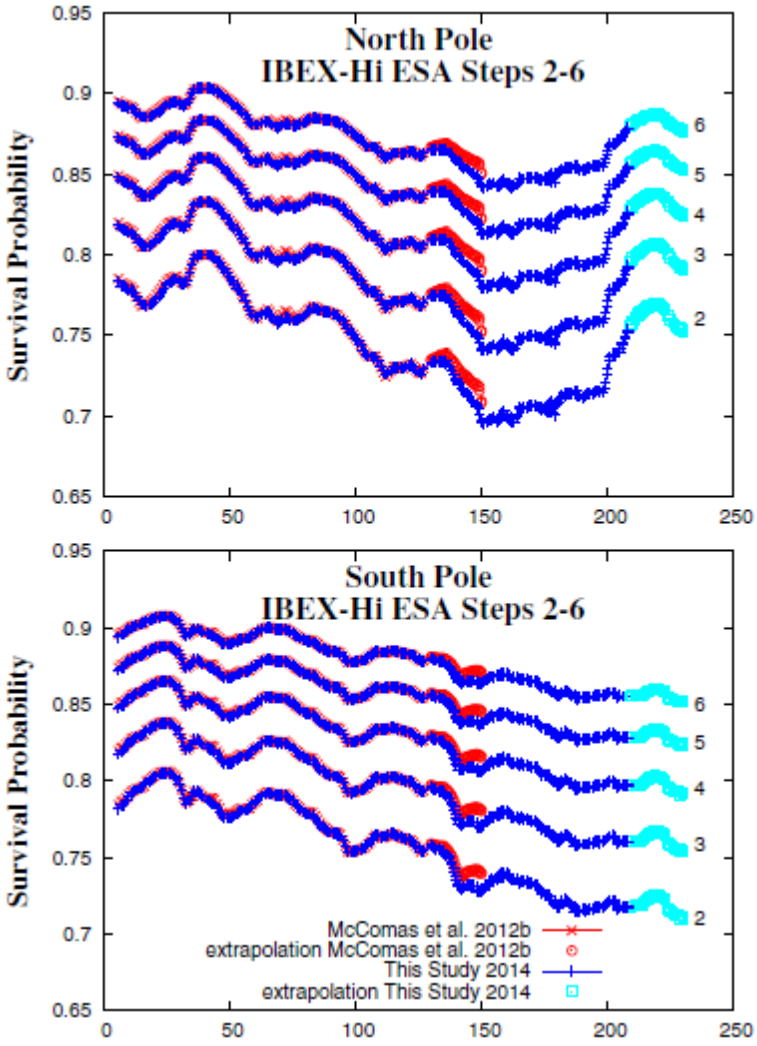

Figure 115: Calculated survival probabilities for ENAs coming in from the outer heliosphere and arriving in IBEX's northern (top) and southern (bottom) polar pixels.

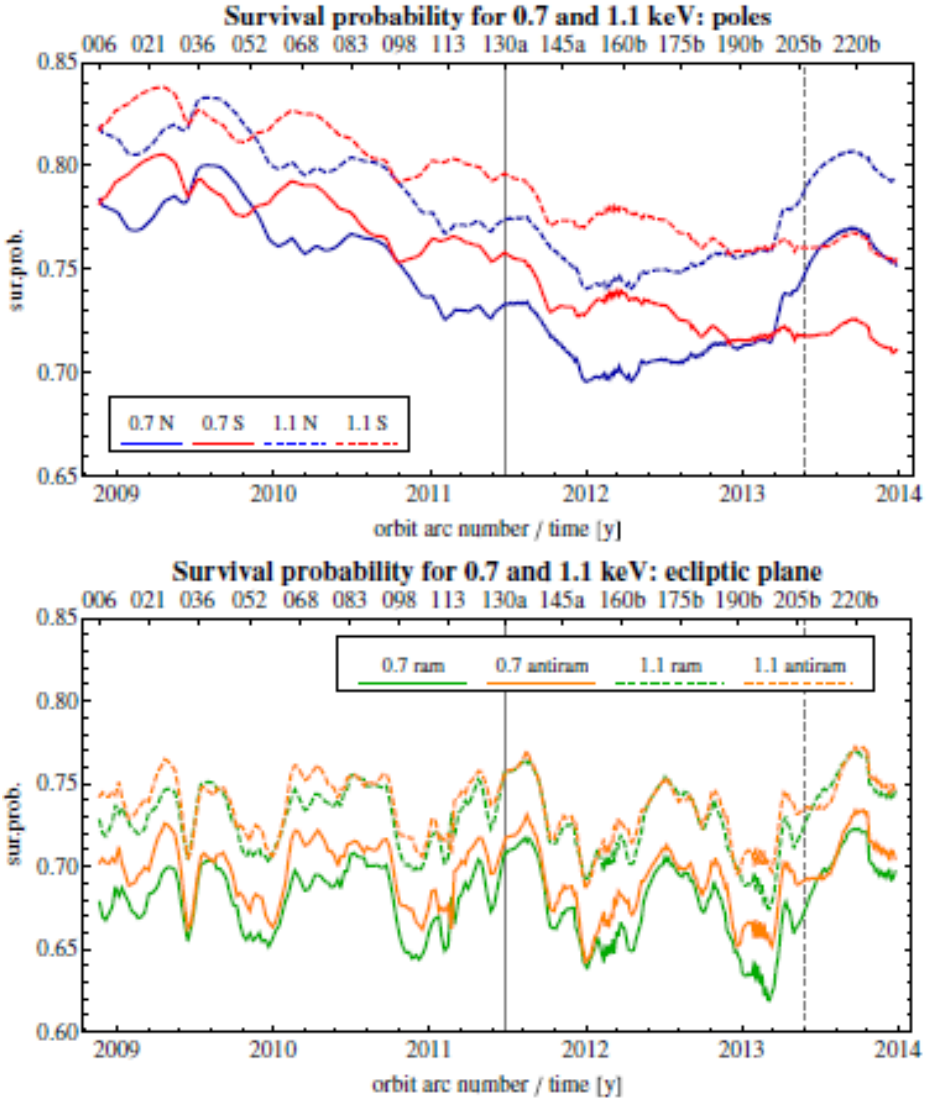

Figure 116: Survival probabilities for the north and south polar directions (upper panel) and for the in-ecliptic ram and anti-ram directions (lower panel), shown for the entire duration of the IBEX mission. The dotted vertical line marks the freezing of the solar wind structure in the present calculation.

5.5.3.6 Updated Survival Probability Corrections for IBEX-Hi and IBEX-Lo

The physics and important considerations for survival probabilities of ENAs observed at 1 au were discussed extensively by Bzowski (2008), and details of the calculations of survival probabilities for IBEX observations were presented by McComas et al. (2012c) and will not be repeated here. For this study, we updated survival probabilities for the majority of the IBEX mission. Updates were made for orbits 8 through 286b due to changes in the composite $Ly\alpha$ time series from LASP (Laboratory for Atmospheric and Space Physics at the University of Colorado—http://lasp.colorado.edu/lisird), which are used to calculate the radiation pressure and photoionization rates. The changes are

small for the first few years of IBEX observations and increase slightly over time compared to the previous values. Survival probabilities for orbits 256a to 311b were also updated to include a new set of solar wind speed data from the interplanetary scintillation (IPS) observations for 2015.

After the solar activity maximum in 2012–2013, when the slow and dense solar wind flows spread nearly from pole to pole, the solar wind started to reorganize again toward the standard bi-modal structure typical for solar activity minima (e.g., McComas et al. 1998). We took this change of the solar wind structure as a function of latitude into account in the calculation of the survival probabilities of the H ENAs inside the heliosphere. The survival probabilities of H ENAs against the interactions with solar wind and solar EUV radiation were calculated following the methodology presented in McComas et al. (2012c, 2014).

The most effective ionization process for the ENAs observed by IBEX is charge exchange with solar wind protons (see Figure 117), so we require the solar wind speed and density out of the ecliptic plane. These were reconstructed following the model developed by Sokół et al. (2013) from the in situ inecliptic solar wind measurements compiled in the OMNI data base (King & Papitashvili 2005) and observations of IPS conducted by the Institute for Space-Earth Environmental Research at Nagoya University in Japan (Tokumaru et al. 2012). The survival probabilities reached a minimum around orbit 180, during the maximum of solar activity in 2012, when the ionization rates were the highest; thereafter they started to increase in concert with the decrease of solar activity. The variations in the northern and southern hemispheres are slightly different, which is due to the differences in the solar wind structure between the two hemispheres.

To reconstruct the global distribution of the solar wind speed (Figure 118, top panel) from the IPS observations using the computer assisted tomography method (CAT; Asai et al. 1998; Jackson et al. 1998; Kojima et al. 1998), information of the fluctuations of solar wind electron density (ΔNe) at a time scale of seconds is needed. One of the two CAT analyses assumes an empirical relation between solar wind speed and electron density fluctuations, ΔNe, while the other only uses speed estimates derived from multi-station IPS observations. Other versions do not assume such a model, but use two data sets: g-value data, derived from single-station measurements, and speed estimates from multi-station measurements. The g-value represents integration of ΔNe along the line of sight, and the resulting IPS speed estimate is a convolution integral of the actual speed and ΔNe along the line of sight (Tokumaru et al. 2011, 2012). In the calculation of the survival probabilities, we used the solar wind speed derived from the CAT analysis, which used both g-value and speed data (see more in Sokół et al. 2013, 2015).

IPS observations do not provide reliable information on the global solar wind density. The solar wind density (Figure 118, bottom panel) is calculated from solar wind invariants in heliolatitude using the solar wind thermal advection energy flux (Le Chat et

al. 2012), as presented in Section 5.5.3.5 and discussed by Sokół et al. (2015). In this approach it is assumed that the solar wind energy flux is identical for all heliolatitudes in a given interval of time, as concluded from Ulysses observations. In our calculation, the invariant is calculated from in-ecliptic measurements of solar wind, which together with the solar wind speed as a function of latitude obtained from IPS, enable us to calculate the latitudinal solar wind density structure (see Equation (192)).

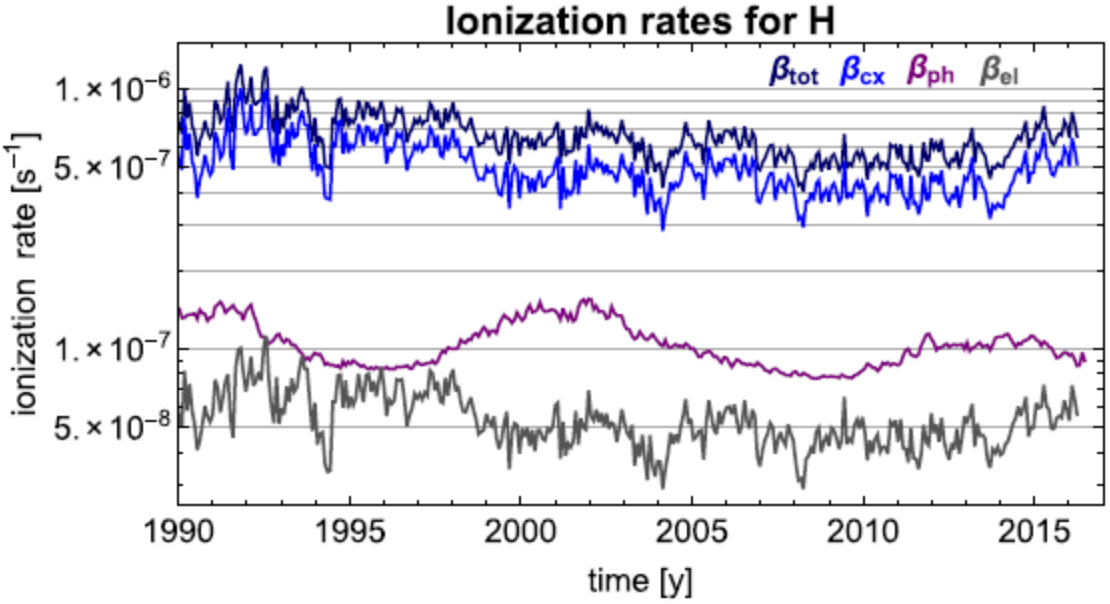

Figure 117: Ionization rates for H in the ecliptic plane. The total ionization due to the three largest ionization processes is illustrated by the dark blue line (β_{tot}); separately, they are ionization from charge exchange (βcx, blue), photoionization (β_{ph}, purple), and ionization due to impact with solar wind electrons (β_{el}, gray).

In the survival probability calculation for H atoms, we include the radiation pressure that competes with solar gravity. As in our previous study, we do this using a model from Tarnopolski & Bzowski (2009), with the total Lyα flux intensity obtained from the composite Lyα series provided by LASP.

Photoionization is of secondary importance for H atoms (Figure 117). Here we calculate it as before, integrating over the solar EUV irradiance measured by TIMED (Woods et al. 2005) and a hierarchy of solar EUV proxies, following Bzowski et al. (2013b), and including the most recent data.

The time-variable survival probabilities for ~1 keV H ENAs observed in the ecliptic plane and toward the north and south poles are illustrated in Figure 119. The steps/jumps in the time series for the poles from orbit 232a to orbit 237a, and subsequently from orbit 270a to orbit 279b in Figure 119 (see also Figure 120), are due

to the changes in the spacecraft spin axis pointing to +/−5° above and below the ecliptic plane, executed to facilitate interstellar neutral gas observations (e.g., Bzowski et al. 2015; Leonard et al. 2015; McComas et al. 2015; Möbius et al. 2015). The survival probabilities after orbit 294b were calculated using the latitudinal solar wind speed and density structure in latitude frozen in time due to the lack of more recent data, but with the in-ecliptic solar wind speed and density, as well as the photoionization rate and radiation pressure measurements taken into account. This is because the most recent information about the solar wind structure out of the ecliptic plane is available up to the middle of 2015 (see details of the model construction in Sokół et al. 2013).

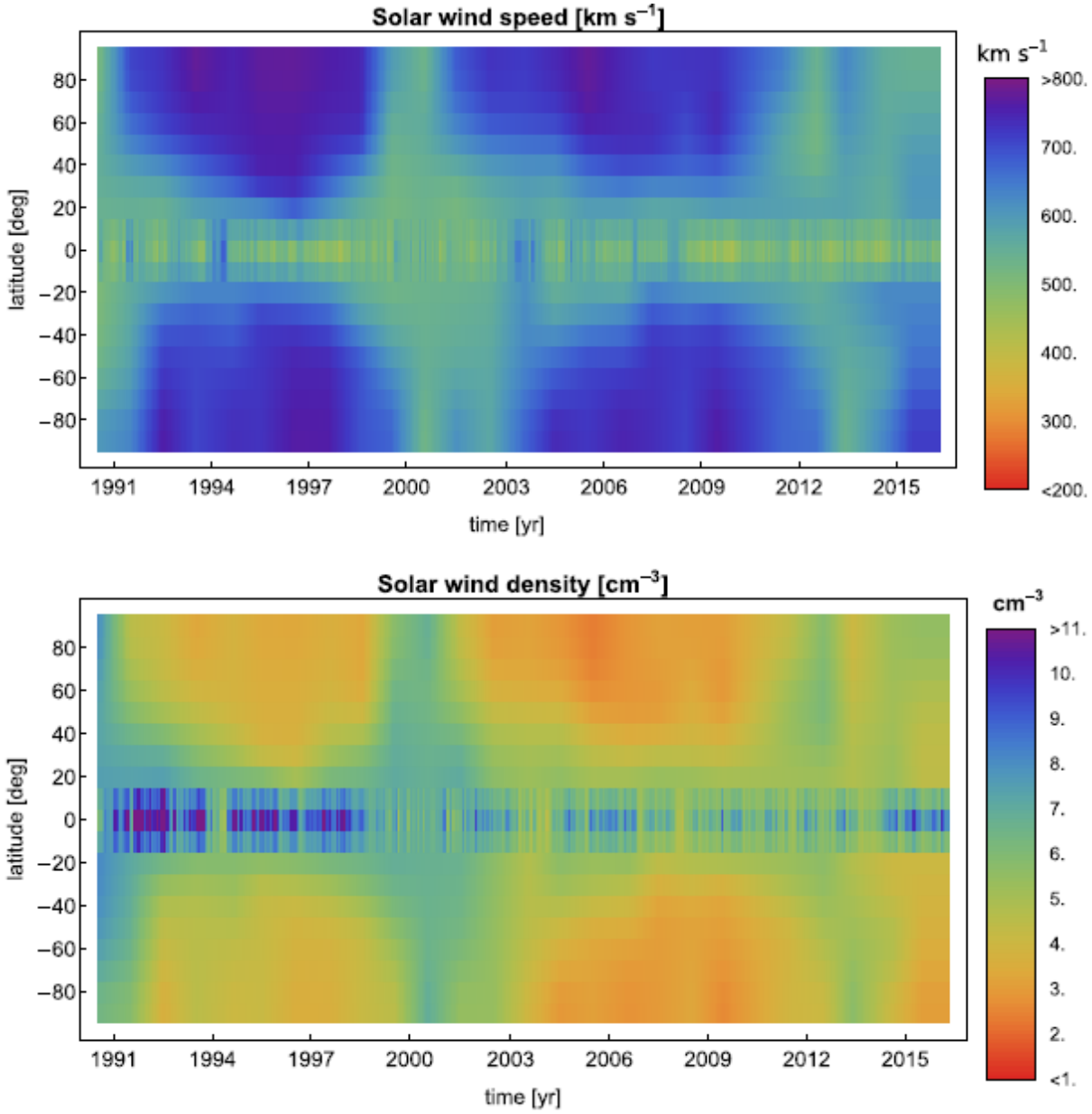

Figure 118: Maps of solar wind speed and density as a function of time and heliolatitude reconstructed following the model described in Sokół et al. (2013).

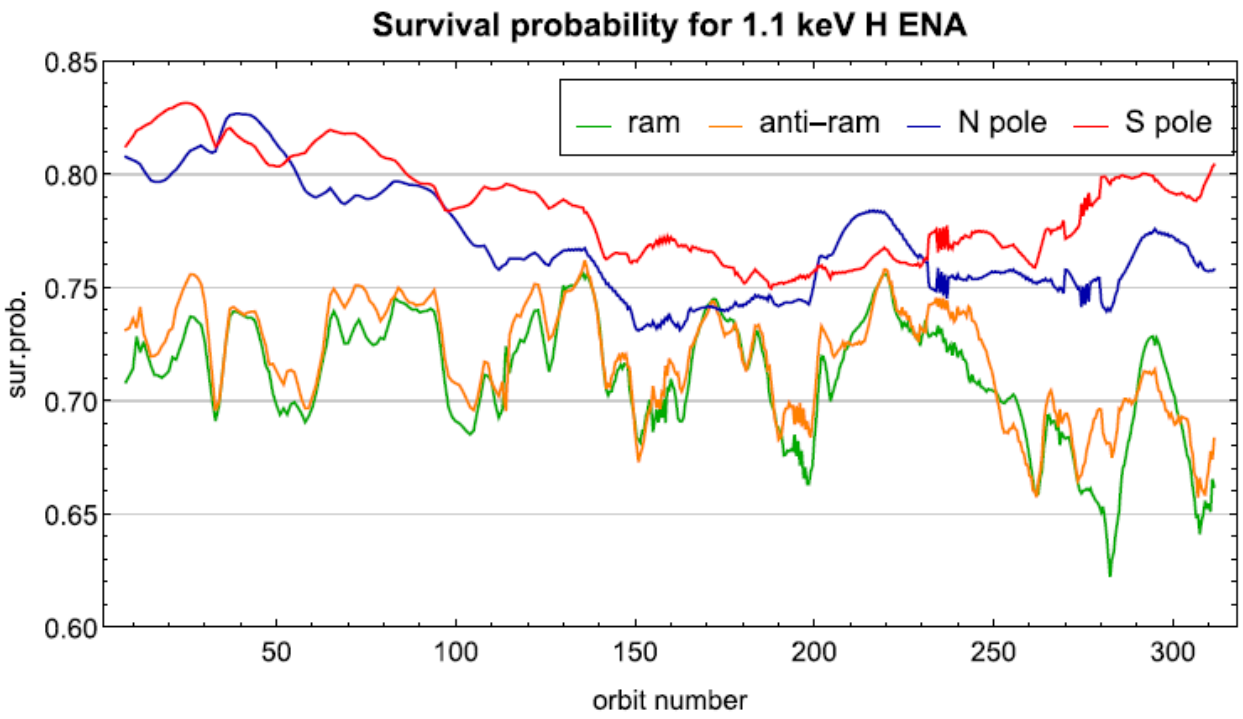

Figure 119: Survival probabilities for H ENAs for the 1.1 keV energy passband. Shows in-ecliptic pixel in the ram and anti-ram direction, and polar pixels toward the north and south.

The uncertainties of survival probabilities are related to the uncertainties of measurements of the contributing factors— that is, the solar wind speed and density, the spectral flux of the solar EUV radiation, and the relevant reaction cross sections. A discussion of these uncertainties for the case of H is provided by Bzowski et al. (2013b), and a detailed discussion of uncertainties of survival probabilities is presented by Bzowski et al. (2013a). In general, these uncertainties can be divided into a systematic uncertainty, affecting the probabilities for all energies and all times in a similar way, and the random measurement errors, which affect the probabilities for individual pixels. The first kind of uncertainty is of secondary importance for the spectra of ENAs measured by IBEX, but it does slightly affect the absolute flux of ENAs at their source region. Effectively, it shifts all the lines upward or downward in Figure 119 and Figure 120. The second kind of uncertainty affects the probabilities calculated for different pixels randomly. They are on the order of a few percent of the actual probability value. Note that this random scatter is small enough to maintain the small differences between survival probabilities for the orbits, with the IBEX spin axis shifted a few degrees away from the Sun in comparison with those where this shift was absent, as illustrated in Figure 120 for orbits 232a to 237a, as well as 270a to 279a.

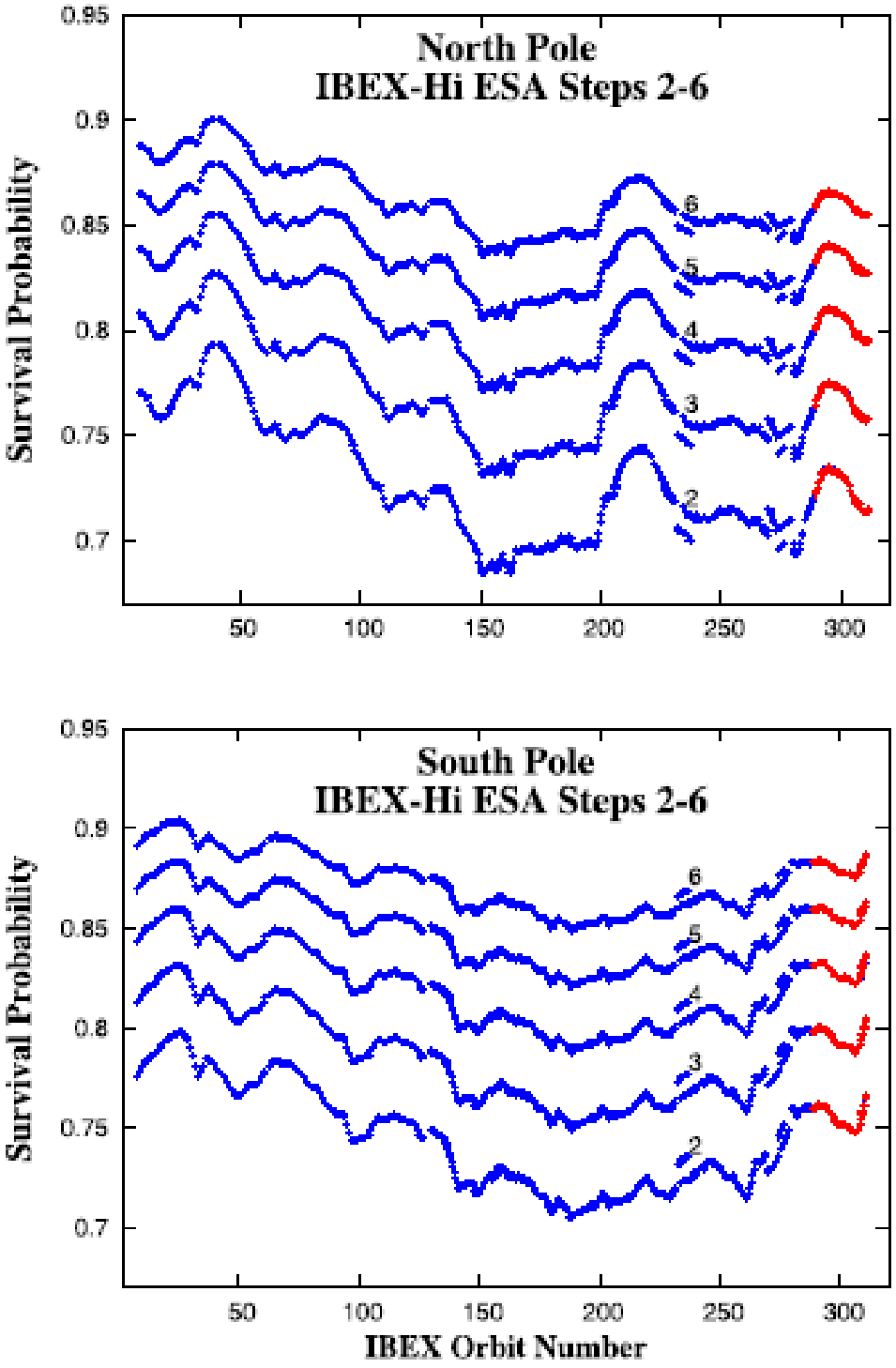

Figure 120: Calculated survival probabilities for ENAs observed in IBEX's northern (top) and southern (bottom) poles. Curves for the different ESA (energies) are indicated by the different number labels in each panel. The blue color marks the probabilities calculated using the full model of the relevant factors, and the red color is used for the probabilities calculated using extrapolations, needed due to the lack of measurements of the latitudinal structure of the solar wind.

5.6 IBEX Signal Estimates and Error Analysis

Table 30 shows the top-level measurement requirements for IBEX and shows how they map onto the different science questions and levels of study described in Section 3.1. Table 31 shows the actual measurement capabilities of IBEX. From this we can see that IBEX-Hi and IBEX-Lo combined exceed the measurement requirements shown in Table 30, both in terms of spatial resolution and in the number of energy steps. The pre-collimators and collimator set the intrinsic angular resolution of our measurements to ~6.5° FWHM in both sensors. In addition, IBEX-Lo has a higher angular resolution quadrant (~3.2° FWHM) that is used for direct detection of the low-energy interstellar oxygen. Table 32 and Table 33 show the baseline and minimum requirements on the IBEX mission as a part of NASA's Small Explorer (SMEX) program, all of which have been met or exceeded by IBEX.

Table 34 and Table 35 show the energy resolution information used to calculate fluxes for each energy step and for both double and triple coincidence types for both IBEX-Hi and IBEX-Lo, respectively. These energy ranges are determined by the ESA voltage settings for each energy step. The calculations for signal uncertainties are described in sections 5.3.2 and 5.4.1 for IBEX-Hi and IBEX-Lo, respectively

Table 30: IBEX top-level measurement requirements, including how they map onto the specific science questions and levels of study described in Section 3.1

The IBEX approach and measurement requirements				
The sole IBEX objective to discover the global interaction between the solar wind and the interstellar medium is achieved by answering four fundamental science questions				
Fundamental Science Questions / **Levels**	**I:** *TS Strength/ Structure*	**II:** *Energetic Protons Near TS*	**III:** *Solar Wind Flow Patterns of Inner Heliosheath*	**IV:** *Interstellar Flow and Interaction*
Discover (Straightforward interpretation of IBEX data products)	All-sky survey: strong vs. weak TS	Intensity and spectra of energetic protons near TS	Nose/tail asymmetries	First direct measurement of filtered interstellar neutral, O
Explore (Interpretation based on simple physics-based calculations and limited modeling)	All-sky map of shock strength	Modification of TS dynamics due to energetic particle pressure	Solar wind flow direction beyond TS vs. angle from the nose	Bulk speed, direction, and temperature of interstellar O inside TS
Understand (use data products to iteratively define, revise, and refine 3D models of the heliosphere)	-3D TS configuration incl. distance scale and strength -Energy partition of solar wind, pickup protons, and energetic protons	Bound injection processes at TS	-3D solar wind flow patterns beyond TS -LISM B	-Filtration -Ionized fraction of O in the LISM -Interstellar flow patterns beyond heliopause -Bow shock existence
Measurements Requirements				
Global heliospheric ENA imaging	7°x7° pixels	21°x21° pixels	7°x7° pixels	Determine O Direction to 2.0° FWHM
H energy spectra: Solar wind through energetic particle ENAs	0.01-1 keV in 7 energy bands	1-6 keV in 4 energy bands	0.01-1 keV in 7 energy bands	
O fluxes and velocity direction vs. time of year				0.01-0.5 keV in 6 energy bands

Raw Images

Detailed Models

TA050718 1

Table 31: Key IBEX payload parameters and resources

	IBEX-Hi	IBEX-Lo	CEU
Energy Range	300 eV–6.0 keV	10 eV–2 keV	N/A
Energy resolution ($\Delta E_{FWHM}/E$)	0.47–0.66	0.8	N/A
Number of Energy Steps	6	8	N/A
FOV (FWHM)	6.5° × 6.5°	6.5° × 6.5° 3.2° × 3.2°	N/A
Geometric Factor for H near 1 keV (double coincidence)	3×10^{-3} cm^2 sr eV/eV at 1.1 keV	8.1×10^{-4} cm^2 sr eV/eV at 0.78 keV	N/A
Geometric Factor for H near 1 keV (triple coincidence)	7.3×10^{-4} cm^2 sr eV/eV at 1.1 keV	2.9×10^{-4} cm^2 sr eV/eV at 0.78 keV	N/A
Mass	7.70 kg	12.09 kg	5.42 kg
Volume	43.94 cm Dia × 23.75 cm	40 cm Dia × 31.45 cm	43.82 cm × 27.9 cm × 9.5 cm
Power	0.7 W	3.5 W	11.2 W
Telemetry	102.6 bps	122.8 bps	11.8 bps

Table 32: The baseline requirements of the IBEX mission as part of NASA's SMEX program

Baseline Science Requirements
IBEX shall obtain global (at least 95% of 4π sr) ENA images unobscured by the magnetosphere over a period of two years
IBEX shall acquire images of ENAs from near the termination shock with an angular resolution no coarser than 7° x 7° FWHM.
IBEX shall measure the energy spectrum of heliospheric hydrogen at energies from 0.01-6 keV in 14 energy bands, at least 3 of which overlap between IBEX-Hi and IBEX-Lo
IBEX shall measure incoming oxygen atoms from the interstellar medium and determine their direction of arrival to within 2° FWHM
IBEX shall identify pixels that view the magnetosphere and remove them from the heliospheric data set as a separate magnetospheric data set
IBEX shall accumulate magnetospheric data in a separate data set

Table 33: The minimum success criteria of the IBEX mission as part of NASA's SMEX program

Minimum Science Requirements
IBEX shall obtain global (at least 50% of 4π sr) ENA images unobscured by the magnetosphere over a period of six months
IBEX shall acquire images of ENAs from near the termination shock with an angular resolution no coarser than 21° x 21° FWHM.
IBEX shall measure the energy spectrum of heliospheric hydrogen at energies from 0.5-4 keV in at least 4 energy bands.

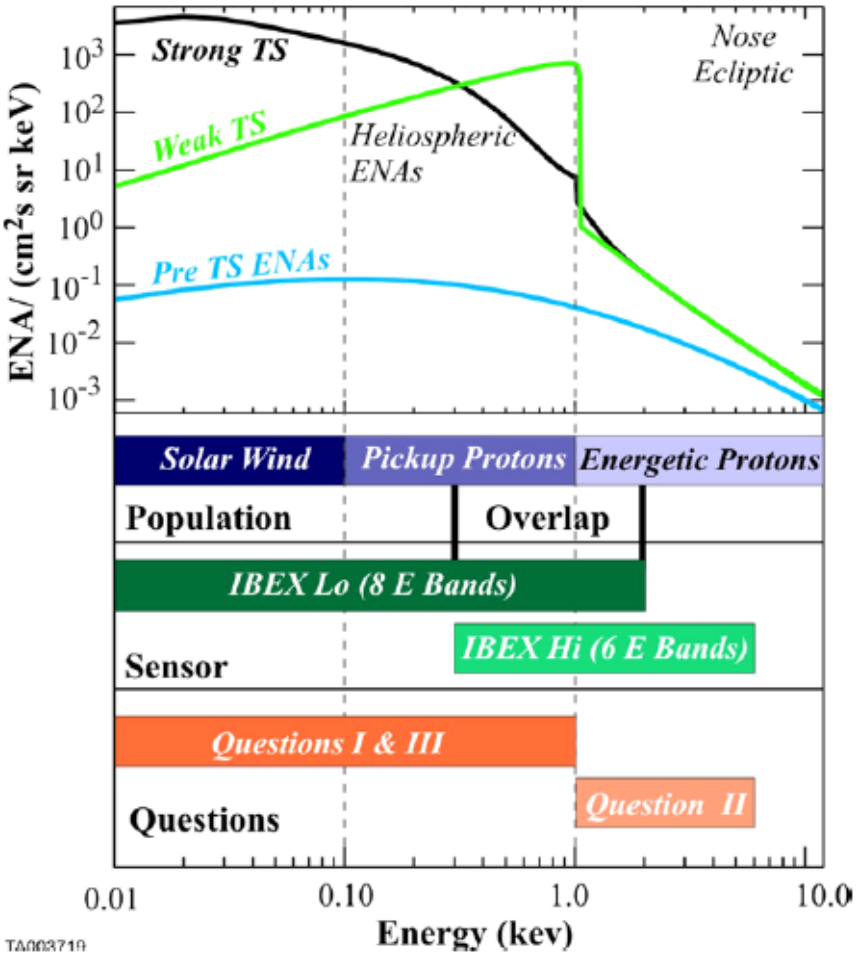

Figure 121: The IBEX H ENA energy range is designed to provide the critical distributions needed to reveal the global properties of the proton populations of the inner heliosheath. Shown here are predicted ENA energy distributions near the nose of the heliosphere for a strong (black curve) and weak (green curve) TS (Gruntman et al. 2001). These curves are for a nominal, slow (1 keV) solar wind. The blue curve shows the predicted ENA flux due to energetic protons inside the TS. Energetic ENA distributions >1 keV (black and green curves) are predicted from observed energetic proton tails (Gloeckler et al. 1994, 2000; Schwadron et al. 1996) assuming that the

intensity of the tails scale with the intensity of interstellar pickup protons (Vasyliunas and Siscoe 1976)

Table 34: Flight energy passbands for double and triple coincidence events as derived from the sensor end-to-end model for each of the six IBEX-Hi energy steps. The full-width-at-full-maximum values (E+FW − E−FW) represent the 99% level and central energy E0 represents the energy of the maximum (peak) value of the response function

ESA setting			Double coincidences: Long AB + Long BC + Qual(Not_C) AC					
ESA Step	Outer ESA [kV]	Inner ESA [kV]	E_{-FW} [keV]	E_{-HW} [keV]	E_0 [keV]	E_{+HW} [keV]	E_{-FW} [keV]	$\Delta E/E_0$ [keV]
1	−0.09	−0.78	0.26	0.38	0.45	0.58	0.75	0.20
2	−0.08	−1.28	0.36	0.57	0.78	0.98	1.25	0.41
3	−0.02	−1.85	0.62	0.89	1.21	1.56	1.91	0.68
4	0	−2.88	1.07	1.45	1.92	2.53	3.02	1.08
5	0	−4.46	1.68	2.15	2.80	3.82	4.54	1.67
6	0	−7.00	2.57	3.34	4.51	6.14	6.93	2.80
ESA setting			Triple coincidences: Qual(Not_C) ABC					
ESA Step	Outer ESA [kV]	Inner ESA [kV]	E_{-FW} [keV]	E_{-HW} [keV]	E_0 [keV]	E_{+HW} [keV]	E_{-FW} [keV]	$\Delta E/E_0$ [keV]
1	−0.09	−0.78	0.24	0.38	0.45	0.59	0.75	0.47
2	−0.08	−1.28	0.35	0.52	0.71	0.95	1.23	0.60
3	−0.02	−1.85	0.58	0.84	1.08	1.55	1.93	0.65
4	0	−2.88	1.07	1.36	1.85	2.50	3.02	0.62
5	0	−4.46	1.68	1.99	2.70	3.75	4.54	0.65
6	0	−7.00	2.57	3.13	4.09	6.00	6.93	0.70

Table 35: GΔE/E for the IBEX-Lo sensor, determined from calibration

Energy Step	Center Energy (eV)	$G\Delta E/E$ for any double coincidence hydrogen (cm^2 sr eV/eV)	$G\Delta E/E$ for triple coincidence hydrogen (cm^2 sr eV/eV)
1	14	7.5×10^{-5}	2.7×10^{-5}
2	27	1.5×10^{-4}	5.3×10^{-5}
3	52	2.2×10^{-4}	8.1×10^{-5}
4	102	2.5×10^{-4}	9.1×10^{-5}
5	197	2.5×10^{-4}	9.0×10^{-5}
6	451	2.9×10^{-4}	1.0×10^{-4}
7	908	5.4×10^{-4}	1.9×10^{-4}
8	1903	7.6×10^{-4}	2.7×10^{-4}

List of Variable Definitions

Variable	Definition
A	aperture area
b	lattitude
B	background rate
C	count rate; counts
E	particle energy; central energy
E_0	incident energy
F	ENA flux
G	geometric factor
G_m	gravitational constant
J	particle flux
k_F	foil constant
l	angular momentum; longitude; inverse probability of observing counts
m	atom mass
M	spin-phase distribution
M_s	solar mass
N	particle number density; number of data points
P	point spread function or transmission function; probability of observing counts
P(Ω)	point spread function
$p_n(t)$	probability of n events being stored in buffer at time t
r	count rate; radial distance from the Sun
R	signal rate; radial distance from the Sun
$R_i(E)$	sensor response function
S_p	survival probability
T	transparency of the collimator; transmission efficiency; transmission function; exposure time
t	time
V	bulk speed
v	particle speed
w	particle velocity
W	solar wind energy flux
α	NEP angle

γ	ratio of the total event rate to the rate of transmitted events
ΔE/E	throughput
ε	coicidence efficiency
ϵ	eccentricity
ζ	longitude
θ	incident beam angle
θ_{FWHM}	angle of FWHM
λ	transmisstion rate; flow angle
μ	ratio of radiation pressure to gravity
σ	variance
σ_{ψ}	width of the spin-angle distribution
τ	exposure time
ϕ	IBEX coordinate petpendicular to the spin phase line
ψ	lattitude; IBEX coordinate along spin axis
$\psi_{1/2}$	angular halfwidth of the scattered beam

List of Acronyms

Acronym	Definition
ACE	Advances Composition Explorer
ASCII	American Standard Code for Information
AU	Astronomical Unit
Bism	Latitude
C	Carbon; Celsius
C-G	Compton-Getting
D	Deuterium
D/H	Deuterium to Hydrogen Ratio
ENAs	Energetic Neutral Atoms
ESA	Electrostatic Analyzer
eV	Electron Volts
FWHM	Full Width at Half Maximum
GCRs	Galactic Cosmic Rays
H	Hydrogen
He	Helium
HS	Heliospheric
HSH	Heliosheath

HP	Heliopause
HQ	Headquarter
IBEX	Interstellar Boundary Explorer
IDL	Interactive Data Language
IHS	Inner Heliosheath
IMAGE	Imager for Magnetopause-to-Aurora Global Exploration
INCA	Ion and Neutral Camera
IPS	Interplanetary Scintillation
ISM	Interstellar Medium
ISN	Interstellar Neutral
ISOC	IBEX Science Operations Center
keV	kilo electron volts
LIC	Local Interstellar Cloud
LISM	Local Interstellar Medium
LISMF	Local Interstellar Magnetic Field
LOS	Line of Sight
LRO	Lunar Reconnaissance Orbiter
MeV	Mega electron Volts
MHD	Magnetohydrodynamic
MIDEX	Mid-size Explorer
MOC	Mission Operations Center
N & S	North and South directions
Ne	Neon
Ne/O	Neon to Oxygen
NASA	National Aeronautics and Space Administration
O	Oxygen
OHS	Outer Heliosheath
PI	Principal Investigator
PM	Prime Mission
PUIs	Pickup Ions
RTN	Radial, Transverse and Normal Coordinate System
SC	Spacecraft
SMEX	Small Explorer
SPDF	Space Physics Data Facility
SPICE	Simulation Program for Integrated Circuits Emphasis
SSR	Solid State Recorder
St	Starboard direction
STEREO	Solar Terrestrial Relations Observatory

SW	Solar Wind
SwRI®	Southwest Research Institute®
T	Temperature
TeV	Tera Electron Volts
TS	Termination Shock
UNH	University of New Hampshire
UV	Ultraviolet
V1	Voyager 1
V2	Voyager 2
WIND	NASA mission launched on November 1, 1994

Algorithms for Data Product Generation

Algorithms for Data Product Generation			
Data Release	**Algorithm**	**Supercedes**	**CMAD Section(s)**
1	IBEX rate calculation		5.3.2 (Hi); 5.4.1 (Lo)
2	Compton-Getting correction		5.5.2
4	IBEX-Hi cosmic ray background removal		5.3.4.1
	Survival probability correction calculations		5.5.3.1-5.5.3.3
6	Effects of radiation pressure on IBEX-Lo observations		5.4.9
	IBEX-Lo parameter fitting uncertainties		5.4.10
7	Variable cosmic ray background correction for IBEX-Hi	4	5.3.4.2
	Updated survival probability	4	5.5.3.4; 5.5.3.5
	IBEX-Hi efficiency over time		5.3.7
	Removal of ion gun background in IBEX-Hi		5.3.5
	Sputtering correction for IBEX-Lo		5.4.3.1
9	Correction for throughput reduction in IBEX-Lo interface buffer		5.4.11
	Two alternative derivations of peak latitude as function of longitude		5.4.12
	Transformation of model fluxes to IBEX-Lo rates		5.4.13
	Analysis of X^2 and calculations of uncertainties (Lo)		5.4.14
10	Updated survival probability corrections	7	5.5.3.6

	Instructions for combining IBEX ENA maps		5.5.1
11	Geometric factors for IBEX-Lo ISN O		5.4.3.1
	IBEX-Lo statistical and propagation uncertainties		5.4.16
	Minimization of X^2 for derivation of background rates and a model scaling factor for IBEX-Lo		5.4.17
	Maximum likelihood for deriving background rates and a model scaling factor for IBEX-Lo		5.4.18
	Statistical and propagation uncertainties in nonlinear forward models using X^2 minimization (Lo)		5.4.19
	Statistical and propagation uncertainties in nonlinear forward models using maximum likelihood (Lo)		5.4.20
	Sputtering correction for IBEX-Lo	7	5.4.7.2
	Geometric factors for IBEX-Lo		5.4.3

References

F. Allegrini, R.F. Wimmer-Schweingruber, P. Wurz, P. Bochsler, Measurement of the ion-induced electron yields from thin carbon foils for low energy ions. Nucl. Instr. Meth. B 211, 487 (2003)

F. Allegrini, D.J. McComas, D.T. Young, J.-J. Berthelier, J. Covinhes, J.-M. Illiano, J.-F. Riou, H.O. Funsten, R.W. Harper, Energy loss of 1–50 keV H, He, C, N, O, Ne, Ar ions transmitted through thin carbon foils. Rev. Sci. Instrum. 77, 044501 (2006)

Allegrini, F., Ebert, R. W., Alquiza, J., et al. 2008, RScI, 79, 096107

F. Allegrini, G.B. Crew, D. Demkee, H.O. Funsten, D.J. McComas, B. Randol, B. Rodriguez, P. Valek, S. Weidner, The IBEX background monitor. Space Sci. Rev. (2009)

Auchere, F. 2005, ApJ, 622, 737

Bame, S. J., McComas, D. J., Barraclough, B. L., et al. 1992, A&AS, 92, 237

V.B. Baranov, Y.G. Malama, Model of the solar wind interaction with the local interstellar medium: Numerical solution of self-consistent problem. J. Geophys. Res. 98, 15157 (1993)

V.B. Baranov, Y.G. Malama, Axisymmetric self-consistent model of the solar wind interaction with the LISM: Basic results and possible ways of development. Space Sci. Rev. 78, 305 (1996)

Bochsler, P., Petersen, L., Möbius, E., et al. 2012, ApJS, 198, 13

Burlaga, L. F. 1984, Space Sci. Rev., 39, 255

Bzowski, M., & Tarnopolski, S. 2006, in Proc. Fifth Annu. IGPP Astrophys. Conf., Physics of the Inner Heliosheath: Voyager Observations, Theory, and Future Prospects, ed. J. Heerikhuisen, V. Florinski, G. P. Zank, & N. V. Pogorelov (AIP CP-858; Melville, NY: AIP), 251

Bzowski, M. 2008, A&A, 488, 1057

Bzowski, M., Kubiak, M. A., M¨obius, E., et al. 2012a, ApJS, 198, 12

Bzowski, M., Sok´oł, J. M., Tokumaru, M., et al. 2012b, in Cross-Calibration of Past and Present Far UV Spectra of Solar Objects and the Heliosphere, Solar Parameters for Modeling Interplanetary Background, ed. R. M. Bonnet, E. Qu´emerais, & M. Snow (ISSI Scientific Report No. 12; Springer), chap. 2, in press (arXiv:1112.2967)

Bzowski, M., Sokół, J. M., Kubiak, M. A., & Kucharek, H. 2013a, A&A, 557, A50

Bzowski, M., Sokół, J. M., Tokumaru, M., et al. 2013b, in Cross-Calibration of Past and Present Far UV Spectra of Solar System Objects and the Heliosphere, Vol. 13, ed. R. M. Bonnet, E. Quémerais, & M. Snow (New York: Springer), 67

Bzowski, M., Swaczyna, P., Kubiak, M. A., et al. 2015, ApJS, 220, 28

Chowdhury, P., Choudhary, D. P., & Gosain, S. 2013, ApJ, 768, 188

Covington, A. E. 1969, J. R. Soc. Canada, 63, 125

D.A. Dahl, SIMION for the personal computer in reflection. Int. J. Mass Spectrom. 200, 3 (2000)

R.B. Decker, S.M. Krimigis, E.C. Roelof, M.E. Hill, T.P. Armstrong, G. Gloeckler, D.C. Hamilton, L.J. Lanzerotti, Voyager 1 in the foreshock, termination shock, and heliosheath. Science 309, 2020 (2005)

Franz, M., & Harper, D. 2002, Planet. Space Sci., 50, 217

H.O. Funsten, D.J. McComas, B.L. Barraclough, Thickness uniformity and pinhole density analysis of thin carbon foils using keV ions. Nucl. Instrum. Meth. B 66, 470 (1992)

H.O. Funsten, D.J. McComas, B.L. Barraclough, Ultrathin foils used for low energy neutral atom imaging of planetary magnetospheres. Opt. Eng. 32, 3090 (1993)

H.O. Funsten, D.J. McComas, M.A. Gruntman, Energetic neutral atom imaging of the outer heliosphere– LIC interaction region, in The Outer Heliosphere: The Next Frontiers, ed. by K. Scherer, H. Fichtner, H.-J. Fahr, E. Marsch. COSPAR Colloquia Series, vol. 11 (Pergamon, New York, 2001), pp. 237–244

H.O. Funsten, R.W. Harper, D.J.McComas, Absolute detection efficiency of space-based ion mass spectrometers and neutral atom imagers. Rev. Sci Instrum. 76, 053301 (2005)

H. Funsten, F. Allegrini, D. Everett, S. Fuselier, R.W. Harper, P. Janzen, A. Guthrie, D. McComas, E. Moebius, S. Pope, D. Reisenfeld, S. Weidner, Interstellar boundary explorer high energy (IBEX-Hi) neutral atom imager. Space Sci. Rev. (2009a)

Funsten, H. O., Allegrini, F., Crew, G. B., et al. 2009b, Science, 326, 964

S.A. Fuselier, A.G. Ghielmetti, E. Hertzberg, A. Moore, D. Isaac, J. Hamilton, C. Tillier, E. Moebius, M. Granoff, D. Heirtzler, B. King, H. Kucharek, S. Longworth, J. Nolin, S. Turco, P. Wurz, M. Wieser, J. Scheer, L. Saul, C. Schlemm, D.J. McComas, D. Chornay, J. Lobell, T. Moore, P. Rosmarynowski, R.J. Nemanich, T. Friedmann, H. Funsten, The IBEX-Lo sensor for the IBEX mission. Space Sci. Rev. (2009a)

Fuselier, S. A., Bochsler, P., Chornay, D., et al. 2009b, Space Sci. Rev., 146, 117

Fuselier, S. A., Funsten, H. O., Heirtzler, D., et al. 2010, GeoRL, 37, L13101

Fuselier, S. A., Allegrini, F., Bzowski, M., et al. 2012, ApJ, 754, 14

A. Galli, P. Wurz, S. Barabash, A. Grigoriev, R. Lundin, Y. Futaana, H. Gunell, M. Holström, E.C. Roelof, C.C. Curtis, K.C. Hsieh, A. Fedorov, D. Winningham, R.A. Fram, R. Cerulli-Irelli, P. Bochsler, N. Krupp, J. Woch, M. Fraenz, Direct measurements of energetic neutral hydrogen in the interplanetary medium. Astrophys. J. 644, 1317 (2006).

A.G. Ghielmetti, E.G. Shelley, S.A. Fuselier, F. Herrero, M.F. Smith, P. Wurz, P. Bochsler, T. Stephen, Mass spectrograph for imaging low energy neutral atoms, in Instrumentation for Magnetospheric Imaging II, ed. by S. Chakrabarti, Proc. SPIE 2008, pp. 105–112, 1993; Opt. Eng. 33, 362 (1994)

J. Giacalone, in The Outer Heliosphere: The Next Frontiers, ed. by K. Scherer, H. Fichtner, H.J. Fahr, E. Marsch. COSPAR Colloquia Series, vol. 11 (Pergamon, Elmsford, 2001), p. 377

G. Gloeckler et al., Acceleration of interstellar pickup ions in the disturbed solar wind observed on Ulysses. J. Geophys. Res. 99, 17637 (1994)

G. Gloeckler, L.A. Fisk, T.H. Zurbuchen, N.A. Schwadron, Sources, injection and acceleration of heliospheric ion populations, in Acceleration and Transport of Energetic Particles Observed in the Heliosphere: ACE 2000 Symposium, ed. by R.A. Mewaldt et al. AIP Conference Proceedings, vol. 528 (AIP, New York, 2000), p. 221

Gosling, J. T., Baker, D. N., Bame, D. N., et al. 1985, JGR, 90, 6354

Gruntman, Magnetospheric imaging (1993)

M. Gruntman, Energetic neutral atom imaging of space plasmas. Rev. Sci. Instrum. 68(10), 3617 (1997)

M.A. Gruntman, A.A. Kozochkina, V.B. Leonas, Multielectron secondary emission from thin foils bombarded by accelerated beams of atoms. JETP Lett. 51, 22 (1990)

M. Gruntman, E.C. Roelof, D.G. Mitchell, H.J. Fahr, H.O. Funsten, D.J. McComas, Energetic neutral atom imaging of the heliospheric boundary region. J. Geophys. Res. 106, 15,767–15,781 (2001)

J. Heerikhuisen, N.V. Pogorelov, V. Florinski, G.P. Zank, J.A. le Roux, The effects of a κ-distribution in the heliosheath on the global heliosphere and ENA flux at 1 AU. Astrophys. J. 682(1), 679–689 (2008)

Hirahara, M., Terasawa, T., Mukai, T., et al. 1997, JGR, 102, 2359

Hovestadt, D., Hilchenbach, M., Burgi, A., et al. 1995, Sol. Phys., 162, 441

S. Jans, P. Wurz, R. Schletti, T. Fröhlich, E. Hertzberg, S. Fuselier, Negative ion production by surface ionization using aluminum-nitride surfaces. J. Appl. Phys. 85, 2587 (2000)

D.C. Jones, J.D. Bernardin, Thermal modeling and experimental verification of the interstellar boundary explorer's high energy neutral atom imaging instrument (IBEX-Hi), 2007 AIAA InfoTech at Aerospace Conference (2007), vol. 3, pp. 2364–2375

Judge, D. L., McMullin, D. R., Ogawa, H. S., et al. 1998, Sol. Phys., 177, 161

Kasper, J. C., Stevens, M. L., Lazarus, A. J., et al. 2007, ApJ, 660, 901

King, J. H., & Papitashvili, N. E. 2005, J. Geophys. Res., 110, A02104

R. Korde, C. Prince, D. Cunningham, R.E. Vest, E. Gullikson, Present status of radiometric quality silicon photodiodes. Metrologia 40, S145 (2003)

A.A. Kozochkina, V.B. Leonas, V.E. Fine, Statistics of heavy particle-induced electron emission from a foil, in Ionization of Solids by Heavy Particles, ed. by R.A. Baragiola (Plenum, New York, 1993), pp. 223– 237

Kubiak, M. A., Swaczyna, P., Bzowski, M., et al. 2016, ApJS, 223, 25

Le Chat, G., Issautier, K., & Meyer-Vernet, N. 2012, SoPh, 279, 197

M. Lee, Acceleration of energetic particles on the Sun, the heliosphere, and in the galaxy, in Acceleration and Transport of Energetic Particles Observed in the Heliosphere, ed. by R.A. Mewaldt, J.R. Jokipii, M.A. Lee, E. Möbius, T.H. Zurbuchen. AIP Conf. Proceedings, vol. 528 (AIP, New York, 2000), p. 3

Lee, M. A., Kucharek, H., M¨obius, E., et al. 2012, ApJS, 198, 10

Leonard, T. W., Möbius, E., Bzowski, M., et al. 2015, ApJ, 804, 42

T.J. Linde, A three-dimensional adaptive multifluid MHD model of the heliosphere. Thesis (Ph.D.) The University of Michigan, Ann Arbor, Source DAI-B 59/02, p. 709 (1998)

T.J. Linde, T.I. Gombosi, P.L. Roe, K.G. Powell, D.L. Dezeeuw, Heliosphere in the magnetized local interstellar medium—Results of a three-dimensional MHD simulation. J. Geophys. Res. 103, 1889 (1998)

Lindsay, B. G., & Stebbings, R. F. 2005, J. Geophys. Res., 110, A12213

Livadiotis, G. 2007, PhyA, 375, 518

A. Marti, R. Schletti, P. Wurz, P. Bochsler, Calibration facility for solar wind plasma instruments. Rev. Sci. Instrum. 72, 1354 (2001)

McComas, D. J., Barraclough, B. L., Funsten, H. O., et al. 2000, J. Geophys. Res., 105, A5, 10419

McComas, D. J., Elliot, H. A., Gosling, J. T., et al. 2002, Geophys. Res. Lett., 29, 1290

McComas, D. J., Elliot, H. A., Gosling, J. T., & Skoug, R. M. 2006, Geophys. Res. Lett., 33, L09102

McComas, D. J., Ebert, R. W., Elliott, H. A., et al. 2008, Geophys. Res. Lett., 35, L18103

D.J. McComas, F. Allegrini, C.J. Pollock, H.O. Funsten, S. Ritzau, G. Gloeckler, Ultra-thin (~10 nm) carbon foils in space instrumentation. Rev. Sci. Instrum. 75(11), 4863–4870 (2004)

D.J.McComas, F. Allegrini, J. Baldonado, B. Blake, P.C. Brandt, J. Burch, J.

Clemmons,W. Crain, D. Delapp, R. DeMajistre, D. Everett, H. Fahr, L. Friesen, H. Funsten, J. Goldstein, M. Gruntman, R. Harbaugh, R. Harper, H. Henkel, C. Holmlund, G. Lay, D. Mabry, D. Mitchell, U. Nass, C. Pollock, S. Pope,M. Reno, S. Ritzau, E. Roelof, E. Scime, M. Sivjee, R. Skoug, T.S. Sotirelis, M. Thomsen, C. Urdiales, P. Valek, K. Viherkanto, S.Weidner, T. Ylikorpi,M. Young, J. Zoennchen, The TwoWide-angle Imaging Neutralatom Spectrometers (TWINS) NASA mission-of-opportunity. Space Sci. Rev. 142, 157 (2009a)

McComas, D.J., Allegrini, F., Bochsler, P. et al. IBEX—Interstellar Boundary Explorer. Space Sci Rev 146, 11–33 (2009). https://doi.org/10.1007/s11214-009-9499-4

McComas, D. J., Alexashov, D., Bzowski, M., et al. 2012a, Sci, 336, 1291

McComas, D. J., Dayeh, M. A., Allegrini, F., et al. 2012b, ApJS, 203, 1

McComas, D. J., Dayeh, M. A., Allegrini, F., et al. 2012c, ApJS, 203, 1

McComas, D. J., Angold, N., Elliott, H. A., et al. 2013, ApJ, 779, 2

McComas, D. J., Allegrini, F., Bzowski, M., et al. 2014, ApJS, 213, 20

McComas, D. J., Bzowski, M., Fuselier, S. A., et al. 2015, ApJS, 220, 22

E. Möbius, D. Hovestadt, B. Klecker, L.M. Kistler, M.A. Popecki, K.N. Crocker, F. Gliem, M. Granoff, S. Turco, A. Anderson, H. Arbinger, S. Battell, J. Cravens, P. Demain, J. Distelbrink, I. Dors, P. Dunphy, J. Gaidos, J. Googins, A. Harasim, R. Hayes, G. Humphrey, H. Kästle, E. Künneth, J. Lavasseur, E.J. Lund, R. Miller, G. Murphy, E. Pfeffermann, K.-U. Reiche, E. Sartori, J. Schimpfle, E. Seidenschwang, M. Shappirio, K. Stöckner, S.C. Taylor, M. Vosbury, W. Wiewesiek, V. Ye, The solar energetic particle ionic charge analyzer (SEPICA) and the data processing unit (S3DPU) for SWICS, SWIMS and SEPICA. Space Sci. Rev. 86, 447 (1998)

E. Möbius, L.M. Kistler, M. Popecki, K. Crocker, M. Granoff, Y. Jiang, E. Sartori, V. Ye, H. Rème, J.A. Sauvaud, A. Cros, C. Aoustin, T. Camus, J.L. Médale, J. Rouzaud, C.W. Carlson, J.P. McFadden, D.W. Curtis, H. Heetderks, J. Croyle, C. Ingraham, E.G. Shelley, D. Klumpar, E. Hertzberg, B. Klecker, M. Ertl, F. Eberl, H. Kästle, E. Künneth, P. Laeverenz, E. Seidenschwang, G.K. Parks, M. McCarthy, A. Korth, B. Gräwe, H. Balsiger, U. Schwab, M. Steinacher, The 3-D plasma distribution function analyzers with time-of-flight mass discrimination for CLUSTER, FAST and Equator-S, measurement techniques in space plasmas, ed. by R. Pfaff, J. Borowski, D. Young. Geophys. Monograph 102 (1998b), p. 243

E. Möbius, S. Fuselier, M. Granoff, E. Hertzberg, B. King, H. Kucharek, S. Livi, S. Longworth, N. Paschalidis, L. Saul, J. Scheer, C. Schlemm, M. Wieser, P. Wurz, Time-of-flight detector system of the IBEXLo sensor with low background performance for heliospheric ENA detection, Proc. of the 30th Int. Cosmic Ray Conf., on CD (2007)

E. Moebius, H. Kucharek, L. Petersen, M. Bzowski, L. Saul, P. Wurz, S. Fuselier, V. Izmodenov, D. Mc- Comas, H. Mueller, D. Alexashov, Diagnosing the neutral interstellar gas flow at 1 AU with IBEX-Lo. Space Sci. Rev. 2009

Mobius, E., Bochsler, P., Bzowski, M., et al. 2012, ApJS, 198, 11

Möbius, E., Bzowski, M., Frisch, P. C., et al. 2015a, ApJS, 220, 24

H. Moestue, The electric field and geometrical factor of an annular curved plate electrostatic analyzer. Rev. Sci. Instrum. 44, 1709–1713 (1973)

T.E. Moore, D.J. Chornay, M.R. Collier, F.A. Herrero, J. Johnson, M.A. Johnson, J.W. Keller, J.F. Laudadio, J.F. Lobell, K.W. Ogilvie, P. Rozmarynowsky, S.A. Fuselier, A.G. Ghielmetti, E. Hertzberg, D.C. Hamilton, R. Lundgren, P. Wilson, P. Walpole, T.M. Stephen, B.L. Peko, B. Zyl, P. Wurz, J.M. Quinn, G.R. Wilson, The low-energy neutral atom imager for IMAGE, in The IMAGE Mission, ed. by J.L. Burch. (Kluwer, Dordrecht, 2000). Space Sci. Rev. 91 (2000), pp. 155–195

H.-R. Müller, G.P. Zank, A.S. Lipatov, Self-consistent hybrid simulations of the interaction of the heliosphere with the local interstellar medium. J. Geophys. Res. 105(A12), 27419–27438 (2000)

Park, J., Kucharek, H., Möbius, E., et al. 2014, ApJ, 795, 97

Park, J., Kucharek, H., Möbius, E., et al. 2015, ApJS, 220, 34

N.P. Paschalidis et al., A CMOS time of flight system on a chip for spacecraft instrumentation. IEEE Trans. Nucl. Sci. 49, 1156–1163 (2002)

N.P. Paschalidis, Advanced system on a chip microelectronics for spacecraft and science instruments. Acta Astronaut. 52(2–6), 411–420 (2003)

G. Paschmann, E.G. Shelley, C.R. Chappell, R.D. Sharp, L.F. Smith, Rev. Sci. Instrum. 41, 1706 (1970)

Pollock et al., Medium energy neutral atom (MENA) imager for the IMAGE mission, in The IMAGE Mission, ed. by J.L. Burch (Kluwer, Dordrecht, 2000), pp. 113–154

Pryor, W. R., Ajello, J. M., Barth, C. A., et al. 1992, ApJ, 394, 363

F.H. Read, N.J. Bowring, P.D. Bullivant, R.R.A. Ward, Penetration of electrostatic fields and potentials through meshes, grids, or gauzes. Rev. Sci. Instrum. 69, 2000 (1998)

W.K.M. Rice, G.P. Zank, J.A. Le Roux, An injection mechanism for shock waves of arbitrary obliquity. Geophys. Res. Lett. 27, 3793–3796 (2000)

S.M. Ritzau, R.A. Baragiola, Electron emission from carbon foils induced by keV ions. Phys. Rev. B 58, 2529 (1998)

Roelof, E. 1987, GeoRL, 14, 652

E. Roelof, M. Bzowski, Motion of neutrals and ENA inversion. Space Sci. Rev. (2009)

Saul, L., Wurz, P., Rodriguez, D., et al. 2012, ApJS, 198, 14

J.A. Scheer, M. Wieser, P. Wurz, P. Bochsler, E. Hertzberg, S.A. Fuselier, F.A. Koeck, R.J. Nemanich, M. Schleberger, High negative ion yield from light molecule scattering. Nucl. Instr. Meth. Phys. Res. B 230(1–4), 330–339 (2005). doi:10.1016/j.nimb.2004.12.063

J.A. Scheer, M. Wieser, P. Wurz, P. Bochsler, E. Hertzberg, S.A. Fuselier, F.A. Koeck, R.J. Nemanich, M. Schleberger, Conversion surfaces for neutral particle imaging detectors. Adv. Space Res. 38(4), 664–671 (2006)

J. Scheer, P. Wahlström, P. Wurz, E. Hertzberg, S. Fuselier, Scattering properties of hydrogen and oxygen on artificial diamond surfaces using in space flight, Nucl. Instr. Meth. B (2008)

Scherrer, J., Carrico, J., Crock, J. et al. The IBEX Flight Segment. Space Sci Rev 146, 35–73 (2009). https://doi.org/10.1007/s11214-009-9514-9

N.A. Schwadron, L.A. Fisk, G. Gloeckler, Statistical acceleration of interstellar pickup ions in corotating interaction regions. Geophys. Res. Lett. 23, 2871 (1996)

Schwadron, N. A., Crew, G., Vanderspek, R., et al. 2009, SSRv, 146, 207

Schwadron, N. A., Allegrini, F., Bzowski, M., et al. 2011, ApJ, 731, 56

Schwadron, N. A., Möbius, E., Kucharek, H., et al. 2013, ApJ, 775, 86

Schwadron, N. A., Möbius, E., Leonard, T., et al. 2015, ApJS, 220, 25

E.G. Shelley, A.G. Ghielmetti, H. Balsiger, R.K. Black, J.A. Bowles, R.P. Bowman, O. Bratschi, J.L. Burch, C.W. Carlson, A.J. Coker, J.F. Drake, J. Fischer, J. Geiss, A. Johnstone, D.L. Kloza, O.W. Lennartsson, A.L. Magoncelli, G. Paschmann, W.K. Peterson, H. Rosenbauer, T.C. Sanders, M. Steinacher, D.M. Walton, B.A. Whalen, D.T. Young, The toroidal imaging mass-angle spectrograph (TIMAS) for the Polar mission. Space Sci. Rev. 71, 497 (1995)

Sok´oł, J. M., Bzowski, M., Tokumaru, M., et al. 2012, Sol. Phys.,

Sok´oł, J. M., Bzowski, M., Tokumaru, M., et al. 2013, SoPh, 285, 167

Sokół, J. M., Swaczyna, P., Bzowski, M., & Tokumaru, M. 2015, SoPh, 290, 2589

Spence, H. E., Case, A. W., Golightly, M. J., et al. 2010, Space Sci. Rev., 150, 243

Tapping, K. F. 1987, J. Geophys. Res., 92, 829

Tarnopolski, S., & Bzowski, M. 2009, A&A, 493, 207

Tokumaru, M., Kojima, M., & Fujiki, K. 2010, J. Geophys. Res., 115, A04102

Tokumaru, M., Kojima, M., Fujiki, K., et al. 2011, RaSc, 46, RS0F02

Tokumaru, M., Kojima, M., & Fujiki, K. 2012, JGR, 117, A06108

O.L. Vaisberg et al., Complex plasma analyzer SKA-1, in Interball: Mission and Payload, ed. by A.A. Galeev (Russian Space Agency–French Space Agency, 1995), pp. 170–177

V.M. Vasyliunas, G.L. Siscoe, On the flux and the energy spectrum of interstellar ions in the solar system. J. Geophys. Res. 81, 1247 (1976)

Viereck, R., & Puga, L. C. 1999, J. Geophys. Res., 104, 9995

Viereck, R. A., Floyd, L. E., Crane, P. C., et al. 2004, SpaceWeather, 2, S10005

P. Wahlström, J. Scheer, P. Wurz, E. Hertzberg, S. Fuselier, Calibration of charge state conversion surfaces for neutral particle detectors. J. Appl. Phys. 104, 034503-1–034503-6 (2008). doi:10.1063/1.2957064

M. Wieser, P. Wurz, Production of a 10 eV—1000 eV neutral particle beam using surface neutralization. Meas. Sci. Technol. 16, 2511–2516 (2005)

M.Wieser, P.Wurz, R.J. Nemanich, S.A. Fuselier, Secondary electron emission of chemical-vapor-deposited diamond by impact of slow H+, D+, H+ 2 , C+, O+, and O+ 2 ions. J. Appl. Phys. 98, 034906 (2005). doi:10.1063/1.1996855

M. Wieser, P. Wurz, E. Möbius, S.A. Fuselier, E. Hertzberg, D.J. McComas, The ion-optical prototype of the low energy neutral atom sensor of the interstellar boundary explorer mission (IBEX). Rev. Sci. Instr. 78, 124502-1–124502-14 (2007)

M. Wieser, P. Wurz, E. Möbius, S.A. Fuselier, E. Hertzberg, D.J. McComas, Development of the low energy neutral atom sensor of the Interstellar Boundary Explorer Mission (IBEX). Rev. Sci. Instrum. (2008)

Woods, T. N., Eparvier, F. G., Bailey, S. M., et al. 2005, J. Geophys. Res., 110, A01312

P. Wurz, Detection of energetic neutral particles, in The Outer Heliosphere: Beyond the Planets, ed. by K. Scherer, H. Fichtner, E. Marsch (Copernicus Gesellschaft e.V., Katlenburg-Lindau, 2000), pp. 251–288

P.Wurz, P. Bochsler, A.G. Ghielmetti, E.G. Shelley, F. Herrero, M.F. Smith, Concept for the Hi-LITE neutral atom imaging instrument, in ed. by P. Varga and G. Betz, Proceedings of Symposium on Surface Science, Kaprun, Austria (1993), p. 225

P. Wurz, R. Schletti, M.R. Aellig, Hydrogen and oxygen negative ion production by surface ionization using diamond surfaces. Surf. Sci. 373, 56–66 (1997)

P. Wurz et al., Formation of negative ions by scattering from a diamond (111) surface, in Proc. of the Week of Doctoral Students, ed. by J. Safrankova, A. Koruka (Charles University, Prague, 1998), p. 257

P. Wurz, J. Scheer, M. Wieser, Particle scattering off surfaces: application in space science. e-J. Surf. Sci. Nanotechnol., 4, 394–400 (2006)

P. Wurz, L. Saul, J.A. Scheer, E. Möbius, H. Kucharek, S.A. Fuselier, Negative helium generation upon surface scattering: Application in space science. J. Appl. Phys. 103, 054905 (2008a)

P.Wurz, A. Galli, S. Barabash, A. Grigoriev, Energetic neutral atoms from the heliosheath. Astrophys. J. 683, 248–254 (2008)

P. Wurz, J. Scheer, L. Saul, M. Wieser, S.A. Fuselier, A.G. Ghielmetti, E. Hertzberg, E. Moebius, H. Kucharek, P. Brandt, D. McComas, F. Allegrini, H. Funsten, IBEX Backgrounds and signal to noise ratio. Space Sci. Rev. (2009)

G.P. Zank, H.L. Pauls, L.L. Williams, D.T. Hall, Interaction of the solar wind with the local interstellar medium: A multifluid approach. J. Geophys. Res. 101, 21639 (1996)

J.F. Ziegler, J.P. Biersack, U. Littmark, Stopping and Range of Ions in Solids, vol. 1 (Pergamon, New York, 1985)